UNIVERSITY OF OKLAHOMA

GRADUATE COLLEGE

SPIN-MIXING AND INTERFEROMETRY IN MICROWAVE-DRESSED SODIUM SPINOR BOSE-EINSTEIN CONDENSATES

A DISSERTATION

SUBMITTED TO THE GRADUATE FACULTY

in partial fullfillment of the requirements for the

Degree of

Doctor of Philosophy

By

SHAN ZHONG
Norman, Oklahoma
2022

Downloaded from SHAREOK. Persistent Handle URL: https://hdl.handle.net/11244/336886

SPIN-MIXING AND INTERFEROMETRY IN MICROWAVE-DRESSED SODIUM SPINOR BOSE-EINSTEIN CONDENSATES

A DISSERTATION APPROVED FOR THE
HOMER L. DODGE DEPARTMENT OF PHYSICS AND ASTRONOMY

BY THE COMMITTEE CONSISTING OF

Dr. Arne Schwettmann, Chair

Dr. Doerte Blume

Dr. Alberto Marino Valle

Dr. Lloyd A. Bumm

Dr. Bin Wang

© Copyright by SHAN ZHONG 2022
All Rights Reserved.

In memory of my grandfather

Acknowledgements

I want to acknowledge many people who helped me through this fantastic journey. First, I would like to express my sincere gratitude to my thesis advisor Dr. Arne Schwettmann, who introduced ultracold quantum gases and advised me throughout my Ph.D. study. It has been a truly rewarding and privileged experience to perform my Ph.D. study under his guidance. I could not have done this without his help. I also want to thank my doctoral committee members, Dr. Arne Schwettmann, Dr. Alberto M. Marino, Dr. Doerte Blume, Dr. Lloyd A. Bumm, and Dr. Bin Wang, for their advice and support during my Ph.D. study.

Next, I would like to thank our collaborators, Dr. Doerte Blume, Dr. Jianwen Jie, and Dr. Qingze Guan, for their outstanding theoretical support and insights on the spin-mixing dynamics experiment. I benefited a lot from the weekly spinor meetings and discussions. I also would like to thank Dr. Alberto M. Marino for offering me a postdoc position so I can continue to explore some exciting physics and pursue my dream.

During my seven-plus years at the University of Oklahoma, I had unique experiences working with many wonderful people on the research team. Many thanks to my current colleagues, Hio Giap Ooi, Sankalp Prajapati, and Sean A. Manley. Special thanks to Dr. J. E. Furneaux, who is very professional and knowledgeable in laser and optics design. I learned a lot from him. I also want to thank the former member Dr. Qimin Zhang, Isaiah Morgenstern, Anita Bhagat, and Delaram Nematollahi for their friendship and dedicated teamwork.

Moreover, I would like to express my appreciation to Chad Cunningham, who is the supervisor of the electronic and instrument shop. Chad was the first person who came into my mind if we needed to build something in the lab. I also want to thank the former and current members of the machine shop for helping us design and make

lab instruments.

Last but not least, I would like to express my profound gratitude to my parents, Chengguo Zhong and Yuxia Ma, for providing unfailing support and continuous encouragement throughout my years of study and through researching and writing this thesis.

Table of Contents

List of Tables **ix**

List of Figures **xxi**

Abstract **xxii**

1 Introduction **1**
1.1 Background 1
1.2 Thesis Summary 4

2 Theory of Laser Cooling and Trapping **6**
2.1 Laser Cooling with Near-resonant Light 6
2.1.1 Doppler Cooling 7
2.1.2 Sub-Doppler Cooling 10
2.2 Magneto-optical Trap 14
2.3 Optical Dipole Force 18
2.3.1 Optical Dipole Trap 19
2.3.2 Evaporative Cooling 21

3 Vacuum System **24**
3.1 Overview of the Vacuum System 24
3.1.1 Na Vapor Generation 25
3.1.2 Zeeman Slower Design 29
3.1.3 UHV Main Chamber 30
3.1.4 Pumping Mechanisms 31
3.2 Cleaning, Assembling, Baking and Pumping the UHV Parts 35
3.2.1 UHV Components Cleaning 35
3.2.2 UHV Components Assembling 36
3.2.3 UHV System Baking and Pumping 37
3.3 Sodium Replacement and Vacuum Maintenance 40
3.3.1 System Venting 40
3.3.2 Sodium Replacement 40
3.3.3 Nozzle Cleaning 41
3.3.4 UV LIAD 42

4 Laser Cooling and Trapping Setup **44**
4.1 Main Laser System 44
4.1.1 Saturated Absorption Spectroscopy 45
4.1.2 Main Laser Setup 51
4.2 Zeeman Slower 56
4.2.1 Zero-crossing Zeeman Slower 57
4.2.2 Zero-crossing Zeeman Slower Design 58
4.3 3D MOT 62
4.3.1 MOT Setup 62
4.3.2 Water-cooling of MOT Coils 64

4.3.3 MOT Coils Electrical System . . . 64
4.3.4 Bias Coils . . . 66
4.4 Imaging System . . . 70
4.4.1 Fluorescence and Absorption Imaging . . . 71
4.4.2 Design of the Imaging System . . . 73
4.4.3 Fringe Reduction . . . 78
4.4.4 Image Acquisition . . . 79
4.5 Control System . . . 81

5 Microwave and RF System 86
5.1 Microwave Transitions . . . 87
5.1.1 Na Ground-state Hyperfine Structure . . . 87
5.1.2 Oscillatory Magnetic Field . . . 90
5.1.3 Microwave Dressing . . . 91
5.2 Microwave Signal Generation . . . 94
5.2.1 Hardware . . . 94
5.2.2 Workflow of the Microwave Source . . . 98
5.2.3 Antenna . . . 101
5.3 Microwave Source Performance . . . 103
5.3.1 Microwave Calibration . . . 105
5.3.2 Microwave Rabi Oscillations . . . 106
5.4 Radio-Frequency Signal . . . 109

6 All-optical Generation of Spinor Sodium Bose-Einstein Condensates 112
6.1 Theory of Bose-Einstein Condensate . . . 115
6.1.1 Ideal Boson Gas . . . 115
6.1.2 Bose-Einstein Condensate in a Trap . . . 117
6.2 Crossed Optical Dipole Traps . . . 121
6.2.1 ODT Setup . . . 121
6.2.2 ODT Beam Alignment . . . 125
6.2.3 Stabilization of ODT . . . 128
6.2.4 Loading Cold Atoms into the ODT . . . 129
6.3 Evaporatively Cooling Atoms . . . 135
6.3.1 Modelling Evaporation . . . 135
6.3.2 Scaling Laws . . . 137
6.3.3 Experimental Realization . . . 139
6.4 BEC Detection and Imaging Analysis . . . 139
6.4.1 Imaging System for BEC . . . 139
6.4.2 Detecting Bose-Einstein Condensation . . . 141
6.4.3 Characterizing Bose-Einstein Condensation . . . 143

7 Spinor Bose-Einstein Condensate 148
7.1 Theoretical Model of Spin Interaction . . . 149
7.1.1 Hamiltonian in the Mean-field Picture . . . 149
7.1.2 Spin Dynamics in the $F = 1$ Ground State . . . 153
7.1.3 Single-mode Approximation . . . 155
7.2 Spin-mixing Dynamics in an Anti-ferromagnetic Spin-1 BEC: Experiment . 158

7.2.1 Spin-mixing in $F = 1$ Manifold . . . 158
7.2.2 Experimental Procedures . . . 160
7.3 Data Analysis . . . 163
7.3.1 Spin Oscillations within the Single-mode Approximation . . . 163
7.3.2 Spin Oscillations Beyond the Single-mode Approximation . . . 165
7.4 Summary . . . 174

8 Spin-mixing Atom Interferometry **177**
8.1 Theory of Interferometry . . . 179
8.1.1 SU(2) and SU(1,1) Interferometry . . . 179
8.1.2 Theoretical Background of Spin-1 Interferometry . . . 182
8.1.3 Phase Estimation: Fisher Information and Cramér-Rao Bound . . . 185
8.2 Single- and Double-Sided Seeding Atom Interferometers . . . 188
8.2.1 Initial State Preparation . . . 188
8.2.2 Experimental Interferometry Sequence . . . 191
8.3 Experimental Results . . . 192
8.3.1 Spin-mixing Dynamics of Different Initial States . . . 192
8.3.2 Interference Fringes . . . 194
8.3.3 Phase Sensitivity Measurement . . . 198
8.4 Summary . . . 204

9 Conclusions **206**
9.1 Final Remarks . . . 206
9.2 Future Plans . . . 208

References **212**

A Angular Momentum Coupling **224**

B Bias Coils Current Control Circuits **225**

List of Tables

4.1 Camera Specifications 77
4.2 Analog Channel Specification 84
4.3 Digital Channel Specification 85

List of Figures

2.1 Optical damping force in one dimensional optical molasses with $s_0 = 2$ and $\delta = -\gamma$. The blue dashed trace shows the force from the light beam which atoms move toward, the red one is the force generated from the atoms moving along with the light beam, and the black dashed trace is the sum of the two. The black solid line shows the linear relation between the damping force and the velocity if the velocity is small enough within the so-called capture velocity range. 9

2.2 Polarization gradient cooling in lin $\perp$ lin configuration. The electrical dipole transition happens between two levels with angular momenta $J = 1/2$ and $J' = 3/2$, where the manifolds in $J' = 3/2$ are not shown. The polarization changes from $\sigma+$ to $\sigma-$ over a distance of $\lambda/4$, and the light has elliptical or linear polarization between these positions. Atoms starting at $z = 0$ in the $m = -1/2$ must climb the potential hill as they approach the $z = \lambda/4$ where the light becomes pure $\sigma+$ polarization, and there they are optically pumped to the $m = 1/2$ sublevel, this process repeats several times until the kinetic energy is not enough for atoms to climb the hill anymore. 12

2.3 The mechanism of a magneto-optical trap in one dimension, illustrated for an atom with an atomic transition between $J = 0$ and $J' = 1$. Two counter-propagating beams of circularly-polarized light illuminate the atom in a magnetic field gradient. The magnitude of Zeeman splitting between three magnetic sublevels depends on the atom's position. The restoring force from the laser beam and magnetic field gradient pushes the atom back toward the center of the trap. The energy diagrams are not to scale. 15

2.4 Schematic of the 3D MOT. Three orthogonal pairs of circularly polarized laser beams intersect at the center where the magnetic field is zero. A pair of coils with opposite currents generates a quadruple magnetic field. This setup traps and cools atoms at the center of the configuration. 17

2.5 A schematic representation of atoms confined in a one-dimensional ODT. By lowering the intensity of the dipole trap laser beam, the trap depth is reduced so that energetic atoms (red) can leave the trap. After collisions between the remaining atoms, a new Boltzmann distribution with a lower average temperature re-establishes itself: atoms occupy a lower energy state with a lower temperature and an increased phase-space density. 23

3.1 CAD rendering of the UHV system consisting of the sodium oven, the differential pumping chamber, the Zeeman slower, and the main chamber. In addition, ion pumps, titanium sublimation pump, and a turbo pump (not shown in the figure) are attached to the system to create and maintain UHV pressure. 25

3.2 a) The sodium reservoir is made of a stainless steel cup filled with sodium. A nozzle is placed inside of the CF 1.33" tee that was mounted on the top of the reservoir. b) A 11.4 cm long nozzle to direct the hot sodium vapor away from the sodium reservoir. The 2.3 mm diameter hole is used to collimate the sodium vapor to create an atomic beam. c) 3D rendering of the cold plate. The top of the cold plate is inside the oven chamber to collect the hot sodium atoms. The thick copper feedthrough is in the air connected to a water-cooled of six TEC elements, as shown in d). 26
3.3 a) Photo of the UHV system, the Zeeman slower is marked in the picture. b) Photo of oven chamber taken through the oven chamber's viewport. The cold plate has a central hole that is aligned with the front nozzle. A mechanical shutter behind the cold plate can shut the atomic flux on or off. The yellow light is the fluorescence of the sodium beam. c) The UHV chamber where cooling and trapping mechanisms occur. 28
3.4 Pump setup for the main chamber. Two ion pumps are mounted to the main chamber through two 2.7" CF ports, and a TSP is installed next to one of the ion pumps. Two mini NEG pumps are mounted onto 1.33" CF ports with electrical feedthroughs. 31
3.5 The data from our RGA shows the vacuum chamber's pressure as a function of atomic mass. Different mass of atoms indicates the gas composition in the vacuum chamber. The figure shows that the residual gas is made of H_2, CH_4, H_2O, CO, N_2, Ar, and CO_2. Figure (a) shows that all the gases were at a higher pressure on the first day of baking and pumping; after one day, the pressure of each gas went down significantly except H_2, as shown in figure (b). Because H_2 is a tiny molecule that can penetrate through the chamber, the chamber must be continuously pumped by the ion pumps, NEG pumps, or the TSP. 39
3.6 Photo of a mounted UV LED array used for removing sodium atoms from the viewport surfaces. 43

4.1 The main optical system fits on a 5' × 10' optical table that generates cooling, repumping and imaging beams. The main light source is generated from a commercial SHG laser system (TOPTICA TA-SHG PRO), designed to operate at wavelength $\lambda \approx 589$ nm with a continuous output power of 1 W. 45
4.2 Probe beam absorption profile for laser spectroscopy. By blocking the pump beam and scanning the laser frequency over the sodium D2 line, we observe two distinct but not fully resolved absorption dips, as shown in (a). In (b), when the pump beam is unblocked, Lamb dips appear within the absorption profile. The leftmost and the rightmost peaks correspond to the transitions within the hyperfine structure, and the middle peak results from crossover resonances at frequencies directly between the other peaks. 47
4.3 Experimental setup for FM-modulated saturated absorption spectroscopy. The pump beam (red solid line) and probe beam (blue dash line) are derived from the main laser. The pump is frequency shifted and FM modulated through an AOM to allow tuning of the lock point and lock-in detection to generate a derivative signal. 49

4.4 Sodium vapor cell used in our saturated absorption spectroscopy setup. We wrapped the vapor cell with aluminum foil and heated it up to ~ 110 °C. The windows are kept a few degrees hotter than the body. 50
4.5 The output of the lock-in amplifier is shown in red. The grey curve is the absorption profile of the F=2 to F' transition. The red curve represents the amplitude derivative of the absorption signal. We lock the laser at the largest cross over peak which is the zero crossing of the error signal. 51
4.6 Schematic of the laser system used to generate MOT cooling, MOT repumping, imaging, imaging repumping, Zeeman slowing and Zeeman slower repumping beams. All cubes are polarizing beamsplitter cubes and all laser powers are measured before the PM fibers 52
4.7 Frequencies of laser light used in the experiment compared to the hyperfine structure of sodium D2 line. Frequencies are not drawn to scale. 53
4.8 Double-pass AOM configuration can mitigate the shift in laser pointing due to frequency changes, and also provide a doubled frequency detuning. In this figure, f_0 is the original laser's frequency and f is the frequency of the rf signal sent to the AOM. The first order of the final output laser's frequency after the double-pass configuration is $2f + f_0$. The lenses are chosen so that the AOM is in the focus of both lenses. 54
4.9 3D rendering of the Zeeman slower. The first 20 segments produce a positive field, the following ten segments produce a negative field, and the last coil produce positive current to tune the final velocity of atoms. 59
4.10 Measured longitudinal component of the magnetic field generated along the center of the Zeeman slower with 4 A of current through each segment of wires (black dots) compared to the simulated field (red line) 60
4.11 The 4' × 10' non-magnetic optical table that holds the MOT optical system, and the vacuum system. The laser beams generated on the main laser table are delivered to this table via PM fibers to generate the MOT. 61
4.12 CAD rendering of MOT, MOT repump, and imaging beams entering the main experimental chamber. 63
4.13 The MOT coil switch circuit is made of a high-power IGBT with two TVS diodes. When the IGBT switch opens, the TVS diodes start conducting, and the current starts to decrease, according to Eq. (4.4). 66
4.14 a) 3D printed plastic Helmholtz bias coils frame. b) The three pairs of Helmholtz bias coils surrounding the main chamber generate a uniform background magnetic field. 67
4.15 A homemade current controller for the bias coil. There are six individual channels that can output a current range from -5 A to 5 A. Each of them uses a commercial ultra-low noise TC (Wavelength Electronics PTC5K-CH) as a current controller. An extra external setpoint circuit and a sensing circuit are used to convert the signal to a readable signal for the TC. 69
4.16 A photo of the fluorescence of our sodium MOT locates in the center of the UHV chamber. After optimization of the cooling light power, polarization, and frequency, as well as the bias magnetic field and the magnetic field gradient, we trap $\sim 3 \times 10^8$ sodium atoms in the MOT. 70

4.17 An example of how an absorption image is constructed. a) The raw image that includes information about both atoms and light. b) The reference image that only includes light. c) The background image that contains no light and no atoms. d) The image of optical density calculated using Eq. (4.8). e) The false-color image of d). Axes are labeled in the unit of camera pixels. 74
4.18 Schematic diagram of the optical configuration used for our imaging system. Lens 1 and lens 2 comprise the f-$2f$-f configuration with unit magnification. The inverted image after lens 2 is further magnified by lens 3 and imaged with a CCD camera. The black dashed line is the image of the atom cloud, and the solid red line is the imaging beam. The lenses are achromatic doublets (47718 and 47713 for side imaging and 49285 and 49284 for top imaging) from Edmund Optics. QWP is an abbreviation for quarter wave plate. 75
4.19 Top and side absorption imaging systems are used to take absorption images of the MOT and BECs inside our vacuum chamber. The side imaging system comprises a CCD camera along with L1, L2, L3, and a QWP between L1 and L2. The other components comprise the top imaging system. A polarizing beam-splitter is used to split the top-down imaging beam and the MOT beam. In experiments, we can move lens L3 and CCD (side) or L6 and CCD (top) to change the magnification of our side and top imaging system, respectively. 76
4.20 False color images from absorption imaging. (a) The MOT absorption image taken after a few milliseconds of time-of-flight. (b) Stern-Gerlach absorption image showing BEC in different spin states after 10 ms time of flight. From left to right are absorption images of m_F=1, m_F=0, m_F=-1 states 81
4.21 A control panel of the LabVIEW interface. There are 24 digital channels with green circles as on/off switches. Bright green represents status "on" while dark green represents "off". There are 16 analog channels with input boxes. The value in the "Delay" column defines the time duration for each step. These steps are stacked vertically to create any desired timing sequence, with time increasing towards the bottom. 83

5.1 Schematic of microwave signal generation hardware. The parameters for the low-frequency signal are sent from the computer to the FPGA via USB. The FPGA then communicates with the DDS after it receives a TTL signal, which produces a low-frequency (MHz) signal. Next, the low-frequency signal is mixed with a high-frequency signal of 1.73 GHz in a single-sideband modulator. The modulator produces the desired sum-frequency signal close to the hyperfine splitting of the sodium ground state. After filtering, amplification, and impedance matching, the signal is emitted from a half dipole antenna to irradiate a sample of trapped cold atoms. 87
5.2 Breit-Rabi diagram of the sodium ground state hyperfine structure. The interaction between the external magnetic field and the magnetic dipole moment lifts the degeneracy of the hyperfine state and leads to the splitting of the magnetic sublevel. A dimensionless parameter is introduced in the plot: $x = \frac{(g_J - g_I)\mu_B B}{\Delta E_{hf}}$, where $B_0 = \frac{(g_J - g_I)\mu_B}{\Delta E_{hf}}$. 89

5.3 Schematic of microwave and rf transitions. Red, blue and green arrows represent microwave fields coupling to transitions between $F = 1$ and $F = 2$. Black arrows represent rf field coupling to transitions between $F = 1$ Zeeman sublevels. 92
5.4 Microwave dressing in the presence of an applied magnetic field allows us to selectively shift only the $m_F = 0$ level and control the magnitude and sign of the effective quadratic Zeeman shift q. 94
5.5 Enclosure of the FPGA system. a) FPGA board (left) and DDS board (right). b) Front panel of the FPGA system, the LCD screen is on the left side and the input control panel with buttons and switches is on the right side. . . . 95
5.6 A screenshot of the DDS AD9954 LabVIEW user interface. Frequency, amplitude, and phase values are stored in several RAM memory addresses on the FPGA board. Later, these parameters arre used to update the DDS chip when it receives a ASCII sequence starting with the letter "L". 99
5.7 (a) CAD rendering of the microwave and RF antennas mounted inside the vacuum chamber. The microwave antenna is a half-dipole antenna mounted about 3 cm from the center of trapped atoms inside the vacuum chamber via an SMA CF 1.33" electrical feedthrough. The RF antenna is a small copper loop with a diameter of 25 mm. The RF antenna is also installed close to the center of the atomic cloud to ensure high RF intensity at the position of the atomic cloud. (b) A photo of the chamber showing microwave and rf antennas. 102
5.8 The Yagi antenna shown in the image is used in the experiment. The antenna consists of three components: the reflector, transmitter, and director. The reflector reflects the signal which help to collimate to the beam and increases the gain. The transmitter emits the microwave signal. The director resonates with the wave creating constructive interference, also increasing gain. 104
5.9 Microwave power as a function of Rabi frequency used for microwave power calibration. Black dots are the real power obtained by measuring each Rabi frequency. Red squares are the power set points, used in programming the microwave source. The black dots are closely matching the red squares which means that the set power matches the real power, indicating a good calibration. 107
5.10 Na ground state hyperfine energy levels and associated Rabi couplings. The linear Zeeman splitting between hyperfine sublevel is 300 kHz at an applied magnetic field of 0.428 G. 108
5.11 (a)-(c) show the Rabi oscillations measured on resonance for the Ω_π, $\Omega_{\sigma-}$ and $\Omega_{\sigma+}$ transition, respectively when B_0 is along the x direction. (d)-(f) show the Rabi oscillations on resonance for the Ω_π, $\Omega_{\sigma-}$ and $\Omega_{\sigma+}$ transition, respectively when B_0 is in the z direction. (a) and (d) show the atom number in $|F = 1, m = 0\rangle$ as a function of microwave pulse length. (b)-(f) show the atom number fraction in $|F = 1, m = 0\rangle$ as a function of microwave pulse length. 110
5.12 Experimental data of RF Rabi oscillations in $F = 1$ hyperfine state manifold. The B-field is set to generate a 300 kHz linear Zeeman shift in $F = 1$ hyperfine state, and the on-resonant RF field is turned on for 100 μs. ρ_0, ρ_{-1} and ρ_{+1} are the population fraction number of $|F = 1, m = 0\rangle$, $|F = 1, m = -1\rangle$, and $|F = 1, m = +1\rangle$, respectively. 111

5.13 Schematic of the RF system. The RF signal generated from a function generator after receiving a TTL signal is filtered by a low-pass filter before passing through the RF amplifier. A home-built RF coil antenna is installed inside the vacuum chamber so that it is close to the atoms to ensure large Rabi frequencies. 111

6.1 An illustration of how the de Broglie wavelength λ_{dB} changes with decreasing temperature. When the temperature is high, λ_{dB} is much smaller than the inter-particle distance. As we lower the temperature, quantum effects start to become visible. The wavefunctions of the atoms start to overlap with each other. At T=0 K, all particle waves are overlapped and become a single "giant matter wave." Adapted from [1]. 118
6.2 Representations of a crossed beam dipole trap. a) Shows that the two focusing beams are crossed at the center of the chamber to form a crossed optical dipole trap. b) Presents the corresponding calculated potentials. c) Shows a false color absorption image of our crossed optical dipole trap when the two beams are not overlapped. Atoms can be seen to fill the arms and the focus area of the trap geometry. 122
6.3 Schematic of crossed ODT setup. The high-power IR laser is expanded by an optical telescope after going through an AOM, then focused by a 400 mm plano-convex lens. The IR laser beam travels through the chamber twice so that the two foci overlap at the center of the MOT to form the crossed ODT. PD stands for photodetector, and H stands for half-wave plate. The D-shape mirror, the zeroth order light and the corresponding beam dump after the AOM are not shown. 124
6.4 False-color TOF absorption images of the MOT and ODT from side view (a) and top view (b). The red color indicates the high-density regime where the atoms are trapped inside the ODT. The TOF was 5 ms. 127
6.5 Lifetime measurements of sodium atoms in $F = 1$ hyperfine ground state. The black dots are the experimental data, and the red curve is an exponential decay function $N(t) = N_0 e^{-\frac{t}{\tau}}$, where N_0 is the initial atom number in the trap, and τ is the time constant. From the fitting we obtain $\tau \approx 14.7 \pm 2$ s. Atoms in the $F = 1$ ground state show an exponential decay mainly due to the one-body losses. 130
6.6 Atom number loaded in the optical dipole trap as a function of (a) the cooling laser detuning from resonance, (b) the cooling laser power, and (c) the repumping laser power. (a) The larger effective detuning reduces the excitation rate of the atoms in the dipole trap and thus reduces light-induced collisions and heat. (b) Atoms are maximum in the ODT when the MOT cooling laser power is about 30 mW. Below this level, the MOT is not sustained. (c) The intensity of the repumping laser is decreased so that the atoms are pumped into the $F = 1$ ground state. The optimum repumping laser beam intensity is $\sim$600 μW. 133
6.7 Empirically optimized experimental cooling sequence for optical molasses using polarization gradient cooling before evaporative cooling. CMOT stands for the compressed MOT. 135

6.8 False-color absorption images of our ODT. a) A typical top view absorption image of our crossed ODT in the presence of MOT atoms after a short free evaporation time of 10 ms. b) A typical top view absorption image of our crossed ODT after 1.5 s free evaporation. OD stands for optical density. The time-of-flight for a and b are 10 μs. 136
6.9 Optimized ODT ramping sequences in the experiment. The ODT is kept at a relatively small trap depth during the laser cooling process. It is then linearly ramped to U_{max} within 5 ms. After 1.5 s of free evaporation, it is exponentially ramped down during 5 s, as depicted. 140
6.10 Absorption images are taken after interrupting an optimized evaporation curve at various laser powers, followed by a 10 ms time-of-flight. Figure a) to f) show the evaporation curve interrupted at the laser power of 281.2 mW, 233.7 mW, 197.6 mW, 178.6 mW, 142.5 mW, and 125.4 mW, respectively. OD stands for optical density. There is no indicate of condensates in figure a) and b). The condensate atoms appear as a sharp density peak in the images c), d), e), and f) as the condensate fraction increases. Finally, we have an almost pure BEC in image f). 142
6.11 (Right) False-color absorption images of the atomic cloud are taken after interrupting an optimized evaporation curve at 4 s, 4.5 s, 4.7 s, and 5 s. The z direction is aligned with gravity. (Left) Column optical density data along the dashed lines on the right side pictures. The red solid curve is the revert of the bimodal fit, and the blue dashed curve is the classical Boltzmann distribution specifically showing only the thermal gas. The condensate fraction (CF) can be determined as $CF = n_{TF}/(n_{TF} + n_{th})$. The CF is about 32% when the evaporation time is 4 s and increases to about 97% when the evaporation time is 5 s. 145
6.12 (a) to (c) are trap frequencies measured along the x, y, and z directions, respectively. Here, z is the vertical (axial ODT) direction aligned with gravity. We use a gravity kick method to excite motion of the trap frequency in the z direction and a Stern-Gerlach pulse kick method to excite the motion of the trap frequency in the x and y directions. The black dots are the measured data, and the red curve is the sine-wave fit. The fit gives trap frequencies of $\omega_z = 2\pi \times 275.3$ Hz, $\omega_x = 2\pi \times 127.3$ Hz, and $\omega_y = 2\pi \times 138.5$ Hz. 147

7.1 Mean-field energy contours in phase space for a ferromagnetic condensate (a) and an anti-ferromagnetic condensate (b) with magnetization $m = 0$. The color scale shows the energy, which is scaled by c. The low energy region is shaded in blue, and the high energy region is shaded in yellow. For an initial state ($\theta = 0, \rho_0 = 0.5$), if $q/|c| \leq 1$, the spin evolution of ρ_0 are in the periodic-phase which the oscillations are bounded in the spinor phase θ. If $q/|c| \geq 2$ the spin evolution of ρ_0 is in the running-phase region where the spinor phase keeps accumulating. If $q/|c| = 1$, the spin evolution is on separatrix marked in red dashed lines with an infinite period. The sidebar on the right is the color legend for the dimensionless energy defined as ϵ/c. . . 157

7.2 Cartoon of a spin-exchange collision in $F = 1$ system. Two atoms in the magnetic sublevel $m = 0$ can coherently and reversibly scatter into a pair of atoms in the $m = 1$ and $m = -1$ states, and vice versa, creating entanglement denoted by the wavy line. 159
7.3 Schematic of a quenching process illustrated with pair energy levels of the $m = 0$ and $m = \pm 1$ states with single-particle detuning q. The linear Zeeman shift has been rotated out. The blue dashed arrow means no spin exchange happens, and the solid red arrow means spin exchange can happen. Left: before quenching the Hamiltonian, the effective quadratic Zeeman shift q is large, and the spin mixing dynamic is energetically forbidden. Right: after quenching, the spin mixing starts, and the competition between the spin-interaction c and q determines the exact dynamics of the spin oscillations. 161
7.4 (a) A radio-frequency pulse is applied to transfer atoms from the $m = -1$ state to the $m = 0$ and $m = +1$ states. (b) The pulse length is 15 μs such that the fractional populations of the $m + 1$, $m = 0$, and $m = -1$ are $\rho_{-1} = 0.25$, $\rho_0 = 0.5$, and $\rho_{+1} = 0.25$, respectively. The circles are experimental data, the lines show the theory of the three-level system 162
7.5 Quench-induced spin population oscillations of the $F = 1$ $m = 0$ state. The black dots are the measured experimental data. The error bars on each data point indicate the statistical uncertainty (standard error), which arises from an average of five measurements for each time t. The red dashed line is the mean-field SMA with the best fitting q. The spin oscillation data in (a), (b), and (c) correspond to experimental parameter of $q/h = 45$, $q/h = 38$, and $q/h = 35$ Hz, the best mean-field SMA fitting is at $q/h = 42$, $q/h = 35$, and $q/h = 33$ Hz, respectively. In (d), an upward drifting appears accompanied by the damping in amplitude, indicating the mean-field SMA does not fully capture the spin dynamics. 164
7.6 Mean-field driven beyond the SMA process. The effective mean-field potential generates ground (dashed lines) and excited states (dash-dotted lines) for both $m = \pm 1$ (left) and $m = 0$ (right), which are characterized by different spatial modes. If the excitation energy is equal to $2q$, two possible coupling channels occur (A) two atoms in $m = \pm 1$ ground states collide; one goes to $m = 0$ ground state, and the other goes to m=0 excited state or vice versa. (B) one atom in $m = \pm 1$ excited state and one atom in $m = \pm 1$ ground state collide, becoming two atoms in $m = 0$ excited states or vice versa. We thank Dr. D. Blume's group for this figure. 167

7.7 Quench-induced spin oscillation for q away from the resonance (a) and q close to resonance (b). The black dots are the measured experimental data showing the number fraction of atoms in $F = 1,\ m = 0$ hyperfine level. The red error bands are standard erros for the average of 9 or 10 data sets for each time t. The blue squares and the green diamonds are simulations using the mean-field SMA equations and coupled GP equations. The simulation data are the theoretical best fit with $q/h = 37.6$ Hz for (a) and $q/h = 28.2$ Hz for (b). A good agreement between the experimental data and the mean-field SMA simulation is shown in (a), where the system is away from resonance. In contrast, in (b), when the system is close to resonance the experimental data agree well only with the coupled GP equations, but not with the SMA equation. This indicates physics beyond the SMA. Figures are complied by Dr. Jianwen Jie from our experimental data and his theoretical simulations. 169

7.8 Density plot from GP simulation and experimental data. (a) and (b) show the density profile of n_0. (c) and (d) show the density profile of $n_{\pm 1}$. In (a) and (c), the three-dimensional densities are shown as functions of vertical (axial ODT) axis z and the horizontal (radial ODT) axis ρ; the normalization is $\int n_m(\vec{r}, t)d\vec{r}$. (b) and (d) are the integrated two-dimensional densities as functions of z and $e_{xy} = (x + y)/\sqrt{2}$, which has the same representation as the experimental pictures. (e) Experimental images of the density profiles in $m = -1$, $m = 0$, and $m = +1$ from top to bottom; the sidebar on the right defines the color code for the experimental images. Figures are complied by Dr. Jianwen Jie from our experimental data and his theoretical simulations. 171

7.9 Resonance mapping of the quench-induced spin oscillations by scanning $q/h = 35$ Hz to $q/h = 27$ Hz. The black dots are the measured experimental data showing the number fraction of atoms in the $F = 1,\ m = 0$ hyperfine level. The error bars on top of the experimental data as the standard errors that arise from averaging ten data sets for each time t. The trap frequencies in the x, y, and z directions are $\omega_x = 147.24$ Hz, $\omega_y = 132.05$ Hz, and $\omega_z = 245.96$ Hz, respectively. The mean value of the total atom number is $\sim$ 26K. In (a), the spin oscillation has no drift at $q/h = 35$ Hz, which indicates the system is away from the resonance. The spin oscillation in (b) to (g) shows upward drifting, indicating the system is close to resonance. In (h) and (i), the upward drifting is gone, but the oscillations amplitude decay and data uncertainty increase as the increase of evolution time. 173

7.10 Mapping the spin-spatial resonance via histogram bars of the density distribution of ρ_0 at the spin oscillation time $t = 60$ ms. The trap frequency and the total atom number are the same as for Fig. 7.9, and a total of 90 data points were taken for each q value. When $q/h = 35$ Hz, away from the resonance, the density distribution of ρ_0 is Gaussian-like, and the mean value is about 0.25. As q/h decreases, the density distribution deviates from a Gaussian. At $q/h = 31$ Hz, the distribution is non-Gaussian, and the mean value is about 0.45 with large uncertainty. At $q/h = 27$ Hz, the distribution changes back to Gaussian-like distribution, and the mean value is back to $\sim$0.3. 175

8.1 (a) A SU(2) Mach-Zehnder interferometer. Light enters one of the two input ports a_1 or a_2 and is split by a 50/50 linear beam splitter BS1. The two light beams accumulate a relative phase shift ϕ before entering another 50/50 linear beam splitter. The two light beams b_1 and b_2 leaving the interferometer are detected by photodetectors D1 and D2. (b) A SU(1,1) interferometer. The passive linear beam splitters in the SU(2) Mach-Zehnder interferometer are replaced with active nonlinear parametric amplifiers, such as four-wave mixers (FWM1 and FWM2). The pumping light is phase shifted by ϕ. The outgoing light beams b_1 and b_2 are quantum correlated. 180
8.2 The performance of a Mach-Zehnder SU(2) interferometer can be represented using a Bloch sphere. The input state is prepared at the north pole of the sphere (a). The first beam splitter performs a $\frac{\pi}{2}$ rotation about the J_x (b). The phase shifts accumulated along the beam path correspond to a rotation ϕ about the J_z (c). The second beam splitter performs a $-\frac{\pi}{2}$ rotation about the J_x axis (d). 181
8.3 Schematic of our three-mode nonlinear interferometer based on spin-mixing dynamics. Initial state ($N_-1,\ N_0,\ N_1$) is made of pure BECs in the $m = 0$ state with some initial seeds in the $m = \pm 1$ states. The spin-mixing dynamics Hamiltonian H triggers the nonlinear "path" splitting or recombining by creating (annihilating) paired atoms in $|F = 1,\ m = \pm 1\rangle$ components from (into) $|F = 1,\ m = 0\rangle$. The phase encoding shifts the spin component $|1,\ 0\rangle$ and adds a relative phase $\phi = 2\pi \times 2q\tau$ to the overall spinor phase $\phi = \phi_1 + \phi_{-1} - 2\phi_0$. In the end, the total number of atoms, $N_s = N_+ + N_-$, in $|F = 1,\ m = \pm 1\rangle$ is measured. 183
8.4 State preparation. We adiabatically sweep the microwave field (black arrows) to transfer atoms from unwanted $F = 1$ states to the $F = 2$ manifold, followed by resonant light pulses (yellow arrows) to clean those atoms out of the trap. The single-sided seeding is realized using two consecutive microwave π pulses (blue dash arrows). The double-sided seeding is realized by applying a radio-frequency pulse (red dot arrows) to seed $|F = 1,\ m = \pm 1\rangle$, simultaneously. 190
8.5 Spin-exchanging collisions with initial states are prepared by (a) double-sided seeding and (b) single-sided seeding. The black dots and lines are experimental data of fractional population in the $|1,\ 0\rangle$ component, ρ_0, as a function of spin evolution time. The error bars are the standard error of over five experimental runs. Red dashed lines are the TWA simulation fitted with $q/h = -5$ Hz, $c/h = 18.5$ Hz, and $N = 21000$. The red error bands indicate the statistical uncertainty that arises from averaging 1000 data sets at each time step. . . 193

8.6 Interference fringes for the double-sided seeding interferometer presented in terms of fractional population in the $|1,\ 0\rangle$ component, ρ_0, as a function of imprinted phase Φ. The spin-mixing time $t_1 = t_2$ of "splitting" and "recombining" steps from (a) to (d) are 8 ms, 10 ms, 13 ms, and 18 ms, respectively. Black circles are the mean values of experimental data. Error bars are standard errors calculated from averaging five separate measurements. Red dashed lines are TWA simulation results with parameters $q/h = -5$ Hz, $c/h = 19$ Hz, and $N = 21000$. The red error bands arise from averaging over an ensemble of 100 trajectories for each phase value. The experimental data and the TWA simulation show close-to-sinusoidal fringe patterns in (a) at the short spin-mixing time of 8 ms. Interference fringes become non-sinusoidal in (b), (c), and (d) when the spin-mixing time increases, which indicates the nonlinear nature of the interferometer. 196

8.7 Interference fringes for the single-sided seeding interferometer presented in terms of fractional population in the $|1,\ 0\rangle$ component, ρ_0, as a function of imprinted phase Φ. The spin-mixing time $t_1 = t_2$ of "splitting" and "recombining" steps from (a) to (d) are 8 ms, 10 ms, 13 ms, and 18 ms, respectively. Black circles are the mean values of experimental data. Error bars on each data point are standard errors calculated from averaging five separate measurements. Red dashed lines are TWA simulation results with parameters $q/h = -5$ Hz, $c/h = 22$ Hz, and $N = 21000$. The red error bands arise from averaging over an ensemble of 100 trajectories each phase value. The single-sided seeding interferometer performs similarly to the one with double-sided seeding in terms of interference patterns. 197

8.8 Phase sensitivity measurement using error propagation method. Black circles in (a) and (c) are the experimental data showing the mean value of the total number in the $|F = 1,\ m = \pm 1\rangle$ states as a function of phase. Each point is an average of ten data. Black circles in (b) and (d) are the standard deviation of the experimental data. The experimental data are fitted with a polynomial regression model up to the eighth order in (a) and (b), and are interpolated using the Hermite function up to the third order in (c) and (d), as shown in the red lines. Black lines in (e) are the phase sensitivity estimation using the fitting from (a) and (b). Black lines in (f) are the phase sensitivity using the fitting from (c) and (d), respectively. Results are normalized to the SQL. The red lines in (e) and (f) are the normalized SQL defined as $1/\sqrt{\langle N_s(t_1)\rangle}$ where $t_1 = 10$ ms. Red bands are the standard deviation that arises from averaging 30 data points measured at t_1. Blue dash lines are the quantum Cramér-Rao bound of the probe states, and green dash and dot lines are the Heisenberg sensitivity limit. 200

8.9 Phase sensitivities of single-side seeded spin-mixing interferometers with the spin-mixing time, t_1, of (a) 10 ms, (b) 13 ms, and (c) 18 ms. When $t_1 = 10$ ms, the maximum metrological gain is obtained at $\Phi = 2\pi \times 1.54$ with $G = 3.69$ dB indicating a metrological gain. Dashed black lines are the phase sensitivities calculated from the TWA simulated data, with a gain of 5.25 dB at $\Phi = 2\pi \times 1.58$. The gain becomes smaller at $t_1 = 13$ ms, and there is no gain at $t_1 = 18$ ms. 202

8.10 Phase sensitivities of double-sided seeding atom interferometers with the spin-mixing time, t_1, of (a) 8 ms, (b) 13 ms, and (c) 18 ms. When $t_1 = 8$ ms, the maximum metrological gain is obtained at $\Phi = 2\pi \times 0.56$ with $G = 4.77$ dB indicates a metrological gain. Dashed black lines are the phase sensitivities calculated from the TWA simulated data, with a gain of 5.53 dB at $\Phi = 2\pi \times 0.66$. The gain becomes barely visible at $t_1 = 13$ ms, and no gain at $t_1 = 18$ ms. 203

9.1 Energy diagrams of different light pulse schemes for interferometry. Energies are not drawn to scale. (a) Raman diffraction is realized with a two-photon transition in a three-level system. Atoms are transferred from the ground states $|g_1\rangle$ to $|g_2\rangle$ via an exited state $|e\rangle$ with two-photon detuning δ and one-photon detuning Δ. (b) Bragg diffraction with n=4 Bragg order and $8\hbar k$ momentum has been transferred. Solid lines are the resonance transition between the initial and final momentum states. Dashed lines are virtual transitions. 209

9.2 (a) Mach-Zehnder light-pulse atom interferometry. A sequence of three Raman pulses ($\pi/2$-π-$\pi/2$ configuration) is applied to a free-falling BEC separated with free propagation time of T. Atoms exchange between two ground states F=1 and F=2 as well as their momentum due to the sequence of three Raman pulses. (b) A simplified optical layout for generating stimulated Raman pulses. 210

B.1 Circuit diagram of the temperature controller. Point 5 receives the external set point signals. Points 1 and 2 pick up the current signal from the Helmholtz coil and send it to the sensor of the temperature controller at points 3 and 4 225

B.2 Circuit diagram to generate the external set point. U_p is the signal generated from the LabVIEW. 226

B.3 Circuit diagram of the sensing circuit. The current in Helmholtz Coils is picked up in points 1 and 2, and converted to a value which can be interpreted by the temperature controller at points 3 and 4. 226

Abstract

This thesis presents my research on spin-mixing and interferometry in an all-optically generated spinor Bose-Einstein condensate (BEC) of sodium atoms. The sodium atoms are loaded from a magneto-optical trap into a crossed optical dipole trap and are subsequently evaporatively cooled down to quantum degeneracy by ramping down the laser power. With our setup, we obtained nearly pure sodium BECs with atoms number of approximately 20,000 to 40,000.

We study the spin-mixing dynamics in the $F = 1$ sodium spinor system. I present experiments on a resonant coupling between spin and spatial degrees of freedom beyond the single-mode approximation (SMA) during non-equilibrium dynamics in our sodium spin-1 BEC. These quench-induced spin oscillation experiments rely on microwave dressing of the $F = 1$ hyperfine states, where F denotes the total angular momentum of the Na atoms. Our data show a slow baseline drift of the coherent spin population oscillation between $m = 0$ and $m = \pm 1$ pairs when the effective quadratic Zeeman shift q is tuned via microwave dressing to certain values. The baseline drifting indicates spin dynamics beyond the SMA. Our data agree well with the recent theory based on a q-dependent, resonant coupling between spin and spatial degrees of freedom. We further explore these effects by scanning q around the point of maximum baseline drift to map out this new resonance phenomenon as a function of q.

I also present the result of our spin-mixing atom interferometer experiments. We experimentally demonstrate two new types of interferometry based on different initial states: single-sided seeding and double-sided seeding interferometers. The entangled probe states of the interferometers are generated via spin-exchange collisions in $F = 1$ spinor BECs, where two atoms with the magnetic quantum number $m_F = 0$ collide and change into a pair with $m_F = \pm 1$. Our results show that our spin-mixing interferometers beat the standard quantum limit with a metrological gain of 3.96 dB

in the single-sided atom interferometer with spin-mixing time $t = 10$ ms and 4.77 dB in the double-sided atom interferometer with spin-mixing time $t = 8$ ms. Our research on spin-mixing interferometry is useful for future quantum technologies such as quantum-enhanced microwave sensors, and quantum parametric amplifiers based on spin-mixing. Our work paves the way for future light-pulse atom interferometry experiments, which involve the coupling between the spin and momentum degrees of freedom, and are useful for quantum-enhanced inertial sensing and gravimetry with BECs.

Chapter 1

Introduction

1.1 Background

Since the last century, scientists and researchers have pursued lower and lower temperatures than one could ever achieve, and each advancement toward absolute zero temperature has led to novel and rich physics. In June 1907, the Dutch physicist and Nobel prize winner Heike Kamerlingh Onnes successfully liquefied helium and achieved a temperature of $\sim$ 1.5 K, which was the lowest temperature at that time, and this led to the discovery of a new state called superconductivity. In the following years, superfluid helium-4 was discovered at the transition temperature of about 2.2 K. In 1972, superfluidity in helium-3 was revealed by Lee, Richardson, and Osheroff at the temperature of 2 mK [2, 3]. At one time, liquid helium was thought to define the regime of cryogenic physics until the invention of the laser, which pushed cooling techniques into a new era.

The idea of using a laser to cool atoms or ions was first introduced in 1975 by two different research groups: Wineland and Dehmelt [4], and Hansh and Schawlow [5]. In 1978, Wineland, Drullinger, and Walls took the idea from Ashkin [6] and experimentally demonstrated the cooling of atoms via radiation pressure and successfully cooled magnesium ions below room temperature [7]. In 1982, William D. Phillips and Harold Metcalf developed a Zeeman slower to effectively slow down sodium atoms to 40 percent of their initial velocity [8]. In 1985, Steven Chu's team at Bell Labs succeeded in loading cold sodium atoms into an optical molasses and further lowered the temperature to 240 μK [9]. Two years later, in 1987, E. L. Raab and co-workers generated the first magneto-optical trap (MOT), which trapped $\sim 10^7$ sodium atoms for 2 min with a temperature below one millikelvin [10]. A year later, Claude Cohen-

Tannoudji of the École Normale Supérieure in Paris and his colleagues cooled ^{4}He atoms down to a temperature of 2 μK based on velocity-selective optical pumping, which broke the recoil limit [11]. In 1997, the Nobel Prize in Physics was awarded jointly to Steven Chu, Claude Cohen-Tannoudji, and William D. Phillips for their contributions to laser cooling and trapping.

The cold atomic gas generated with laser cooling and trapping techniques has a temperature many orders of magnitude below the temperature of liquid helium. At an extremely low temperature, the de Broglie wavelength of atoms in the gas becomes comparable to or longer than the chemical bond, approaching the wavelength of the cooling light, and some of the wave properties of matter are expected to happen, such as resonances and interferences. As the temperature becomes even lower (below 1 μK), where the de Broglie wavelength becomes comparable to the interparticle distance, the phase-space density of the atomic gas also becomes very high. When the number of particles per cubic de Broglie wavelength equals a value of 1 or higher, the atomic gas experiences a phase transition to form a Bose-Einstein condensate (BEC) for bosonic species or a degenerate Fermi gas for fermionic species. A BEC forms when a macroscopic number of the atoms in a bosonic atomic gas occupies the lowest energy state of the trapping potential. The coherence and macroscopic nature of this new type of matter wave have paved the way for many new fields of physics and many fascinating research areas, such as many-body physics, precision measurements, quantum information science, and quantum optics. The beauty of a BEC is that it provides a highly controllable experimental platform to investigate interactions among atoms and reveals quantum behavior on a macroscopic scale. On the one hand, weak interactions in BECs lead to interesting non-linear physics such as the generation of entanglement [12], quantum phase transitions in spin space [13], domain formation [14], and BEC vortex experiments [15]. On the other hand, tuning

a Feshbach resonance is a direct way to reach the strong interaction regime in dilute and ultracold gases [16]. Related research includes forming various molecular BECs from paired fermions and studying the BEC-BCS crossover region [17]. Another interesting research field is investigating the BEC in an optical lattice. A quantum phase transition from a superfluid to a Mott-insulating state is performed by loading a BEC into an optical lattice and adjusting its potential depth [18]. Supersolids, a state of matter that has a crystalline structure, like a solid, but can flow without friction like a superfluid, has also been proven with BECs in optical lattices and optical cavities [19, 20]. Besides this, since BECs are highly controllable, for example the phase and amplitude of matter waves can be controlled, they have been recently applied to generate new atom interferometry for high precision measurements [21]. The Cold Atom Laboratory of NASA has launched a BEC-based atom interferometer into the International Space Station to study general relativity, searches for dark energy and gravitational waves, and spacecraft navigation.

In addition to generating quantum degeneracy in an atomic gas, laser cooling and trapping technologies are also shining new light on many other research fields. For example, laser cooling and trapping of cold molecules has drawn considerable interest and has many applications within quantum chemistry, many-body physics, and fundamental physics. Several molecules such as strontium fluoride (SrF) [22], calcium fluoride (CaF) [23, 24], and yttrium oxide (YO) [25] have been successfully cooled down to realize their quantum degeneracy. Besides, cold atoms also connect fundamental physics to real applications. Optical lattice clocks based on ytterbium or strontium atoms have been shown to have better precision for timekeeping than original atomic clocks [26, 27]. For inertial sensing, cold atom interferometers offer a promising route towards the next generation of navigation systems. They can effectively tackle the bias drifts of gyroscopes and accelerometers in long-term inertial

navigation [28, 29]. Another ongoing research interest are Rydberg atoms, due to their controllable long-range interaction [30], which are the foundation of today's neutral-atom quantum computers. This new generation of programmable neutral atom quantum computers has recently matured enough that the technology has begun to transfer from academic labs to startup companies. In addition, the Rydberg blockade offers quantum optimization algorithms for solving the maximum independent set mechanism, which is considered to be in the class of non-polynomial hard problems if solved classically [31]. This technology has real industrial applications such as antenna placement, 5G network optimization, incremental store placement, and many more [32].

1.2 Thesis Summary

This thesis reports on research done using the first sodium spinor BEC ever made at the University of Oklahoma, applying an all-optical approach. I present research results on spin-mixing dynamics and atom interferometry in spin space with F=1 microwave-dressed antiferromagnetic spinor BECs.

After this introductory chapter, chapter two mainly focuses on the theory of laser cooling and trapping techniques. Chapter three to chapter six describe how we experimentally realized our sodium spinor BEC from the ground up. Since I spent more than half of my Ph.D. research time on designing and building the apparatus, I will explain, in detail, how the experiment works. Chapter three elaborates on our ultra-high vacuum system with pressure in a range of low 10^{-11} Torr. Chapter four presents the main experimental setup for cold atoms, including laser locking, Zeeman slower setup, magneto-optical trap setup, imaging system, and the digital and analog control systems. Chapter five describes our homemade versatile microwave system. Chapter six illustrates how we load atoms into the optical dipole trap and how the

evaporative cooling technique leads us to almost pure BECs with about 3×10^4 atoms in the trap.

In chapter seven, we explore some interesting physics with our spinor BEC. We study spin-exchange collision where two atoms in the magnetic sublevel $m = 0$ can coherently and reversibly scatter into a pair of atoms in the $m = +1$ and $m = -1$ states and vice versa. We further explore the regime in which these dynamics can be accurately explained within the single spatial mode approximation (SMA) and when the approximation is violated. We map a new type of resonance between spin and spatial degrees of freedom, which is not driven by quantum fluctuations, but by the mean-field. In chapter eight, we switch gears to study one of the potential applications of the spinor BEC, which is atom interferometry. We will mainly focus on atom interferometry in spin space and investigate metrological gain by comparing phase sensitivities to the standard quantum limit. Chapter nine is a summary and future outlook, which includes a brief discussion of light-pulse interferometry, which we plan to do in the future.

Chapter 2

Theory of Laser Cooling and Trapping

It is well known that light can exert a force on atoms immersed in the light field to slow the atomic motion and manipulate atoms. This force can be divided into two types: a dissipative, spontaneous force and a conservative, dipole force. The spontaneous force relies on the atom absorbing or emitting a quantum of photon momentum, whereas the dipole force, from the classical point of view, is the interaction between the transition dipole and the light field. The two different types of light force generated on atoms directly contribute to the laser cooling methods we use for generating Bose-Einstein condensates in our experiments.

In this chapter, we review some instances of the two different types of light forces and study the physics behind the key ingredients of laser cooling and trapping. The discussion starts with laser cooling with resonant light, including Doppler and sub-Doppler cooling, which leads directly to the magneto-optical trap (MOT). After that, we review the cooling techniques using far-off resonance light, which includes the optical dipole trap and evaporative cooling.

2.1 Laser Cooling with Near-resonant Light

Because light beams carry momentum, the scattering of light by an object produces a force. The idea of using near-resonant laser light to cool atoms stems from the fact that atomic absorption of light is more likely to happen when the frequency of a photon is on resonance with the atomic transition. This type of radiation force is velocity-dependent because of the velocity dependent Doppler shift, which shifts the laser frequency seen by the atoms moving relative to the laboratory-fixed laser. Laser cooling narrows the Doppler-broadened absorption lines by cooling the atomic gas,

resulting in increased phase space density. Laser cooling of atoms in gases is a strong dissipative process because of the momentum loss by the atoms during the absorption of a plane light wave and re-emission of a spherical light wave.

2.1.1 Doppler Cooling

Photons have energy $E = \hbar\omega$ and momentum $P = \hbar k$ ($\hbar$ is the Plank constant divided by 2π). When a moving atom absorbs a photon from a near-resonant light field, the photon momentum $\hbar k$ is transferred to the atom. At the same time, the atom undergoes a transition to the excited state. After this primary momentum kick from a photon due to absorption, the atom re-emits a photon and receives a secondary momentum kick due to spontaneous emission. The primary momentum kick due to absorption is directional. However, the secondary kick is in random directions, and purely isotropic due to the spontaneous emission. Therefore over many absorption-emission cycles, the contribution of the net momentum from the secondary momentum kick is averaged out. In contrast, the primary momentum kicks all add up. As a result, the net scattering force acts on the atom is in the direction of the laser beam propagation. This force is also called radiation pressure.

To better understand how the Doppler effect plays a role in atom cooling, we first illustrate a case for an atom at rest in a two-level system. The scattering force from absorption followed by spontaneous emission can be written as [33]

$$F_{sc} = \hbar k \gamma \rho_{ee}, \tag{2.1}$$

where ρ_{ee} is the probability for the atoms to be in the excited state, which can be obtained by solving the two-level optical Bloch equation to be

$$\rho_{ee} = \frac{1}{2} \frac{s_0}{1 + s_0 + 4\delta^2/\gamma^2}, \tag{2.2}$$

where $\delta = \omega - \omega_0$ is the laser detuning with respect to the two-level atomic transition ω_0, γ is the spontaneous decay rate from the excited state, and the saturation parameter

$s_0 = I/I_s$, where I is the laser beam intensity and I_0 is the saturation intensity. The scattering force becomes

$$F_{sc} = \hbar k \frac{\gamma}{2} \frac{s_0}{1 + s_0 + 4\delta^2/\gamma^2}. \tag{2.3}$$

For a system at rest and with laser detuning $\delta = 0$, when the laser beam intensity I is small compared to the saturation intensity I_s, the spontaneous force is small. Increasing the laser intensity thus will increase the magnitude of the cooling force. However, if the laser intensity is large, where $s_0 \gg 1$, the cooling force saturates at $\hbar k\gamma/2$. Because of the saturation, the natural linewidth of the transition is broadened. This phenomenon can be observed by experimentally scanning the frequency detuning. This broadening is called the power-broadened linewidth of the transition.

In a moving frame, atoms with a certain velocity are most likely to absorb photons with a certain detuning δ with respect to the atomic resonance frequency ω_0 due to the Doppler effect. For atoms moving with velocity v, the laser beam in the co-moving frame has the Doppler-shifted frequency $\omega' = \omega - \mathbf{k}\cdot\mathbf{v}$. If the laser beam is red-detuned with respect to the atomic resonance, the atoms moving toward the beam see the beam Doppler-shifted to the blue and closer to resonance than the atom moving away from the light beam. Atoms will, therefore, mostly scatter photons from the beams towards which they are propagating and less from the other beams. The atoms experience a viscous force opposing their motion. The force is proportional to the atom's velocity. For two counter-propagating light beams with the same frequency, intensity, and polarization, the net scattering force is the sum of the forces from each beam. In one dimension, the net scattering force becomes $\mathbf{F}_s = \mathbf{F}_+ + \mathbf{F}_-$, where

$$\mathbf{F}_\pm = \pm\hbar k \frac{\gamma}{2} \frac{s_0}{1 + s_0 + (2(\delta \mp \mathbf{k}\cdot\mathbf{v})/\gamma)^2}, \tag{2.4}$$

and therefore the sum of the two forces is

$$\mathbf{F}_s \cong \frac{8\hbar k^2 \delta s_0}{\gamma(1 + s_0 + (2(\delta/\gamma)^2)} \mathbf{v} \equiv -\beta\mathbf{v}, \tag{2.5}$$

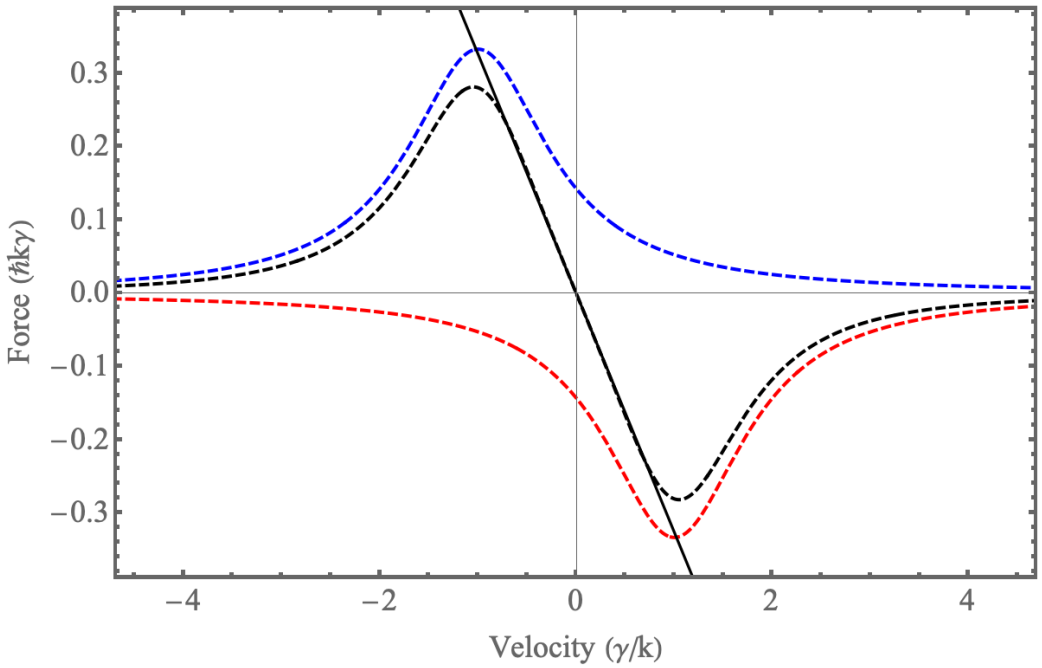

Figure 2.1: Optical damping force in one dimensional optical molasses with $s_0 = 2$ and $\delta = -\gamma$. The blue dashed trace shows the force from the light beam which atoms move toward, the red one is the force generated from the atoms moving along with the light beam, and the black dashed trace is the sum of the two. The black solid line shows the linear relation between the damping force and the velocity if the velocity is small enough within the so-called capture velocity range.

where the higher-order terms with respect to velocity have been neglected. In a low light intensity regime, the stimulated emission is neglected, and the net scattering force and the velocity relation are illustrated in Figure 2.1. As Fig. 2.1 shows, the force is negative for $v > 0$ and positive for $v < 0$, so the force decelerates atoms. We also see the net scattering force $\mathbf{F}_s = -\beta\mathbf{v}$ in one-dimension is linearly proportional to velocity when the atoms are moving with small enough velocities, equivalent to viscous damping, where the friction coefficient is β. This configuration damps the motion of atoms just like that on a particle in a viscous fluid and is hence called the optical molasses technique, similar to motion in honey [34]. In addition, we know

from Fig. 2.1 that there are velocities for which the force cease to act like friction, we call it capture velocity. Atoms that enter the optical molasses within the capture velocity range can be cooled efficiently, atoms outside the range are not cooled. A three-dimensional optical molasses is formed with three pairs of counter-propagating beams intersecting each other, each pair of beams along one of the Cartesian axes. In the overlap region of the beams, atoms can be cooled in three dimensions.

Figure 2.1 and Eq. (2.5) give an unphysical prediction that Doppler cooling is able to cool the sample down to zero velocity. The heating from fluctuations in the force has not been taken into account. The spontaneous emissions cause the atom to perform a random walk in momentum space with discrete step size $\hbar k$, and their kinetic energy changes by at least the recoil energy $E_r = \hbar^2 k^2/2m$. The competition between the heating and cooling process determines the minimum temperature that the Doppler cooling is able to reach, which defines as $T_D = \hbar\gamma/2k_B$ [35], where k_B is Boltzmann's constant and T_D is also referred as the Doppler cooling limit. For ^{23}Na, the Doppler cooling limit is 240 μK.

2.1.2 Sub-Doppler Cooling

In 1988, William Phillip's group used three pairs of counter-propagating laser beams to cool down sodium atoms in three-dimensional optical molasses and surprisingly found that the temperature of the atoms was much lower than the Doppler cooling limit. The responsible mechanism for this sub-Doppler cooling was identified soon by Jean Dalibard and Claude Cohen-Tannoudji. It is called Sisyphus cooling or polarization gradient cooling [36], and experimentally realized by Steven Chu and co-workers [37].

Polarization gradient cooling usually occurs when atoms have multiple degenerate ground states (*e.g.* hyperfine structure and Zeemann sublevels). In the presence of a

light field, ground states are split due to the AC Stark shift. For atoms moving in a light field where the polarization varies in space, optical pumping will adjust the atomic orientation in the ground state to the changing polarization of the light field in a non-adiabatic process. This leads to a stronger viscous damping force experienced by the atoms than in Doppler cooling. For Alkali atoms such as Rb and Na, the atomic structures are much more complicated than a basic two-level system. They can be cooled to temperatures of sub-Doppler limit, which is much lower than the Doppler limit via more sophisticated processes. In this section, we mainly discuss two types of polarization gradient cooling: linear $\perp$ linear polarization gradient cooling and σ^+-σ^- polarization gradient cooling in one dimension.

We use the simplest transition where the light field couples $J = 1/2$ and $J = 3/2$ states to show the polarization gradient cooling in linear $\perp$ linear configuration. We consider two orthogonal linearly polarized laser beams with the same intensity and frequency that counter-propagate each other. The polarization of this light field varies depending on the relative phase of the two laser beams and varies with position, as shown in Fig. 2.2. Over half of a wavelength, the light polarization changes from linear position at $\lambda/8$ to σ^+ at $\lambda/4$, and back to linear at $3\lambda/8$. Then the polarization changes to σ^- at $\lambda/2$, and the paths repeat. Light shifts play an important role in this cooling mechanism. In the presence of the light field, the atomic ground state is shifted towards lower energies for a laser tuning below resonance ($\delta < 0$) and causes a splitting of the degenerate ground state based on the coupling strength between light and atoms. For the ground state $J = 1/2$, two magnetic sublevels $m = 1/2$ and $m = -1/2$ are split due to the light shift. On the one hand, the light shift for magnetic sublevel $m = 1/2$ is stronger than that of the $m = -1/2$ when the light field is purely σ^+. On the other hand, the light shift for the magnetic sublevel $m = -1/2$ is stronger when the light polarization is purely σ^-. Polarization gradient cooling relies

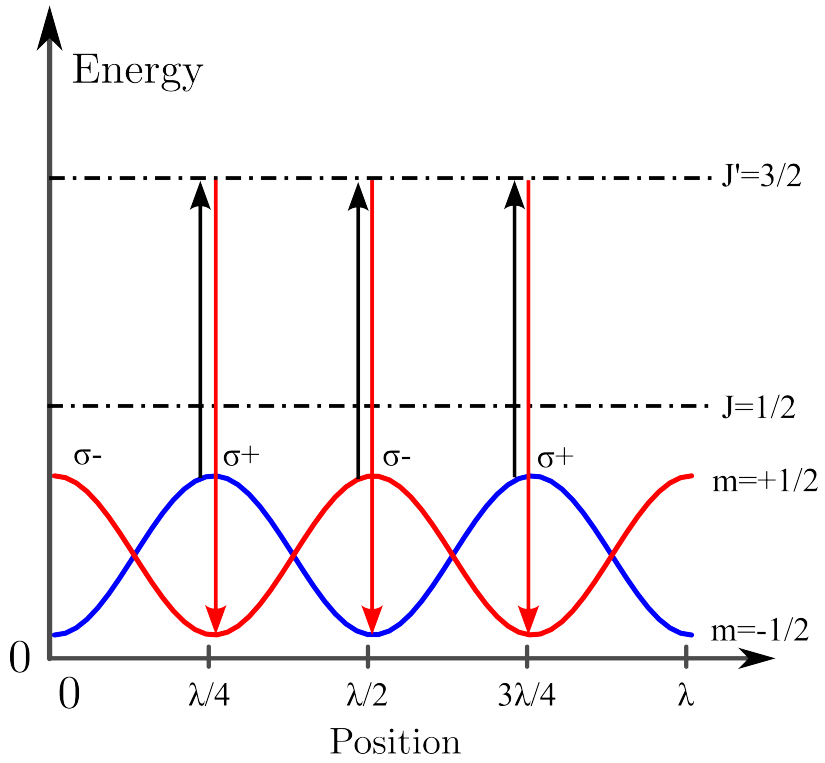

Figure 2.2: Polarization gradient cooling in lin $\perp$ lin configuration. The electrical dipole transition happens between two levels with angular momenta $J = 1/2$ and $J' = 3/2$, where the manifolds in $J' = 3/2$ are not shown. The polarization changes from $\sigma+$ to $\sigma-$ over a distance of $\lambda/4$, and the light has elliptical or linear polarization between these positions. Atoms starting at $z = 0$ in the $m = -1/2$ must climb the potential hill as they approach the $z = \lambda/4$ where the light becomes pure $\sigma+$ polarization, and there they are optically pumped to the $m = 1/2$ sublevel, this process repeats several times until the kinetic energy is not enough for atoms to climb the hill anymore.

on the absorption and re-emission of the photon to dissipate energy and, therefore, cool atoms. When an atom is in the $|J = 1/2, m = -1/2\rangle$ ground state and moves along the polarization gradient, the kinetic energy is converted to potential energy while the atom is climbing the potential hill. The strongest coupling between light and atom happens at the top of the hill at $\lambda/4$. Hence, atoms experience a pure σ^+ polarized light and are optically pumped, via excited states $|J = 3/2, m = -1/2\rangle$, to the ground state $|J = 1/2, m = 1/2\rangle$, where the σ^+ light is weakly coupled. The spontaneous emission radiates the potential energy away from the light-atom system, causing the system to lose energy. The same cycles repeat until the atoms do not have enough kinetic energy to climb the hill. This cooling mechanism is also called Sisyphus cooling, named after the Greek mythological character who was doomed by the Greek gods to forever roll a large boulder to the top of a hill.

For σ^+-σ^- polarization gradient cooling, two counter-propagating beams with opposite circular polarization create a light field where the polarization is linear everywhere, but directions are rotated about the beam axis. In this configuration, the polarization does not vary from linear to circular; therefore, no "hills" or "valleys" are formed because there are no spatially dependent light shifts, and atoms are no longer cooled by the Sisyphus effect. Instead, the net friction force generated is based on motion-induced orientation in the atomic ground state, and it requires at least the transition between ground state $J_g = 1$ to excited states $J_e = 2$.

For atoms at rest in the light field, local linearly polarized light populates most of the atoms in the $m = 0$ ground state, and the rest are equally shared in $m = \pm 1$ ground states. By contrast, in a moving frame, atoms experience a rotating linear polarized light field, and this cause the population to re-distribute depending on the velocity of atoms. For atoms traveling toward the laser beam with σ^+ polarization, $|J_g = 1, m = 1\rangle$ is most likely to be populated, and the σ^+ light is scattered more

efficiently than the σ^- light because of the different Clebsch-Gordan coefficients. The atoms that scatter σ^+ light experience a momentum kick in the opposite direction of the light, and this damps the motion of atoms. Similarly, atoms traveling toward the σ^- beam preferentially stay in the $|J_g = 1, m = -1\rangle$ state, scatter σ^- light, and recoil in the opposite direction. Overall the unbalanced radiation pressure generated from the different scattering rates for atoms in $m = \pm 1$ states leads to a net force that opposes atoms' motion. It is also worth noting that the overall imbalance induced by the atom motion is not due to the Doppler effect but to a difference of populations in the ground state. As shown in Ref [36], this type of cooling mechanism achieves at velocities much lower than those achievable via Doppler cooling alone.

2.2 Magneto-optical Trap

The optical molasses can cool an atomic gas down to the micro-Kelvin regime. However, both Doppler and sub-Doppler cooling are velocity-dependent damping effects and therefore do not localize the atoms. The optical molasses can be transformed into a trap for atoms by applying an inhomogeneous magnetic field in addition to the optical field. The magnetic field gradient-induced Zeeman effect creates a spatially dependent shift of the laser-cooling transition frequency such that the velocity-dependent damping force is transformed into a position-dependent restoring force. This trapping mechanism combines a magnetic quadrupole field and an optical field named magneto-optical trap (MOT). The first demonstration of a MOT was in 1987, and since then, various types of MOT have been introduced, such as pyramid MOT [38], a 2-dimensional (2D) MOT [39], and a surface MOT [40]. Here, we mainly focus on the widely used three-dimensional MOT, which we apply in our BEC system.

The principle of the MOT in one dimension is illustrated in Fig. 2.3. We assume the simplest case of an atomic transition between the hyperfine levels $J = 0$ and $J' = 1$.

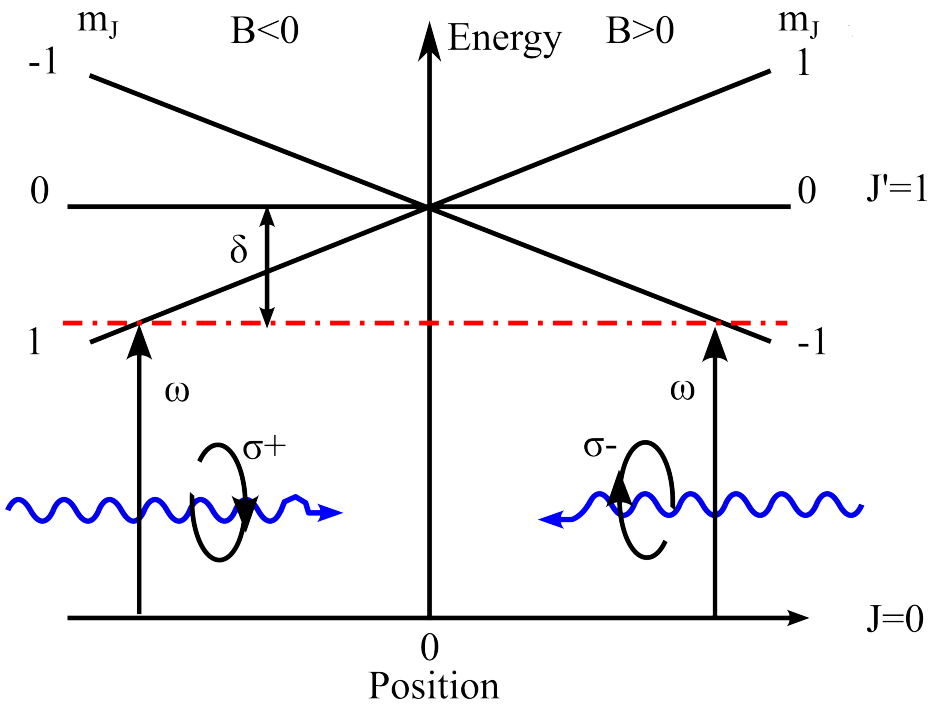

Figure 2.3: The mechanism of a magneto-optical trap in one dimension, illustrated for an atom with an atomic transition between $J = 0$ and $J' = 1$. Two counter-propagating beams of circularly-polarized light illuminate the atom in a magnetic field gradient. The magnitude of Zeeman splitting between three magnetic sublevels depends on the atom's position. The restoring force from the laser beam and magnetic field gradient pushes the atom back toward the center of the trap. The energy diagrams are not to scale.

A magnetic quadrupole field is applied such that there is a zero magnetic field at the center of the z axis ($z = 0$) and the field increases in magnitude away from the center. Two orthogonal circularly polarized lasers are counter-propagating, with frequency detuned below the zero fields atomic resonance by δ. Because of the Zeemann shift, three magnetic sublevels of $J' = 1$ ($m_J = 0$ and $m_J = \pm 1$), overlapped at $z = 0$, split as the magnetic field increases away from the center. As shown in Fig. 2.3 for $B > 0$, the $m_J = 1$ state is shifted up, whereas the $m_J = -1$ state is shifted down. The polarization of the laser beam that is incident from the right is chosen to be σ^-. The $m_J = -1$ sublevel of the excited state is shifted closer to resonance, and due to the

selection rule, $\Delta M = -1$, only the σ^- beam can be absorbed. Thus the atoms will prefer to scatter σ^- light at this position and be pushed toward $z = 0$. This process generates a position-dependent restoring force due to the inhomogeneous magnetic field. The restoring force tends to push atoms back to the center where the magnetic field is zero. Similarly, for a σ^+ laser beam propagating to the right in the $B < 0$ regime, the $m_J = 1$ state is shifted down and closer to resonance. Therefore atoms in the $m_J = 1$ state will only scatter σ^+ light. The resulting position-dependent restoring force will also push the atoms back towards the center.

As illustrated in Fig. 2.3, after taking the Zeemann shift into account, the effective detuning of the $\sigma^\pm$ beam in the MOT is $\Delta = \delta \mp (\mathbf{k} \cdot \mathbf{v} \mp \mu B/\hbar)$, take this expression into Eq. (2.4), the total force acting on an atom in the MOT is

$$\begin{aligned} \mathbf{F}_{MOT} &= \mathbf{F}_+ + \mathbf{F}_- \\ &= \frac{\hbar k \gamma}{2} \frac{I/I_s}{1 + I/I_s + (2\delta - (\mathbf{k} \cdot \mathbf{v} - \mu B/\hbar)/\gamma)^2} \\ &- \frac{\hbar k \gamma}{2} \frac{I/I_s}{1 + I/I_s + (2\delta + (\mathbf{k} \cdot \mathbf{v} + \mu B/\hbar)/\gamma)^2}, \end{aligned} \tag{2.6}$$

where μ is the effective magnetic moment, and B is the position-dependent magnetic field. After expanding the force in terms of the small Doppler and Zeemann shifts, we obtain both a velocity and a position-dependent force

$$\mathbf{F}_{MOT} = -\beta \mathbf{v} - \kappa \mathbf{z}, \tag{2.7}$$

where β is the damping coefficient associated with the velocity, as explained before, and κ is another damping coefficient caused by the Zeeman effect. In the MOT, the restoring force appears in addition to the damping force of the optical molasses.

So far, the discussion has been limited to a 1D MOT. However, the scheme can be easily extended to a 3D MOT using six laser beams instead of two. The schematic of a typical three-dimensional MOT setup is shown in Fig. 2.4: A pair of anti-Helmholtz coils is placed outside the vacuum chamber to generate a quadruple magnetic field.

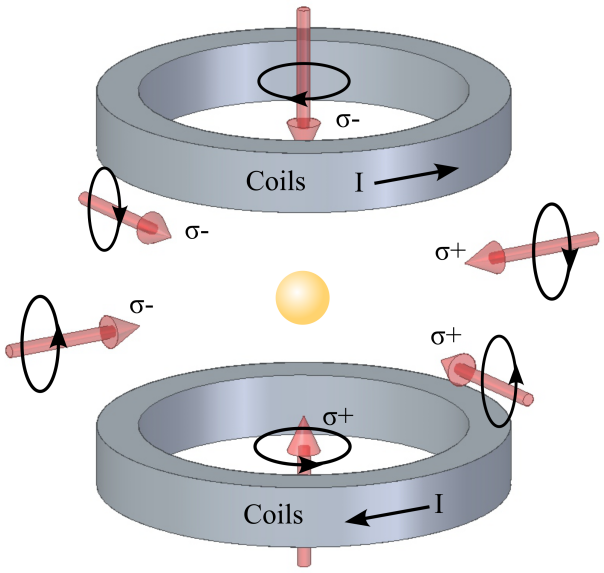

Figure 2.4: Schematic of the 3D MOT. Three orthogonal pairs of circularly polarized laser beams intersect at the center where the magnetic field is zero. A pair of coils with opposite currents generates a quadruple magnetic field. This setup traps and cools atoms at the center of the configuration.

Three pairs of counter-propagating laser beams, perpendicular to each other, intersect at the center of the vacuum chamber where the magnetic field is zero. σ^+ and σ^- polarizations are generated by putting quarter wave plates along each beam path. The MOT is a very robust trap since the power and polarization of laser beams do not need to be precisely balanced. In some setups, a pair of counter-propagating beams can be simply generated by one beam with its own mirrored retro-reflected beam. In this setup, the circular polarization of the retro-reflected beams is enforced to be correct at the expanse of the power imbalance between the incident and retro-reflected beams due to losses from mirror reflection, atom absorption, etc. To compensate for this loss,

we prepare six independent incident beams in our setup, which allows us to precisely control both power and polarization for each beam to optimize the MOT shape and number of atoms. Inside the MOT, densities exceeding 10^{11} cm^{-3} can be reached, and hundreds of millions to billions of atoms can be accumulated within seconds. Atom loss happens in the MOT due to background gas collisions and two-body loss, such as the photoassociation of atom pairs. The repulsion between atoms that arises when an atom absorbs a photon emitted by another atom (multiple scattering) keeps an upper bound on the density.

For alkali atoms, the trapping schemes become more complicated due to the multiplicity of the ground states. For example, in Na, $F = 1$ and $F = 2$ are two hyperfine levels of the ground states. Usually, the MOT is generated using the $F = 2$ to $F' = 3$ transition. However, since the $F' = 3$ excited state is very close to the $F' = 2$ excited states, there is a small probability of off-resonant excitation from $F = 2$ to $F' = 2$. Spontaneous emission will cause the atoms not only to decay to $F = 2$ state but also to $F = 1$ because of the selection rule $\Delta F = 0, \pm 1$. Since the hyperfine splitting in the ground states is large, ~ 1.7 GHz, the $F = 1$ state is decoupled from the cooling beam. Atoms that decay in this way to the $F = 1$ state leave the cooling cycle, leading to atom loss in the MOT. In order to compensate for the losses, another laser beam is applied to pump atoms out of the $F = 1$ state. This "repumping" beam overlaps with the MOT beam and couples the $F = 1$ to $F' = 2$ transition, will pump the atoms back to the cooling cycle.

2.3 Optical Dipole Force

The optical dipole force is another type of force acting on atoms due to light. It arises from the transition dipole induced by the oscillating electric field of the light. The magnitude of the dipole force is related to the gradient of the light field and the

detuning of the optical frequency. The blue or red shift with respect to the atomic transition determines the sign of the force acting on the atom. Unlike the scattering force we discussed earlier, the dipole force is a non-dissipative force that conserves energy. There exists, in principle, no upper limit on the magnitude of the dipole force since it is a function only of the field gradient and detuning.

2.3.1 Optical Dipole Trap

When an atom is placed into a light field, the oscillating electric field $\mathbf{E}$ will induce an atomic dipole moment $\boldsymbol{\mu}$ that oscillates at driving frequency ω. The interaction potential of the induced dipole moment in the electric field can be written as

$$U_{dip} = -\boldsymbol{\mu} \cdot \mathbf{E}. \tag{2.8}$$

The dipole force is then the negative of the gradient of the potential,

$$\mathbf{F} = -\nabla U_{dip}. \tag{2.9}$$

Unlike the radiation force, which is due to photon scattering, the mechanism of the dipole force relies on the electric dipole interaction. Therefore, the frequency of the light field can be far-detuned from resonance to minimize optical excitations and the recoil associated with it. The magnitude of the optical dipole potential depends on the laser intensity. A focused laser beam generates a position-dependent light intensity. Atoms tend to be trapped where the intensity is the largest if the detuning is to the red. Since atoms are trapped in the light field, they still experience a scattering force that heats the atoms, especially where the laser intensity is large. Therefore the atoms that are trapped in an optical dipole trap experience both the dipole potential, which is

$$U_{dip}(\vec{r}) = -\frac{3\pi c^2}{2\omega_0^3}\left(\frac{\Gamma}{\omega_0 - \omega_L} + \frac{\Gamma}{\omega_0 + \omega_L}\right) I(\vec{r}), \tag{2.10}$$

and the scattering rate induced heating, which can be written as

$$\Gamma_{scatt}(\vec{r}) = \frac{3\pi c^2}{2\hbar\omega_0^3}\left(\frac{\omega_L}{\omega_0}\right)^3\left(\frac{\Gamma}{\omega_0-\omega_L}+\frac{\Gamma}{\omega_0+\omega_L}\right)^2 I(\vec{r}). \tag{2.11}$$

Here, ω_0 is the atomic resonance, ω_L is the frequency of the laser beam, Γ is the natural linewidth ($2\pi\times 9.8$ MHz for the D2 transition of ^{23}Na), and $I(\vec{r})$ is the spatially dependent beam intensity for a Gaussian laser beam $I(\vec{r}) = I_0 e^{-r^2/\omega_0^2}$. We define $\Delta = \omega_L - \omega_0$ and apply the rotating-wave approximation to eliminate the $\omega_L + \omega_0$ terms. We then obtain

$$U_{dip}(\vec{r}) = -\frac{3\pi c^2}{2\omega_0^3}\left(\frac{\Gamma}{\Delta}\right) I(\vec{r}) \tag{2.12}$$

and

$$\Gamma_{scatt}(\vec{r}) = \frac{3\pi c^2}{2\hbar\omega_0^3}\left(\frac{\omega_L}{\omega_0}\right)^3\left(\frac{\Gamma}{\Delta}\right)^2 I(\vec{r}). \tag{2.13}$$

These expressions tell us two important features of dipole trapping. First, the detuning Δ can be tuned to either negative (red-detuned) or positive (blue-detuned), and both of them can be used in atom trapping. A red-detuned beam will generate a negative potential that will attract the atoms toward the light field. On the other hand, a blue-detuned beam will generate a positive potential that pushes atoms away from the light field. Therefore, dipole trap configurations are different for red or blue detuning. Second, the dipole trap potential $U_{dip}(\vec{r})$ is proportional to $I(\vec{r})/\Delta$ while the scattering rate Γ_{scatt} scales with $I(\vec{r})/\Delta^2$. Higher laser intensity and small Δ can provide tighter confinement for atoms. However, a small Δ can also lead to a high scattering rate. As a result, it is useful to apply a laser beam with a large detuning combined with a high intensity to get stronger confinement and lower scattering rates in the optical dipole trap.

In real optical dipole trapping experiments, the consequences of the optical dipole potential acting on multi-level atoms could lead to more complicated situations because

the optical dipole potential affects different atomic sub-levels differently. In a multi-level system, the electric dipole moment $\vec{\mu}_{ij} = \langle e_i | \vec{\mu} | g_j \rangle$ is known as the dipole matrix element between ground and excited states. Therefore energy shifts also depend on the coupling strength between specific sub-levels i and j of the electronic ground and excited states, which relates to laser polarization and the electronic and nuclear angular momenta involved.

For the alkali atoms that are used in most optical dipole trapping experiments, spin-orbit coupling gives the hyperfine splitting in the excited states, which leads to the well-known D line doublet ${}^2S_{1/2} \rightarrow {}^2P_{1/2}$ (D1 line) and ${}^2S_{1/2} \rightarrow {}^2P_{3/2}$ (D2 line). If the laser detuning Δ is comparable to the fine splitting frequency Δ_{FS}, then Eq. (2.10) becomes:

$$U_{dip}(\vec{r}) = -\frac{\pi c^2}{2}\left[\frac{\Gamma_{D1}}{\omega_{D1}^3}\left(\frac{1}{\omega_{D1}-\omega}+\frac{1}{\omega_{D1}+\omega}\right)+\frac{2\Gamma_{D2}}{\omega_{D2}^3}\left(\frac{1}{\omega_{D2}-\omega}+\frac{1}{\omega_{D2}+\omega}\right)\right] I(\vec{r}), \tag{2.14}$$

where Γ_{D1} and Γ_{D2} are the natural line widths of the $D1$ and $D2$ transition, respectively. ω_{D1} and ω_{D2} are the $D1$ and $D2$ transition frequencies. For far-off resonance light, which means $\Delta \gg \Delta_{FS}$, this double splitting and any polarization effects can be ignored.

2.3.2 Evaporative Cooling

Even though sub-Doppler cooling can cool atoms to the μK temperature regime, the resultant temperature is still limited by the heating caused by spontaneous emission. The photons will always be scattered and the atoms will undergo recoil kicks. This limit is called recoil limit and the recoil temperature is defined as $T_r = (\hbar k)^2/mk_B$. For Na, this temperature is $\sim$2.39 μK [41]. In order to generate a quantum degenerate gas such as a BEC, the atomic gas needs to be cooled below the recoil limit. Therefore other cooling schemes, different from laser cooling, have to be used. There are several

ways to break the recoil limit, for example, Velocity-Selective Coherent Population Trapping (VSCPT) [42], Raman cooling [43], and evaporative cooling.

Evaporative cooling was first demonstrated with magnetically trapped spin-polarized hydrogen in 1986 [44] and was extended to alkali atoms later in 1995 [45]. Since this mechanism does not involve density-limiting interactions with light, it turns out to be one of the most common ways to cool the atoms below the recoil limit and greatly increase the phase space density. Evaporative cooling has been demonstrated in both magnetic traps and optical traps. In magnetic traps, a radio-frequency field is used to remove hot atoms from a trapped spin state to a non-trapped spin state. In optical dipole traps (ODTs), this is done by lowering the power of the laser beam. Compared to a magnetic trap in which only atoms at weak-field-seeking states can be confined, an ODT can simultaneously trap all spin components and thus can be applied to generate spinor BECs for experiments involving two or more magnetic sublevels.

The mechanism behind evaporative cooling is based on the principle of removing atoms with higher-than-average kinetic energy from the trap, followed by re-thermalization of the remaining atoms inside the trap. One way to think about evaporative cooling is to consider cooling a cup of coffee. The hottest molecules of the coffee are evaporated away from the cup, leaving the rest of them at a lower temperature. After some hot atoms are removed from the trap, the remaining atoms have much lower average energy and occupy a smaller volume at the bottom of the trap, thereby increasing their density. In the ODT, the removal of hot atoms is done by adiabatically lowering the depth of the trapping potential by lowering the dipole trap beam intensity, as shown in Fig. 2.5. During this process, atoms with high average energy are removed from the trap as the potential depth of the trap becomes lower and lower. Then the collision-induced re-thermalization creates a new Boltzmann distribution of atoms with a lower average temperature and reduces the sample volume,

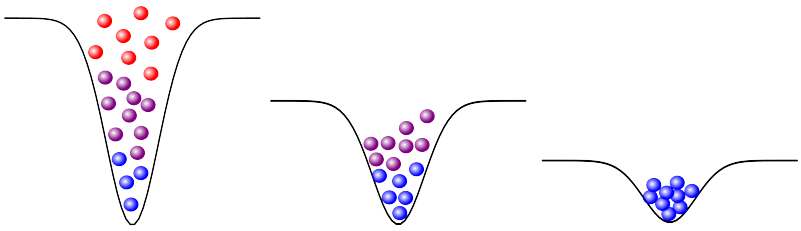

Figure 2.5: A schematic representation of atoms confined in a one-dimensional ODT. By lowering the intensity of the dipole trap laser beam, the trap depth is reduced so that energetic atoms (red) can leave the trap. After collisions between the remaining atoms, a new Boltzmann distribution with a lower average temperature re-establishes itself: atoms occupy a lower energy state with a lower temperature and an increased phase-space density.

increasing the phase space density. The time scale of evaporative cooling usually lasts for seconds. During forced evaporative cooling, a large fraction of atoms is removed from the trap and the remaining atoms in the trap occupy a high phase-space density. As a result, the temperature can go down to the nK regime, far below the recoil limit, and quantum statistics become important [46] (see chapter six for more detail).

Chapter 3

Vacuum System

In cold atom experiments, the number of atoms in a trap is limited by atom loss processes. One-body loss, which is described as the interaction between the trapped atoms and background, contributes to most of the atom loss when the background pressure is high. One-body loss can be dramatically reduced by isolating atoms from the environment. This is done by placing them in a vacuum. Building a well-performing vacuum system is crucial for most cold atom experiments because it will minimize the impacts of the background gas and prolong the lifetime of the trapped atoms. For MOT or BEC, building an ultra-high vacuum (UHV) system or an extreme high vacuum (XHV) system will be helpful to reach a lifetime to tens of seconds.

This chapter presents our vacuum system for generating a MOT and BEC. The first section introduces the layout of our UHV system with a pressure in the 10^{-11} Torr range. Section two discusses the installation, including cleaning, baking, and pumping. The last section describes the standard procedure of maintaining the vacuum system, including sodium refill and the nozzle clog cleaning procedure.

3.1 Overview of the Vacuum System

Our main experiment is carried out in a stainless steel ultra-high vacuum system fits on a 4' $\times$ 10' non-magnetic optical table as shown in Fig. 3.1. Our apparatus is divided into three main sections. The middle part is a Zeeman slower that connects the oven part of the system, which is used for sodium atomic beam generation, and the experimental chamber part, which is used for sodium gas cooling and trapping. First, the hot sodium vapor is created inside a sodium oven chamber with the average speed of atoms $\sim$ 1000 m/s. Two Varian classic style ion pumps and a differential

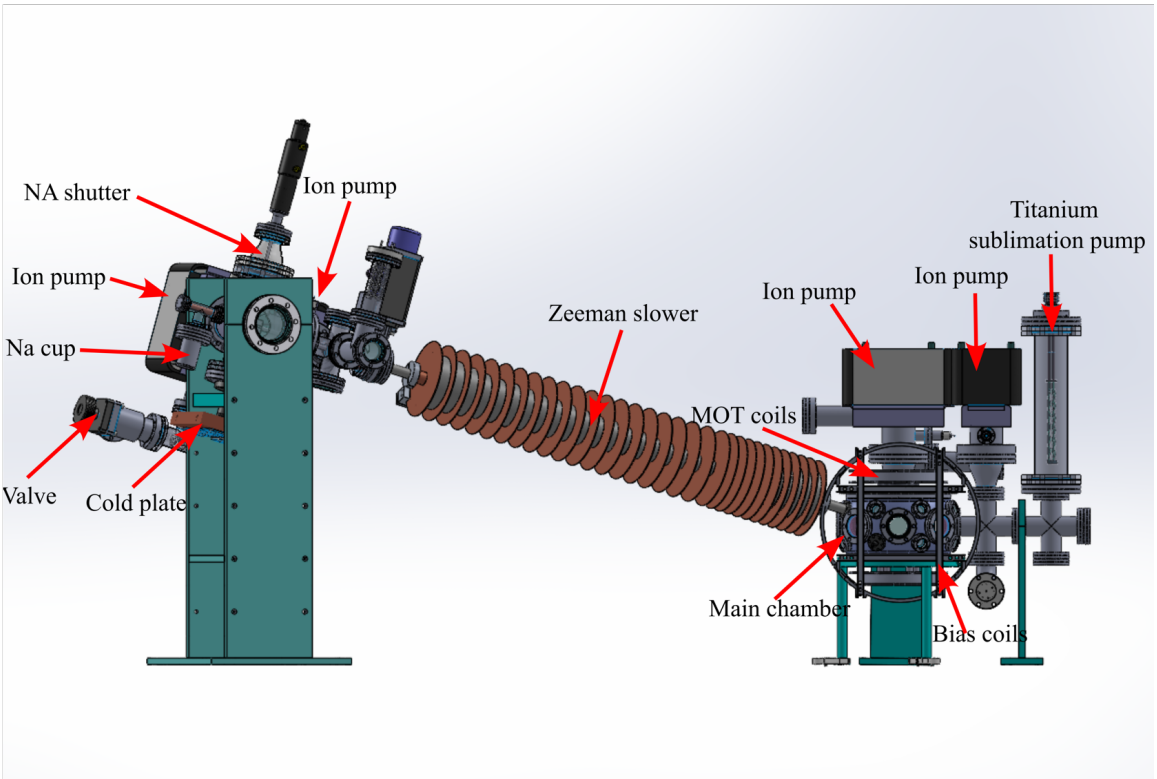

Figure 3.1: CAD rendering of the UHV system consisting of the sodium oven, the differential pumping chamber, the Zeeman slower, and the main chamber. In addition, ion pumps, titanium sublimation pump, and a turbo pump (not shown in the figure) are attached to the system to create and maintain UHV pressure.

pumping section are used in this area to maintain a low sodium background pressure before the sodium atoms go to the main chamber. An atomic beam is formed by a custom nozzle. Then, atoms are further slowed by a Zeeman slower to a speed which can be effectively captured by the MOT in the main chamber.

3.1.1 Na Vapor Generation

The sodium oven chamber is made of a stainless steel 4.5" 6-way cross where the sodium atomic beam is generated. A sodium reservoir is attached to the oven chamber, which is made of a stainless steel cup filled with a 10-gram 99.95% pure, pre-scored

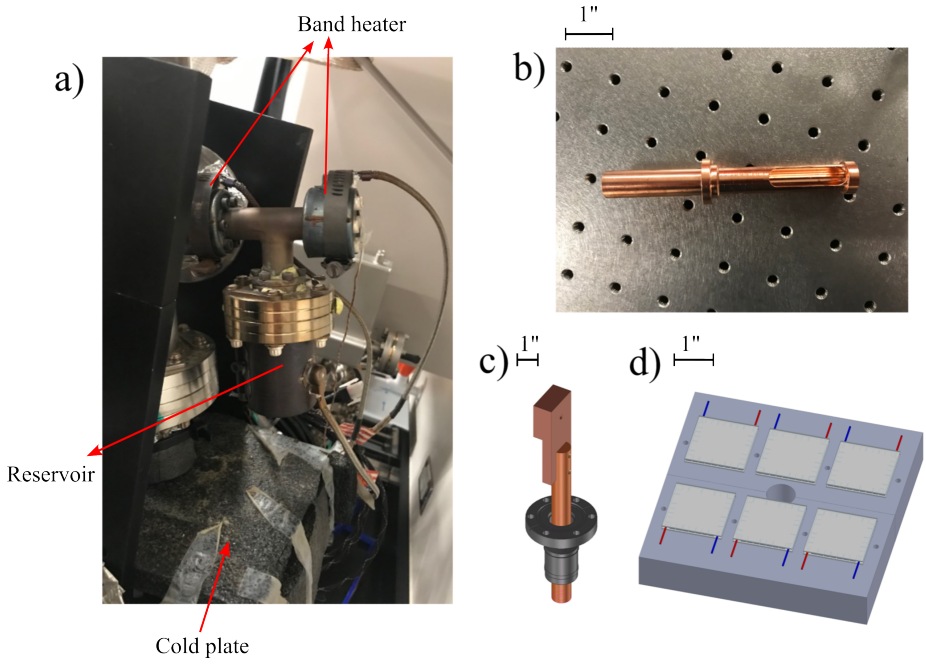

Figure 3.2: a) The sodium reservoir is made of a stainless steel cup filled with sodium. A nozzle is placed inside of the CF 1.33" tee that was mounted on the top of the reservoir. b) A 11.4 cm long nozzle to direct the hot sodium vapor away from the sodium reservoir. The 2.3 mm diameter hole is used to collimate the sodium vapor to create an atomic beam. c) 3D rendering of the cold plate. The top of the cold plate is inside the oven chamber to collect the hot sodium atoms. The thick copper feedthrough is in the air connected to a water-cooled of six TEC elements, as shown in d).

glass, sodium ampoule. The sodium cup is a stainless steel 2.75" ConFlat (CF) flange half nipple, custom welded with a cupped end. A reducing flange connects the sodium reservoir to a 1.33" CF tee, where we insert our custom copper nozzle, as shown in Fig. 3.2a and Fig. 3.2b.

The nozzle is 11.4 cm long with a ring that functions as a CF 1.33" copper gasket connecting to the oven chamber. The front nozzle with a center hole of 2.3 mm diameter is inserted into the oven chamber to collimate the atomic beam. Since the ring of the nozzle is in direct contact with one end of the CF 1.33" tee, it can be

efficiently heated up from outside via a band heater. We use two band heaters as flange heaters to heat the front and back of the nozzles. The temperature of the two nozzles is 400 °C when running the experiment and is decreased to 375 °C and 250 °C, respectively, when in standby mode. Note that the nozzle's temperature must remain high to prevent sodium from condensing and clogging the nozzle. We use a third band heater to heat the sodium reservoir and stabilize the temperature close to 300 °C to provide continuous and stable atomic flux when running the experiment. When the experiment is not running, we decrease the temperature of the sodium reservoir to 135 °C, so no sodium is wasted. All three band heaters' temperatures are read and precisely controlled by our PID-based temperature controller (Automation Direct SL4848-CR). In order to keep our oven region insulated, a mineral wool insulation material is used to keep the temperature high in the oven region and protect the people in the lab from high-temperature hazards. One thing that needs to be pointed out is that even though the oven and the nozzle are hot, in our setup the reduced flange used to connect the reservoir and the tee is relatively cold. Therefore, a small fraction of sodium gas will condense in this part. Over several years, it reacts with the copper gasket, and can cause leaking. Therefore, after running the experiments for some time, we decided to switch the copper gaskets to silver plated gaskets for all flanges exposed to high temperature. This greatly improved the longevity of the system.

A customized copper cold plate is placed inside the oven chamber. It is mounted onto a copper feedthrough which is cooled to -12°C using a water-cooled array of six TEC elements (6* TEC1-12706) on a custom copper heatsink, as illustrated in Fig. 3.2c and Fig. 3.2d. The cold plate acts to collect the hot sodium atoms at large angles. It prevents the sodium background pressure from increasing in the oven chamber. The nozzle is aligned with the center of the hole of the cold plate in order

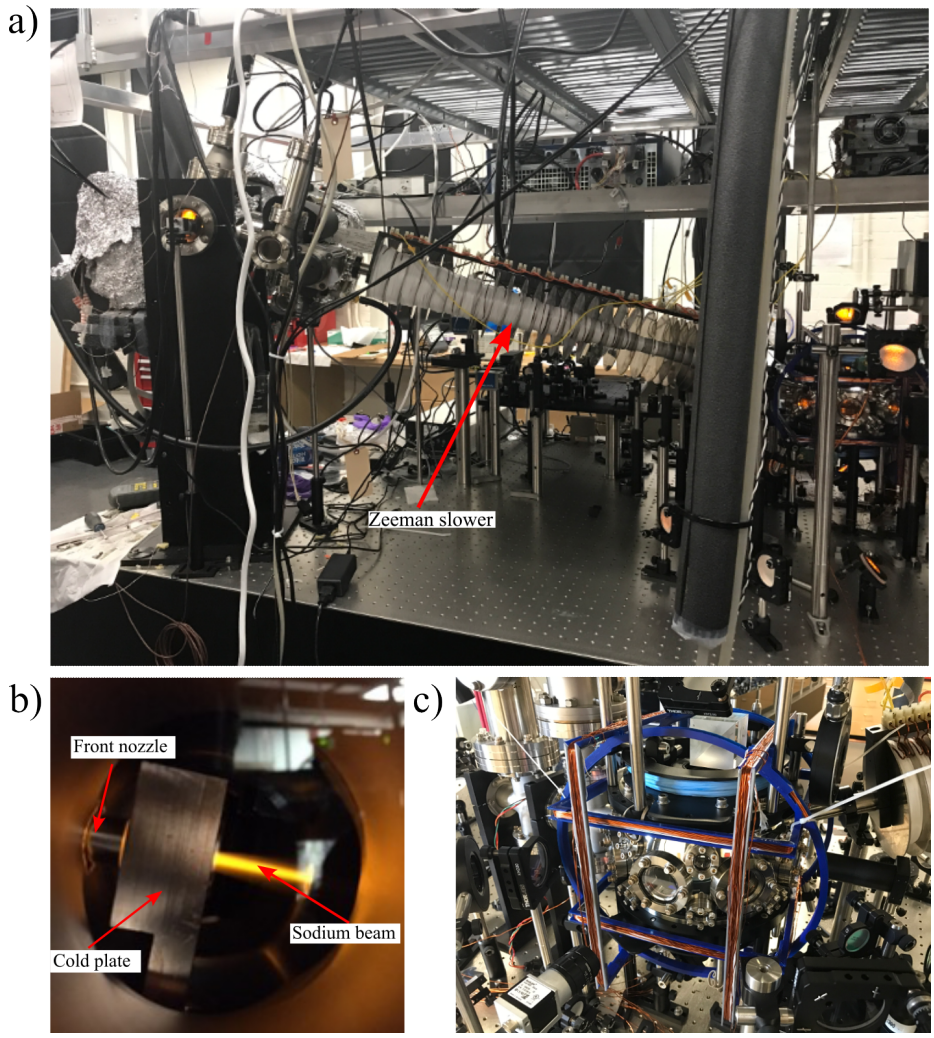

Figure 3.3: a) Photo of the UHV system, the Zeeman slower is marked in the picture. b) Photo of oven chamber taken through the oven chamber's viewport. The cold plate has a central hole that is aligned with the front nozzle. A mechanical shutter behind the cold plate can shut the atomic flux on or off. The yellow light is the fluorescence of the sodium beam. c) The UHV chamber where cooling and trapping mechanisms occur.

to collimate the atomic beam, as shown in Fig. 3.3b. A pneumatic mechanical shutter is placed between the cold plate and the front nozzle and can be remotely controlled to turn the atomic beam on or off before it enters the differential pumping chamber during experiments.

The differential pumping chamber is made of a stainless steel 2.75" 6-way cross which connects the oven chamber and the Zeeman slower. It is used to further reduce the pressure via a custom differetial pumping tube made of stainless steel. A 50 liter/second ion pump is attached to one port of the 6-way cross to pump the chamber. Another 2.75" 4-way cross is connected to one of the remaining ports of the 6-way cross and an ion gauge is connected to read the vacuum pressure when the system is baking. A pneumatic gate valve is installed at the end of the differential pumping chamber, which can be manually switched off to protect the vacuum of the main experimental chamber when the oven is exposed to air, for example when sodium needs to be refilled. The pneumatic gate valve can also be automatically shut off via the ion pump controller's interlock. If the main chamber's pressure is above the set point, the gate valve will shut off automatically to prevent the chamber's pressure from increasing. Additionally, another two viewports used for viewing the atomic beam are connected to the 6-way cross and the 4-way cross, respectively. These two viewports enable us to perform a careful alignment of the Zeeman slowing and repumping beams.

3.1.2 Zeeman Slower Design

Our Zeeman slower is situated between the differential pumping chamber and the main experimental chamber, as illustrated in Fig. 3.3a. The Zeeman slower consists of a 1.33" CF, 42" long custom stainless steel nipple as its main body. 32 copper plates which are used to dissipate the heat, are evenly mounted on a stainless steel tube that surrounds the nipple and divide the body into small sections. Double-insulated copper wire is wrapped around each section of the body to form copper coils used to generate magnetic fields. The whole body of the Zeeman slower is oriented $\sim 20^\circ$ above the table surface so it can attach to one of the 1.33" CF ports of the main chamber. The Zeeman slower's function and design will be detailed in the next chapter.

3.1.3 UHV Main Chamber

On the lower side of the Zeeman slower, which is shown in Fig. 3.3c, is the main experimental chamber, where cooling and trapping occurs. For cold-atom and BEC experiments, the background pressure of the experimental chamber should be as low as possible to reduce one-body loss. Therefore we want our vacuum system to be on the order of 10^{-11} Torr. The base pressure of the chamber is determined by the gas load divided by the effective pumping speed. The effective pumping speed will decrease as the pressure becomes lower, so it is essential to lower the gas load to reach the UHV regime.

In an ideal leak-free system, the gas load is determined by the amount of gas entering the chamber due to outgassing. Therefore, choosing materials with low outgassing rates is crucial to reaching the UHV regime. We choose low outgassing materials such as 304 stainless steel to build the main body of the UHV system, kodial glass for the viewports, Kapton insulated UHV compatible coaxial wire and OFHC copper gaskets. The UHV main chamber is a commercially available 8" extended-spherical octagon made from non-magnetic stainless steel (Kimball Physics MCF800-ExtOct-G2C8A16) with twenty-six CF ports. Furthermore, we installed two 8" CF kodial glass viewports used for the two vertical MOT beams and top-down imaging beam, eight 2.75" CF viewports on the side used for MOT cooling, MOT repumping beams, dipole trap beams, and sideways imaging beams, and two 1.33" CF viewports for Zeeman slower and Zeeman slower repumping beams. We also use two 1.33" CF ports for SMA electrical feedthroughs to connect two homemade antennas inside the chamber. The antennas are used for generating radio frequency pulses (kHz range) and microwave pulse (GHz range), respectively. Baking is used to decrease the outgassing rate, which will be discussed in detail in the next section.

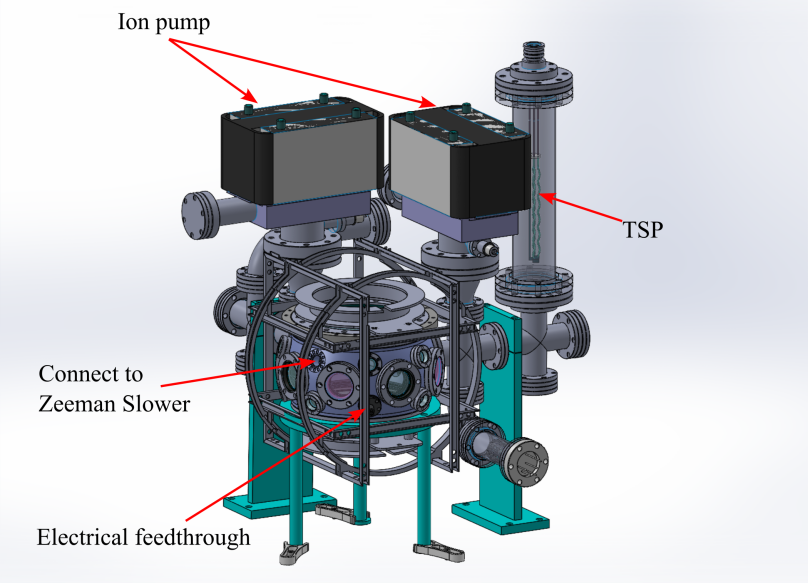

Figure 3.4: Pump setup for the main chamber. Two ion pumps are mounted to the main chamber through two 2.7" CF ports, and a TSP is installed next to one of the ion pumps. Two mini NEG pumps are mounted onto 1.33" CF ports with electrical feedthroughs.

3.1.4 Pumping Mechanisms

Adding pumps increases the pumping speed, thus lowering the base pressure. Our system uses two ion pumps, two non-evaporable getter (NEG) pumps, and a titanium sublimation pump to reach the UHV regime. The setup is shown schematically in Fig. 3.4.

Two ion pumps are mounted to the main chamber through two 2.75" CF ports. Ion pumps use an electrical, ionizing discharge maintained under vacuum conditions and chemically active metals, such as titanium. We apply 7.5 kV across the ion pump; under a high electrical and magnetic field combination, ion pumps pump the system by first ionizing the gas molecules and then attracting them with titanium cathode at the pumping speed of 50 L/s. Ion pumps are designed to operate continuously in the range between 10^{-4} to 10^{-8} Torr or below, so we keep them on at all time with the

UHV regime. A standard ion pump is ideal for pumping oxygen and nitrogen. Once atoms and molecules are pumped, they are permanently removed from the vacuum system. Small atoms such as hydrogen and helium can be pumped efficiently at room temperature. However, since some heavy noble gas, such as argon, is chemically neutral, they must be pumped by burial and covered by sputtered material. In our setup, we use a standard ion pump (Duniway Standard Diode Ion Pump) to pump chemically active gas such as oxygen and nitrogen. In addition, we use a Galaxy-Diode ion pump (Duniway Galaxy Diode Ion Pump) to pump noble gas such as argon.

In addition to the two ion pumps, two NEG pumps (SAES Getters Capacitorr CF16 MK2) are mounted onto the two 1.33" CF ports of the UHV main chamber. The NEG pump consists of a porous getter pump head and a CF16 support flange with an electrical feedthrough. Compared to the ion pump, the size of the NEG pump is much smaller, so the pump head can be directly put inside the vacuum chamber through a short CF16 port. At the same time, it can still maintain a significant pumping rate (20 L/s for H_2) due to the relatively large surface area of the porous getter. Additionally, the operation of the NEG pump does not rely on an external power supply. Once activated, the NEG getter pumps can be operated at room temperature. The activation of our NEG pumps is straightforward; they are powered using two DC power supplies (XANTREX XFR 100-12) by connecting the wires to their electric feedthrough. The first time activation was carried out with five Ampere current for 45 minutes. During activation, the NEG pump gets heated to promote the migration of the surface bonded species into the bulk of the material, and the stored H_2 is partially released from the porous getter. At the end of activation, the released H_2 is reabsorbed when the NEG pump cools down and the chamber is at room temperature. Usually, the NEG pump should be activated at the end of the baking with the vacuum pressure less than 10^{-6} Torr. The NEG pump must be reactived once it is exposed

to air or when its pumping speed falls below acceptable limits. The reactivation procedure is similar to the first-time activation. However, if the reactivation is carried out in a vacuum without air venting, the activation procedure can be performed with less time and a smaller current. During activation, we activate our two NEG pumps simultaneously. The ion pumps are turned off during NEG pump activation so the ion pumps will not absorb the hydrogen emitted by the hot getter.

We also employ a titanium sublimation pump (TSP) next to one of the ion pumps. Our TSP consists of a controller (Varian Sublimation Controller) and a TSP cartridge which is made of a 4.5" CF flange and contains three titanium-molybdenum filaments. New titanium (Ti) filaments or ones that have been up to air must be degassed before activation. We apply 30 Amps for 6 minutes to degas the filaments before activating them. Once degassing is finished, we set the current to 47 Amps for 1 minute with 30 minutes of cooling every cycle to activate the sublimation. During sublimation, the TSP deposits a fresh layer of Ti onto the nearby surfaces. Since clean Ti is very reactive, components of the residual gas in the chamber which collide with the coated walls are likely to react and form a stable, solid product. Thus the gas pressure in the chamber is reduced. After several activation cycles, we turn off the current and wait for the system to cool down. Care has to be taken to avoid direct line of sight from the TSP to any viewports to prevent coating the viewports.

In our system, we use both the NEG pump and the TSP. However, reconciling the two different types of pumps can be difficult. Theoretically, TSP can deposit a clean Ti surface during sublimation. On the other hand, the NEG pump gets heated and releases the stored H_2 during activation. Typically, all released H_2 will be reabsorbed as the NEG pump cools down. However, if a clean Ti surface is present, some H_2 will be pumped by the side surface. As a result, the Ti surface will be saturated with H_2, and instead of pumping, it becomes a source of releasing gas. Of course, the TSP

can be flashed by generating a new layer of Ti. However, the filament heating up to the necessary temperature will release active gases such as CO, which may partially saturate the active NEG, slowing the NEG pumps down. Our setup minimizes the effects by positioning the TSP relatively far away from the NEG pump.

We also use two standard 50 L/s ion pumps in the sodium generation section to pump the differential pumping chamber and oven chamber, respectively. The differential pumping chamber is a 2.75" 6-way cross with three viewports to give optical access. The ion pump mounted on another port can pump the pressure down to 10^{-9} Torr regime. The differential pumping chamber serves as an intermediate chamber connecting the high vacuum area on one side and the UHV area on the other. It provides a pressure gradient to prevent the main chamber from being directly exposed to the relatively high pressure. The oven chamber usually operates at 10^{-8} Torr. The ion pump is mounted on a 4.5" CF flange right next to the oven chamber. Since the oven chamber is directly connected to the sodium reservoir, a large amount of sodium gas enters the chamber when the reservoir is hot, causing the sodium background pressure to increase. The ion pump helps to keep the pressure from going too high. However, after a long time of exposure to the sodium vapor, the remaining sodium will poison the ion pump, causing the pressure to increase. While running the experiment, keeping the ion pump warm at about 80°C helps to sufficiently mitigate this problem.

Apart from the ion pump, we also have a portable turbo pumping station (Pfeiffer Vacuum HiCube 80 Eco) to pump our system mechanically. The turbo pumping station is mounted on a 2.75" CF port via a long stainless steel bellows at the end of the vacuum system. The turbo pumping station consists of a turbo pump (Horace 80) and a specially matched oil-free backing pump (MVP 015-2) that can pump the system from the atmospheric pressure. Once it turns on, the backing pump starts to

pump the system. The turbo pump turns on automatically after it meets a feasible pressure and gradually increases its speed until the maximum setting is reached. This process usually takes less than eight minutes. The vacuum system can be pumped down below 10^{-8} Torr with the mechanical pumping station running at full speed. The mechanical pump is only used to roughly pump the vacuum system while baking or after breaking vacuum. We close the angle valve and disconnect the turbo pumping station from the vacuum system while running experiments to minimize the vibration noise from the mechanical pump.

3.2 Cleaning, Assembling, Baking and Pumping the UHV Parts

3.2.1 UHV Components Cleaning

Cleaned surfaces are a prerequisite to achieve low pressure in the 10^{-11} Torr range. All impurities must be removed from the surfaces, so they do not desorb under vacuum conditions and produce gas loads or deposit on components. Cleaning vacuum parts is an efficient way to remove the contaminants before installing the vacuum equipment. Usually, vacuum components are inspected, cleaned, and packaged in the factory's cleaning room. Most of the contaminants have already been eliminated before shipping. However, some contamination may be left over, such as residual oil and grease on the surface of the vacuum surface, or small dust and particles. Typically, we clean and rinse the vacuum parts via the following steps:

- Wash the vacuum components with hot deionized water and detergent to remove the worst oils and dust. Then rinse with cleaned deionized water.
- Carefully immerse the components in a beaker with fresh acetone and clean them in an ultrasonic bath for 20 minutes at room temperature. Repeat this procedure

several times to completely remove the residual oil, grease, and detergent.

- Rinse the components with methanol and ultrasonically clean them in methanol for another 20 minutes at room temperature to remove the residual acetone.
- Pour out the vacuum components onto clean Kimwipes to soak up methanol. Then, carefully wrap them to prevent them from accumulating dust.

It is worth knowing that grease-free or powder-free gloves should be worn while cleaning and handling the vacuum components to prevent contaminants such as fingerprints and protect people from chemical hazards such as acetone and methanol. All fragile vacuum components such as gate valves, ion gauges, and electrical feedthrough should not be ultrasonically cleaned. Acetone should not be used to clean the components made of rubber, like O-rings (which are not UHV compatible) and copper [47].

3.2.2 UHV Components Assembling

The assembling procedure can be straightforward, but extra caution must be taken. It is required for at least two people to work together when assembling the UHV components. Grease-free or powder-free gloves should be worn and frequently changed while assembling parts. A copper gasket should be used whenever two CF flanges are connected since it mechanically seals the space between the two CF flanges' mating surfaces and prevents leakage into the vacuum while under compression. We use silver-plated gaskets instead of regular copper gaskets when the components are frequently exposed to high temperature and sodium. During the installation process, gaskets should be aligned well and evenly placed onto the knife edge of the CF flange before tightening with bolts. We use silver plated bolts and nuts to avoid using anti-seize grease. Using a wrench with a torque-click limiter is a proper way to avoid applying too much torque to break the bolt.

3.2.3 UHV System Baking and Pumping

Pumping is the next step after assembling the vacuum components. However, directly pumping at room temperature is inefficient to reach UHV regime because the inner surface of the cleaned components may still contain a large number of residual gases, such as adsorbed water molecules and traces of hydrocarbons. Baking while pumping the UHV system can dramatically accelerate the molecules emanating from the surface and reduce the time to reach the UHV pressure requirement. We start the bakeout by covering all the vacuum components with one layer of aluminum foil, followed by heating tape wrapped around the foil and covered with another layer of aluminum foil. Two layers of aluminum foil distribute the heat evenly through the surface of the vacuum parts. We take precautions to avoid hot spots due to crossed-wrapping which might damage the system. While pumping on the system with the turbo pump, the temperature of the heating tape should be increased smoothly to the designated value. The maximum bakeout temperature should be determined based on the material's properties. For example, the baking temperature for pure stainless steel vacuum parts can go as high as 400°C. However, a standard glass viewport can only withstand up to 200°C, and an ion pump can be baked to 150°C while operating with the magnets on and to 450°C with the magnets and cables removed. Our complete bakeout procedure consists of the following steps and precaution:

- We use a bakeout temperature at 120°C to degas water entirely. We make sure there are no cold spots or hot spots on the components to prevent damage to the components or inefficient baking.

- For the first-time baking, we turn on the turbo pump and its angle valve, and bake both chamber and ion pumps for 24 hours with ion pumps turned off. we keep the ion pumps' temperature between 110°C to 120°C.

- We then degas ion gauges and the TSP multiple times and note down the pressure. The pressure increases because of the degassing and eventually decreases after continuously baking and pumping.

- We pump for another 12 hours, or longer if needed, until the pressure reading from the ion gauge no longer improves. Next, we activate the NEG pumps, as mentioned before, followed by turning on the ion pumps. At this point, we close the turbo pumping angle valve and continue pumping with the ion pumps while still heating both the ion pumps and the chamber.

- We then switch off the ion pump heaters while we keep heating the chamber for another 12 hours, so the ion pump start to pump the chamber effectively.

- We switch off the heaters on the main chamber and let the whole system cool down. The vacuum chamber should reach the 10^{-10} to 10^{-11} Torr range with this procedure.

- We activate the TSP if the pressure does not reach the designated value, to further decrease the pressure.

It might take longer to bake the whole system because of the cold spot or leaks. To find the leak, we spray methanol onto the suspect flanges to detect large leaks. For small leaks, we spray helium gas onto the suspect flanges and use a residual gas analyzer (RGA) to detect the target helium. We also use an RGA to keep tracking the amount of gas that remains inside the vacuum system during baking and pumping to analyze the composition of the remaining gas. The RGA data in Fig. 3.5 clearly shows the composition of the gas and pressure changes after one day of baking and pumping.

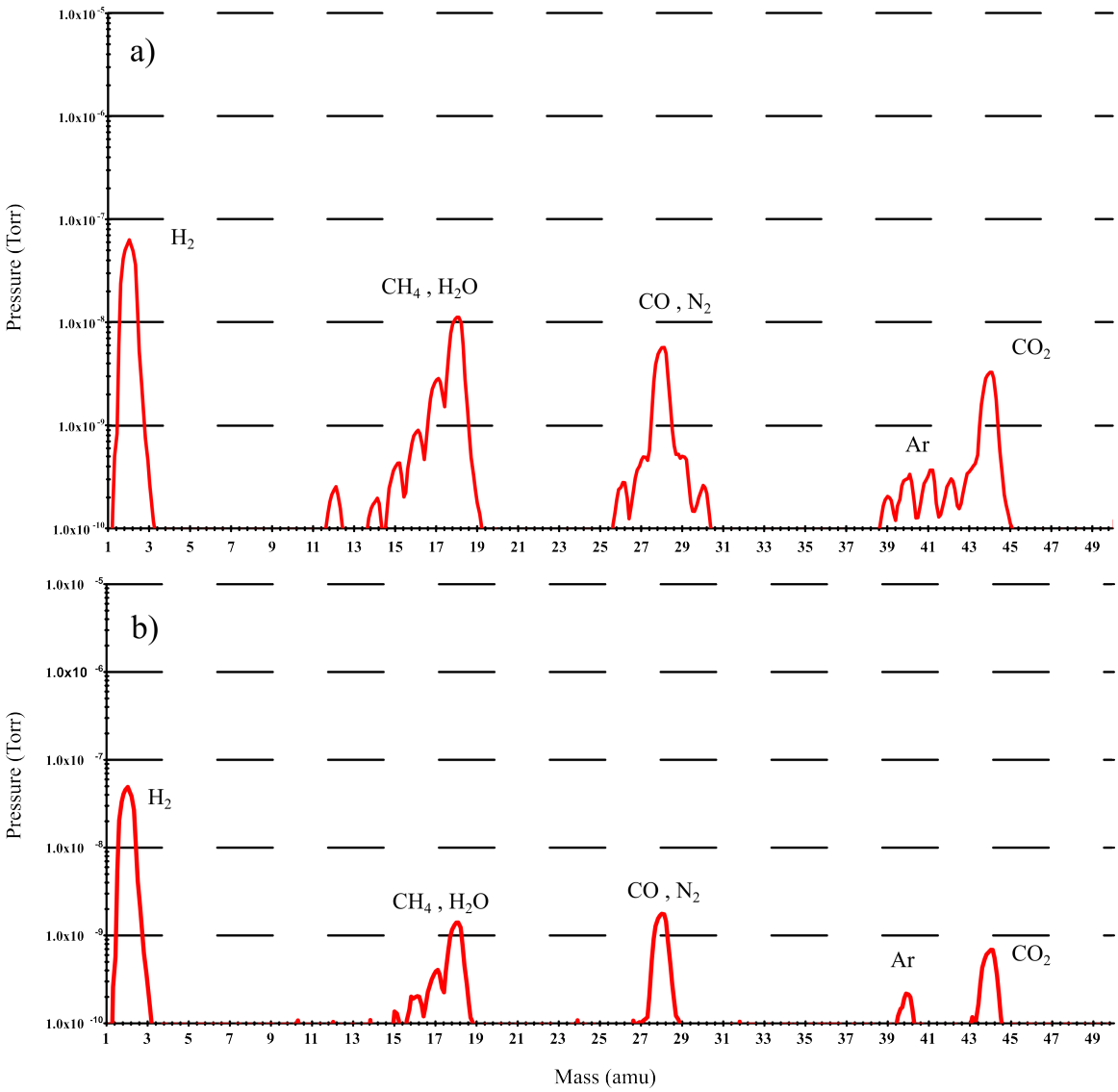

Figure 3.5: The data from our RGA shows the vacuum chamber's pressure as a function of atomic mass. Different mass of atoms indicates the gas composition in the vacuum chamber. The figure shows that the residual gas is made of H_2, CH_4, H_2O, CO, N_2, Ar, and CO_2. Figure (a) shows that all the gases were at a higher pressure on the first day of baking and pumping; after one day, the pressure of each gas went down significantly except H_2, as shown in figure (b). Because H_2 is a tiny molecule that can penetrate through the chamber, the chamber must be continuously pumped by the ion pumps, NEG pumps, or the TSP.

3.3 Sodium Replacement and Vacuum Maintenance

3.3.1 System Venting

Venting is necessary when we break the vacuum to install new components, refill sodium, or clean the nozzle. The turbo pumping station provides a venting function to vent the turbo pump and vacuum chamber. In our system, venting starts after the turbo pump is switched off and the turbo pump's rotating speed ceases to zero. We installed a venting valve (Flutventil Venting valve PM Z01 290 B) to the turbo pump to limit the pressure rise rate to below the maximum set value when the turbo pump shuts down or in the event of a power failure. It prevents the possible damage to the pump's rotor and magnetic bearing caused sudden pressure increase when the turbo pump is tuned off.

Vacuum chambers should be vented with dry nitrogen instead of air to prevent water vapor and other contaminates from depositing on the chamber walls. The OU Physics department offers clean dry N_2. We installed an air pressure regulator to control the N_2 backfill pressure just above one atmosphere so that there is a small outthrow of N_2 when a viewport is removed. This prevent dust and other contaminates from entering the system.

3.3.2 Sodium Replacement

Sodium needs to be refilled every few years. We typically load the reservoir with 10 grams of ≥ 99.95 % pure sodium packaged in pre-scored glass ampoules. The sodium replacement needs to be done in a clean environment with extra caution, and the vacuum system should be vented with dry N_2.

In order to pump the vacuum pressure from atmospheric pressure back to the UHV regime quickly, we have developed a standard sodium change procedure. First, before replacing the sodium, we ensure the pneumatic gate valve is closed to protect the

main experimental chamber and Zeeman slower. The apparatus should be at room temperature, including the temperature of the front nozzle, back nozzle, and reservoir, as well as the cold plate and ion pumps. The TEC elements that control the cold plate should be unplugged. It is crucial to wait until the cold plate temperature has finished slowly rising to room temperature. Otherwise, water condensation will form on the surface of the copper feedthrough inside the oven chamber and cause contamination. Second, we connect the portable turbo pumping station and pump for 30 minutes or until the reading of the rough gauge stays at its minimum value. We unwrapped the insulators and aluminum foil around the reservoir and nozzles and clean them with compressed air. Third, we turn off the turbo pump angle valve and let the dry N_2 fully vent the bellows connecting the turbo station. We then slowly open the angle valve until a hissing sound appears, then fully open the valve and let the dry N_2 fully vent the oven chamber. Fourth, we reload a new ampoule of sodium into a new half-nipple reservoir to replace the old one as quickly as possible to avoid excessive oxidation of the sodium metal. It should be pointed out that the glass ampoule of sodium should be wiped with acetone and methanol several times before putting it inside the reservoir to avoid contamination. At last, after this sodium change, we turn on the turbo pump to pump the oven chamber for 1-2 days until the pressure reaches the UHV regime.

3.3.3 Nozzle Cleaning

After running experiments for some time, the sodium atoms collected on the cold plate grow and generate a tip that grows back towards the front nozzle. If this happens, the sodium tip growth will block the atomic beam that comes out of the front nozzle and cause a reduction of atoms in both MOT and BECs. To solve this problem, we break the vacuum of the oven chamber by opening the 4.5" CF viewport

mounted on the oven chamber. To clean the nozzle, we first keep the apparatus at room temperature and vent the oven chamber with dry N_2 just as we do for refilling the sodium. Then, we start to remove the viewport after the dry N_2 saturates the oven chamber. After the oven chamber is fully open, one person should clean the viewport with acetone and methanol, and the other should clean the nozzle and cold plate by scraping with specific tools made of copper and stainless steel wires. Grease-free or powder-free gloves should be worn during cleaning, and all tools should be cleaned with acetone and methanol before being used in the vacuum chamber. A stainless steel wire should be inserted into and removed from the nozzle opening to ensure the nozzle is not clogged. After cleaning the nozzle and cold plate, we turn on the turbo pump to pump the oven for 1-2 days until the pressure reaches the UHV regime.

3.3.4 UV LIAD

Ultraviolet light-induced atom desorption (UV LIAD) is a method to control the alkali pressure in the vacuum chamber. It has been shown that alkaline metals atoms like sodium that are adsorbed by the walls of a vacuum chamber can be desorbed by irradiation with weak and incoherent UV light [48]. The effect of LIAD depends on both intensity and wavelength of the light. In our setup, we applied this technique to clean sodium atoms that form a film on some viewport surfaces which were directly exposed to the flow of sodium. To obtain a feasible intensity and wavelength, we use a 10W LED array (LED Engin LZ4-40B208-0000) with a wavelength centered at 400 nm. The LED array is driven by a regulated LED driver (Buckpuck 3021-D-I-700) at 700 mA and mounted on a heat sink with cooling fans, as shown in Fig. 3.6.

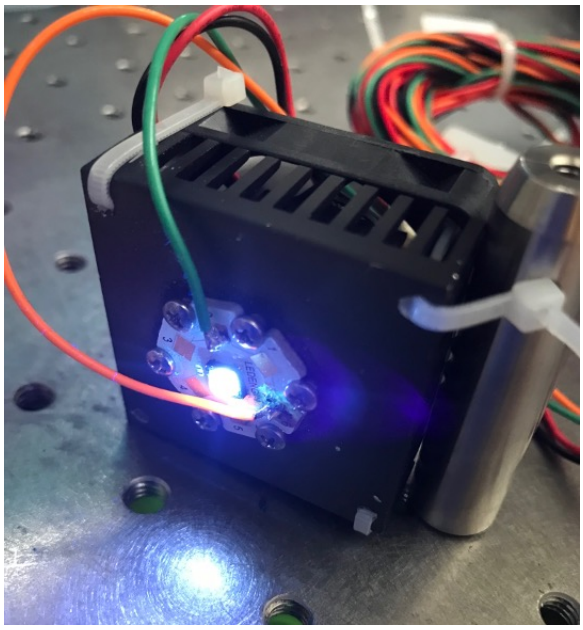

Figure 3.6: Photo of a mounted UV LED array used for removing sodium atoms from the viewport surfaces.

Chapter 4

Laser Cooling and Trapping Setup

In this chapter, our laser cooling and trapping setup for all-optical generation of Na spinor BECs is described. Section one presents our primary yellow laser system for cooling and trapping sodium atoms and generating the MOT, including our FM-modulated saturated absorption spectroscopy setup to lock the laser. Section two presents our setup for the Zeeman slower. Section three shows the sodium MOT setup, including laser cooling and repumping beams, water-cooling system, anti-Helmholtz coils for generating a quadruple magnetic field, and bias coils. In section four, the imaging system and imaging method are discussed in detail. The last section introduces our computer control system and how we implement it in running experiments.

4.1 Main Laser System

Our yellow laser system used for sodium cooling, repumping, and imaging fits on a 5' × 10' optical table, separated from the 4' × 10' optical table that holds the vacuum system, as shown in Fig. 4.1. In our setup, the main light source is a commercial second-harmonic generation system (TOPTICA TA-SHG PRO). It generates infrared light at the wavelength of 1179 nm via an external cavity diode laser (ECDL). The light is amplified by a tapered amplifier. The amplified light is then frequency doubled in a bowtie cavity crystal setup into visible light at 589 nm wavelength. The system can emit a continuous beam at a power of approximately 1 W over a tunable wavelength range of 589 ± 3 nm with instantaneous linewidth on the order of a few kHz. The IR laser frequency in the ECDL before doubling is monitored on an external wavelength meter, HighFinesse WS7, using a diagnostic low-power signal. The wavelength meter delivers excellent absolute accuracy of 30

MHz with a measurement speed of up to 500 Hz for pulsed and continuous lasers, which allows us to monitor the laser frequency. In order to have long-term frequency stability of about 1 MHz to meet our experimental requirements, we actively lock the laser frequency through FM modulated saturated absorption spectroscopy.

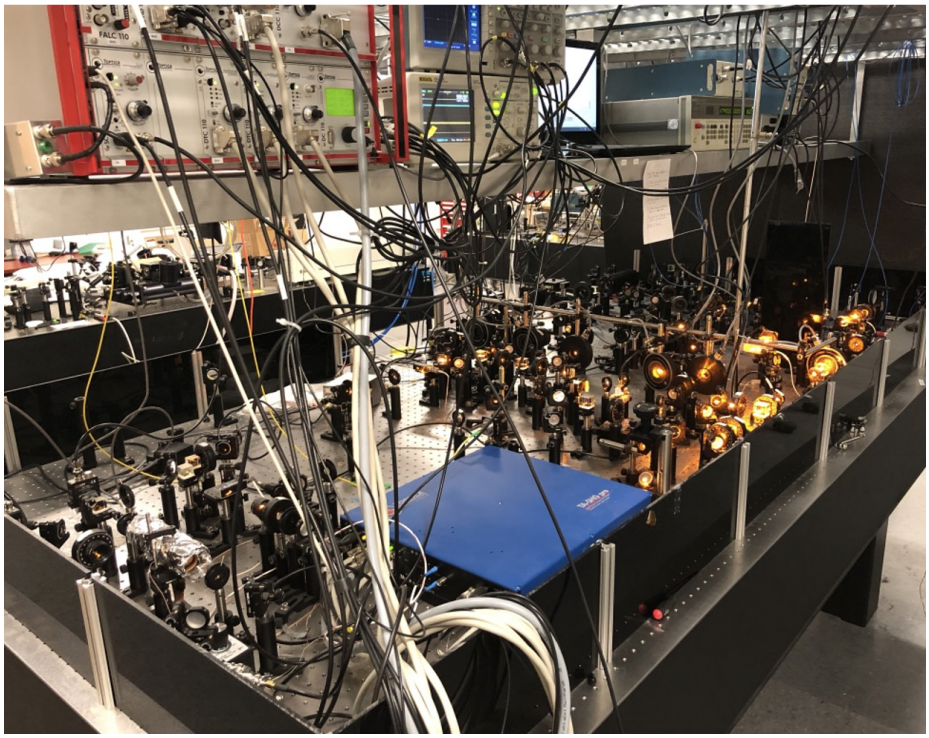

Figure 4.1: The main optical system fits on a 5' × 10' optical table that generates cooling, repumping and imaging beams. The main light source is generated from a commercial SHG laser system (TOPTICA TA-SHG PRO), designed to operate at wavelength $\lambda \approx 589$ nm with a continuous output power of 1 W.

4.1.1 Saturated Absorption Spectroscopy

The saturated absorption spectroscopy (SAS) technique is commonly used to determine the atomic transition frequencies in a Doppler-free way [49]. In regular laser spectroscopy, only one laser beam propagates through a hot atomic vapor cell. The hyperfine structure of the excited state manifold cannot be resolved due to the

large Doppler-broadening. Since atoms obey the Maxwell distribution of velocities at a given temperature, the Doppler shift broadens the absorption profile by a few hundred MHz to GHz, leading to a Doppler broadened spectrum much larger than the hyperfine splitting of the excited state of a few tens of MHz.

Doppler-free SAS was developed to eliminate the Doppler broadening and thus allows the splitting between energy levels of atoms to be measured with much greater precision [50, 51]. SAS uses two counter-propagating laser beams, an intense pump beam and a weak probe beam, overlapped in a hot atomic vapor cell with both beams derived from the same source, tuned to the same resonant frequency. When atoms are moving at close-to-zero longitudinal velocity, both pump and probe beams can be absorbed. The strong pump beam saturates the atomic transition along the beam path due to its high intensity. At the same time, the weak probe beam that counter-propagates the pump beam will no longer pump atoms from the ground state to the excited state since the atoms are already optically saturated. Instead, the probe beam interacts with the atoms in the excited state and causes stimulated emission, creating transmission peaks in the Doppler-broadened profile. These peaks are monitored on a photodiode detector.

Additionally, crossover peaks occur for a system with more than two states. For example, when two atomic transitions are within a single Doppler-broadened feature and share a common ground state, a moving atom sees both pump and probe beams resonant with two separate transitions simultaneously. Therefore the crossover peak occurs at a frequency precisely between two transitions. Crossover peaks can be quite strong, often stronger than the main saturated absorption peaks.

Fig. 4.2 shows an example of absorption spectroscopy of sodium with and without using the SAS technique. By blocking the pump beam and scanning the probe beam frequency over the sodium D2 line, we can perform normal laser spectroscopy on

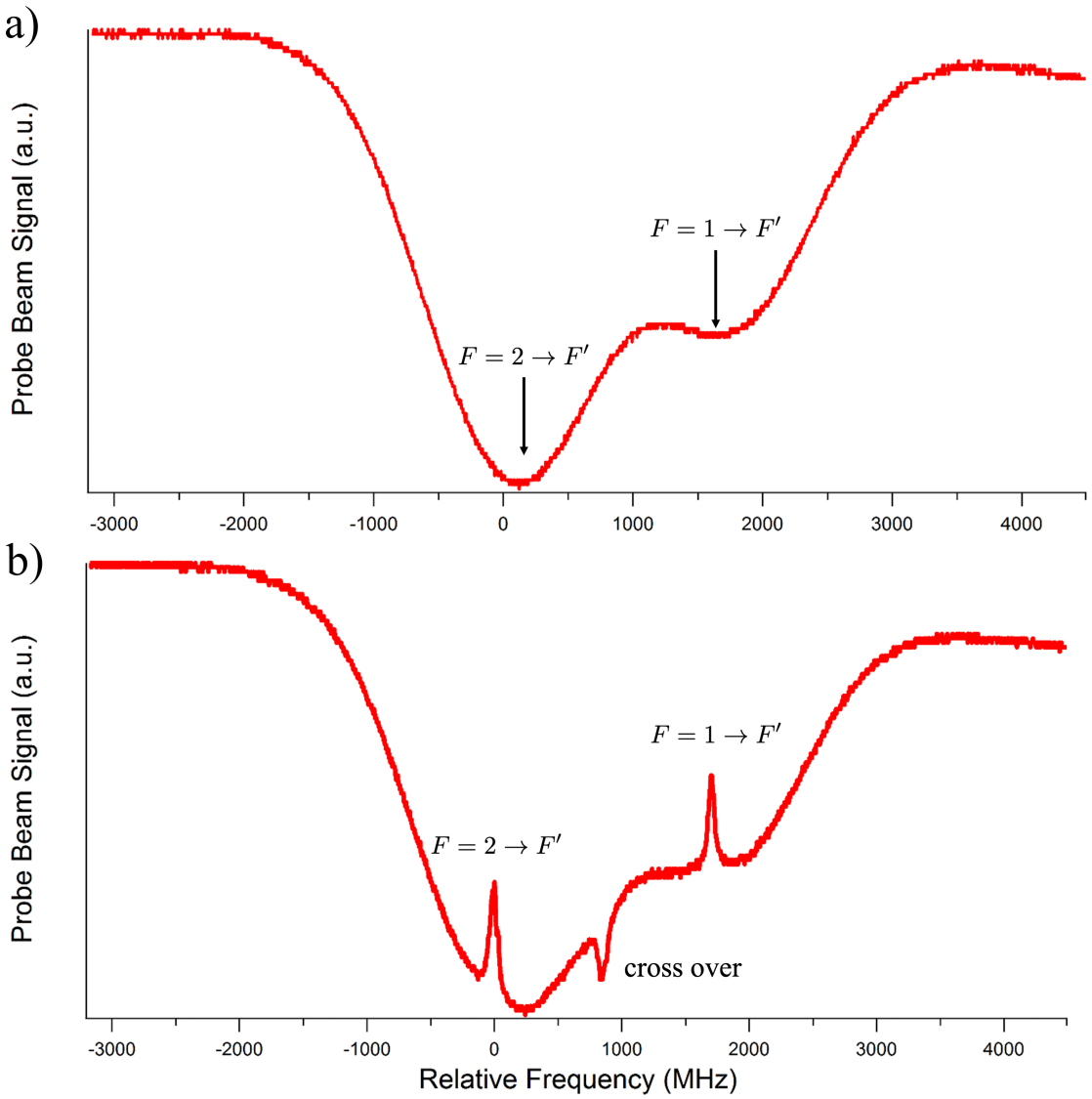

Figure 4.2: Probe beam absorption profile for laser spectroscopy. By blocking the pump beam and scanning the laser frequency over the sodium D2 line, we observe two distinct but not fully resolved absorption dips, as shown in (a). In (b), when the pump beam is unblocked, Lamb dips appear within the absorption profile. The leftmost and the rightmost peaks correspond to the transitions within the hyperfine structure, and the middle peak results from crossover resonances at frequencies directly between the other peaks.

the sodium vapor, which yields the Doppler-broadened absorption profile shown in Fig. 4.2a. Within this profile, two distinct but not fully resolved absorption dips are caused by the two ground states within the sodium hyperfine structure. The absorption on the left, at lower frequency, corresponds to the transitions between the $3^2S_{1/2}$ F = 2 ground state and $3^2P_{3/2}$ F' = 1, 2, 3 excited states. The absorption on the right, at higher frequency, corresponds to the transitions between the $3^2S_{1/2}$ F = 1 state and the $3^2P_{3/2}$ F' = 1, 2 states. When the pump beam is unblocked, we now perform saturated absorption spectroscopy, which causes the Lamb dips to appear within the absorption profile. As shown in Fig. 4.2b, the leftmost peak contains the Lamb dips associated with transitions involving the F = 2 ground state and their crossover resonances. The rightmost peak is similar to the left peak but for the F = 1 ground state. The Lamb dip in between these results from crossover resonances at frequencies directly between the other peaks.

The schematic of our SAS setup is shown in Fig. 4.3. The laser used for SAS is originated from the primary yellow laser (TA-SHG Pro 589 nm). The first half-wave plate and the following polarized beam splitter (PBS) distribute laser power to the SAS setup. Another half-wave plate and PBS split the beam into an intensive pump beam and a weak probe beam which counter-propagate in a hot sodium vapor cell. We use aluminum foil to wrap our glass sodium vapor cell and heat it with a heating tape, as illustrated in Fig. 4.4. The heating tape is positioned so that a temperature just above ~ 100°C is maintained and the windows are kept slightly hotter than the other parts of the cell. The sodium will neither condense on the cell windows nor react with the glass. We choose the leftmost peak in Fig. 4.2b which involves the transition between F=2 ground state to F' excited states to lock our laser. Specifically, we use the crossover peak between the F = 2 to F' = 3 and F = 2 to F' = 2 transitions as our locking point because it provides the strongest signal. In addition, we frequency-modulate

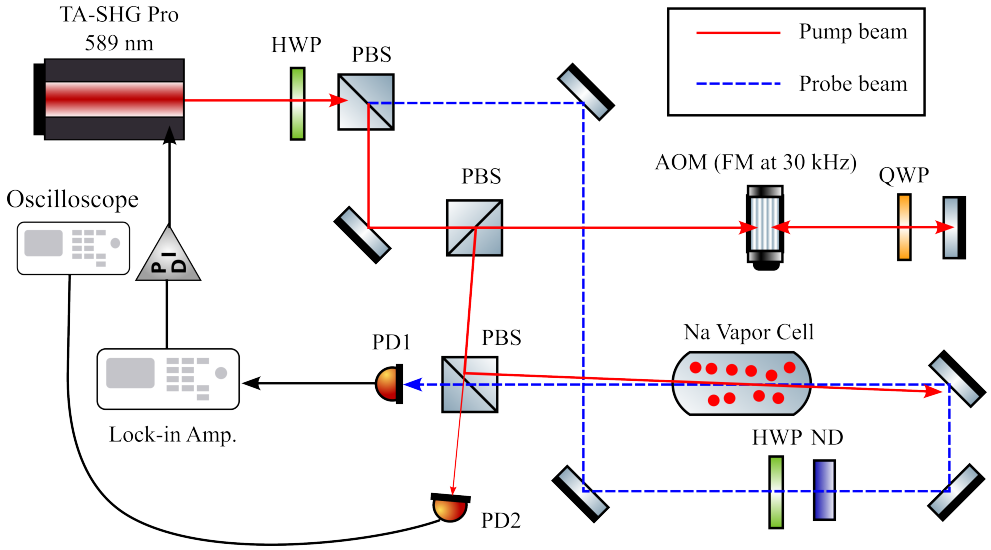

Figure 4.3: Experimental setup for FM-modulated saturated absorption spectroscopy. The pump beam (red solid line) and probe beam (blue dash line) are derived from the main laser. The pump is frequency shifted and FM modulated through an AOM to allow tuning of the lock point and lock-in detection to generate a derivative signal.

our pump beam via an acousto-optic modulator (AOM) set at a carrier frequency equal to 80 MHz. The AOM is set up in a double-pass configuration, so the total shift of the pump beam is red-detuned by 160 MHz. The modulation signal is generated by a lock-in amplifier reference signal which outputs a sine wave at a frequency of 30 kHz. We use a variable gain and offset circuit to make this signal compatible with FM input of the AOM driver. The resulting probe beam signal after de-modulation by the lock-in amplifier is proportional to the derivative of the original signal, which will have zero crossings for each of the well-defined Lamb dips in the absorption profile.

To lock the laser, the lock-in amplifier is used both to obtain a better signal-to-noise ratio as well as generate the error signal used to create the feedback loop for locking the laser. The probe beam is monitored by a photodiode (PD1), as shown in Fig. 4.3. The photodiode signal is fed into a lock-in amplifier (EG&G 5207 Lock-in Amplifier from Princeton Applied Research) to generate the error signal. The input probe beam

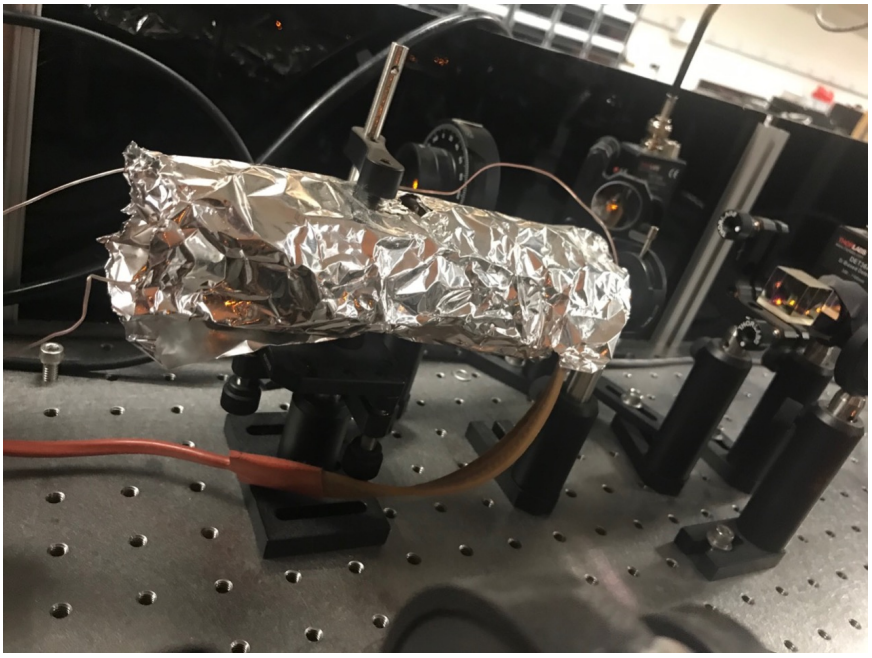

Figure 4.4: Sodium vapor cell used in our saturated absorption spectroscopy setup. We wrapped the vapor cell with aluminum foil and heated it up to ~ 110 °C. The windows are kept a few degrees hotter than the body.

signal can be detected by the lock-in amplifier via phase sensitive detection with a high signal-to-noise ratio [52]. This error signal generated by the lock-in amplifier is then fed into a home-built analog PID controller. It creates the feedback signal fed into the laser control circuit to stabilize the laser frequency via grating angle piezo and current feed-forward control, as shown in Fig. 4.5. To mitigate the residual amplitude modulation in the pump beam due to the AOM, we generated another sine wave signal, derived from the lock-in reference output, and feed it into the AM input of the AOM to stabilize the pump power. With the lock-in amplifier and PID controllers implemented in the SAS setup, we can lock our main diode laser for over 15 hours with a frequency accuracy within 1 MHz.

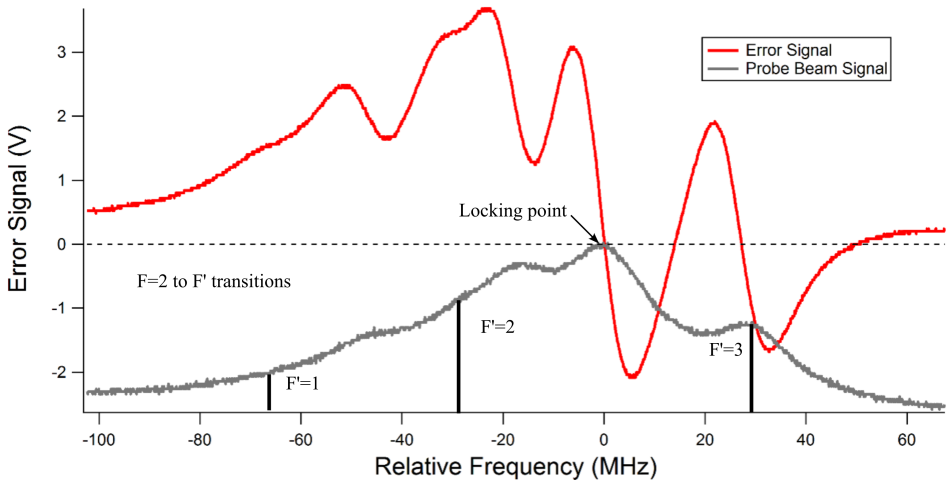

Figure 4.5: The output of the lock-in amplifier is shown in red. The grey curve is the absorption profile of the F=2 to F' transition. The red curve represents the amplitude derivative of the absorption signal. We lock the laser at the largest cross over peak which is the zero crossing of the error signal.

4.1.2 Main Laser Setup

Apart from the weak diagnostic beam used for locking the laser via SAS, all laser power is sent to the main optics setup to generate the Na atom cooling, Zeeman slowing, imaging laser beams, and their corresponded repumping beams, as shown in Fig. 4.6.

As discussed in Chapter 2, Doppler cooling happens when the cooling beam is red-detuning with respect to the atomic transition frequency. We use two AOMs to manipulate the frequency of the MOT cooling and Zeeman slowing beams, respectively, and another three AOMs to manipulate their repumping laser beams. The energy level diagram with the relevant transitions used for laser cooling is shown in Fig. 4.7. The initial laser frequency is locked ∼80 MHz red-shifted from the crossover transition between the F=2 to F'=3 and F=2 to F'=2 atomic transitions. The repumping beams' frequency is set to bring the atom from the F=1 ground state back into the cooling

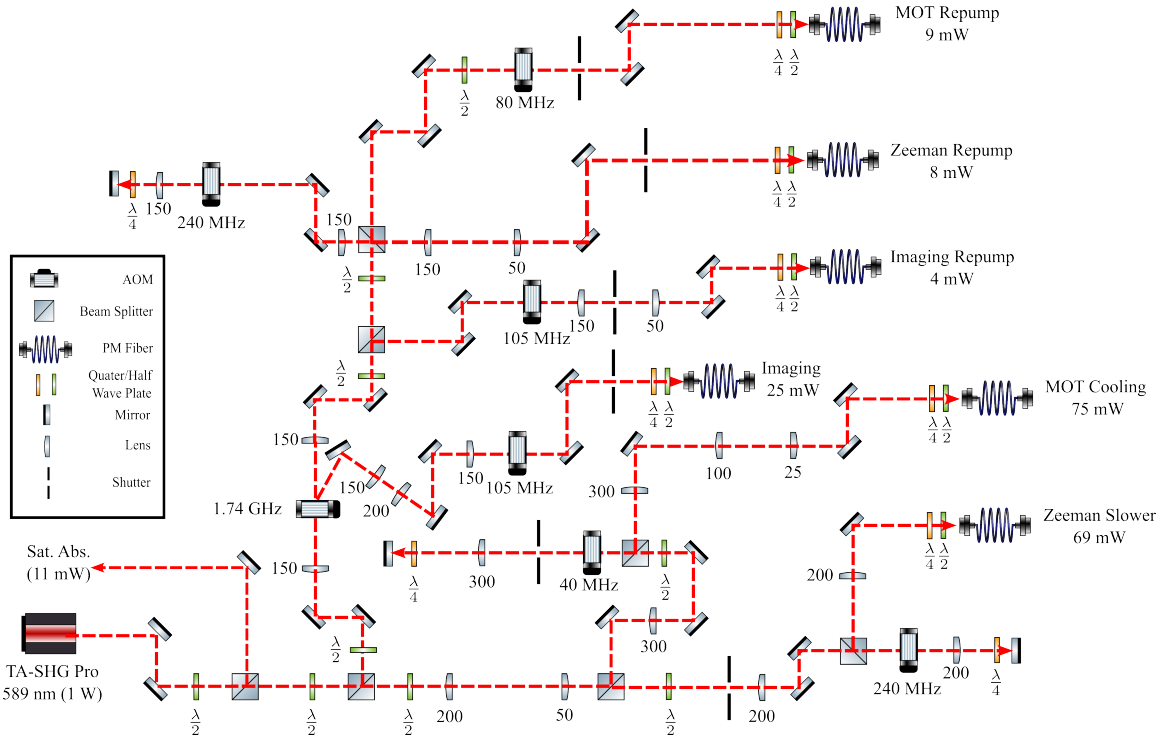

Figure 4.6: Schematic of the laser system used to generate MOT cooling, MOT repumping, imaging, imaging repumping, Zeeman slowing and Zeeman slower repumping beams. All cubes are polarizing beamsplitter cubes and all laser powers are measured before the PM fibers

cycles. Thanks to the energy structure of sodium atoms, the two hyperfine levels of the ground states are only about 1.77 GHz away from each other. This spacing is rather rather small compared to other alkaline atoms, such as rubidium (6 GHz) and cesium (9.8 GHz). It allows us to do cooling and repumping with only one laser. The necessary 1.77 GHz frequency shift to the blue is realized with a large frequency AOM (Brimrose GPF-1800-200-589) with a carrier frequency equal to 1800 MHz. Since the AOM is designed to shift large frequency, the diffraction efficiency is only about 30% to 40%. To get the maximum diffraction efficiency, we mounted this AOM onto a translational and rotational stage that can be adjusted precisely to set the x, y and z translation, as well as the z-axis rotations, and the y-axis tilt. In addition, this AOM

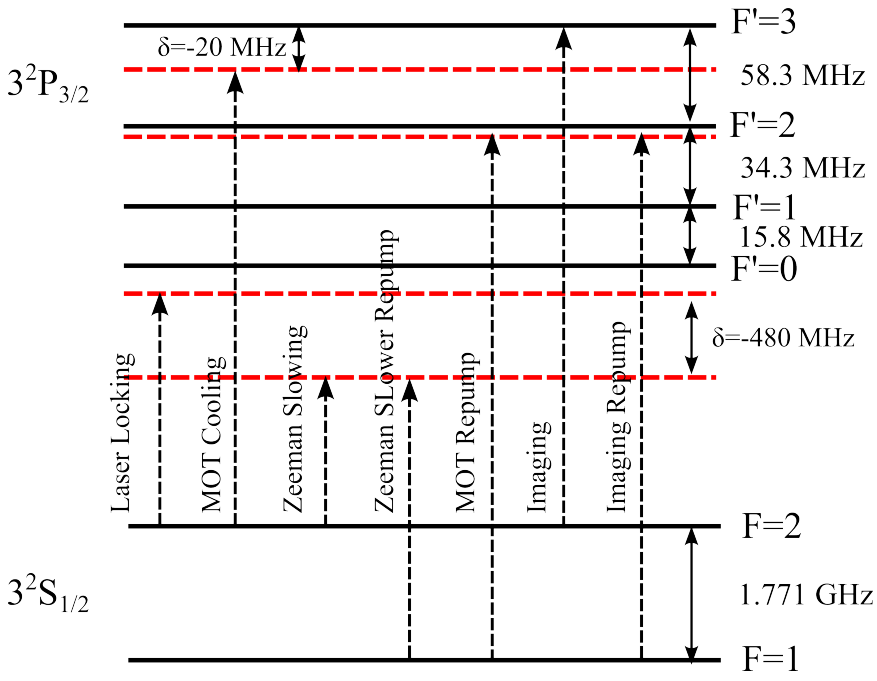

Figure 4.7: Frequencies of laser light used in the experiment compared to the hyperfine structure of sodium D2 line. Frequencies are not drawn to scale.

is driven by a frequency generator (Agilent 8657B) which produces a center frequency at 1.74 GHz with 1 W of RF power. Our final output power is about 200 mW, and it is distributed to three repumping beams, including MOT repumping, Zeeman slower repumping, and imaging repumping beams. Care has to be taken to ensure that both the RF power and light intensity remain below the damage threshold of the AOM.

Our detuning of the MOT cooling beam is about 20 MHz to the red of the strongest atomic transition $F = 2 \rightarrow F' = 3$. During polarization gradient cooling, this detuning is increased. To allow such changes of detuning while still keeping a high fiber coupling efficiency, the corresponding AOM is double passed. The double-pass AOM scheme maintains the laser beam pointing over a large range of frequency detunings. Figure 4.8 shows a schematic of the double-pass AOM configuration. The incoming laser beam passes through the AOM, and its first order diffracted beam is retro-reflected by a mirror and passes back through AOM again. Then, the beam is deflected in the

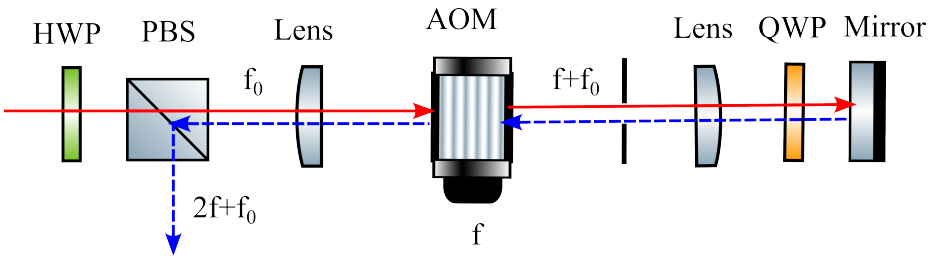

Figure 4.8: Double-pass AOM configuration can mitigate the shift in laser pointing due to frequency changes, and also provide a doubled frequency detuning. In this figure, f_0 is the original laser's frequency and f is the frequency of the rf signal sent to the AOM. The first order of the final output laser's frequency after the double-pass configuration is $2f + f_0$. The lenses are chosen so that the AOM is in the focus of both lenses.

AOM at the same angle as the incoming beam and counter-propagates along with the original zero-order beam. A quarter-wave plate in front of the mirror will change the beam polarization by $\pi/2$. Therefore the PBS can separate the outgoing beam from the incoming beam. In order to optimize the efficiency of the AOM, the beam width needs to be adjusted close to the size of the active aperture when it goes through the crystal inside the AOM. Usually, a lens is placed before the AOM to focus the beam size such that the relay length is well overlapped with the AOM position. Another lens with the same focal length is placed after the AOM to collimate the beam and ensure that the reflected beam going back through the lens will focus at the same spot as the incoming beam. The outgoing beam will end up having the doubled frequency after two deflections in the AOM with respect to the zero-order incoming beam. The efficiency depends on the AOM specification. With a double-pass AOM scheme, the final diffracted beam overlaps with the incident beam regardless of the frequency changes made by the AOM, which is essential for laser cooling and trapping experiments. The same double-pass configuration is also used in our Zeeman slower beam and the Zeeman slower repumping beam to achieve a double frequency shift

(∼480MHz), see Fig. 4.6.

In our setup, AOMs and shutters in Fig 4.6 are either analog or digitally controlled via NI or Spincore DAQ cards, which is dicussed in detail in section five. The AOMs for the MOT (Zeeman slower) cooling and repumping beam can receive an analog signal, and their frequency and power can be manually adjusted via LabVIEW at any time. The rest of the AOMs have pre-set frequencies. The drivers receive a digital TTL signal so the beams can be switched from on to off within nanoseconds to stop the light from going into the main experimental chamber. Shutters can also be turned on and off digitally within milliseconds during our experiments. When the shutters are turned off, they can help block the light leaking from the AOM zero-order scattering. All laser beams with their designated frequencies are then delivered to the main chamber with single-mode polarization-maintaining (PM) optical fibers from Thorlabs. All laser beams should be carefully aligned to their fibers to ensure the system's performance. The first step of the alignment is to connect a fiber optic tracer (PRO-VFL-10) to the outgoing end of the PM fiber. Red tracer light then appears out of the fiber input. The yellow beam is now aligned to overlap with the red tracer beam. Next, fine alignment is done by walking the laser beam using two mirrors until the maximum output power is achieved. We use fiber collimators (CFC8-A Thorlabs) to move the laser beam focus onto the PM fiber tip to further optimize the power output and have maximum efficiency.

We aligned the polarizations to the slow axis of the PM fibers, using both $\lambda/2$ and $\lambda/4$ wave plates in front of the fiber collimators. The $\lambda/4$ wave plate is used to generate a pure linear polarized light before entering the fiber, and the $\lambda/2$ wave plate is used to align the linear polarization axis of the laser beam with the slow axis of the fiber. We use a polarization-extinction ratio meter to measure the output polarization extinction ratio from a PM fiber to see how much of the output beam is

linearly polarized along the slow axis. If the laser beam is well coupled into the fiber, we should get at least 70 % efficiency measured in this way.

4.2 Zeeman Slower

The MOT can only capture atoms within the capture velocity range of a few tens of meters per second for sodium. However, the average velocity of the hot sodium gas generated in the oven chamber is about 700 m/s, far above the capture velocity. Therefore, to slow the atoms down and efficiently load them into the MOT, a number of slowers have been invented. For example, one can chirp the laser frequency or use a broadband laser to keep a laser beam always on resonance with a slowing atomic beam [53, 54]. In another example, one can use diffused light such that the Doppler shift varies with the angle of the laser beam; therefore, the atoms can be efficiently slowed by scattering the counter-propagating light at different angles [55]. Another convenient way is to keep the laser's frequency unchanged and tune the atomic transition by applying a spatially varying magnetic field along the atomic beam path. This method is known as Zeeman slowing and was first demonstrated in 1982 by William D. Phillips and Harold Metcalf. They built a Zeeman slower to reduce the velocity of a sodium atomic beam from hundreds to a few tens of meters per second [8].

The Zeeman slower is often used in atom cooling and trapping laboratory. We designed and implemented a passively cooled zero-crossing Zeeman slower in our lab to help us load the MOT and achieve BEC. In chapter three, we briefly mentioned the setup of the Zeeman slower. In this section, we focus on the mechanism of the Zeeman slower and how we implemented it in our system.

4.2.1 Zero-crossing Zeeman Slower

In a Zeeman slower, a laser beam is counter-propagating an atomic beam to decelerate the atomic beam. The frequency of the laser beam is red-detuned from the atomic transition. When laser light is nearly resonant with the atoms, from chapter two, we know the deceleration due to the scattering is

$$a = \frac{\hbar k \Gamma}{2m} \frac{s_0}{1 + s_0}, \tag{4.1}$$

where k is the laser wave number, Γ is the natural linewidth of the atomic transition, and $s_0 = I/I_s$ is the ratio between the laser intensity and the atomic saturation intensity. At large laser intensity, this reduces to

$$a = \frac{\hbar k \Gamma}{2m}. \tag{4.2}$$

To continuously generate a scattering force on the atoms, the magnetic field is spatially changed such that the Zeeman splitting of the hyperfine level matches the Doppler shift of the moving atoms. It satisfies the equation $kv(x) + 2\pi\delta + \mu B(x)/\hbar = 0$. In an ideal case, we assume that the deceleration of the atoms is constant and only due to the laser. The velocity of the atom at any position x can then be written as $v(x) = \sqrt{v_0^2 - 2ax}$. The ideal magnetic field is given by

$$B_{ideal}(x) = \frac{\hbar k}{\mu} \sqrt{v_0^2 - 2\eta a x} - B_0, \tag{4.3}$$

where η is a safety factor to account for magnetic field imperfections in any realistic slower, $\mu = \mu_B(g_e m_e - g_g m_g)$ is the magnetic moment of the atomic transition, μ_B is the Bohr magneton, g is the Landé factor and $m_{e(g)}$ is the Zeeman substate of the excited (ground) states. The bias field $B_0 = \hbar\delta/\mu$ is a constant value that depends on the detuning of the Zeeman slowing laser. According to Eq. (4.3), the magnetic field gradually decreases along the longitudinal direction (x) of the Zeeman slower, and it reaches $B(x) = 0$ based on the value of bias field B_0. Then the direction of

the B-field starts to reverse, but the velocity keeps decreasing at the same rate. This type of Zeeman slower is called a zero-crossing slower since its magnetic field changes from positive to negative. The zero-crossing configuration offers several practical advantages. The magnetic field has positive and negative regions, which means the magnetic field's maximum is reduced. Therefore, the heat dissipation in the coils is decreased. The atoms exit a nonzero field, quickly decoupling from the slowing laser to preserve a narrow velocity distribution. The zero-crossing position can be chosen to match the detuning of the slowing laser [56].

4.2.2 Zero-crossing Zeeman Slower Design

Figure 4.9 shows the design of our Zeeman slower. It is made of a 1-meter long stainless steel tube, that can slide on a long 1.33" nipple with a CF flange on each side. In order to allow sliding the tube onto the nipple, a special removable 1.33" flange is used on the side close to the experimental chamber. We wound the stainless steel tube with AWG14 double-insulated Kapton magnet wires, which have a diameter of 0.0641". The wires were wound around the tube tightly with multiple horizontal and vertical loops to generate the designated magnetic field. Based on numerical simulation, our zero-crossing Zeeman slower consists of 31 segments, where the first 20 segments produce a positive field, and the following ten segments produce a negative field. An additional coil with a positive current was added to the end to control the minimum of the field at the end of the slower, which precisely tunes the final velocity and prevents atoms from being pushed back into the slower after they exit. The magnetic field for a Zeeman slower is typically generated by a solenoid of current-carrying wire with a varying number of layers. The field strength is derived from the Biot-Savart Law. The total magnetic field of the Zeeman slower is formed by summing the contribution from each layer. From our numerical calculations, the magnetic field at the beginning of

the Zeeman slower should be 600 G to capture the hot sodium gas entering the slower. Instead of using a high current to generate such a high magnetic field, our solution is to add more coil layers since adding more layers could get the equivalent magnetic field. In practice, we only apply low current of a few Amperes through the wires since less current generates less heat. In addition, copper disks between segments serve as heat sinks to dissipate the heat into the air via convection. Our design replaces the need for water cooling with completely passive cooling. No cooling fans are needed either.

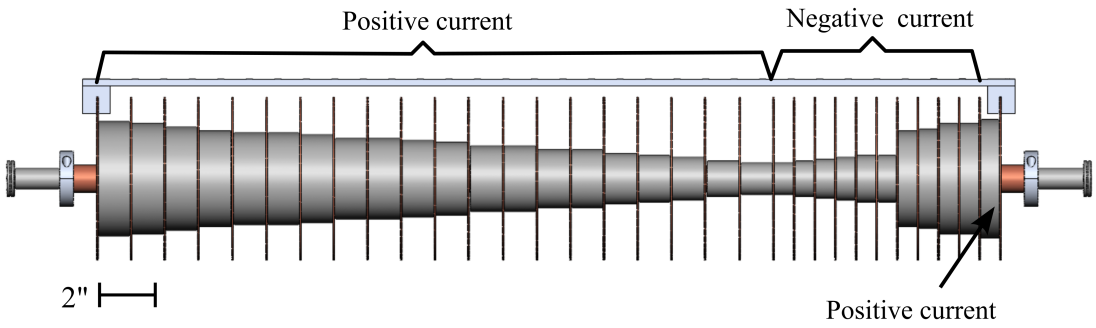

Figure 4.9: 3D rendering of the Zeeman slower. The first 20 segments produce a positive field, the following ten segments produce a negative field, and the last coil produce positive current to tune the final velocity of atoms.

We tested our slower by applying 4 A of current through all segments of wires and measuring the magnetic field in the center of the Zeeman slower with a Hall-effect based Gaussmeter. A comparison with the simulation results is shown in Fig. 4.10. As can be seen, our measurement data matches very well with the simulation. Note that the change of the magnetic field experienced by the atomic beam must not be too fast. In other words, it must satisfy the adiabatic theorem, which says that it takes a finite amount of time for atoms to slow down during each absorption and emission cycle. If we decelerate the atoms too quickly as they travel along the slower,

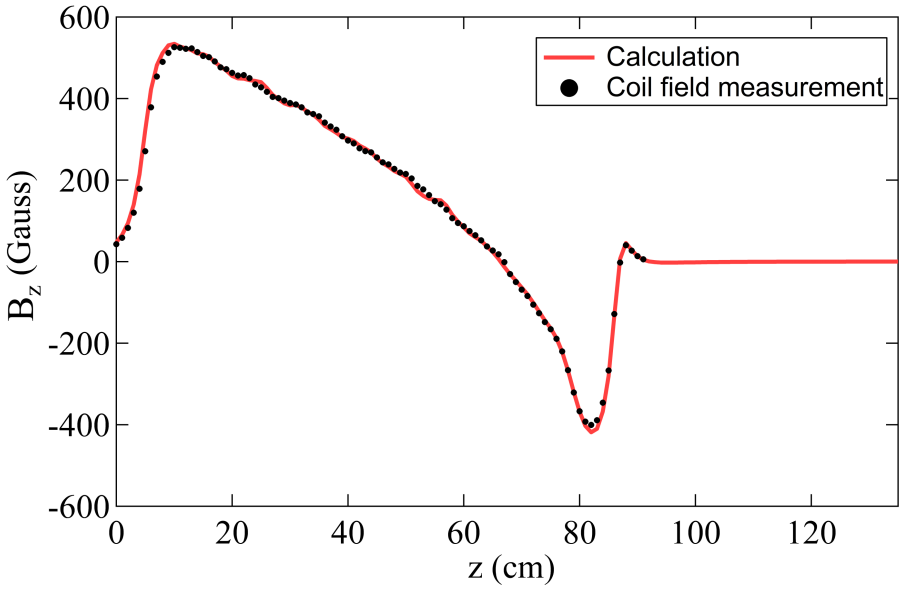

Figure 4.10: Measured longitudinal component of the magnetic field generated along the center of the Zeeman slower with 4 A of current through each segment of wires (black dots) compared to the simulated field (red line)

they will be removed from the slowing process. Therefore, atoms must be decelerated slowly enough, so the laser remain on resonance with them when they relax back to the ground state.

The Zeeman slower is oriented diagonally upwards, as shown in Fig. 4.11 connected to one of the 1.33" CF ports of the UHV chamber. The diagonal configuration keeps it out of the way of other components, and allow us to keep better optical access provided by the bigger windows. The window on the opposite side of the Zeeman slower is periodically cleaned by UV LIAD. The Zeeman slower beam incident to this window has a power of about 17 mW which is high enough to saturate the ${}^2S_{1/2}F = 2 \rightarrow 3^2P_{3/2}F = 3$ atomic transition and a $\lambda/4$ wave plate is used to rotate the light polarization from linear to circular to match the selection rule for the strongest transition. The frequency of the Zeeman slowing beam is red-detuned from the laser locking point by $\delta = 480$ MHz, as shown in Fig. 4.7. The Zeeman slower repumping

beam with a power of 1.6 mW is overlapped with the Zeeman slowing beam. Its frequency is further tuned by 1.74 GHz used to pump the atoms back to the cooling cycle. The current setting for the Zeeman slower is different from the testing data due to the influence of the ambient magnetic field generated from other sources, such as MOT coils and magnets of the ion pumps. After carefully tuning the current in each segment, we eventually set 3.8 A, 3 A, and 1 A for the three sections along the path of the atomic beam, respectively, to optimize the number of atoms trapped in the MOT.



Figure 4.11: The 4' × 10' non-magnetic optical table that holds the MOT optical system, and the vacuum system. The laser beams generated on the main laser table are delivered to this table via PM fibers to generate the MOT.

4.3 3D MOT

4.3.1 MOT Setup

The MOT setup fits on a 4' × 10' non-magnetic optical table, as shown in Fig. 4.11. After sodium atoms are slowed down with our Zeeman slower, we use a magneto-optical trap (MOT) to further cool them down from ∼ 20 m/s to a few centimeters per second and trap them at the center of the main experimental chamber. Our 3D MOT consists of three pairs of counter-propagating cooling beams in three orthogonal directions. Each of the cooling beams has a Gaussian profile. We use a telescope to expand the size of the MOT beams to about 0.8" diameter before they intersect in the center of the chamber. The larger size of the beam can potentially trap more atoms in the MOT. The total power of the MOT beams during the MOT loading phase is ∼ 30 mW, evenly distributed into six beams by several polarizing beam splitters (PBS), so each beam has a power of ∼5 mW. The linear polarization of the cooling beams after the PM fiber is changed to circular polarization by a $\lambda/4$ wave plate before entering the main chamber. The frequency of the MOT cooling beam is red-detuned with respect to the $F = 2$ to $F' = 3$ cooling transition by $\delta = -20$ MHz during the MOT loading phase and is then changed during each phase for further cooling. The MOT cooling beam's power and frequency can be changed programmatically via an AOM (ISOMET M1201E-SF40-1.7). This AOM is set up in a double-pass configuration, so the laser beam pointing will be maintained even when a large frequency detuning is applied to the AOM.

The MOT cooling beams can excite the atoms to the F' = 2 excited state, from which atoms can decay to the F = 1 ground state via spontaneous emission, causing loss from the trap. In order to keep most of the atoms in the cooling cycle, two pairs of ∼3.8 mW, 0.8" diameter repumping beams, overlapping with cooling beams, are turned on at the same time to optically pump atoms from the F = 1 state to the

$F' = 2$ excited state. The MOT cooling and repumping beam configuration is shown in Fig. 4.12.

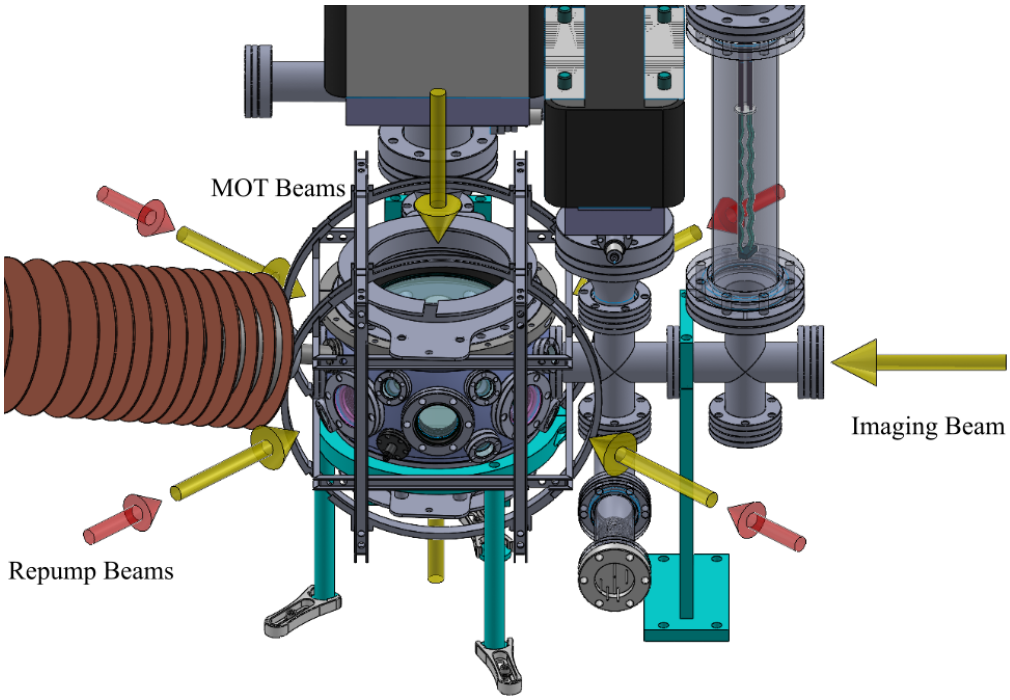

Figure 4.12: CAD rendering of MOT, MOT repump, and imaging beams entering the main experimental chamber.

In addition to the cooling and repumping laser beams, magnetic field gradients are required to create a position-dependent force to trap the atoms. The magnetic field gradient is generated by a pair of coils in anti-Helmholtz configuration, where current goes through each pair of loops in the opposite direction and generates a linear gradient at the center. Two coils are mounted on the top and bottom of the vacuum chamber. Each of them is wound with 20 loops of hollow core insulated copper wires. The maximum current on each coil is up to 80 A and provides a maximum quadrupole field gradient of 12 G/cm at the center of the chamber, sufficient to create a strongly compressed MOT. We use water-cooling method to keep the coils from melting due to resistive heating. The cooling water is pumped through the center core of the

hollow-core wires with an inner diameter of 0.125".

4.3.2 Water-cooling of MOT Coils

The water cooling system consists of a heat exchanger (Coolflow Liquid/Liquid Recirculator System I), an external water micro-pump (Micropump GAF-T23-DENSE), and a flow meter (Omega FSW 530 series). The heat exchanger pumps the water through the water-cooling system and transfers heat from the hot recycled water to the cold water from the building loop. To maintain a reasonable flow rate, we use 0.5" inner diameter plastic water tubing which connects to the anti-Helmholtz coils via compression tube fittings. The water tubing is opaque to prevent algae from growing. Using distilled water mixed with a few drops of alcohol as cooling water also reduces the number of algae in the water. The cold water is fisrt pumped by an internal water pump (Procon PD2 Series) in the heat exchanger, then further pumped by an external micro-pump installed just before the copper coil. The micro-pump can provide an extra pressure of up to 250 psi, which further boosts the water flow going through the small inner diameter of the hollow core copper wire. A flow meter is installed before the micro-pump to indicate the flow rate of the cooling water. In addition, an extra mesh filter is placed in the water line to collect the debris and algae, thereby increasing the pumps' lifetime. Two interlock controls are set up on the heat exchanger and the flow meter, respectively. If the heat exchanger is shut down or the water flow is too small, the interlock will automatically shut off the current that goes through the copper coils to prevent the coils from melting.

4.3.3 MOT Coils Electrical System

The current going through the MOT coils is provided by a 16 V, 310 A power supply (Sorensen DCR 16-310T). The output voltage and current can be manually

or remotely controlled from either the front panel or the rear panel in the back of the power supply. After the MOT is fully set up, the control system is switched from manual to remote control. We use a calibrated analog signal generated via LabVIEW and a NI DAQ card to control the output current for the power supply. The power supply should be set to run in constant current mode to provide a stable current during the experiment. Since the power supply can generate very high DC current (up to 310 A), we use a carolprene 4/0 GA welding cable to conduct the current to the experiment. We also set the current limit at 88 A to protect the apparatus from overheating. In order to transfer atoms most effectively from the MOT into the dipole trap, the MOT has to be switched off in less than a few milliseconds. Since the MOT coil has a large inductance and generates back emf when switched off, slowing down the switching, another circuitry needs to be added to increase the switching speed. Our solution uses a high-power insulated gate bipolar transistor (IGBT, Semikron SKM200GB125D), connected in series with the coil return, as depicted in Fig. 4.13. A number of reverse transient voltage suppression (TVS) diodes are connected in parallel to the IGBT to bypass the current to the ground at large voltage. The IGBT gate is driven by a commercial IGBT driver (SKHI 10/12 (R)), which is controlled via a TTL input. When the IGBT is in conducting mode, the voltage across it is low, usually about a few volts, and the TVS diodes appears as an open circuit. When the IGBT is switched into the non-conducting mode, the back-emf becomes equal to the breakdown voltage of the TVS array, at which point the diodes start conducting. The current in the coils then decreases quickly according to

$$\frac{dI}{dt} = -\frac{V_z}{L}, \tag{4.4}$$

where V_z is the breakdown voltage of the TVS array and L is the inductance of the MOT coils. The switching time can be adjusted by adjusting the number of TVS diodes. The fastest switching is obtained when V_z is just below the maximum IGBT

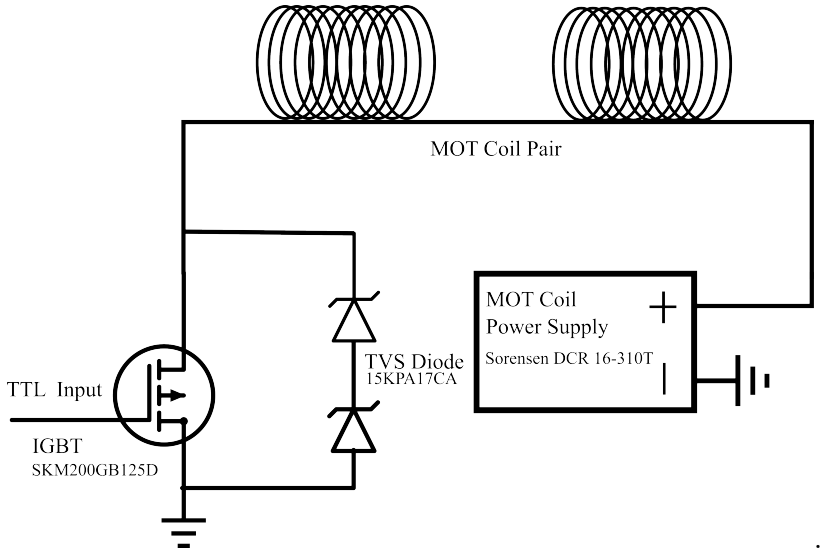

Figure 4.13: The MOT coil switch circuit is made of a high-power IGBT with two TVS diodes. When the IGBT switch opens, the TVS diodes start conducting, and the current starts to decrease, according to Eq. (4.4).

voltage. It is worth noting that the breakdown voltage of the TVS diode should always be lower then the maximum IGBT voltage to protect the IGBT circuit. In the experiment, we use two TVS diodes (Little Fuse 15KPA17CA) which gives us $V_z = 2 \times 17$ V. The inductance of the MOT coil is 194.6 μh and the calculated switching time of the MOT coil is ~ 900 μs. In principle, the switching time could be further reduced by using more TVS diodes. However, fast switching time proved problematic due to fast voltage spikes that are picked up by other electronics such as digital signal lines.

4.3.4 Bias Coils

Besides the anti-Helmholtz coils for the MOT, we also set up three pairs of bias coils around the main chamber, as illustrated in Fig. 4.14. The bias coils are in Helmholtz configuration, generating a constant magnetic field in the region of the MOT. The constant magnetic field can be used to center the MOT position by shifting

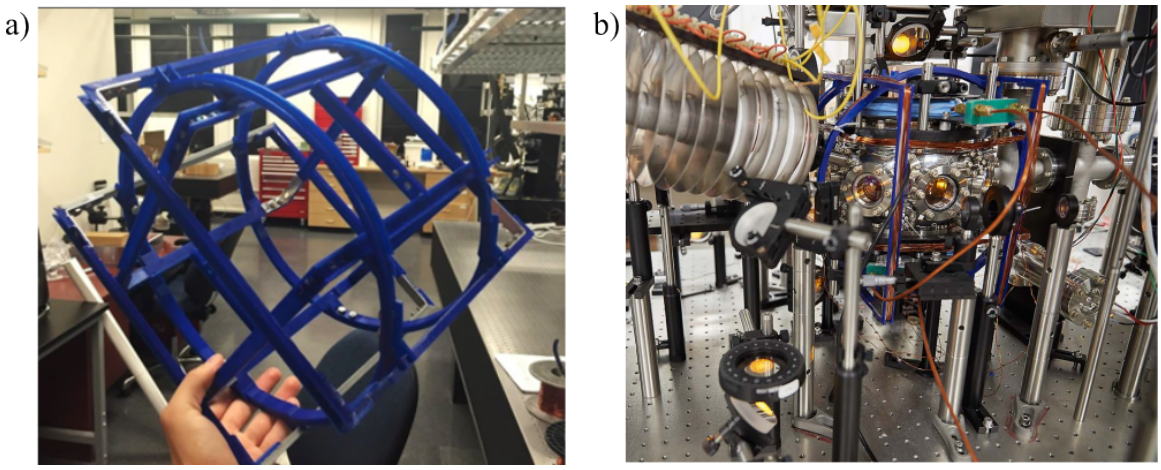

Figure 4.14: a) 3D printed plastic Helmholtz bias coils frame. b) The three pairs of Helmholtz bias coils surrounding the main chamber generate a uniform background magnetic field.

the magnetic field zero. The bias field is also used to define a quantization direction and apply Zeeman shifts to the magnetic sublevel of the hyperfine states in our spinor BEC experiments, which is significant for controlling the rate of spin-exchange collisions in the BEC.

The bias coils are made of three pairs of 3D printed plastic frames with 33 turns of copper wires wound on each. The coils in the vertical z-direction and north-south x-direction have square shapes with side lengths of 235.5 mm and 275 mm, respectively. The coils in the east-west y-direction (side way imaging beam axis) are circular with a diameter of 294 mm. Three pairs of coils are mounted around the vacuum chamber, as illustrated in Fig. 4.14b. Since the space around the chamber is relatively compact, the coils are made of thin wires so they cannot be water cooled from inside. After applying current on a test coil, we limited the magnitude of the current to be no larger than 4 A to prevent the 3D printed plastic coil frame from melting.

It turns out that the current fluctuation in the bias coils, which leads to magnetic field fluctuation and corresponding Zeeman shift fluctuation, has a significant impact

on the spin-mixing dynamics in the BEC, which are our focus of study. Therefore a current control system that can generate a low-noise and stable current is needed. In addition, to fulfill our requirements, the magnetic field generated by the bias coils must be quickly adjustable, not only in amplitude but also in direction during the experiment, as necessary. In order to satisfy these requirements, we designed coils with a highly stable, home-built, bipolar DC supply, which has six individual channels whose outputs are controlled by analog input voltages and stabilized by PID controllers. Our first design used a commercial DC power supply and homemade PID circuits to generate the current. Even though we could switch the currents very fast, the noise that appeared on the signal was hard to minimize, and the high-power transistors used to control the circuit was easily destroyed by the high back emf voltages generated during switching. To tackle this problem, we switched to another design based on the idea of using ultra-low noise temperature controllers (TC) as current controllers. We replaced the homemade current controllers with commercial temperature controllers (Wavelength Electronics PTC5K-CH) that can output $\pm$ 5 A control current with faster ramp time and lower noise. To make the TC work properly in our system, we built an additional homemade circuit to convert an external setpoint analog voltage channel signal generated via LabVIEW and our NI-DAQ card to a signal which is within the range allowed by the TC. We also built a sensing circuit which can convert the current signal from the Helmholtz coil to a fake temperature sensor signal which can be sensed by the TC. After adding these circuits, the sensor of the TC, instead of measuring the load temperature, now measures the voltage across a 10 kΩ resistor. The voltage across the sensor is compared with the setpoint voltage, and the TC minimizes this difference using PID control. Our new bias coil current control box is shown in Fig. 4.15. The external setpoint circuit and the sensing circuit are illustrated in Appendix B.



Figure 4.15: A homemade current controller for the bias coil. There are six individual channels that can output a current range from -5 A to 5 A. Each of them uses a commercial ultra-low noise TC (Wavelength Electronics PTC5K-CH) as a current controller. An extra external setpoint circuit and a sensing circuit are used to convert the signal to a readable signal for the TC.

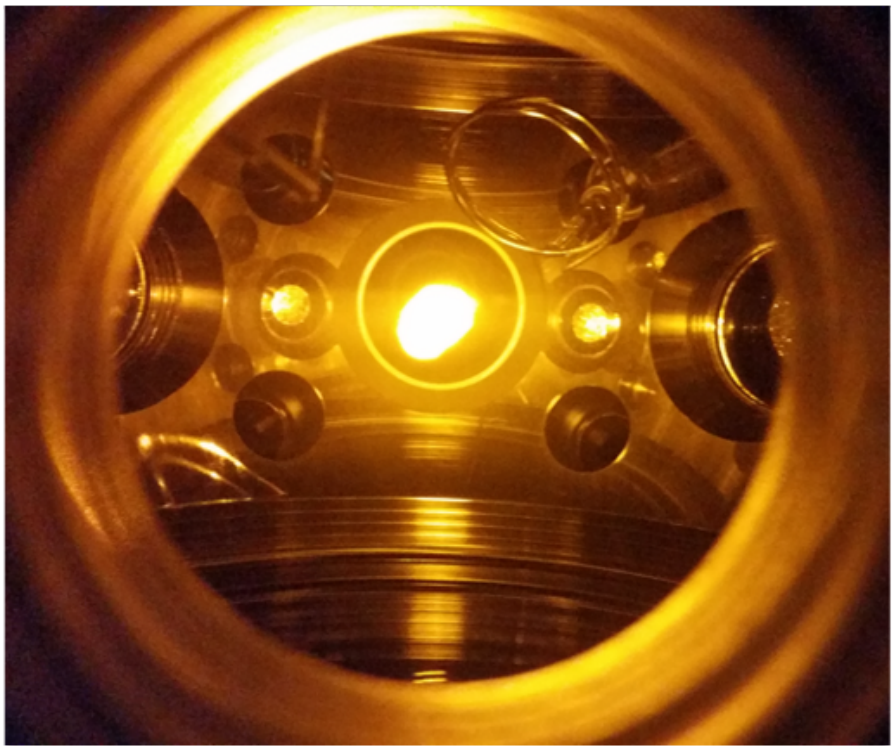

Figure 4.16: A photo of the fluorescence of our sodium MOT locates in the center of the UHV chamber. After optimization of the cooling light power, polarization, and frequency, as well as the bias magnetic field and the magnetic field gradient, we trap $\sim 3 \times 10^8$ sodium atoms in the MOT.

After carefully optimizing the power and the frequency of the MOT cooling and repumping beams, as well as the magnetic quadruple field and the bias field, we routinely create sodium MOTs with $\sim 3 \times 10^8$ atoms located at the center of the UHV chamber, as illustrated in Fig. 4.16.

4.4 Imaging System

Trapped ultracold atomic gases such as MOTs and BECs are usually small in size, typically around a few micrometers to a few millimeters across, and are isolated in ultra-high vacuum chambers. Therefore it is not feasible to interrogate the trapped

atoms with material probes, such as a thermometer. Using light beams to probe the ultracold atom cloud and measure the optical power radiated from or transmitted through it is a feasible way to detect the density distribution of the atom cloud and extract quantitative information like shape, size, atomic number density, and temperature. This section presents the imaging techniques we employ to image the MOT and BECs.

4.4.1 Fluorescence and Absorption Imaging

Fluorescence and absorption imaging are two standard methods to probe ultra-cold atomic clouds with near-resonant light [57, 58, 59, 60]. Implementing fluorescence imaging techniques is straightforward by shining a near-resonant light beam on the atomic gas. The atoms absorb photons and scatter them due to spontaneous emission. The scattered photons generate fluorescence signals on photodiodes or CCD cameras. The higher the system's scattering rate, the larger the fluorescence signals that will be obtained. Therefore, saturated light beams are typically used to maximize the fluorescence signal magnitude. However, this will unavoidably distort the shape of the atomic sample and heats the atoms. The radiation pressure from the imaging beam and the subsequent isotropic reemission will blur the images [61]. In addition, a small collection solid angle when applying the fluorescence imaging will also limit the number of scattered photons detected. As the number of atoms decreases, the signal quickly gives way to background scattering light and detector noise. Due to these drawbacks, we only use fluorescence imaging to monitor the MOT qualitatively for optimization of its position and shape, since the MOT can move and become distorted if there is an imbalance in the intensity of cooling beams.

For quantitative measurements, we use absorption imaging to probe the ultracold atoms and obtain essential properties such as optical density, number density, atom

number in the cloud, and cloud shapes. Absorption imaging is a standard method to probe the atomic cloud in situ or time-of-flight. In our absorption imaging, a collimated probe beam of resonant light which couples the $3^2S_{1/2}$, $F = 2$ and $3^2P_{3/2}$, $F' = 3$ states of Na is illuminating the cold sodium cloud, and the shadow of the cloud is imaged onto a CCD camera. Absorption imaging for cold atomic clouds works best when the probe intensity is weak (weaker than the saturation intensity), and the optical density of the atomic cloud is equal to or lower than one [62].

Suppose a weak probe laser beam propagates along the z direction and passes through an atomic cloud. The intensity profile of the probe beam after the absorption follows the Lambert-Beer law

$$I(x, y) = I_0(x, y)e^{-OD(x,y)}, \tag{4.5}$$

where I_0 is the initial intensity before light passes through the cloud, $OD(x, y)$ is the optical density profile, x and y are the transverse directions. The optical density is defined as

$$OD(x, y) = \sigma \int n(x, y, z)dz = \sigma n_c(x, y), \tag{4.6}$$

where z is the longitudinal direction of the beam path, $n(x, y, z)$ is the number density, $n_c(x, y)$ is the column density, and σ is the absorption cross section which depends on the intensity, polarization, and detuning of the probe beam. The cross section can be written as

$$\sigma = \frac{\sigma_0}{1 + 4(\frac{\Delta}{\Gamma})^2 + (\frac{I}{I_{sat}})}, \tag{4.7}$$

where σ_0 is the on-resonance cross-section which depends on the light polarization and atomic transition, Δ is the detuning of the imaging light from the atomic resonance, and Γ is the natural linewidth of the optical transition. From Eq. (4.5), we see that the optical density can be obtained by measuring the transmission of the probe laser beam with and without atoms. Here, we denote them as raw images and reference images,

respectively. Probe beam profiles are recorded by a CCD camera. In addition, a third image needs to be taken without the probe beam or any cold atomic cloud. This third image serves as a background image to be subtracted from the raw and reference images. It can remove contamination from stray scattering light and any background offsets added by the camera electronics. The optical density can be calculated from the three images according to Eq. (4.5)

$$OD(x,y) = -\ln\frac{I(x,y)}{I_0(x,y)} = \ln\frac{I_{ref}(x,y) - I_{bg}(x,y)}{I_{raw}(x,y) - I_{bg}(x,y)}. \tag{4.8}$$

Here, I_{raw} is the first raw image which includes both the cloud and the laser beam signal, I_{ref} is a second reference image taken without the cloud but with the same laser beam as I_{raw}. I_{bg} is a background image that is taken with no cloud and no light. An example of how to take the absorption images is illustrated in Fig. 4.17. Once optical density is determined from the three images, the column number density of atoms can be calculated from Eq. (4.6). The total number of atoms is obtained by integrating the column number density over x and y, using the known pixel size and magnification of the imaging system.

4.4.2 Design of the Imaging System

Our experiment requires us to acquire images of atomic clouds with reliable density distribution in either trapped or ballistic expansion from both side and top-down views. In addition, our imaging system should be flexible enough to switch between imaging the MOT and BECs. To accomplish these tasks, we developed two identical imaging systems, so we can detect either the MOT, which has a radius of a few millimeters across, or BECs, which have Thomas-Fermi radii of a few micrometers across.

To find the lens configuration that gives us variable magnification for imaging the MOT and BECs, respectively, is not enough. The resolution of the system also needs to be good enough to not blur the BEC images. Resolution is defined as the smallest

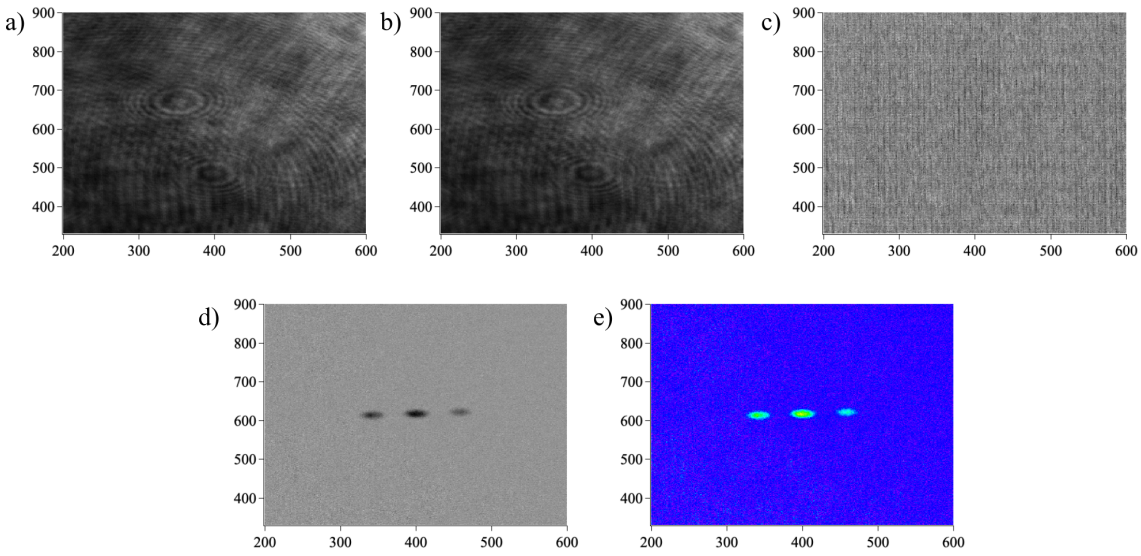

Figure 4.17: An example of how an absorption image is constructed. a) The raw image that includes information about both atoms and light. b) The reference image that only includes light. c) The background image that contains no light and no atoms. d) The image of optical density calculated using Eq. (4.8). e) The false-color image of d). Axes are labeled in the unit of camera pixels.

distance between two points in a sample that can still be distinguished as two separate entities. The resolution of an imaging system is determined by the numerical aperture of the detection optics. Usually, the higher the numerical aperture of the total system, the better the resolution. For a thin lens approximation, the equation of resolution is given by

$$R = \frac{0.61\lambda}{\mathrm{NA}}, \tag{4.9}$$

where NA is the numerical aperture, λ is the wavelength of the light in the air, and R is the smallest distance between two distinguishable points [63]. The equation tells us that a large numerical aperture corresponds to better resolving power. In addition, the numerical aperture is determined as the ratio of entrance pupil D and focal length f, $NA = D/(2f)$, which means the resolution can be optimized by optimizing the lens

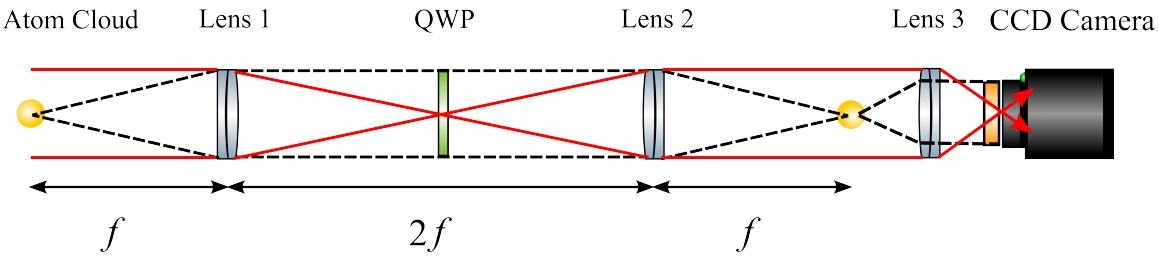

Figure 4.18: Schematic diagram of the optical configuration used for our imaging system. Lens 1 and lens 2 comprise the f-$2f$-f configuration with unit magnification. The inverted image after lens 2 is further magnified by lens 3 and imaged with a CCD camera. The black dashed line is the image of the atom cloud, and the solid red line is the imaging beam. The lenses are achromatic doublets (47718 and 47713 for side imaging and 49285 and 49284 for top imaging) from Edmund Optics. QWP is an abbreviation for quarter wave plate.

configuration. In our system, the position of the cloud in the center of the vacuum chamber limits the distance at which we can place the detection optics to obtain a high numerical aperture. Therefore, we use a relay telescope. The lens configuration of the relay telescope was simulated using the software package OSLO, as shown in Fig. 4.18. The side imaging system consists of two sets of achromatic lenses (Edmund Optics, 47718) with identical focal distance $f = 150$ mm, to produce a relayed image of the cold atom cloud far away enough from the experiment chamber and to minimize spherical aberration. In addition, another magnification lens (Edmund Optics, 47713) is installed in front of the CCD camera to enlarge the image size of the atomic cloud. All optics are AR coated and designed for visible light (400 nm - 700 nm). The optical configuration in Fig. 4.18 can be used in both fluorescence and absorption imaging for the side view of the cold atomic cloud. In order to observe the atomic cloud along the vertical axes, another identical imaging system is set up to have a top-down view. The structure of the top-down imaging system is similar to the side imaging system. Two achromatic doublet lenses with $f = 150$ mm (Edmund Optics,

49285 lens ach 50 × 150 vis 0 ts) are used to construct the relayed image of the cold cloud and another achromatic doublet lens with $f = 100$ mm to enlarge the size of the image for top-down imaging. Since the top-down imaging laser beam overlaps the top-down MOT laser beams, we choose the polarization of the top-down imaging beam orthogonal to the polarization of the top-down MOT beam. We combine them below the chamber using a polarizing beam-splitter. A second polarizing beam-splitter is used above the chamber to separate the imaging beam from the cooling beam before it exposes the camera. Since the top-down imaging beam's optical path is longer than the side beam's and it passes through more optics, the images taken from the side CCD camera have better resolution than the ones from the top-down camera. The complete imaging optical system setup is shown in Fig. 4.19.

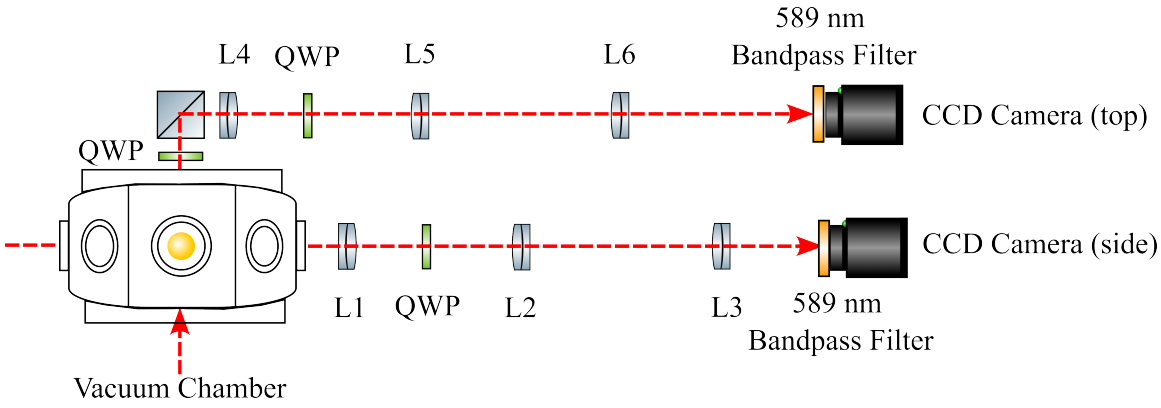

Figure 4.19: Top and side absorption imaging systems are used to take absorption images of the MOT and BECs inside our vacuum chamber. The side imaging system comprises a CCD camera along with L1, L2, L3, and a QWP between L1 and L2. The other components comprise the top imaging system. A polarizing beam-splitter is used to split the top-down imaging beam and the MOT beam. In experiments, we can move lens L3 and CCD (side) or L6 and CCD (top) to change the magnification of our side and top imaging system, respectively.

The imaging devices in our experiments are scientific CCD cameras (14-bit PCO

Pixelfly USB). The most important specifications of our cameras are listed in Table. 4.1. The cameras have a resolution of 1392 $\times$ 1040 pixels with pixel size of 6.45μm $\times$

Table 4.1: Camera Specifications

Quantity	Specification
Type of sensor	CCD
Quantum efficiency	62 %
Spectral range	290 nm .. 1100 nm
Dynamic range A/D	14 bit
Pixel size	6.45 μm $\times$ 6.45 μm
Resolution	1392 $\times$ 1040 pixel
Dark current	1 e^-/pixel/s at 23°C
Full well capacity	16000 e^-
Size	39 mm $\times$ 39 mm $\times$ 71 mm
Double Shutter Mode	2 images in rapid succession $\sim\mu$s

6.45μm. These ultra-compact cameras can be remotely controlled via LabVIEW and digital I/O card using TTL signals. The camera exposure time ranges from 2 μs to 60 s. When taking a picture, cameras are triggered, and the CCD chips start to convert the light signal to electrons captured on each pixel during 150 μs of exposure time, then are read off by the CCD electronics. The quantum efficiency determines the conversion efficiency from photon to electron of the CCD chip. The number of electrons that can accumulate in each pixel is referred to as well depth. The full well depth of our cameras is 16000 electrons per pixel, so it is very important to adjust the exposure time such that the capacity of the well depth is not exceeded and the saturation of the CCD is avoided. Dark current is another factor that could potentially increase the camera's detection noise, which is defined as the charge accumulated in

a well in the absence of light. Dark current is an inherent property of the camera and is affected by the temperature. At room temperature, the dark current for PCO pixelfly is one electron per pixel per second. For an average exposure time of 150 μs, the number of electrons by dark current noise in each pixel is about 10^{-4} e^-/pixel which computes to a total of $\sim$ 200 e^- over the entire CCD array. Therefore taking reference images is necessary to subtract out the dark current while the dark noise remains since it is a statistical variation of the dark current.

In addition, the camera has a large spectral range which ranges from 290 nm to 1100 nm. It means it has great flexibility to image laser beams with different wavelengths ranging from ultraviolet to infrared. However, unwanted light with other wavelengths will also be counted, leading to unwanted exposure of pixels. To remove this noise, we put a bandpass filter (FB590-10, Thorlabs) in front the of the camera to only allow the light with a wavelength of 589 nm to pass through. The two cameras are placed on precise translation stages with micrometer screws to adjust the focus.

4.4.3 Fringe Reduction

Image analysis works best when the imaging signal is clear and any background noise in the image is as small as possible. Apart from the inherent properties, such as the dark current of the camera, which could lead to noise on the absorption image, there are other factors due to optics and environment which could also potentially contribute noise to the image. For example, interference fringes on the imaging beam due to etaloning can happen when the beam passes multiple lenses and windows and bounces back and forth between them. The etaloning of the imaging beam can be effectively reduced by inserting a quarter wave plate between two optics. The incoming beam and the retro-reflected beam pass through the quarter wave plate, resulting in an orthogonal polarization and preventing the generation of interference fringes.

In addition, fringes on the final images could be caused by mechanical vibration from the environment. Suppose there is a large time elapsed between taking the background images and the images with atoms. In that case, the mechanical vibration of the lenses and camera can change the intensity profile of the imaging beam between the two images and create fringes on absorption images that can not be easily subtracted out. We minimize mechanical vibration by firmly securing all the optics in the imaging setup and floating the optical table. We also mount cameras and some optics for imaging on thick 1" diameter posts to mitigate the mechanical vibrating effect. Some mechanical devices such as the shutters and piezo in the IR diode laser also generate vibrations when they are running, so it is important to place them on a separate platform or damp them using vibration-damping material such as Sorbothane. For example, we hang all of our shutters from overhead shelves to remove their vibrations on the optics table.

4.4.4 Image Acquisition

Our imaging system is controlled from two synchronized desktop computers via LabVIEW with two analog NI-DAQ PCI cards and one digital Spincore pulse-blaster PCI card. The first computer is used to run the experimental sequences and sends a TTL signal to trigger the camera. The second computer connects to the camera via a USB cable. After each experiment cycle, the camera sends the image back to the second computer, where the images are stored and analyzed automatically using the Igor Pro software data analysis package.

As mentioned in the previous section, different magnifications are used for detecting the large MOT or small BEC. For example, we use a small magnification of M = 0.6 to image the MOT and a larger magnification of M = 2 to image the BEC. This can be achieved by using different lens configurations. The BEC cloud inside the trap

can be imaged in situ or during time of flight (TOF) after release. While the in situ probes can measure the original geometric configuration of the atomic cloud inside the trap, the BEC cloud, with the size of a few μm, only occupies a few pixels on the CCD camera and the image is too dense to measure quantitatively because the BEC shadow becomes utterly black in the images with high optical densities larger than 2. The TOF measurement has a better resolution on small and dense atomic clouds by turning off the trap and allowing the atoms to expand freely for a few milliseconds, resulting in a larger could with smaller optical density. The TOF method is commonly used to measure the temperature of cold gases. In a time of flight expansion, the atomic cloud expands ballistically. The momentum distribution of the atoms converts to a spatial distribution from which the temperature can be extracted. If we assume $\omega(\tau)$ is the size of the MOT after some time τ of free expansion, the following equation described the ballistic expansion

$$\omega(\tau) = \sqrt{\omega_0^2 + v\tau^2} \tag{4.10}$$

where ω_0 is the initial size of the cold atom cloud, v is the velocity of the atoms defined as $v = \sqrt{3k_BT/m}$ according to the equipartition theorem. The temperature of the atomic cloud is found via

$$\omega(\tau) = \sqrt{\omega_0^2 + (3k_BT/m)\tau^2}. \tag{4.11}$$

This method can be used to determine the temperature of the MOT.

Figure 4.20 shows the absorption pictures of the MOT (Fig. 4.20a) and the picture of the spinor BEC (Fig. 4.20b). The sequences for taking MOT and BEC images are also different. For MOT images, we take an absorption image after a few millisecond of time-of-flight. For taking the images of our spinor BEC, we use the method of Stern-Gerlach absorption imaging. A strong magnetic gradient pulse to separate the three spin states during time-of-flight. Figure 4.20b shows examples of Stern-Gerlach

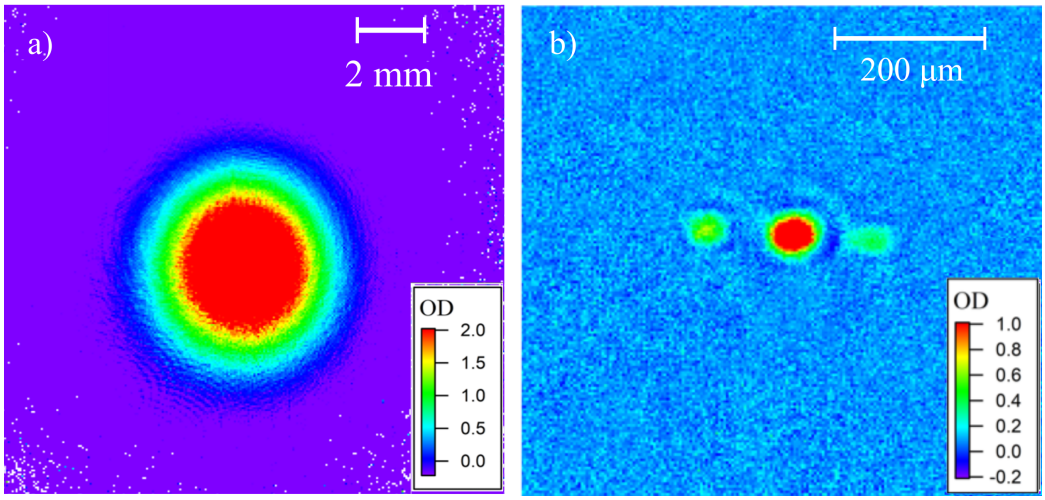

Figure 4.20: False color images from absorption imaging. (a) The MOT absorption image taken after a few milliseconds of time-of-flight. (b) Stern-Gerlach absorption image showing BEC in different spin states after 10 ms time of flight. From left to right are absorption images of m_F=1, m_F=0, m_F=-1 states

absorption images of three spin components of our spinor BEC after 10 ms time of flight, from left to right are m_F=1, m_F=0, m_F=-1 magnetic sub-level states of F=1 hyperfine level, respectively.

4.5 Control System

To achieve programmable, fast and precise remote control over various devices, such as AOMs, optical shutters, function generators, rf switches, and camera triggers, we employ analog and digital signals. We use two National Instruments (NI) DAQ cards (PCI-6733) with eight analog channels each and a sample update rate of 1 MHz to generate analog voltage signals. Digital signals are generated with a Spincore PulseBlaster PCI card, providing 24 digital channels with a standard clock frequency of 100 MHz. The three PCI boards are synchronized using a single clock signal from the PulseBlaster PCI card.

We use two computers to send commands to and receive data from our experimental apparatus. One computer is used to program timing sequences via LabVIEW and send them to the PulseBlaster PCI card to generate digital signals and to the NI DAQ boards to generate analog signals, respectively, to control running experiments. After each experiment's cycle, the images taken by the camera are sent to the second computer for a real-time analysis via Igor to obtain the desired information, such as atom numbers, spin population fractions, atomic cloud sizes, or temperatures. The imaging data can also be stored by the Igor program to do a more detailed analysis at a later time. LabVIEW is programmed to have a user-friendly interface, which helps us to visualize the timing sequence when running the experiment. Figure 4.21 shows an example panel of our LabVIEW interface that controls all the 24 digital channels and 16 analog channels. An arbitrary amount of such steps are stacked vertically, row by row, to program a timing sequence, with time increasing from top to bottom.

Table 4.2 and Table 4.3 summarize the channels used in experiments. We can manually update the configurations of each channel after the system completes a full cycle of an experiment. The "Delay" column in Fig. 4.21 shows the time it takes for the corresponding step, the total time of each experiment cycle is the sum of the times in the "Delay" column of all rows. Usually, the time of running one cycle of an experiment varies from 23 seconds to 28 seconds. We also wait for one extra second at the end of each cycle because the re-configuration time for each PCI board takes about a second to complete. The "Delay" column and analog configurations can also be automatically updated in "Run Sequence" mode. When running experiments in this mode, the system will automatically update a channel with pre-programmed values. This mode is convenient when we want to scan some parameter of the experiment, such as time delay after quench, microwave power, or microwave frequency.

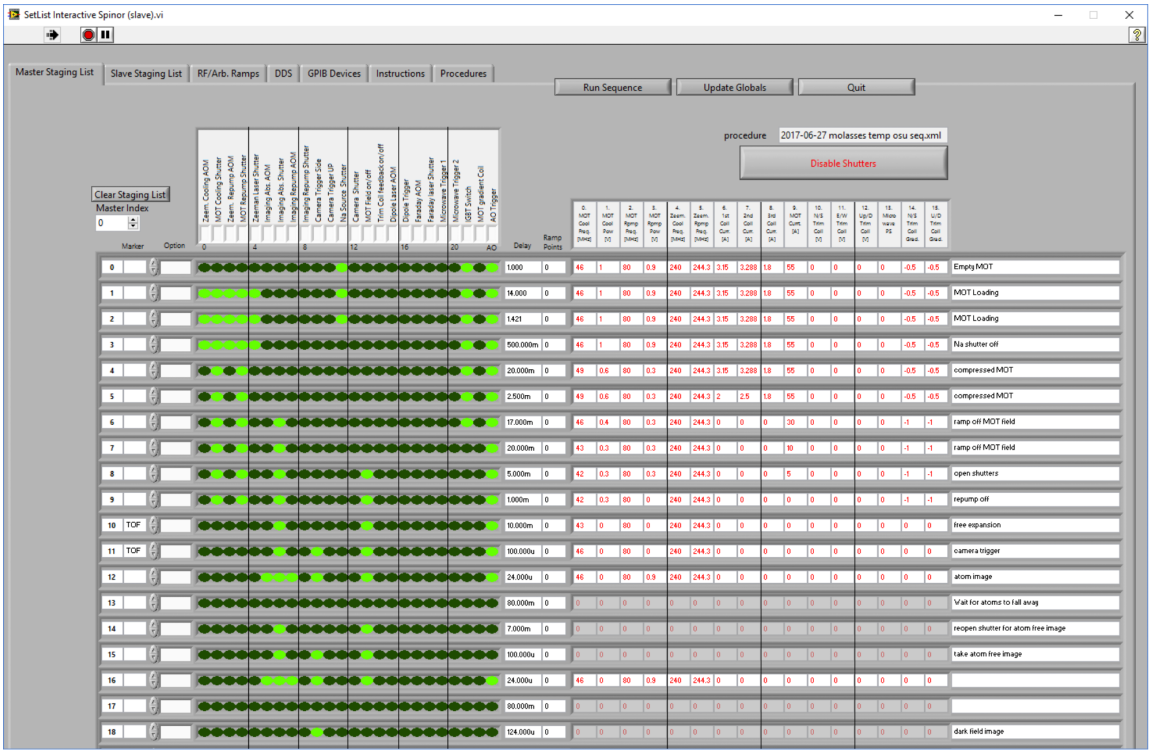

Figure 4.21: A control panel of the LabVIEW interface. There are 24 digital channels with green circles as on/off switches. Bright green represents status "on" while dark green represents "off". There are 16 analog channels with input boxes. The value in the "Delay" column defines the time duration for each step. These steps are stacked vertically to create any desired timing sequence, with time increasing towards the bottom.

Table 4.2: Analog Channel Specification

Usage	Channel	Operational Range
MOT AOM Frequency	AO 0	31.7 $\sim$ 53.2 MHz
MOT AOM Power	AO 1	-0.05 $\sim$ 1 Volt
MOT Repump Frequency	AO 2	60.58 $\sim$ 98.614 MHz
MOT Repump Power	AO 3	-0.05 $\sim$ 1 Volt
Zeeman AOM Frequency	AO 4	197.9 $\sim$ 296.7 MHz
Zeeman Repump Frequency	AO 5	200.8 $\sim$ 422.2 MHz
Zeeman current Seg 1	AO 6	0 $\sim$ 5 A
Zeeman current Seg 2	AO 7	0 $\sim$ 5 A
Zeeman current Seg 3	AO 8	0 $\sim$ 5 A
MOT Current	AO 9	0 $\sim$ 81 A
X1-Bias Current	AO 10	-3.6 $\sim$ 3.6 A
X2-Bias Current	AO 11	-4.2 $\sim$ 4.2 A
Y1-Bias Current	AO 12	-4 $\sim$ 4 A
Y2-Bias Current	AO 13	-4.2 $\sim$ 4.2 A
Z1-Bias Current	AO 14	-4 $\sim$ 4 A
Z2-Bias Current	AO 15	-4.29 $\sim$ 4.29 A

Table 4.3: Digital Channel Specification

Name	Channel	Operational Definition
Zeeman Cooling AOM	CH 0	Turn on/off Zeeman cooling AOM
MOT Cooling Shutter	CH 1	Turn on/off MOT cooling shutter
Zeeman Repump AOM	CH 2	Turn on/off Zeeman repump AOM
MOT Repump Shutter	CH 3	Turn on/off MOT repump shutter
Zeeman Laser Shutter	CH 4	Turn on/off Zeeman cooling shutter
Imaging Abs. AOM	CH 5	Turn on/off imaging beam AOM
Imaging Abs. Shutter	CH 6	Turn on/off imaging beam shutter
Imaging Repump AOM	CH 7	Turn on/off imaging repump AOM
Microwave Trigger	CH 8	Trigger the 1.74 GHz function generator
Camera Trigger Side	CH 9	Trigger side camera
Camera Trigger Top	CH 10	Trigger top camera
Na Source Shutter	CH 11	Open/close Na source shutter
Camera Shutter Top	CH 12	Open/close top camera shutter
Imaging Repump Shutter	CH 13	Turn on/off imaging repump shutter
Bias Coil Feedback	CH 14	Empty
Diode Laser Ramp	CH 15	Empty
RF Trigger	CH 16	Trigger the RF function generator
Dipole Trap AOM	CH 17	Turn on/off dipole trap AOM
MW Power Relay	CH 18	Turn on/off MW power relay
RF Switch	CH 19	Turn on/off RF switch
MW DDS	CH 20	Trigger DDS and FPGA
IGBT Switch	CH 21	Turn on/off the IGBT
Bias Coil Switch	CH 22	Turn on/off switch of bias coil
AO Trigger	CH 23	Enable/disable AO panel

Chapter 5

Microwave and RF System

The transitions between the ground hyperfine states of sodium F=1 and F=2, or magnetic sub-levels within the hyperfine manifold, can not be directly coupled by electric fields because they are electric dipole-forbidden, e.i. $\Delta L = 0$. Luckily, these rules are not obeyed in microwave and RF transitions due to magnetic dipole transitions induced by the oscillating magnetic field of the radiation.

Microwaves are of great utility in AMO physics to coherently manipulate the atomic transitions between hyperfine states and ground-state hyperfine manifolds [64, 65, 66]. Using microwave-dressing to apply AC Zeeman shifts to hyperfine energy levels leads to many applications, for example, generating spin-squeezing and multi-particle entanglements [67, 68, 69]. In our experiment, microwaves with frequencies close to the hyperfine splitting of 1.77 GHz serve two important purposes. First, we can transfer arbitrary populations between the $F = 1$ and $F = 2$ states using a sequence of resonant microwave pulses such as Pi and Pi/2 pulses. This gives us control over the initial state of our spinor BEC. Second, we can create arbitrary effective quadratic Zeeman shifts q using non-resonant microwaves which are detuned slightly from the $F = 1$ to $F = 2$ clock transition. This allows us to apply quenches to the spinor BEC, control the onset of spin-exchange collisions and apply phase shifts during spin-mixing interferometry. A schematic of our home-built microwave source is shown in Fig. 5.1

In this chapter, I will mainly discuss how microwave and radio frequencies are implemented in our experiment. Section one explains the theory of how microwaves couple the hyperfine states. Section two discusses in detail how our FPGA-based versatile microwave source is set up. Section three shows microwave performances

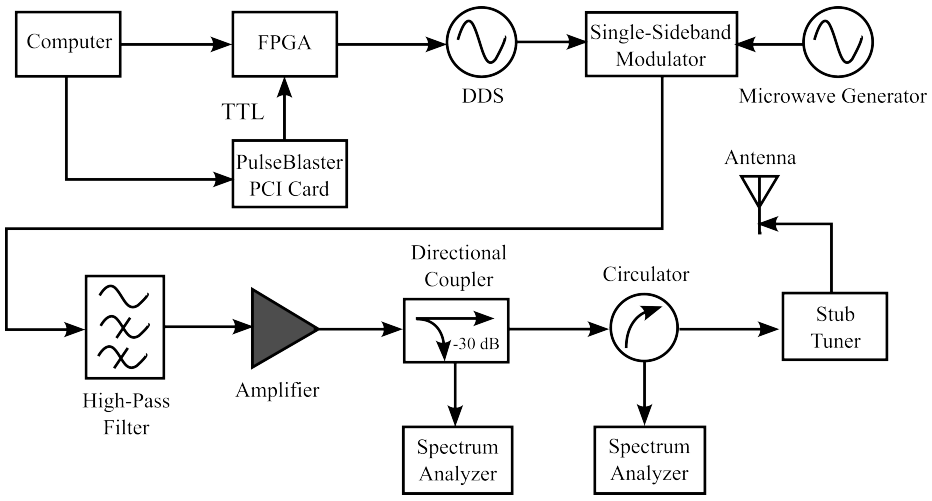

Figure 5.1: Schematic of microwave signal generation hardware. The parameters for the low-frequency signal are sent from the computer to the FPGA via USB. The FPGA then communicates with the DDS after it receives a TTL signal, which produces a low-frequency (MHz) signal. Next, the low-frequency signal is mixed with a high-frequency signal of 1.73 GHz in a single-sideband modulator. The modulator produces the desired sum-frequency signal close to the hyperfine splitting of the sodium ground state. After filtering, amplification, and impedance matching, the signal is emitted from a half dipole antenna to irradiate a sample of trapped cold atoms.

and calibrations in the experiment, including power calibration and microwave Rabi oscillations. In the last section, the separate, independent radio-frequency system for our experiment is explained.

5.1 Microwave Transitions

5.1.1 Na Ground-state Hyperfine Structure

For ^{23}Na in the ground state, the spin angular momentum quantum number is $S = 1/2$ because there is only one electron in the valence shell. The orbital angular momentum quantum number is $L = 0$. The total angular momentum quantum number

F, which results from the coupling between $J = L + S$ together with the nuclear spin I, is given by $F = J + I$ and can take the values $|J - I| \leq F \leq J + I$. This leads to two ground states $F = 1$ and $F = 2$ for sodium. In the presence of an external magnetic field, the degeneracy of the $2F + 1$ magnetic sub-levels is lifted, known as Zeeman splitting.

For a weak field, the external magnetic field can be treated as a perturbation, and the magnitude of Zeeman splitting is governed by

$$H_B = \mu_B g_F F_z B_z, \tag{5.1}$$

where μ_B is Bohr magneton and

$$g_F = \frac{F(F+1) + J(J+1) - I(I+1)}{2F(F+1)} g_J, \tag{5.2}$$

where g_J is the Landé g-factor and the corresponding Zeeman shifts between the magnetic sub-levels is

$$E = g_F \mu_B B_z M_F. \tag{5.3}$$

In a more general case, the Hamiltonian can be written as the combination of the hyperfine Hamiltonian and the external magnetic field

$$H = H_{hf} + H_z = A_{hf} \mathbf{J} \cdot \mathbf{I} - \mu_B \mathbf{J} \cdot \mathbf{B} - \mu_B \mathbf{I} \cdot \mathbf{B}. \tag{5.4}$$

The different energy eigenvalues are found by diagonalization, which yields an algebraic expression

$$\begin{aligned} E(F = I \pm 1/2, M_F) = &-\frac{\Delta E_{hf}}{2(2I+1)} - g_I \mu_B M_F B_z \\ &\pm \frac{1}{2} \sqrt{\Delta E_{hf}^2 + \frac{4M_F}{2I+1} (g_J - g_I) \mu_B B_z \Delta E_{hf} + (g_J - g_I)^2 \mu_B^2 B_z^2}, \end{aligned} \tag{5.5}$$

known as the Breit-Rabi formula [70]. ΔE_{hf} is the hyperfine splitting for $B = 0$. Figure 5.2 shows the Breit-Rabi diagram of the sodium ground state hyperfine structure,

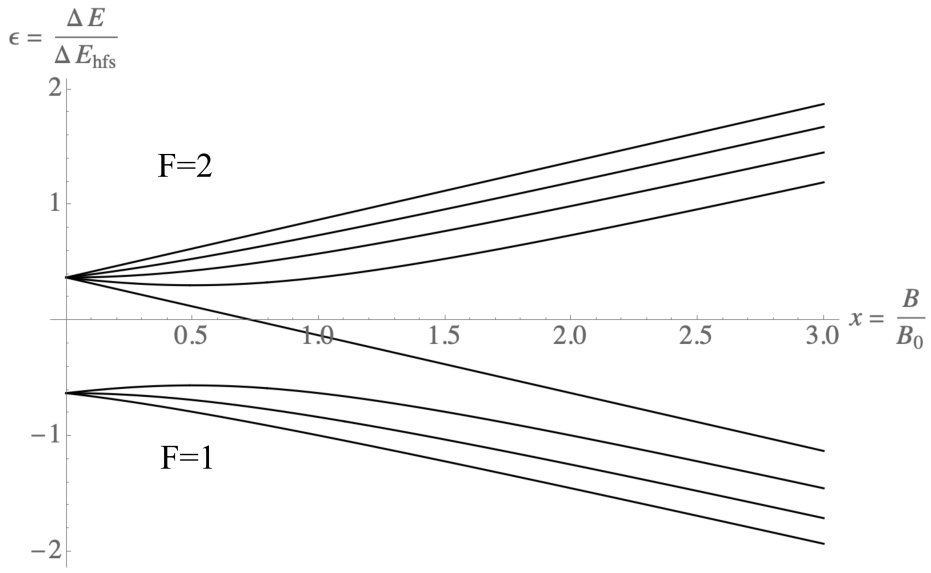

Figure 5.2: Breit-Rabi diagram of the sodium ground state hyperfine structure. The interaction between the external magnetic field and the magnetic dipole moment lifts the degeneracy of the hyperfine state and leads to the splitting of the magnetic sublevel. A dimensionless parameter is introduced in the plot: $x = \frac{(g_J - g_I)\mu_B B}{\Delta E_{hf}}$, where $B_0 = \frac{(g_J - g_I)\mu_B}{\Delta E_{hf}}$.

where the nuclear spin $I = 3/2$. In the low external magnetic field regime, where the Zeeman splitting is much smaller than the energy difference between $F = 1$ and $F = 2$ states, the Zeeman shift is linear and approximately equal to the expression in Eq. (5.3). However, the nonlinear term related to B_Z^2 is also present, which is quadratic in a magnetic field, leads to the quadratic Zeeman effect, which becomes stronger for large fields. The quadratic Zeeman effect is different from the linear Zeeman effect. It shifts the magnetic sublevels in the same hyperfine manifold in the same direction, regardless of the sign of the magnetic quantum number of M_F.

5.1.2 Oscillatory Magnetic Field

Since $\Delta L = 0$, transitions between the hyperfine ground states are forbidden for electric dipole interactions. However, oscillating magnetic fields such as those present in the microwave and radio regimes can interact with the magnetic dipole moment without obeying this selection rule. Like the static magnetic field case, the interaction Hamiltonian for a weak field is

$$H_{os} \approx \mu_B g_S \mathbf{B}_{os} \cdot \mathbf{S}, \tag{5.6}$$

where $\mathbf{B}_{os} = \mathbf{B}_0 \cos(\omega t)$. We can omit the nuclear interaction term because the nuclear magnetic moment is small. We can set z as our quantization direction, and approximate the system as nine separate two-level systems [71]. The spin matrices $\mathbf{S}$ have the Pauli spin matrices' structure, which is defined as $S_i = \frac{\hbar}{2}\sigma_i$, where σ_i is

$$\sigma_x = \begin{pmatrix} 0 & 1 \\ 1 & 0 \end{pmatrix} \qquad \sigma_y = \begin{pmatrix} 0 & i \\ -i & 0 \end{pmatrix} \qquad \sigma_z = \begin{pmatrix} 1 & 0 \\ 0 & -1 \end{pmatrix}. \tag{5.7}$$

Therefore we can workout the transition matrices:

$$\langle F, M_F|\sigma_x|F, M_F\rangle = \begin{pmatrix} 0 & -\frac{1}{2\sqrt{2}} & 0 & -\frac{\sqrt{3}}{2} & 0 & \frac{1}{2\sqrt{2}} & 0 & 0 \\ -\frac{1}{2\sqrt{2}} & 0 & -\frac{1}{2\sqrt{2}} & 0 & -\frac{\sqrt{3}}{2\sqrt{2}} & 0 & \frac{\sqrt{3}}{2\sqrt{2}} & 0 \\ 0 & -\frac{1}{2\sqrt{2}} & 0 & 0 & 0 & -\frac{1}{2\sqrt{2}} & 0 & \frac{\sqrt{3}}{2} \\ -\frac{\sqrt{3}}{2} & 0 & 0 & 0 & \frac{1}{2} & 0 & 0 & 0 \\ 0 & \frac{\sqrt{3}}{2\sqrt{2}} & 0 & \frac{1}{2} & 0 & \frac{\sqrt{3}}{2\sqrt{2}} & 0 & 0 \\ \frac{1}{2\sqrt{2}} & 0 & -\frac{1}{2\sqrt{2}} & 0 & \frac{\sqrt{3}}{2\sqrt{2}} & 0 & \frac{\sqrt{3}}{2\sqrt{2}} & 0 \\ 0 & \frac{\sqrt{3}}{2\sqrt{2}} & 0 & 0 & 0 & \frac{\sqrt{3}}{2\sqrt{2}} & 0 & \frac{1}{2} \\ 0 & 0 & \frac{\sqrt{3}}{2} & 0 & 0 & 0 & \frac{1}{2} & 0 \end{pmatrix} \tag{5.8}$$

and

$$\langle F, M_F|\sigma_z|F, M_F\rangle = \begin{pmatrix} \frac{1}{2} & 0 & 0 & 0 & -\frac{\sqrt{3}}{2} & 0 & 0 & 0 \\ 0 & 0 & 0 & 0 & 0 & -1 & 0 & 0 \\ 0 & 0 & -\frac{1}{2} & 0 & 0 & 0 & -\frac{\sqrt{3}}{2} & 0 \\ 0 & 0 & 0 & -1 & 0 & 0 & 0 & 0 \\ -\frac{\sqrt{3}}{2} & 0 & 0 & 0 & -\frac{1}{2} & 0 & 0 & 0 \\ 0 & -1 & 0 & 0 & 0 & 0 & 0 & 0 \\ 0 & 0 & -\frac{\sqrt{3}}{2} & 0 & 0 & 0 & \frac{1}{2} & 0 \\ 0 & 0 & 0 & 0 & 0 & 0 & 0 & 1 \end{pmatrix}, \tag{5.9}$$

where the basis states from left to right and top to bottom are (1,-1), (1,0), (1,1), (2,-2), (2,-1), (2,0), (2,1) and (2,2), respectively. The 3 × 3 diagonal submatrix in the top left corner and the 5 × 5 diagonal submatrix in the bottom right corner in Eq. (5.8) and Eq. (5.9) are the transition within $F = 1$ and $F = 2$ manifolds, and the rest of them are the magnetic sublevels coupling between $F = 1$ and $F = 2$. For the sodium electronic ground state hyperfine manifold ($3^2S_{1/2}$), the magnetic dipole transitions can be induced by microwaves, which connect $F = 1$ and $F = 2$ (red, green, and blue arrows in Fig. 5.3), and rf, which connect Zeeman sub-levels within the same F state (black arrows in Fig. 5.3). The selection rule for this type of transition becomes apparent from the transition matrices in Eq. (5.8) and Eq. (5.9). If the oscillating field is polarized perpendicular to the quantization direction, $\Delta F = 0, \pm 1$ and $\Delta M_F = \pm 1$. If the oscillation field is parallel to the quantization direction, $\Delta F = \pm 1$ and $\Delta M_F = 0$.

5.1.3 Microwave Dressing

Similar to how the light field can shift the energy levels via the AC Stark shift, the microwave can also shift the energy levels via the AC Zeeman effect, known as

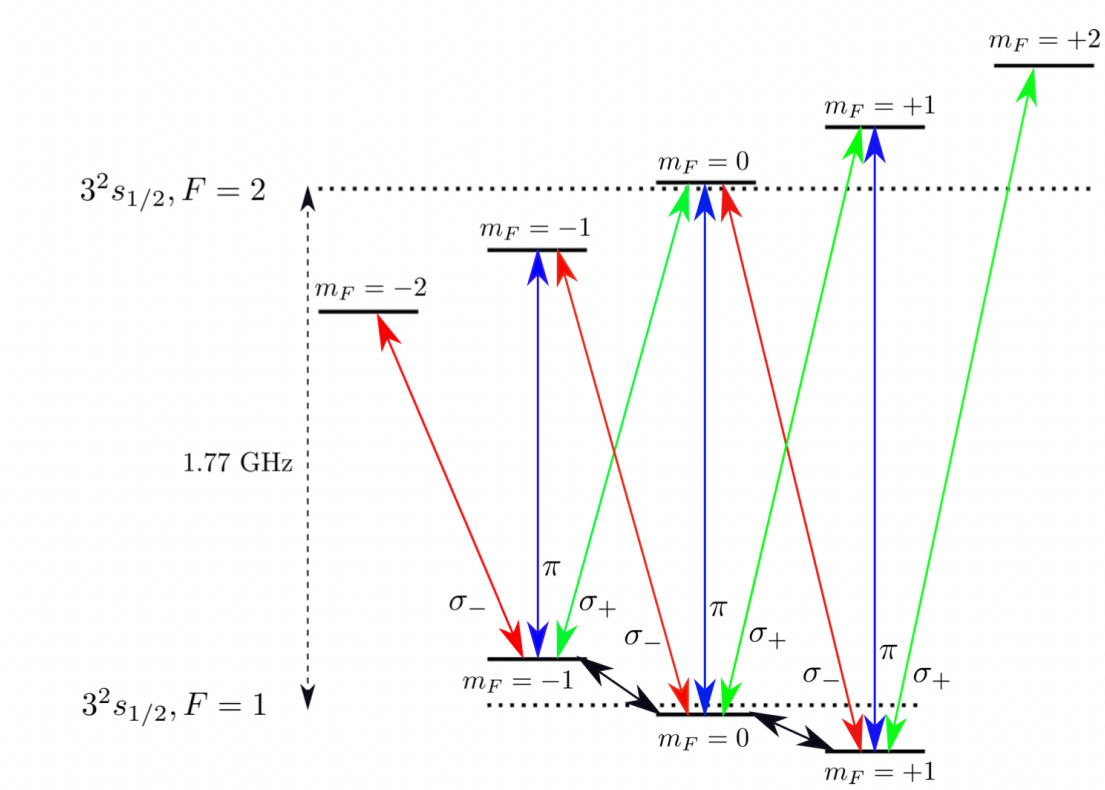

Figure 5.3: Schematic of microwave and rf transitions. Red, blue and green arrows represent microwave fields coupling to transitions between $F = 1$ and $F = 2$. Black arrows represent rf field coupling to transitions between $F = 1$ Zeeman sublevels.

microwave dressing [72]. In contrast to a DC magnetic field-induced quadratic Zeeman shift, which can only be positive, a microwave dressing field can generate an effective quadratic Zeeman shift that can be either positive or negative depending on the sign of microwave detuning Δ. For the simplest case in a two-level system, the Hamiltonian that describes the interaction between an atom and a microwave field can be written with the field interaction representation

$$H' = \frac{\hbar}{2}\begin{pmatrix} -\delta & \Omega \\ \Omega & \delta \end{pmatrix}, \tag{5.10}$$

where δ is the detuning between the microwave field and the atomic transition, and Ω is the Rabi frequency defined as $\mu_b B/\hbar$. If $\delta \gg \Omega$, then the resulting AC Zeeman

shift is

$$\Delta E \approx \pm\frac{\hbar\Omega^2}{4\delta}. \tag{5.11}$$

For sodium with $F = 1$ and $F = 2$ ground state manifolds, the shift of one energy level depends on all the other energy levels that couple to it. Therefore, the AC Zeeman shift of a target energy level is expressed as [73, 74]

$$\begin{aligned}\Delta E_{m_F} &= \frac{\hbar}{4}\sum_{k=0,\pm1}\frac{\Omega^2_{m_F,m_F+k}}{\Delta_{m_F,m_F+k}} \\ &= \frac{\hbar}{4}\sum_{k=0,\pm1}\frac{\Omega^2_{m_F,m_F+k}}{\Delta-(g_F m_F - g_{F'}(m_F+k))\mu_B B},\end{aligned} \tag{5.12}$$

where m_F is the magnetic quantum number in $F = 1$ manifolds, which takes the values -1,0, and 1, respectively. k takes the value of -1, 0, and 1 such that $m_F + k$ defines the magnetic sublevels in the $F = 2$ manifold. We define $\Delta_{m_F,m_F+k} = \Delta - (g_F m_F - g_{F'}(m_F + k))\mu_B B$ as the frequency detuning of the microwave pulse with respect to the $|F = 1, m_F\rangle \rightarrow |F = 1, m_F + k\rangle$ transition, where $g_{F,F'} = \pm 1/2$. Ω_{m_F,m_F+k} is the on-resonance Rabi frequency between m_F and m_F+k states, which can be directly obtained from experiments or calculated using Clebsch-Gordan coefficients. The total effective quadratic Zeeman shift q_{MW} on the magnetic sublevels in the $F = 1$ manifold induced by the microwave field is

$$q_{MW} = \frac{1}{2}(\Delta E_{m_F=1} + \Delta E_{m_F=-1} - 2\Delta E_{m_F=0}). \tag{5.13}$$

In our system, the microwave dressing is realized by tuning the microwave frequency from the clock transition $|F = 1, m_F = 0\rangle \rightarrow |F = 2, m_F = 2\rangle$ by Δ, as illustrated in Fig. 5.4. Choosing a microwave dressing field that is close to the clock transition makes it insensitive to the magnetic field fluctuations. By choosing the detuning to be relatively close to the clock transition but far away from others, we can selectively shift the $m_F = 0$ states without having too much effect on the other states.

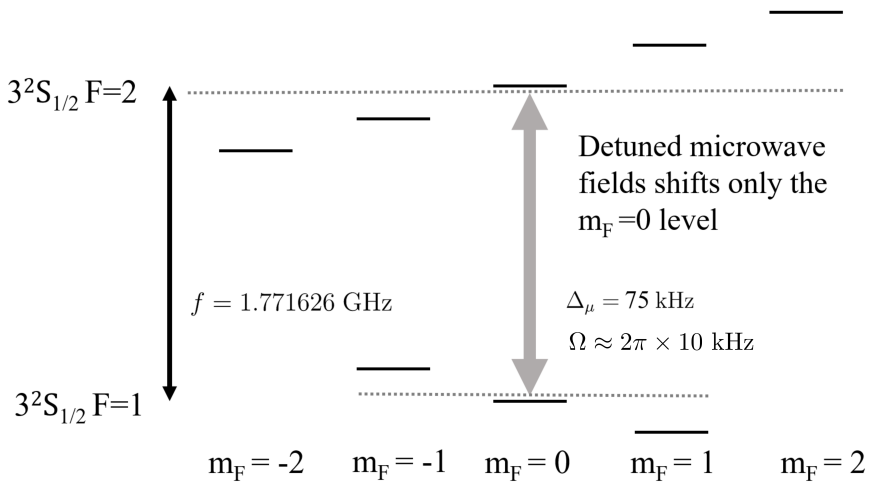

Figure 5.4: Microwave dressing in the presence of an applied magnetic field allows us to selectively shift only the $m_F = 0$ level and control the magnitude and sign of the effective quadratic Zeeman shift q.

5.2 Microwave Signal Generation

In our experiments, a time sequence of changing microwave parameters is stepped through that consists of changing frequencies, amplitudes, and phases during one experiment cycle of creating a BEC and perfoming measurement on it. In order to meet these requirements, we developed a home-built microwave system controlled by a field-programmable gate array (FPGA).

5.2.1 Hardware

Our FPGA controlled microwave generating system consists of an FPGA chip (Cyclone II, Altera), a Direct Digital Synthesizer chip (DDS, AD9954), and other electronic components surface mounted on three commercial boards: an FPGA board, a DDS board, and a USB input board for receiving data. An LCD screen module connected to the output pins of the FPGA board is used to aid user interaction via

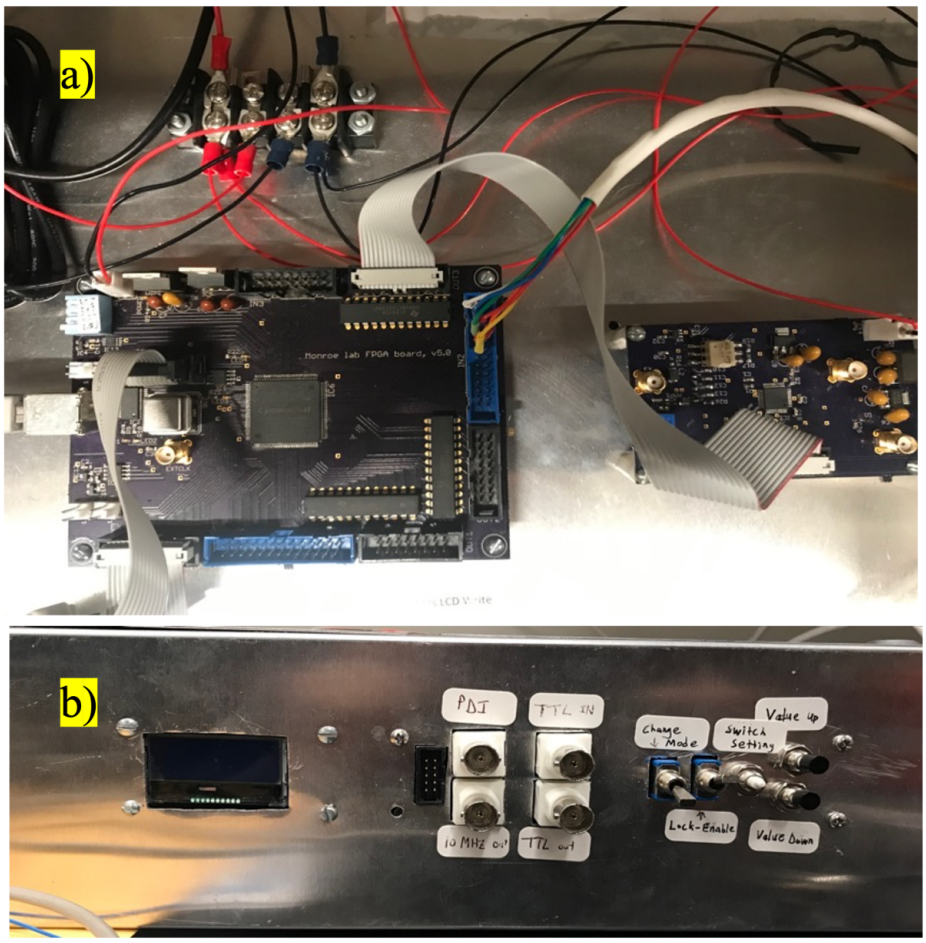

Figure 5.5: Enclosure of the FPGA system. a) FPGA board (left) and DDS board (right). b) Front panel of the FPGA system, the LCD screen is on the left side and the input control panel with buttons and switches is on the right side.

the front panel. These boards are enclosed in a grounded aluminum box, as illustrated in Fig. 5.5.

FPGA

The FPGA is a critical part of our microwave signal generation system because an FPGA we chose to use is versatile. A wide range of functions have been programmed into FPGAs with many applications in experimental physics [65, 75, 76]. One benefit of an FPGA compare to a microcontroller is that an FPGA can run several tasks in

parallel without any slow-down, making it possible to manage experimental equipment in a compact and controllable way without the need to devote extra controllers. FPGAs are also configured to run in some extreme conditions. For example, some FPGAs have been shown to work in cryogenic temperatures with minimal errors [77]. This allows the FPGA to be integrated with devices or detectors in a compact form, removing the physical barrier and limiting electrical losses from separation.

Our Cyclone II FPGA is a low-cost device that is powered by a 5 V power supply. It has 68,000 logic elements (LEs), each of them has a four-input look-up table. LEs serve as re-configurable digital logic gate arrays that can implement arbitrary digital functions. The LEs in FPGAs are configured using Verilog hardware description language. The code is synthesized using the Quartus II synthesizer to configure the FPGA. The configuration data from a host computer are transmitted to a Joint Test Action Group (JTAG) port via a USB Download Cable (USB-Blaster). The JTAG is mounted on the FPGA printed circuit board (PCB) and the configuration data are stored in a serial configuration device (EPCS64). The FPGA has up to 1.1 Mbits of embedded RAM clocked at 260 MHz, which can store data such as lookup tables. There are 16 global clock lines in the global clock network that drive the FPGA. We mounted a 400 MHz external crystal oscillator on the board, which provides the clock to all resources within the chip, such as input/output elements, LEs, embedded multipliers, and embedded memory blocks. The chip has three pairs of I/O banks that support multiple configurable voltage outputs: 1.5, 1.8, 2.5, and 3.3 volts for different types of operation. However, since our LCD screen and DDS need a 5 V input signal, we mounted a buffer (SN64BCT25244NT) before each output port. Some FPGA input pins connect to switches and buttons on the front panel and are programmed to accept user inputs, as shown in Fig. 5.5b. A toggle switch is used to change between manual and remote mode. In manual mode, the user can use the front panel menu display on

the LCD screen to select microwave parameters. We use manual mode to test that the DDS and FPGA are working correctly. In manual mode, a basic menu is displayed on the LCD screen, controlled via "up", "down", and "switch parameter" buttons on the front panel. The switch parameter button cycles between DDS parameters. The "up" and "down" buttons adjust the value of the selected parameter. As the user switches between the parameters, the LCD screen will display the selected parameter and its value. The menu currently allows setting amplitude and frequency. Any change in these parameters causes the output to update immediately. When running the experiment, the FPGA is switched to remote mode, and receives a timing sequence data from a compute running LabVIEW via the USB connection. Once the data sequence is received, it is stored in the RAM on the FPGA board and transmitted to the FPGA when the FPGA receives a rising TTL trigger on one of the inputs. On each trigger, the FPGA will step through the set of parameter values (amplitude, phase, and frequency) in the timing sequence table and updates the DDS accordingly. The FPGA receives TTL signals via a BNC cable, connected to one of the input pins of the FPGA board. In our setup, the TTL signals are generated by a digital output PCI card (PulseBlaster), but they can also be generated by any other function generator or data acquisition board. When in remote mode, the LCD screen displays the words "REMOTE MODE" to indicate that manual user input is disabled.

DDS

The DDS AD9954 is mounted on a PCB separated from the FPGA circuit board. The DDS can receive a digital signal via a serial connector and generate a sinusoidal voltage with analog output with a frequency of up to 160 MHz. In contrast to traditional analog synthesizers, the direct digital synthesizer has various advantages, for example, lower phase noise, extremely fast switching between different phases and

frequencies, and precise control of the output phase and frequency [78]. In our setup, the DDS board is controlled by the FPGA board. The control interface is shown in Fig 5.6. The FPGA can store frequency, amplitude, and phase values in its memory addresses and use as steps in the timing sequence. When the FPGA receives a TTL signal, it steps to the next memory block and sends the corresponding parameters to the DDS chip to update the output signal. We time the DDS board with an external 400 MHz clock, generated by a stable function generator referenced to a Rb atomic oscillator (SRS FS725 Rubidium Frequency Standard). This enables the DDS to produce a change of output amplitude, frequency, or phase within four microseconds of receiving new parameters. The external clock also allows us to bypass the internal clock multiplier on the DDS chip, which removes unwanted sidebands on the output signal. The output of the DDS is passed through a DC block to prevent any DC bias on the output signal. A desktop computer running LabVIEW is utilized. LabVIEW communicates with the FPGA board via a USB connection (FT232R UART) to serial interface. Through this connection, LabVIEW transmits the frequency, amplitude and phase information of each timing sequence, which are stored on RAM or the FPGA board. The timing sequences are transmitted as strings that always start with the letter "L". Thus when the FPGA receives a sequence starting with the letter "L", it decodes the following characters into amplitude, frequency, and phase parameter values that can later be stepped through and used to update the DDS chip.

5.2.2 Workflow of the Microwave Source

The schematic of our home-built microwave system is shown in Fig. 5.1. The microwave system uses a frequency reference from a rubidium atomic oscillator (SRS FS725 Rubidium Frequency Standard), producing a stable 10 MHz reference signal.

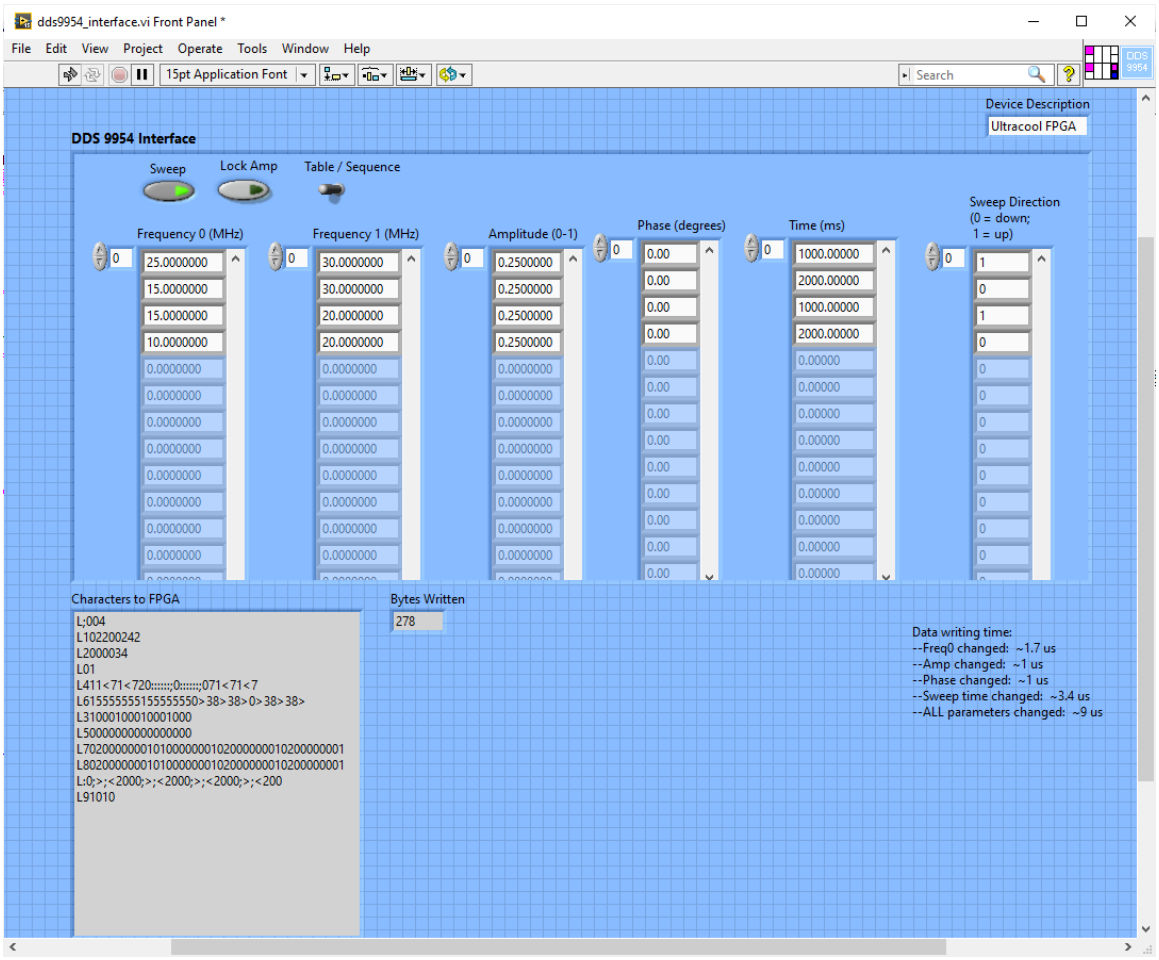

Figure 5.6: A screenshot of the DDS AD9954 LabVIEW user interface. Frequency, amplitude, and phase values are stored in several RAM memory addresses on the FPGA board. Later, these parameters arre used to update the DDS chip when it receives a ASCII sequence starting with the letter "L".

The FPGA board is programmed via a computer at the begining of an experiment cycle. During a cycle, it steps through the timing sequence, sends commands to the DDS chip to create a sine wave with specified frequency, amplitude, and phase. The sine waves' frequency is set to around 30 MHz and mixed with a constant high-frequency signal of 1.7416 GHz from a stable function generator (Stanford Research Systems, Inc. SG382). The mixing is done with a single-sideband modulator (Polyphase Microwave SSB0622A) which passes the sum of the two input frequencies, resulting in the desired frequency. The signal's frequency is very close to the clock transition in sodium at 1.7716 GHz. The parameter of the microwave signal, which includes the frequency, amplitude, and phase shifts, can be conveniently controlled only by changing the DDS while keeping the high-frequency signal generator at a fixed frequency output. The mixed microwave signal is further modulated with a high-pass filter (Mini-Circuit SHP -1000+) to filter out any potential unwanted DC levels or harmonics before sending it to a microwave amplifier. Our microwave amplifier (HD Communication HD 28747) amplifies the signal to a maximum output power of 25 W. The amplifier's power is turned on and off via an SSR relay (SPST-NO 30A 1-50V) which is controlled by a TTL signal sent from the computer running LabVIEW. The amplifier is usually turned on for about 13 s for each experimental cycle, and it becomes excessively hot after a long time of running. To cool the amplifier, we use thermal paste on its mounting surface and to mount it on the optical table with good thermal contact. We also put two fans on top of the amplifier's heat sink so it could be air-cooled as well during the experiment. After the amplifier, the signal is sent through a directional coupler (Pasternack PE2201-30) which provides a -30 dB diagnostic output used to monitor the signal on a spectrum analyzer.

To couple the microwave signal to our home-built antenna, impedance matching is important, since back reflections could go into the amplifier and destroy it when

the signal power is high. Therefore, a stub tuner (Maury Microwave 1819B) is used to match the impedance between the microwave source and the load, which is our home-built half dipole antenna. To match the impedance, the stub tuner is adjusted by moving the stubs back and forth to empirically minimize the back reflections. A coaxial circulator (DiTOM D3C0120) is used to prevent any back reflections from coupling back into the amplifier. While adjusting the stubs, we monitor the back reflections on the third port of the coaxial circulator via a spectrum analyzer. Impedance matching is done at low microwave power to prevent the antenna from heating up and being damaged during operating.

5.2.3 Antenna

We designed two types of microwave antennas for our experiments. The first one is a home-built half dipole antenna mounted inside the vacuum chamber. The other is a home-built Yagi antenna set up outside and underneath the vacuum chamber.

Internal Antennas

Fig. 5.7 shows two antennas located inside the vacuum chamber. Our half-dipole antenna is a quarter wave antenna with a length of 4.2 cm to match the frequency of 1.771 GHz. The antenna is made of UHV-compatible copper wire connected to an electrical feedthrough (Kurt J. Lesker IFTCG012012) via a UHV-compatible Kapton coax wire (Kurt J. Lesker FTAKC060CM1). The antenna is located inside the vacuum chamber approximately 3 cm away from the center, as shown in Fig. 5.7. Inline barrel connectors are used to provide a reliable, UHV-compatible electrical connection between the copper antenna and the coax wire. The half-dipole antenna radiates the microwave fields equally in all azimuthal directions. Therefore, we oriented our antenna parallel to the atoms to maximize the microwave intensity that the atoms

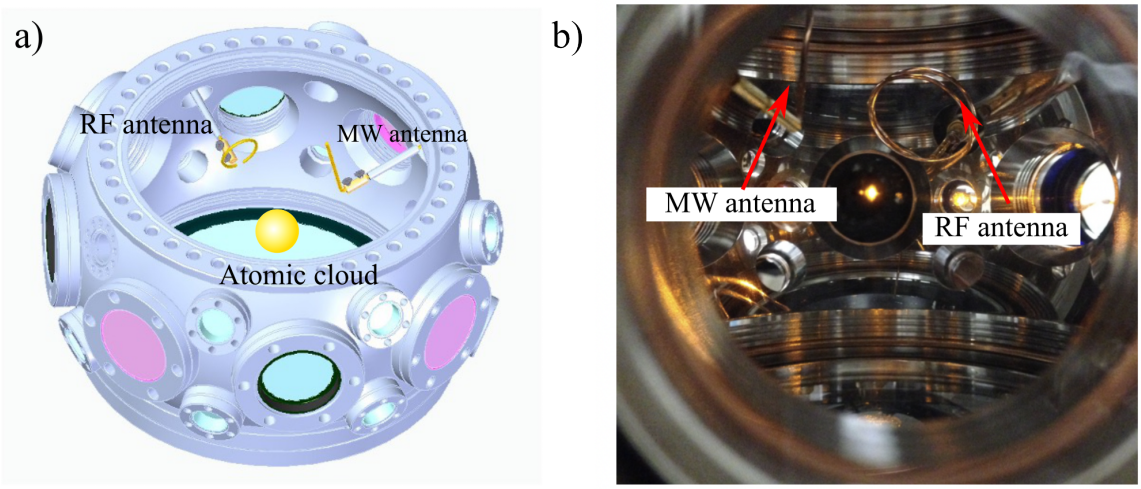

Figure 5.7: (a) CAD rendering of the microwave and RF antennas mounted inside the vacuum chamber. The microwave antenna is a half-dipole antenna mounted about 3 cm from the center of trapped atoms inside the vacuum chamber via an SMA CF 1.33" electrical feedthrough. The RF antenna is a small copper loop with a diameter of 25 mm. The RF antenna is also installed close to the center of the atomic cloud to ensure high RF intensity at the position of the atomic cloud. (b) A photo of the chamber showing microwave and rf antennas.

could receive.

Using the antenna inside the vacuum chamber allows us to irradiate the microwave signal directly onto the cold atom cloud with little loss. However, the internal antenna has two major drawbacks: outgassing and maintenance. An antenna running at high power for relatively long periods would heat up and give off particles (outgassing), causing the chamber pressure to rise and triggering our safety interlocks, stopping the experiment. Our testing data shows excessive outgassing when the microwave source continuously runs for over 100 ms at highest power. Therefore, the internal antenna is not feasible for the experiments which need long-term continuously microwave irradiation.

External Antenna

Due to the outgassing issues with our internal microwave antenna, we switched to an external antenna. The internal antenna is approximately 1.2 inches from the atoms, while the external antenna is approximately 4 inches away. Due to the $1/r^2$ power spread, this corresponds to a large loss of power that can be transmitted to the atoms. In order to mitigate this problem and ensure maximum gain, we used a Yagi antenna design for our external antenna see Fig. 5.8. A general Yagi antenna typically consists of a number of parallel thin rod elements, which include a single driven element, a reflector element, and director elements. The driven element is directly connected to a radio transmitter, and the reflector element is usually slightly longer than the driven element and placed behind the driven element. Directors, on the other hand, are a little shorter, can be used in any number, and are placed in front of the driven element in the intended direction. In our design, we use microwaves with a frequency of 1770 MHz $\pm$ 100 MHz, corresponding to a wavelength of 16.9 cm. Due to the limitation of the experimental space, we built a compact Yagi antenna with a folded dipole that has a length of 8.45 cm which folds the microwave in half. As the wave leaves the antenna, it unfolds into the full 16.9 cm. For a Yagi antenna, the gain increases with the number of directors used. Our current home-built antenna has three directors, which is the maximum given current space limitations.

5.3 Microwave Source Performance

After setting up the microwave system, the microwave power needs to be calibrated and tested before it can be put into use. Since all experimental data in this thesis are taken with the external Yagi antenna, we only show the calibration data and the Rabi frequency testing data using the external antenna.

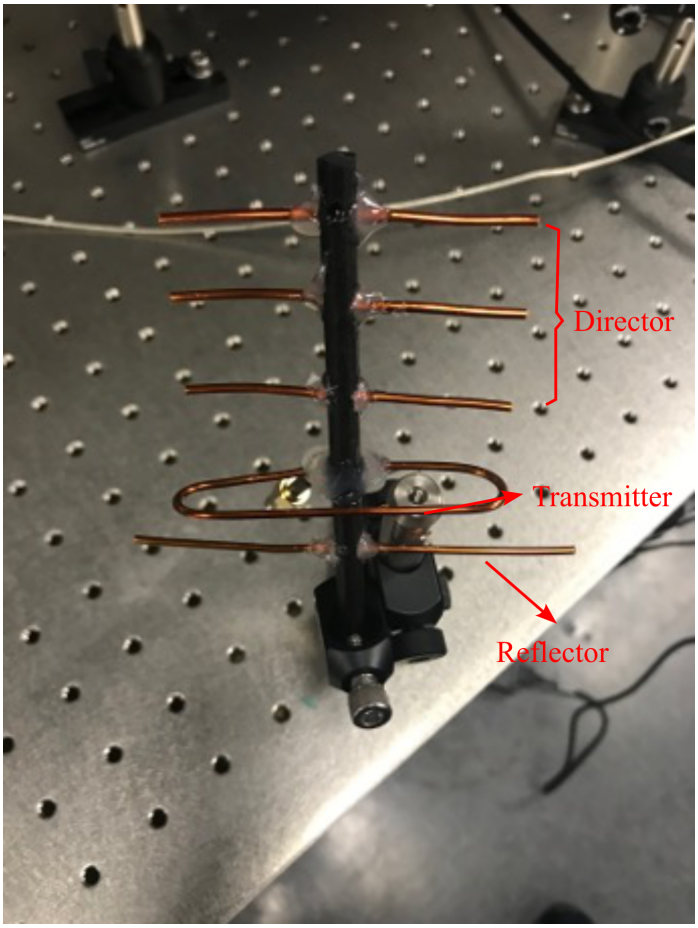

Figure 5.8: The Yagi antenna shown in the image is used in the experiment. The antenna consists of three components: the reflector, transmitter, and director. The reflector reflects the signal which help to collimate to the beam and increases the gain. The transmitter emits the microwave signal. The director resonates with the wave creating constructive interference, also increasing gain.

5.3.1 Microwave Calibration

In a well calibrated system, the set power and the corresponding output power should be equal. In our microwave system, we calculate the real microwave power by measuring the on-resonance Rabi frequency of population oscillation on the clock transition of our sodium BEC and then compare it with the corresponding set power entered in our LabVIEW that is sent to the microwave source. The Rabi oscillations on the clock transition can be treated using an effective two-level system. The Rabi frequency due to an oscillating magnetic field can be expressed

$$\Omega = \eta \frac{< 2|\boldsymbol{\mu} \cdot \mathbf{B}|1 >}{\hbar}, \tag{5.14}$$

where $\boldsymbol{\mu}$ is the magnetic dipole moment, $\mathbf{B} = \vec{B} \cos \omega t$ is the oscillating magnetic field, which in our case is the microwave field, and Ω is the generalized Rabi frequency, which can be expressed as $\Omega = \sqrt{\Omega_0^2 + \Delta^2}$, where Δ is the detuning. η is a loss factor that depends on several aspects, such as the distance between the antenna and the atoms, radiation angle, solid angle, and loss in transmission.

The first step of calibrating the microwave power is to calculate the real power. In general, the microwave power transferred per unit area is related to the Rabi frequency via

$$P_{mw} \propto \Omega_{clock}^2, \tag{5.15}$$

where P_{mw} is the power of the microwave in mW and Ω_{clock} is the Rabi frequency of the clock transition. Since the proportionally factors are the same for different microwave powers, we have

$$\frac{P_{mw}}{\Omega^2} = \frac{P_{0mw}}{\Omega_0^2}, \tag{5.16}$$

where P_{0mw} and Ω_0 are the reference power in mW and reference Rabi frequency in radians, respectively. Equation (5.16) means that given a reference power and corresponding Rabi frequency, we can calculate any real microwave power if we know

the Rabi frequency corresponding to that power. Therefore, the real microwave power in units of dBm can be written as

$$P_{real} = 10 \times \log\left(\frac{\Omega^2}{\Omega_0^2} 10^{P_0/10}\right), \tag{5.17}$$

where P_{real} and P_0 are the real power and reference power in dBm.

The last step is to compare the real power with the set power. If there is a discrepancy, we add a power calibration factor to compensate for the difference. Usually, a list of about 20 points should be measured and calculated. We then enter the set power and the real power multiplied by the calibration function into LabVIEW to do the interpolation. In our calibration data, we took 18 different data points, measured the Rabi frequency for each of them, calculated the real power, and compared it with the set power, as shown in Fig 5.9. We choose 40 dBm as the reference power because the maximum power output of the microwave amplifier is 44 dBm. If the reference power is chosen too close to the saturation point, the real power measurement will not be accurate, because of clipping and saturation of the amplified output waveform.

5.3.2 Microwave Rabi Oscillations

Next, we test the functionality of the calibrated microwave source by exciting Rabi oscillations in our Na spinor BEC in an applied B-field that defines the quantization direction and gives a linear Zeeman shift of $\mu \cdot B_0/\mathrm{h} = 300$ kHz, where μ is the magnetic dipole moment. The applied B-field B_0 is a constant magnetic field generated by our three pairs of Helmholtz coils and can be changed to point in different directions by changing the current through the coils. We set the quantization direction in the vertical z and east-west x directions with respect to the optical table, respectively. The angle between the microwave B-field and the B_0 field affects the Rabi frequencies. In our experiments, we located the microwave antenna underneath the vacuum chamber

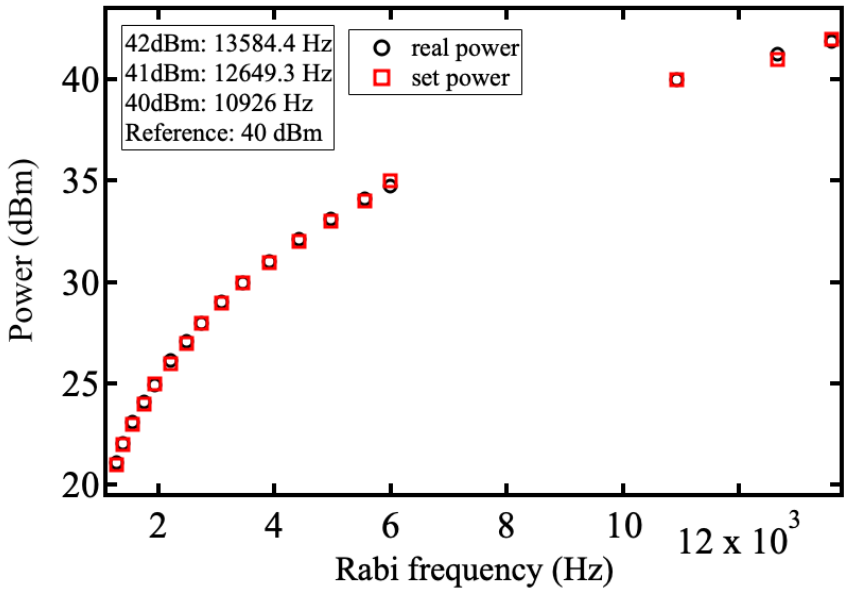

Figure 5.9: Microwave power as a function of Rabi frequency used for microwave power calibration. Black dots are the real power obtained by measuring each Rabi frequency. Red squares are the power set points, used in programming the microwave source. The black dots are closely matching the red squares which means that the set power matches the real power, indicating a good calibration.

and pointed it up at a small angle to the vertical direction of the vacuum chamber. Furthermore, we change B_0 to the x and z directions to measure the Rabi frequencies.

Figure 5.10 shows an energy level diagram for the relevant transitions and Rabi oscillations. For each sublevel of the $F = 1$ hyperfine state, three independent transitions are coupled to sub-levels in the $F = 2$ hyperfine states. Therefore, one might think we would measure nine microwave transitions for our experiments to have a full picture of the coupling between the two hyperfine states. However, we can simplify this effect by measuring only three transition and calculating the other six using the known Clebsch–Gordan coefficients. The three transitions we measure are Ω_π, $\Omega_{\sigma+}$ and $\Omega_{\sigma-}$ which correspondent to the transitions $|F = 1, m = 0\rangle \rightarrow |F = 2, m = 0\rangle$, $|F = 1, m = 0\rangle \rightarrow |F = 2, m = -1\rangle$ and $|F = 1, m = 0\rangle \rightarrow |F = 2, m = 1\rangle$, respec-

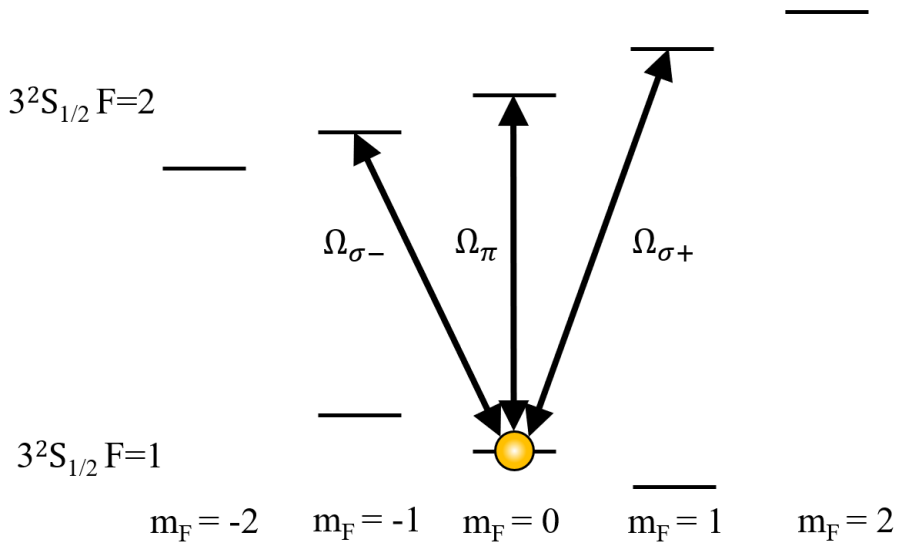

Figure 5.10: Na ground state hyperfine energy levels and associated Rabi couplings. The linear Zeeman splitting between hyperfine sublevel is 300 kHz at an applied magnetic field of 0.428 G.

tively. Figure 5.11 shows the microwave Rabi oscillations of the Ω_{π}, $\Omega_{\sigma+}$ and $\Omega_{\sigma-}$ transitions with B_0-field in the x and z directions, respectively. Rabi oscillations were obtained by scanning the microwave pulse length at a fixed microwave power, and Rabi frequencies were obtained by fitting a sine function to the measured data points. We measured the Rabi frequencies with B_0 field aligned in x direction to be

$$\begin{aligned} \Omega_{\pi} &= 2\pi \times 8363.75 \text{ kHz} \\ \Omega_{\sigma-} &= 2\pi \times 9867.45 \text{ kHz} \\ \Omega_{\sigma+} &= 2\pi \times 5963.22 \text{ kHz}, \end{aligned}$$

with B_0 aligned along the z direction, we obtained

$$\begin{aligned} \Omega_{\pi} &= 2\pi \times 12525.97 \text{ kHz} \\ \Omega_{\sigma-} &= 2\pi \times 6586.63 \text{ kHz} \\ \Omega_{\sigma+} &= 2\pi \times 4322.01 \text{ kHz}. \end{aligned}$$

These Rabi frequencies are large enough to induce fast quenches and phase shifts, because the corresponding time scales are much faster than the ones associated with spin-mixing, which is ∼30 Hz.

5.4 Radio-Frequency Signal

Apart from using resonant microwave fields to transfer population between ground hyperfine states, and microwave dressing with detuned field to cause an AC Zeeman shift. We also designed an independent radio-frequency (RF) source to couple the atoms between the sublevels in the $F = 1$ hyperfine manifold, directly. This gives us more feasibility for different initial state preparation of our spinor BEC. The RF source is designed to remotely couple the magnetic sub-levels in the $F = 1$ ground hyperfine state of sodium with frequencies on the order of a few hundred kilohertz. Figure 5.12 shows the experimental data of the population oscillation in the sublevel of the $F = 1$ manifold due to the rf coupling. The initial state was prepared to be $|F = 1, m = -1\rangle$. The magnetic field was set to generate a 300 kHz linear Zeeman shift between the adjacent $F = 1$ sublevels. Then, the on-resonant RF field was turned on for 100 μs, during which the population in the three sublevels oscillated sinusoidally. The RF generator's design is relatively simple compared to our microwave system. The schematic is shown in Fig. 5.13. The RF signal is generated by a function generator (Agilent 33220A), amplified to 25 W, and then radiated to atoms via a home-built RF coil antenna mounted inside the vacuum chamber, as shown in Fig. 5.7. The required frequency for the RF transitions in our experiments depends on the magnetic field because it has to be resonant with the linear Zeeman shift. For the typical magnetic field used in our experiments, the RF frequency is resonant at 300 kHz.

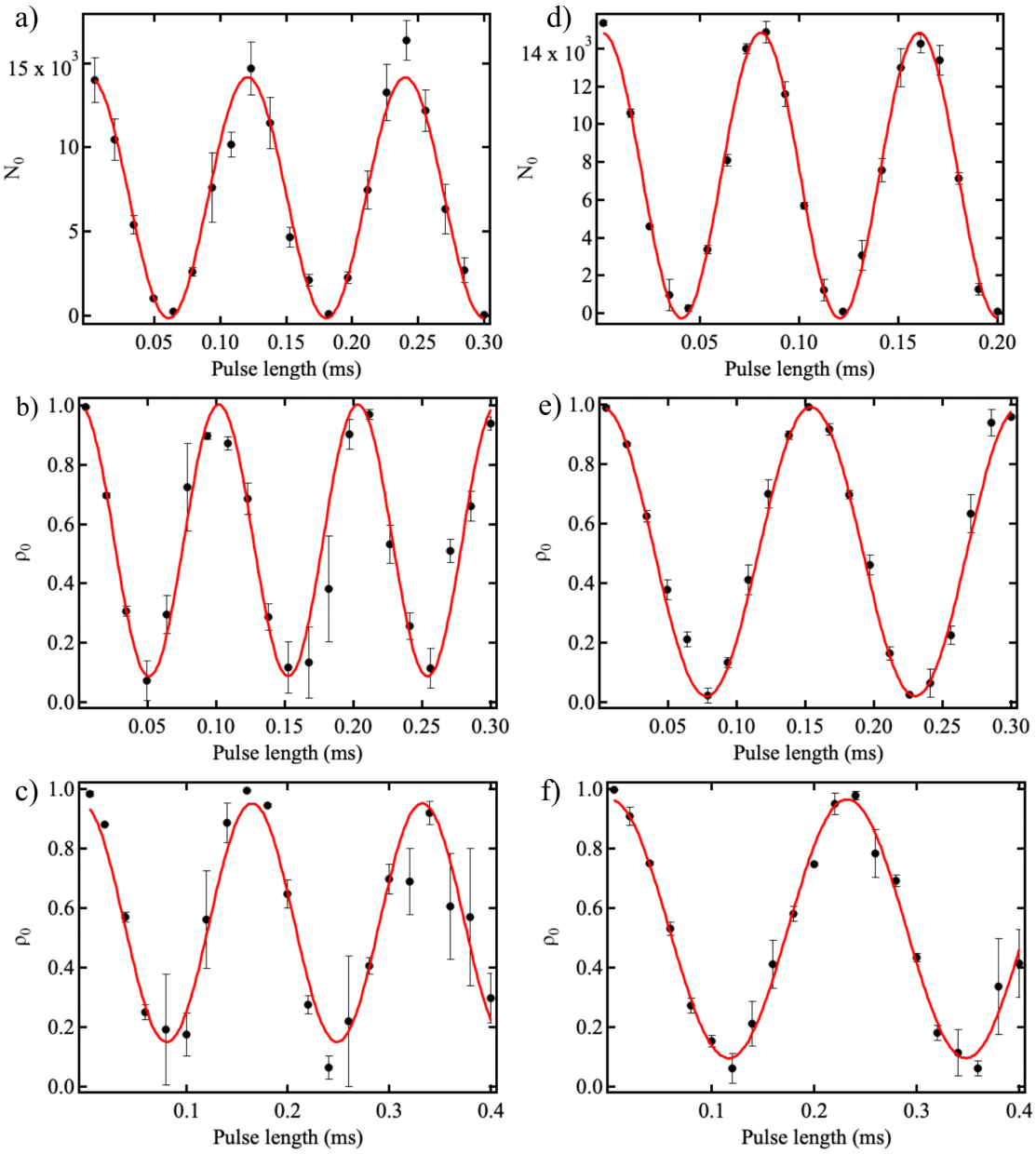

Figure 5.11: (a)-(c) show the Rabi oscillations measured on resonance for the Ω_π, $\Omega_{\sigma-}$ and $\Omega_{\sigma+}$ transition, respectively when B_0 is along the x direction. (d)-(f) show the Rabi oscillations on resonance for the Ω_π, $\Omega_{\sigma-}$ and $\Omega_{\sigma+}$ transition, respectively when B_0 is in the z direction. (a) and (d) show the atom number in $|F = 1, m = 0\rangle$ as a function of microwave pulse length. (b)-(f) show the atom number fraction in $|F = 1, m = 0\rangle$ as a function of microwave pulse length.

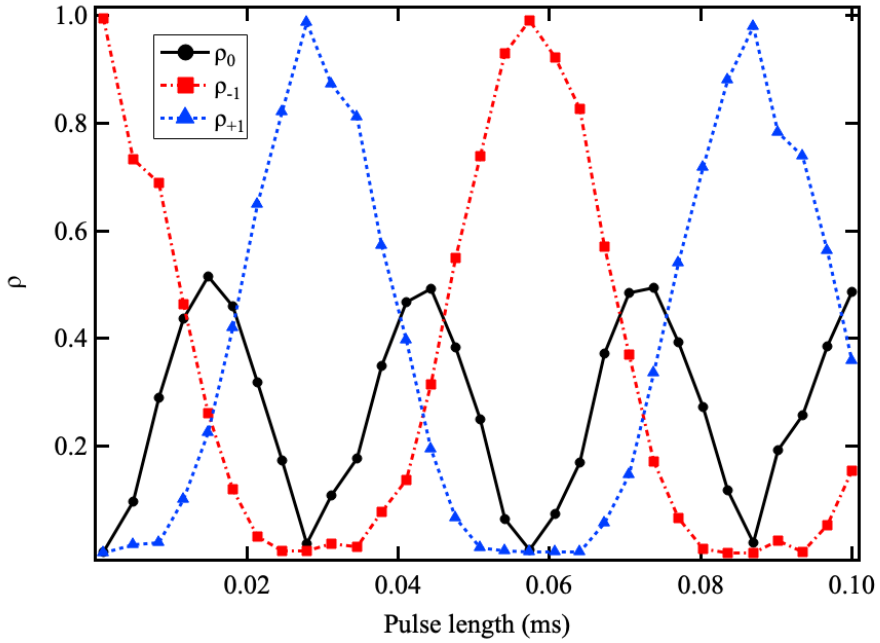

Figure 5.12: Experimental data of RF Rabi oscillations in $F = 1$ hyperfine state manifold. The B-field is set to generate a 300 kHz linear Zeeman shift in $F = 1$ hyperfine state, and the on-resonant RF field is turned on for 100 μs. ρ_0, ρ_{-1} and ρ_{+1} are the population fraction number of $|F = 1, m = 0\rangle$, $|F = 1, m = -1\rangle$, and $|F = 1, m = +1\rangle$, respectively.

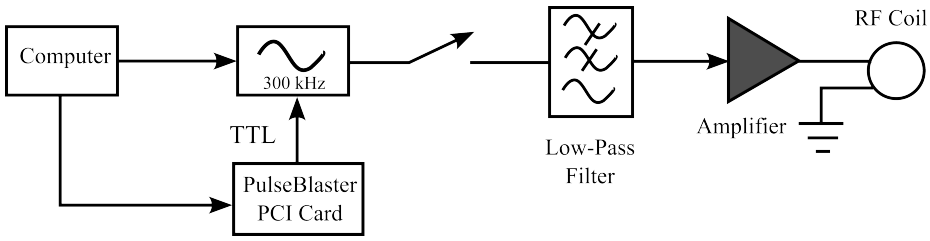

Figure 5.13: Schematic of the RF system. The RF signal generated from a function generator after receiving a TTL signal is filtered by a low-pass filter before passing through the RF amplifier. A home-built RF coil antenna is installed inside the vacuum chamber so that it is close to the atoms to ensure large Rabi frequencies.

Chapter 6

All-optical Generation of Spinor Sodium Bose-Einstein Condensates

Bose-Einstein condensation (BEC) has a long and rich history starting from the 1920s. Satyendranath Bose, an Indian physicist and mathematician wrote a paper in 1924 in which he derived Planck's quantum radiation law without referencing classical physics. However, Bose's article on Planck's law was not accepted for publication. He then sent it directly to Einstein, who recognized its importance, translated it to German, and got it published on behalf of Bose in the scientific journal *Zeitschrift für Physik* [79]. Later, Einstein extended Bose's idea to the case of noninteracting atoms [80], resulting in a phenomenon known as Bose-Einstein statistics. In this prediction, when a bosonic gas is cooled below a critical temperature T_c, a large fraction of atoms would occupy the lowest energy state. At this point, the wavelength of the matter wave, known as the thermal de Broglie wavelength λ_{dB} becomes comparable to the interatomic separation. The atomic wavepackets start to overlap, finally condense in the lowest quantum state, and become indistinguishable. They behave like a single giant "superparticle" or giant "matter wave", a macroscopic quantum object, which can be described by a single wave function which is a product of indentical single atom wave functions. However, this theory was not taken too seriously until the 1930s, when Fritz London and Laszlo Tisza found that the underlying mechanism of BEC could be used to explain the superfluidity in liquid helium 4 [81, 82]. Moreover, it has been recognized now that the properties of superconductivity and superfluidity in helium 3 and helium 4 are related to BEC, even though they are very different from the ideal gas system described by Einstein.

To experimentally realize a real BEC, one needs to cool the bosonic atomic gas

to an extremely cold temperature until λ_{dB} becomes large enough and the atomic wavepackets start to overlap. Meanwhile, the system should be gaseous all the way to the BEC transition. This requires a dilute gas with a density of about a hundred-thousandth the density of normal air, such that it will not form molecules due to three-body collisions or transition to the liquid or solid. One candidate that scientists have tried to form a BEC with is spin-polarized hydrogen. In 1976, Stwalley and Nosanow pointed out that the spin-polarized hydrogen would remain gaseous even at zero temperature, which stimulated lots of interest in generating the spin-polarized hydrogen BEC in the experiment. Experiments were first done using cryogenic cells to cool the sample and compressing it [83], but they failed to reach the requisite phase space densities to form a BEC [84]. Later, by switching to magnetic trapping and evaporative cooling to compress and reduce the temperature of the sample, the spin-polarized hydrogen BEC was eventually accomplished in 1998 by Kleppner, Greytak, and collaborators [85].

At about the same time, laser cooling and trapping technology had been developed and opened a new door to generate BECs with alkali atoms. Atoms can be cooled and trapped in a magneto-optical trap in a ultra-high vacuum chamber, with a temperature of about a few hundred micro-kelvin to a few millikelvin. Then, the temperature of the cold atomic cloud can be further cooled down via the evaporative cooling technique. The atomic gas finally reaches the critical temperature T_c, and the BEC starts to form. In 1995, the first BEC of rubidium atoms was finally achieved by Eric Cornell, and Carl Wieman [86], 70 years after Bose and Einstein made the prediction, while the first sodium BEC was created by Wolfgang Ketterle in the same year [87]. Not long after, the first signatures of the occurrence of BEC in vapors of lithium were also reported [88]. In those systems, atoms were magnetically trapped during the evaporative cooling and confined in a single magnetic sublevel so their spin

degrees of freedom were frozen. In 1998, an optical trap was used to confine sodium BECs in the $F = 1$ hyperfine level [89]. The optical trap simultaneously trapped all magnetic sublevels. Thus, the atomic spin was liberated from the requirements of magnetic trapping and became a new degree of freedom that could be investigated in BECs. Since BECs in optical traps have multi-component spin levels, they are also called spinor BECs. Over the last 27 years, BEC has been experimentally realized in many groups with different atomic species. Apart from alkali atoms such as ^{7}Li, Rb, Na, and Cs [90], BEC has been created in some alkaline-earth-like atoms, such as Ytterbium [91], Calcium [92], Strontium [93, 94], and some high magnetical strongly dipolar atomic species such as Erbium [95], Chromium [96], Dysprosium [97] and Europium [98]. In addition, even light [99] has been condensed to a BEC, which was surprising due to the vanishing interaction.

In this chapter, we present the method we used to achieve the University of Oklahoma's first sodium Bose-Einstein condensate, a sodium spinor BEC, which is achieved by an all-optical route. This chapter is divided into four sections. Section one presents the BEC theory, including basic features of the non-interacting Bose gas and interacting Bose gas in a harmonic trap. Section two introduces our far-detuned crossed optical dipole trap (ODT) setup and method to transfer atoms from the MOT into the ODT. Section three describes how we implement and optimize the evaporative cooling technique to realize the phase transition to generate the BEC. Finally, section four shows our BEC characteristics, including BEC fractions, temperature, and trap frequencies.

6.1 Theory of Bose-Einstein Condensate

6.1.1 Ideal Boson Gas

Atoms are bosonic if they have integer spin, which means the total number of electrons, protons, and neutrons they contain is even. Bose-Einstein Condensates (BECs) are bosonic gases that are so cold that a macroscopic fraction of atoms occupy the same lowest quantum state of the trapping potential. The atoms become indistinguishable from one to another and act as a single giant matter wave. The phase transition to BEC occurs when the temperature falls below the critical temperature T_c, usually in the nano-Kelvin (nK) regime. The process of an atomic system undergoing a phase transition from a thermal gas to a BEC can be related to the change of the thermal de Broglie wavelength λ_{dB} of each particle, which is defined as

$$\lambda_{dB} = \frac{h}{\sqrt{2\pi m k_B T}}, \tag{6.1}$$

where m is the particle's mass, h is Planck's constant, and k_B is the Boltzmann constant. We can think of the particles as wavepackets, and λ_{dB} is the associated wavelength which is inversely related to the momentum. At high temperature, λ_{dB} is very small compared to the average inter-particle distance d. The wavepackets do not overlap, and the atomic gas behaves like billiard balls. When the temperature of the system is lowered, λ_{dB} increases as the temperature decreases. The quantum nature of the particles becomes apparent as the wavepackets of the particles begin to overlap.

For the simplest system, which includes N non-interacting free particles, the Hamiltonian is

$$\mathbf{H} = \sum_{i}^{N} \frac{p_i^2}{2m}. \tag{6.2}$$

Therefore, the the single-particle energy in momentum space is

$$\epsilon_i = \frac{p_i^2}{2m}. \tag{6.3}$$

We consider a non-interacting Bose gas in 3D in thermodynamics equilibrium. The mean occupied number of a single particle state i is given by the Bose distribution

$$f(\epsilon_i) = \frac{1}{e^{\beta(\epsilon_i - \mu)} - 1}. \tag{6.4}$$

The grand partition function can be written as

$$Z(z, V, T) = \prod_i \frac{1}{1 - ze^{-\beta\epsilon_i}}, \tag{6.5}$$

and the grand canonical potential of the ideal Bose gas can be written as [100]

$$\Omega = PV = k_B T \log Z = -k_B T \sum_i \log\bigl(1 - ze^{-\beta\epsilon_i}\bigr), \tag{6.6}$$

where $z = e^{\beta\mu}$ is the fugacity, which is related to the chemical potential μ, and $\beta = (k_B T)^{-1}$. The particle number can be written as

$$N = z\frac{\partial}{\partial z} \log Z(z, V, T) = \sum_i \frac{ze^{-\beta\epsilon_i}}{1 - ze^{-\beta\epsilon_i}}. \tag{6.7}$$

We notice that Eq. (6.7) diverges when atoms are in the state with $p = 0$ with fugacity $z = 1$. Therefore we split the sum into two parts: one indicates atoms in the ground state with $\epsilon_0 = 0$, and the other describes the non-ground states' energy. We also replace the sum over i with integrals over the momentum p. The number density of the Bose gas then becomes

$$n = \frac{N}{V} = \frac{4\pi}{h^3} \int dp\, p^2 \frac{1}{z^{-1}e^{\beta\epsilon} - 1} + \frac{1}{V}\frac{z}{1 - z}, \tag{6.8}$$

where the first term is associated with the number density in the excited states and the second term is associated with the number density in the ground state. Specifically, we can re-write the excited state part in terms of the thermal de Broglie wavelength λ_{dB} [101]

$$n = \frac{1}{\lambda_{dB}} g_{3/2}(z) + \frac{1}{V}\frac{z}{1 - z}, \tag{6.9}$$

where $g_{3/2}(z)$ is defined as $\sum_{n=1}^{\infty} z^n/n^{3/2}$. Only when z is between 0 and 1 is $g_{3/2}(z)$ bounded. Specifically, when $z = 1$ ($\mu = 0$), $g_{3/2}(1)$ becomes the Riemann zeta function with a value ≈ 2.612. We can now write the fraction of the atoms in the ground state as

$$n_0 = n - \frac{g_{3/2}(z)}{\lambda_{db}^3}, \tag{6.10}$$

where $n_0 = \frac{1}{V}\frac{z}{1-z}$. From this equation, when $n > g_{3/2}(1)/\lambda_{dB}^3$, a finite fraction of atoms occupies the ground state, and the phenomenon is known as Bose-Einstein condensation. The critical condition for BEC to happen is $n\lambda_{dB}^3 \approx 2.612$, and the critical temperature T_c can also be derived from this expression. At zero temperature, a pure condensate with all particles in the ground state can be realized, see Fig. 6.1.

6.1.2 Bose-Einstein Condensate in a Trap

In the previous section, we assume the Bose gas is uniform and noninteracting. This section discusses the Bose gas in a harmonic potential with two-body interactions. The Hamiltonian that describes a many-body system with N interacting bosons confined in an external harmonic potential is given, in second quantization, by [102]

$$\hat{H} = \int d\mathbf{r}\ \hat{\Psi}^\dagger(\mathbf{r})(-\frac{\hbar^2\nabla^2}{2m} + V_{ext}(\mathbf{r}))\hat{\Psi}(\mathbf{r}) + \frac{1}{2}\int d\mathbf{r}d\mathbf{r}'\ \hat{\Psi}^\dagger(\mathbf{r})\hat{\Psi}^\dagger(\mathbf{r}')V(\mathbf{r}-\mathbf{r}')\hat{\Psi}(\mathbf{r}')\hat{\Psi}(\mathbf{r}), \tag{6.11}$$

where $\hat{\Psi}^\dagger(\mathbf{r})$ and $\hat{\Psi}(\mathbf{r})$ are the bosonic field operators that create and annihilate, respectively, a particle at the position $\mathbf{r}$. The first two terms are kinetic energy and external harmonic potential field, and $V(\mathbf{r}-\mathbf{r}')$ is the two-body interatomic potential which describes the hardcore interaction. The ground state of this Hamiltonian can be directly calculated using the Monte Carlo method [103]. However, the calculation can be very computationally expensive and impractical when the number of atoms becomes large. The many-body system with interaction is commonly solved using mean-field approximations to simplify the calculation as well as to gain more physical

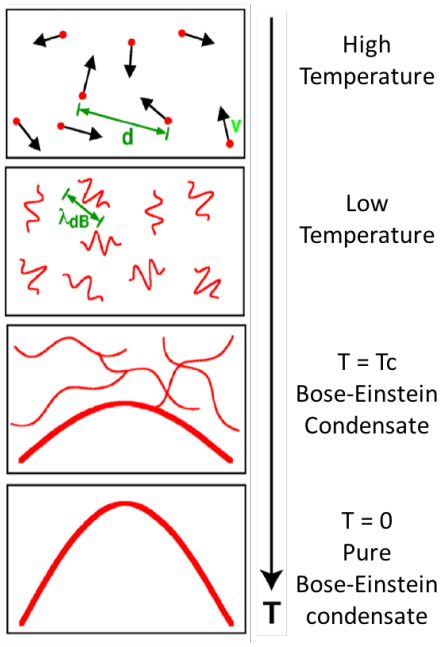

Figure 6.1: An illustration of how the de Broglie wavelength λ_{dB} changes with decreasing temperature. When the temperature is high, λ_{dB} is much smaller than the inter-particle distance. As we lower the temperature, quantum effects start to become visible. The wavefunctions of the atoms start to overlap with each other. At T=0 K, all particle waves are overlapped and become a single "giant matter wave." Adapted from [1].

insights about the system. The basic idea of the mean-field approximation is to assume that the action felt by a given particle due to all other particles is substituted by the mean action of all particles. According to the mean-field approximation [104, 105], we decompose the field operator

$$\hat{\Psi}(\mathbf{r},t) = \Phi(\mathbf{r},t) + \delta\hat{\Psi}(\mathbf{r},t), \tag{6.12}$$

where the complex function $\Phi(\mathbf{r},t) \equiv \langle\hat{\Psi}(\mathbf{r},t)\rangle$ has the meaning of an order parameter and is commonly known as the macroscopic wave function of the condensate. $\delta\hat{\Psi}(\mathbf{r},t)$ describes the non-condensate part, which can be neglected when the temperature of the system is well below the critical temperature T_c. The two-body interaction term

$V(\mathbf{r}-\mathbf{r}')$ in the dilute ultracold gas can be replaced by

$$V(\mathbf{r}-\mathbf{r}') = g\delta(\mathbf{r}-\mathbf{r}'), \tag{6.13}$$

where g is the interaction strength related to the s-wave scattering length a through

$$g = \frac{4\pi\hbar^2 a}{m}. \tag{6.14}$$

Then, the evolution of the condensate wave function $\Phi(\mathbf{r},t)$ can be expressed using the following equation

$$i\hbar\frac{\partial}{\partial t}\Phi(\mathbf{r},t) = \left(-\frac{\hbar^2\nabla^2}{2m} + V_{ext}(\mathbf{r}) + g|\Phi(\mathbf{r},t)|^2\right)\Phi(\mathbf{r},t). \tag{6.15}$$

This equation, known as Gross-Pitaevskii (GP) equation, was derived independently by Gross and Pitaevskii [106, 107]. The GP equation can also be derived through the variational procedure:

$$i\hbar\frac{\partial}{\partial t}\Phi = \frac{\delta E}{\delta\Phi^*}, \tag{6.16}$$

where E is the energy functional, which is given by

$$E(\Phi) = \int d\mathbf{r}\left[\frac{\hbar^2}{2m}|\nabla\Phi|^2 + V_{ext}(\mathbf{r})|\Phi|^2 + \frac{g}{2}|\Phi|^4\right], \tag{6.17}$$

where the three terms inside the square bracket from left to right are the kinetic energy of the system, the harmonic confinement potential, and the interaction energy, respectively. For the mean-field theory in the ground state, the condensate wave function is $\Phi(\mathbf{r},t) = \phi(\mathbf{r})e^{-i\mu\hbar/t}$. Here, μ is the chemical potential and $\phi(\mathbf{r})$ is a time-independent wave function, normalized to the total number of particles in the condensate, $\int d\mathbf{r}\ |\phi(\mathbf{r})|^2 = N_0$. The GP equation for the ground state can then be written as

$$\left(-\frac{\hbar^2\nabla^2}{2m} + V_{ext}(\mathbf{r}) + g|\phi(\mathbf{r},t)|^2\right)\phi(\mathbf{r}) = \mu\phi(\mathbf{r}), \tag{6.18}$$

where $|\phi(\mathbf{r})|^2 = n$ is the particle density, which is a nonlinear term that has no analog in the linear many-body Schrödinger equation. If the kinetic energy is equal to the

interaction energy, and we use $p = \hbar/\xi$, then we get

$$\frac{\hbar^2}{2m\xi^2} = \frac{4\pi\hbar^2 a}{m} n, \tag{6.19}$$

or, more common, it can be written as

$$\xi = \frac{1}{\sqrt{8\pi a n}}, \tag{6.20}$$

where ξ is called "healing length", which is a length scale that indicates the distance over which the wave function tends to its bulk value when subjected to a localized perturbation [108]. The healing length, which is related to the number density and the s-wave scattering length, gives the shortest distance over which the wave function can "heal" from a perturbation effect.

If the interaction term is much larger than the kinetic energy term, one can neglect the kinetic energy term, and Eq. (6.18) becomes

$$n(\mathbf{r}) = |\phi(\mathbf{r})|^2 = g^{-1}[\mu - V_{ext}(\mathbf{r})]. \tag{6.21}$$

This is known as the Thomas-Fermi approximation, which sets a boundary to the cloud beyond which $n(\mathbf{r}) = 0$. The boundary of the cloud is therefore given by

$$V_{ext}(\mathbf{r}) = \mu. \tag{6.22}$$

For a harmonic trap under the Thomas–Fermi approximation the extension of the cloud in the three directions is given by the distance called the Thomas-Fermi radius R_i,

$$R_i^2 = \frac{2\mu}{m\omega_i},\ i = x,\ y,\ z. \tag{6.23}$$

The Thomas-Fermi radius is often used to determine the size of a weakly interacting BEC, and it can also be compared with the healing length ξ. For example, the ratio between the Thomas-Fermi radius and the healing length ξ can be used to determine the critical frequency of a rotating trap for creating a vortex [102, 108].

6.2 Crossed Optical Dipole Traps

Experimentally, we achieve Bose-Einstein condensation by evaporatively cooling the Bose gas in a far-off resonant trap, also known as optical dipole trap (ODT). ODT is a simple way to trap atoms without requiring large magnetic field gradients. Additionally, the tightly confining trapping potential provides a conservative force to localize the atoms, therefore significantly reducing the optical excitations. These characteristics make it an appealing option for various metrology applications, such as magnetometry and inertial sensing. The optical dipole trap (ODT) is one of the most important setups in our system to create all-optical BECs. We load atoms from the MOT or the optical molasses into a crossed ODT formed by focusing two far-off resonance laser beams. Then, we perform forced evaporative cooling to realize BEC.

6.2.1 ODT Setup

We evaporative cooling a gas in an optical dipole trap (ODT), atoms with the highest energy are removed from the trap by lowering the laser power, and the remaining atoms thermalize through two-body elastic collisions. Therefore, relatively high collision rates are necessary, which corresponds to high trapping frequencies. A simple way to make an ODT that has tight confinement in all three dimensions is to cross two focused Gaussian beams at their foci under a 90° angle, as shown in Fig. 6.2. In this case, the intensity distribution of both beams can add up to the total intensity

$$I_{tot} = \frac{2P_x}{\pi\omega^2(x)} e^{-\frac{2(x^2+y^2)}{\omega^2(x)}} + \frac{2P_y}{\pi\omega^2(y)} e^{-\frac{2(x^2+y^2)}{\omega^2(y)}}, \tag{6.24}$$

where P_x, P_y and $\omega(x)$, $\omega(y)$ are the power and the beam waist of the two crossed laser beams, respectively. Usually, the frequency of ODT beams is detuned far below the atomic transition. The wavelength difference is several hundreds of nanometers. Due to the large detuning, this far-off resonant trap (FORT) minimizes optical excitations,

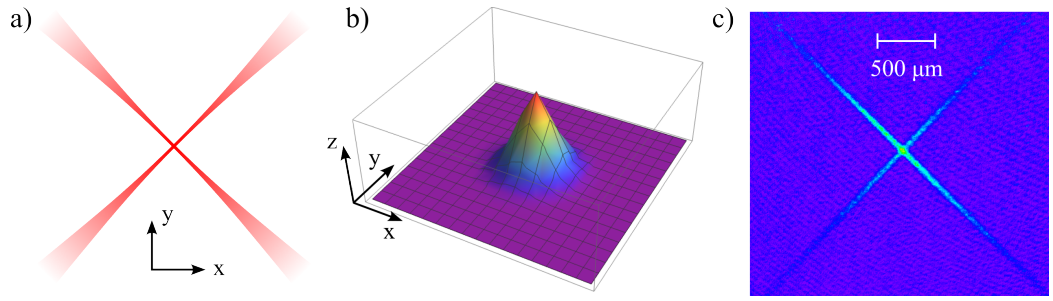

Figure 6.2: Representations of a crossed beam dipole trap. a) Shows that the two focusing beams are crossed at the center of the chamber to form a crossed optical dipole trap. b) Presents the corresponding calculated potentials. c) Shows a false color absorption image of our crossed optical dipole trap when the two beams are not overlapped. Atoms can be seen to fill the arms and the focus area of the trap geometry.

reducing heat generation due to the scattering process. A FORT works as follows: two ODT beams overlap, with the polarization being linear and orthogonal to each other. The overlapping foci of the FORT have the largest light intensity, which leads to the AC Stark shift induced by the trapping light to lower the ground state energy of the atoms proportionally to the local intensity. The spatial dependence of the atomic potential energy is therefore equivalent to a spatial dependence of the light intensity, according to Eq. (2.10). We set up the crossed ODT in the horizontal $(x-y)$ plane so that the strongest dipole force works along the direction of gravity. When the intensity of the light is high, gravity does not play a big role in shaping the dipole trap, and the sagging of the cloud can be neglected.

Our system uses an infrared (IR) laser (IPG photonics YLR-50-1064-LP) with an output power of 50 W at 1064 nm to generate a crossed ODT. The crossed ODT consists of two tightly focused far red-detuned beams overlapping with the MOT at the center of the chamber, and each has a $1/e^2$ beam waist of approximately 24 μm. The schematic of our ODT setup is shown in Fig. 6.3. The laser can produce a linearly polarized Gaussian beam with a maximum power output of 50 W. The output

fiber of the IR laser is set on a separated optical breadboard (Thorlabs MB1224) along with the other dipole trap optics which are anti-reflection coated at 1064 nm wavelength. The optical breadboard is about 7" above the main optical table and held by five 1.5" thick mounting posts to minimize the vibration from the main optics table. The collimated laser beam is output from a commercial optical fiber collimator with a beam waist equal to 3.5 mm in diameter. Then the beam is passed through an AOM (3110-125 Crystal Technology) with a telescope which consists of a plano-convex lens (200 mm focal length) and a plano-concave lens (-20 mm focal length). The telescope shrinks the size of the beam from 3.5 mm diameter to 0.35 mm diameter so it can pass through the center of the hole of the AOM without accidentally heating the metal frame or the transducer inside. A D-shape mirror is used to direct the zeroth order beam after the AOM into a high-power beam dump. The first-order beam passes through an expansion telescope and is then focusing at the center of the chamber via a plano-convex 400 mm focusing lens followed by a dichroic turning mirror. To complete the crossed ODT, we guide this laser beam to return it back into the vacuum chamber from the other side, as shown in Fig. 6.3, so it is orthogonal to the original beam. The reflecting beam is focused by another plano-convex 400 mm focusing lens and a dichroic turning mirror. At the center of the vacuum chamber two foci with approximately the same beam waist are overlapped to generate the optical potential well to trap the cold atoms. In order to implement a fine adjustment, both 400 mm focusing lenses are mounted on travel translation stages (Thorlabs MT1) with micrometer drives which can move the foci back and forth along the beam path. In total, four dichroic-coated mirrors surrounding the chamber are used to guide the beams in and out of the vacuum chamber. They are used to reflect the laser beam at 1064 nm wavelength and allow the yellow MOT laser to transmit. We also replace the standard adjustment knobs on the dichroic mirror with the high precision micrometer

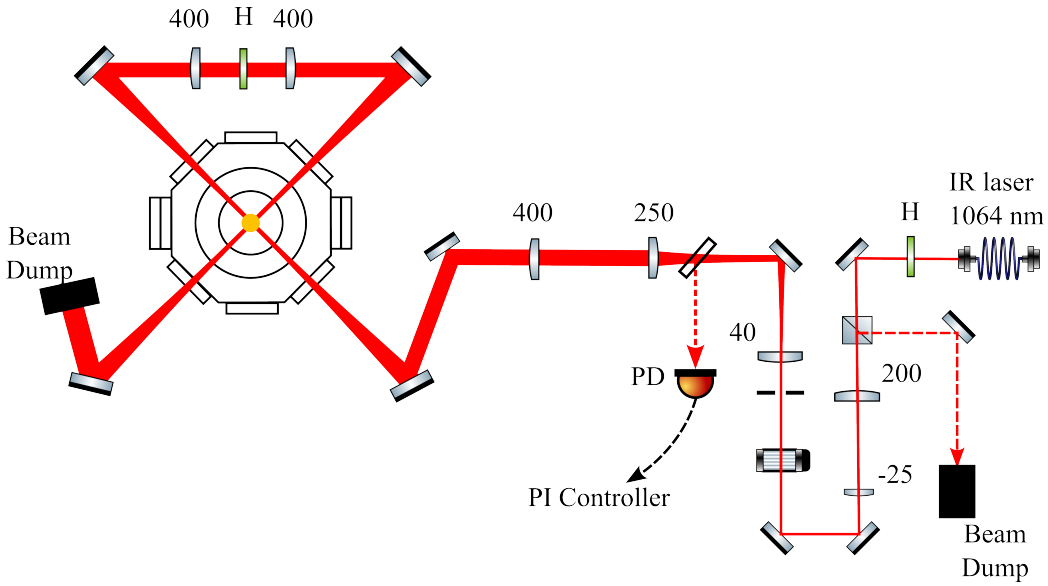

Figure 6.3: Schematic of crossed ODT setup. The high-power IR laser is expanded by an optical telescope after going through an AOM, then focused by a 400 mm plano-convex lens. The IR laser beam travels through the chamber twice so that the two foci overlap at the center of the MOT to form the crossed ODT. PD stands for photodetector, and H stands for half-wave plate. The D-shape mirror, the zeroth order light and the corresponding beam dump after the AOM are not shown.

heads, which have sensitivities better than 1 μm to increase the accuracy.

Given the size of the vacuum chamber and the working space of the dipole trap system, we choose to use a 400 mm plano-convex focusing lens to achieve a beam waist of about 24 μm at the center of the chamber. In order to approximately determine the position as well as the size of the beam waist, we measured the beam size $w(z)$ at ten different spots along the laser propagating direction z after the 400 mm lens and fit them into the equation

$$w(z) = w_0\sqrt{1 + \left(\frac{\lambda z}{\pi w_0^2}\right)^2}. \tag{6.25}$$

This equation describes the evolving beam width of a Gaussian beam, where w_0 is the beam waist, and λ is the laser's wavelength, which is 1064 nm. After fitting the

measured data point, we found that the dipole trap beam waist $w_0 \approx 24$ μm, the Rayleigh length $z(R) = \pi w_0^2/\lambda$ is ~ 1.7 mm, and the distance between the beam waist position and the 400 mm focusing lens is ~ 16.6 cm.

6.2.2 ODT Beam Alignment

The ODT should be overlapped with the highest density part of the MOT or optical molasses to load atoms efficiently. Aligning the ODT with the MOT is challenging. Usually, the beam alignment is performed using a low laser power of about 80 mW. However, when running the experiment, we use 85% of the full power corresponding to ~ 42 W. The high power of the ODT laser beams will generate heat and cause thermal stress on mirrors, lenses, and the crystal inside the AOM and therefore distort the beam path. Additionally, the high-power back-reflection light generated from one optic can be incident on another optic, if not blocked, and will also lead to distortions. To tackle the first challenge, we move both the MOT and ODT to the geometric center of the vacuum chamber as precisely as possible. First, we center the MOT using magnetic bias fields by moving the zero magnetic field position, as explained in chapter four. To help the alignment, we also set up two video cameras aligned with two 1.33" viewports to locate the MOT position, and then align the ODT to the center of the chamber. We align the ODT beam through the center of the two diagonal viewports where the MOT beams also pass through. To overlap the ODT beams with the MOT, we first use the on-resonant imaging repumping beam to approximately overlap and counter-propagate the ODT beam since the on-resonant yellow light interacts with the cold atoms trapped in the MOT and removes them via the scattering force. Once the MOT is extinguished by the imaging repumping beam, it indicates that the beam path of the imaging repump beam crosses the atomic cloud. Then we align the ODT beam carefully with the imaging repumping beam with some reference apertures. To

deal with the thermal effects in the optical system, we put irises along the laser beam path to block the back-reflection light generated from lenses, mirrors, and AOMs. We also observed a decrease of ODT laser power as well as beam path deviation after running the laser at high power for some time due to the thermal stress generated from the high-power laser. In order to minimize the effects, after switching the laser to high-power mode, we do not perform any data-taking until the ODT optical system reaches thermal equilibrium.

The fine alignment of the ODT requires aligning the dipole trap light focus and the MOT. Therefore, we run an experiment sequence that can generate the MOT as well as running the IR laser at the high-power mode simultaneously, such that we can observe the ODT and MOT using absorption imaging if they are on top of each other. We usually start the alignment by aligning a single ODT beam to the MOT, then overlap the second beam with the first one. While aligning the ODT, two cameras are switched on alternately to take pictures from the top and side to locate the ODT positions along horizontal and vertical directions, respectively. At this time, the magnification of the cameras are set to $m = 0.6$, so they can image both MOT and ODT, as illustrated in Fig. 6.4.

After preliminary aligning the ODT to the MOT, we turn off the MOT beam and leave the ODT beam on for at least 500 ms, so atoms from the MOT have fallen and expanded away except for the ones that are trapped in the ODT. The focus of the ODT beam is found by recording the center position of the trapped atoms after some holding time inside the ODT since atoms tend to be attracted to the beam's waist position. The focus position of the ODT beams can be adjusted via a micrometer screw along the beam path by moving the plano-convex 400 mm focusing lenses mounted on the translation stages. The highest intensity of the intersection point of the two ODT beams is generated by crossing two foci of the ODT beam, which creates a

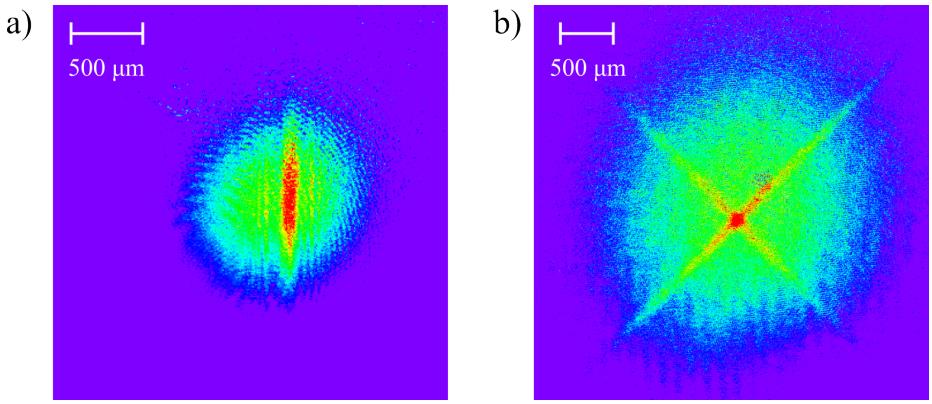

Figure 6.4: False-color TOF absorption images of the MOT and ODT from side view (a) and top view (b). The red color indicates the high-density regime where the atoms are trapped inside the ODT. The TOF was 5 ms.

deep potential depth for trapping the atoms. Since the ODT beam waist is small, the overlapping spot is, therefore, very small compared to the size of the MOT. To achieve a high-resolution image of the two foci when crossing one of them to another, we change the camera's magnification from $m = 0.6$ to $m = 2$ to enlarge the regime of interest. Then, we slightly adjust the high-precision micrometer knobs mounted on the dichroic mirrors between experiment cycles to optimize the alignment. Better alignment means that more atoms can be trapped in the ODT. The number of atoms is obtained using Igor to fit the overlapping spot after each experiment cycle. This number, which automatically updates, is maximized by making small adjustments.

In addition, the polarization of the ODT beam was also found to contribute to the alignment: the best crossed ODT is achieved when the ODT beams' polarization is linear and orthogonal to each other to neutralize any interference effects. The orthogonal polarization configuration of the ODT beam is achieved with a $\lambda/2$ wave-plate rotating the polarization of the second beam by 90°. A well-focused imaging system is essential since one might not be able to identify the initial signal of the ODT beam if the imaging system was defocused too much. In this situation, the ODT

beam in the absorption image tends to be very wide and blurry, although the MOT picture still looks good.

6.2.3 Stabilization of ODT

Our IR laser can output high power (50 W) but also has significant intensity noises which reduces the number of atoms that can be loaded into the dipole trap. Therefore, we built an opto-electronic noise eater to minimize the laser noise as well as controlling the laser power. The system consists of an AOM, a free-space photodetector, a function generator (Agilent 33521A), a current pre-amplifier (SRS Model SR570), and a commercial proportional-integral (PI) controller (New Focus LB 1005 Servo Controller). A small portion of the ODT beam that is reflected from a flat glass plate (Thorlabs WG11010-C) is picked up by a photodetector. The electrical signal is amplified and converted from current to voltage by the current pre-amplifier with a large signal-to-noise ratio. A commercial PI controller generates an error signal by subtracting an amplified photodetector signal from an external setpoint generated from the function generator. The PI controller generates a feedback control signal via the proportional-integral mechanism. The control signal is sent back to the AOM to stabilize the output power of the IR laser beam after the AOM.

In addition to minimizing intensity noise, this electronic noise eater also serves as a laser power modulator, allowing us to realize forced evaporative cooling by exponentially decreasing the power of the ODT. This is done by first using LabVIEW to program an exponential decay curve as a function of time. The curve is empirically determined to have the most efficient cooling rate. The decay curve is programmed into the function generator via a USB, producing an output voltage signal serving as the external setpoint to the PI controller. The Agilent function generator has a 16-bit high resolution (better than 1 mV voltage accuracy), so it can implement an

accurate exponential ramp from large to very small voltage which is critical for the evaporative cooling mechanism. After receiving the exponential ramp-down curve as a time-dependent setpoint voltage, the PI loop controls the power modulation on the AOM to decrease the laser power exponentially to follow the setpoint value. Atoms in the ODT undergo force evaporation until the phase transition to the BEC is accomplished.

6.2.4 Loading Cold Atoms into the ODT

Optimizing the loading efficiency is key to trapping more atoms in an ODT. This is essential for generating Bose-Einstein condensates because forced evaporative cooling causes about 90% of atoms to be lost duing the cooling. The loading efficiency of a system depends on the competition between atoms loading into a trap and atoms leaving the trap. Typically, the loss of atoms in the ODT happens due to three processes: one-body losses, two-body losses, and three-body recombination. One-body losses could come from photon scattering induced by the ODT or background collisions due to the imperfect vacuum. The far-off resonant trap (FORT) light photon scattering can be determined by calculating the photon scattering rate given by Eq. (2.13). Background gas atoms moving at high speed will collide with trapped atoms and kick the atoms out of the trap, leading to atom loss. Two-body losses are induced from two-body collision. Elastic collisions evaporate the hot atoms from the trap and decrease the remaining atoms' temperature, which is crucial to realize evaporative cooling. Elastic collisions are therefore "good" in this context. Two-body inelastic collisions such as photoassociative collisions (induced by the trapping laser light) and ground state hyperfine changing collisions generate heat and cause the atom to leave the trap. Inelastic collision are therefore "bad" in this context. Three-body recombination describes three atoms colliding where two colliding atoms form a

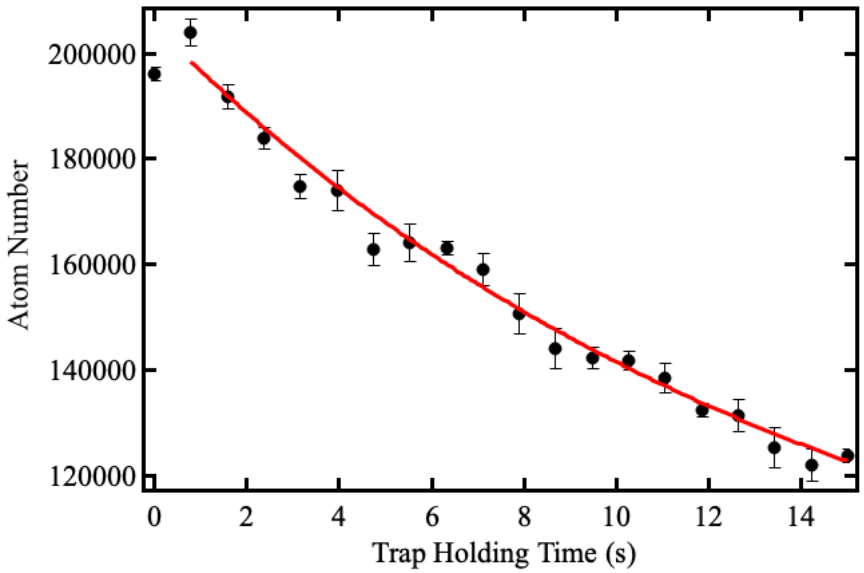

Figure 6.5: Lifetime measurements of sodium atoms in $F = 1$ hyperfine ground state. The black dots are the experimental data, and the red curve is an exponential decay function $N(t) = N_0 e^{-\frac{t}{\tau}}$, where N_0 is the initial atom number in the trap, and τ is the time constant. From the fitting we obtain $\tau \approx 14.7 \pm 2$ s. Atoms in the $F = 1$ ground state show an exponential decay mainly due to the one-body losses.

molecule, and the third carries away the excess energy. Three-body losses are small during the loading procedure and, therefore, can be neglected [46]. For sodium atoms trapped in the $F = 1$ hyperfine state, the primary atom loss comes from the one-body losses, which can be observed from the $1/e$ lifetime of our optical dipole trap, as shown in Fig. 6.5

The lifetime of the dipole trap is measured by observing the number of atoms in the trap for different holding times. All the other light sources are blocked, so that resonant light cannot influence the lifetime of the atoms in the trap. Figure 6.5 shows the decay of sodium atoms in the $F = 1$ hyperfine ground state. Since the atom loss in ODT at high laser power is mainly due to one-body losses, the atom number can therefore fit an exponential decay curve and the time constant from the fitting

is $\tau \approx 14.7 \pm 2$ s. The lifetime of the dipole trap can be increased by decreasing the pressure in the vacuum chamber. With a lower background pressure, the possibility of trapped atoms colliding with background atoms is lowered, resulting in a lower heating rate. Our BEC was reached with a vacuum chamber pressure of 10^{-11} Torr, where the background collision can be mostly ignored.

Our experiment starts with loading $\sim 3 \times 10^8$ atoms in the MOT. The optical dipole trap is turned on during the MOT loading phase so that atoms can transfer directly from the MOT into the tightly focused crossed ODT. The power of the ODT beam is set to 80% of its maximum value during the MOT loading stage and tuned to full power after the optical molasses stage. This will minimize the frequency shift of atoms due to the AC Stark shift induced by the high-intensity FORT laser beam and lessen its impact on the MOT cooling transition. Since the size of the ODT is small compared to the size of the MOT, no visible reduction of atom number in the MOT can be observed.

The dynamics of the loading procedure are complex because it not only depends on the atom loss in the ODT but also depends on atom loading, which involves on-resonant yellow light. For example, one factor determining the loading rate is the flux of atoms into the ODT, which depends on atom number and density in the MOT. To have a large number of atoms in the MOT, a relatively high power of the MOT repumping beam is needed to sustain the MOT. However, the high power of the repumping beam also increases the loss rate, because it generates heat during the repumping cycle. Therefore, finding a mechanism to minimize the loss and increase the flux of atoms in the ODT is necessary. The flux of the atoms into the ODT depends on MOT density, atom temperature, and the potential depth of the ODT. Common ways to increase the MOT's density and obtain a high loading rate while reducing the losses is to generate a dark spot MOT [109, 110] or a compressed MOT [111, 112]. In

our experiment, we compress the MOT by increasing the magnetic field gradient from ∼7 G/cm to 12 G/cm in 20 ms to increase the MOT density and maximize the flux of atoms into the ODT. To further cool and increase the atoms' phase space density, we apply an optical molasses stage to cool the atoms via sub-Doppler cooling during the loading process. The optical molasse stage lasts 32 ms as the MOT is gradually turned off. During this time, the magnetic-field gradient from the MOT coils is decreased from 12 G/cm to zero, and the detuning of the laser cooling beam increased from 20 MHz to 32 MHz. Apart from detuning the MOT cooling beam's frequency during the optical molasses stage, we also empirically found optimal values for the power of the MOT cooling beam and MOT repumping beam during the ODT loading phase that maximizes the atom number in the optical dipole trap.

Figures 6.6a, b, and c show the number of atoms loaded into the optical dipole trap at the optical molasses stage as a function of the MOT cooling beam detuning, the MOT cooling beam power, and the repumping laser beam power, respectively. During the optical molasses stage, the MOT cooling beam frequency is tuned from -20 MHz to -32 MHz to optimize the number of atoms in the ODT, as illustrated in Fig. 6.6a. The larger effective detuning reduces the excitation rate of atoms in the dipole trap and thus reduces light-induced collisions and heat. Increasing the detuning of the cooling laser in this way also helps cool the temperature of the atoms to the sub-Doppler regime, thereby increasing the phase space density and the probability of trapping the atoms in the dipole trap. The intensity of the cooling laser beam also affects the loading rate. Figure 6.6b shows that the number of atoms is maximum in the ODT when our MOT cooling laser power is about 30 mW. Below this level, the MOT is not sustained. To further optimize the transfer of atoms from the MOT into the ODT, we gradually turn down the power of the optical repumping beams from 3.8 mW to a few hundred microwatts during the optical molasses stage. The

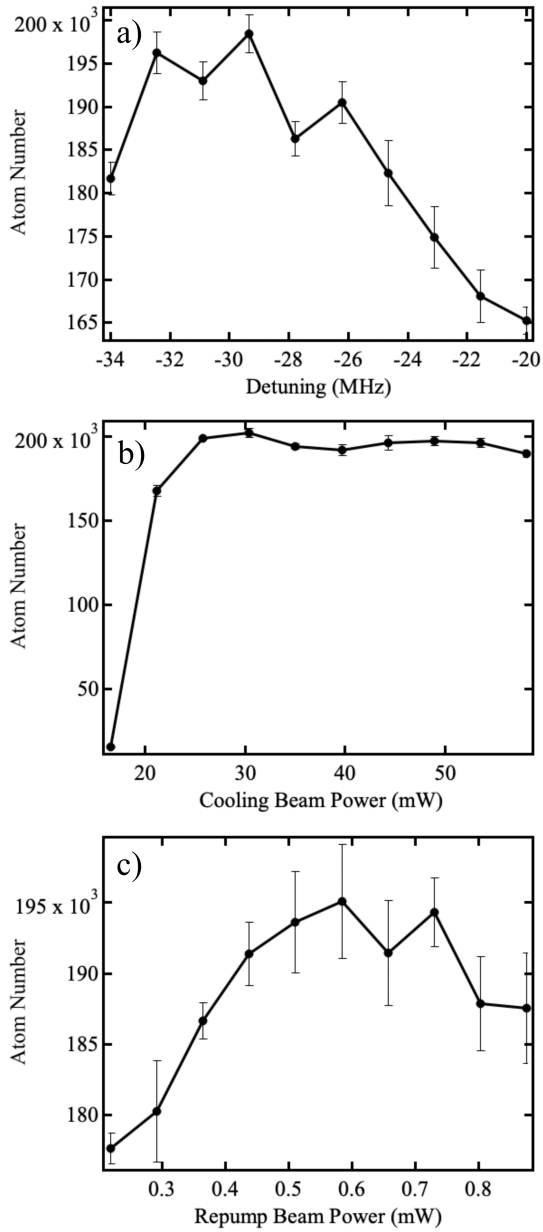

Figure 6.6: Atom number loaded in the optical dipole trap as a function of (a) the cooling laser detuning from resonance, (b) the cooling laser power, and (c) the repumping laser power. (a) The larger effective detuning reduces the excitation rate of the atoms in the dipole trap and thus reduces light-induced collisions and heat. (b) Atoms are maximum in the ODT when the MOT cooling laser power is about 30 mW. Below this level, the MOT is not sustained. (c) The intensity of the repumping laser is decreased so that the atoms are pumped into the $F = 1$ ground state. The optimum repumping laser beam intensity is $\sim$600 μW.

atom number inside the ODT is highest when the repump power equals ∼600 μW, as presented in Fig. 6.6c. The atom number increases when the repumping beam power decreases because the atoms are optically pumped into the $F = 1$ ground state. However, the atom number decreases when the power of the repumping laser is too low because the optical molasses is not sustained for lower intensities.

We use these atom-loading parameters to empirically find the best polarization gradient cooling scheme for our system to optimize the atom loading number in the trap, presented in Fig. 6.7. This is programmed in the computer control experimental sequence using LabVIEW.

At the end of the optical molasses stage, we turn off the MOT beams using an AOM, followed by the mechanical shutter. Then we linearly ramp up the ODT power to its maximum available value within 5 ms and hold it at constant power ($\sim$ 20 W) for 1.5 seconds to perform free evaporation. The trap depth of the ODT can be calculated according to Eq. (2.14), which is $U_{max} \simeq k_B \times 986\ \mu K$. Due to the tight trap confinement, the density in the optical dipole trap is much higher than the density in the MOT, leading to free evaporation caused by elastic two-body collisions. During free evaporation, the most energetic atoms escape from the dipole trap due to the elastic collision, and the temperature of the trapped atomic gas is reduced via re-thermalization. Figure 6.8a shows the absorption images at the early time of the free evaporation stage where the molasses is still visible on top of the ODT. Figure 6.8b shows ODT the after 1.5 s of free evaporation. After optimization and 1.5 seconds of free evaporation, the total number of atoms in the ODT is about 2.5×10^5.

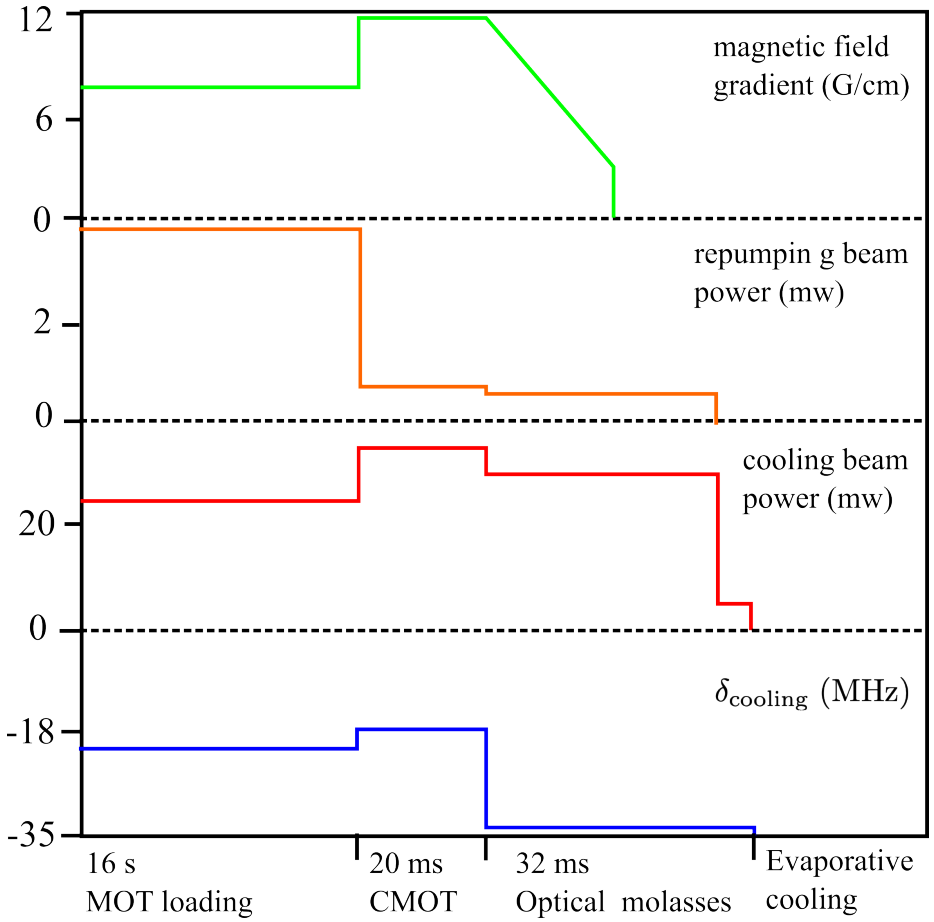

Figure 6.7: Empirically optimized experimental cooling sequence for optical molasses using polarization gradient cooling before evaporative cooling. CMOT stands for the compressed MOT.

6.3 Evaporatively Cooling Atoms

6.3.1 Modelling Evaporation

Frequent elastic collisions between atoms inside the ODT are the key to efficiently performing the evaporative cooling since re-thermalization depends on how often elastic collisions happen. The collision rate is determined by the elastic cross section σ, the density n of the atomic cloud, and the average relative velocity $\sqrt{2}\bar{v}$ of the two

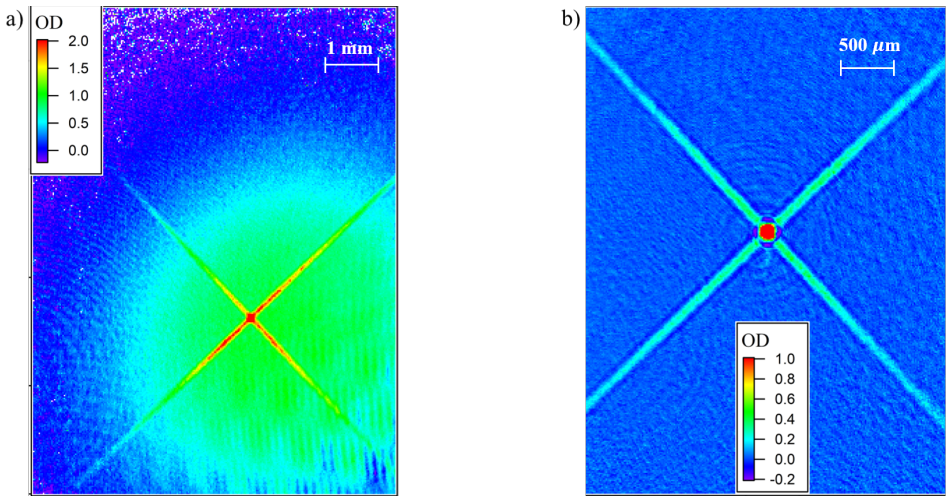

Figure 6.8: False-color absorption images of our ODT. a) A typical top view absorption image of our crossed ODT in the presence of MOT atoms after a short free evaporation time of 10 ms. b) A typical top view absorption image of our crossed ODT after 1.5 s free evaporation. OD stands for optical density. The time-of-flight for a and b are 10 μs.

colliding atoms

$$\Gamma_{el} = n\sigma\sqrt{2}\bar{v}, \tag{6.26}$$

where the elastic cross section is given by $\sigma = 8\pi a$, a is the atom scattering length and $\bar{v}$ is the average thermal velocity which is defined as

$$\bar{v} = \sqrt{\frac{8k_BT}{\pi m}}. \tag{6.27}$$

From this equation, the elastic collision rate depends on the number density n, which is related to the trap frequencies. Therefore, at high densities and high trap frequencies the collision rates are high and allow a faster evaporation ramp. Conversely, at low densities and low trap frequencies the collision rate is low and demands a slower evaporation ramp. This means that the evaporation ramp for atoms in an optical dipole trap should start with a steep slope and flatten out for longer evaporation times.

In our experiment, atoms in the ODT are evaporatively cooled by ramping down the laser power with an AOM with two exponential ramps that optimized empirically. It takes five seconds to complete the forced evaporative cooling and reach BEC. The first exponential ramp has a steep slope with a exponential decay constant $\tau_1 = 0.4$ s, which is only applied for a short time due to the high collision rate. The following ramp has a more moderate decay constant applied for the rest of the time with a time constant $\tau_2 = 0.8$ s. The ramping speed is critical. If the trap depth is ramped down too fast, the atoms do not have enough time to re-thermalize, and the evaporative cooling is not efficient. If the trap depth is ramped down too slowly, inelastic collisions, for example, three-body recombination have time to happen more and more, and evaporative cooling is also inefficient.

6.3.2 Scaling Laws

The dynamics of the phase space density and the atom number in the ODT during the evaporative cooling are determined by scaling laws [113]. It is well known that the evaporation rate of an atomic cloud in a fixed depth ODT decreases as the temperature drops [114]. The cut-off parameter $\eta = \frac{U_{Dip}}{k_B T}$, the ratio of the trap depth and the atom thermal energy, plays an important role in defining the evaporation rate. Usually, $\eta = 10$ is the best condition for evaporation when only elastic collisions are taken into consideration. If $\eta > 10$, the evaporation slows dramatically. On the other hand, if $\eta < 10$, the atoms evaporate out of the trap until η reaches 10 again.

From Ref. [113], scaling laws are derived from the energy loss of the system due to the atom evaporation and adiabatic lowering of the trap depth. With a fixed value $\eta = \frac{U_{Dip}}{k_B T}$, the number of trapped atoms is related to the trap depth as

$$\frac{N}{N_i} = \left(\frac{U}{U_i}\right)^{\frac{3}{2(\eta'-3)}} \tag{6.28}$$

where N_i and U_i are the initial atom number and trap potential, respectively. Here,

$\eta' = \eta + (\eta - 5)/(\eta - 4)$. The phase space density increases during the evaporation and scales with trap potential and atom numbers as

$$\frac{\rho}{\rho_i} = \left(\frac{U}{U_i}\right)^{\frac{3(\eta'-4)}{2(\eta'-3)}} = \left(\frac{N}{N_i}\right)^{\eta'-4}. \tag{6.29}$$

For an energy-independent scattering cross section, the elastic collision rate scales with the trap depth as

$$\frac{\gamma}{\gamma_i} = \left(\frac{U}{U_i}\right)^{\frac{\eta'}{2(\eta'-3)}}, \tag{6.30}$$

and the evaporation rate is given by the s-wave Boltzmann equation [114]:

$$\dot{N} = -2(\eta - 4)e^{-\eta}\gamma N. \tag{6.31}$$

Eventually, the time-dependent potential depth is obtained by

$$\frac{U}{U_i} = \left(1 + \frac{t}{\tau}\right)^{\frac{-2(\eta'-3)}{\eta'}} \tag{6.32}$$

with the time constant τ given by

$$\frac{1}{\tau} = \frac{2}{3}\eta'(\eta - 4)e^{-\eta}\gamma_i. \tag{6.33}$$

It is worth noting that the scaling laws only take into account the atom loss due to elastic collisions. In a real experiment, the atom loss due to background gas collisions, inelastic collisions, and gravity should also be taken into consideration. Therefore, the simulation curve from Eq. (6.32) can only be used as a starting point in the experiment. For the actual evaporation curve used experimentally, the time constant of each ramp is determined empirically by measuring the atom number and the temperature of the atoms at the end of each ramp. The optimum duration of the ramp is determined by obtaining the most atoms for a given final laser power. The final laser power determines the final temperature of the atoms that can be reached, and is chosen such that the final temperature is well below T_c.

6.3.3 Experimental Realization

Figure 6.9 shows our optimized experimental sequence for evaporative cooling. The dipole trap laser is tuned on during the MOT loading phase and the optical molasses phase. After 1.5 seconds of free evaporation, the forced evaporative cooling takes place by exponentially lowering the trap depth U_{dip}. This is realized by lowering the trapping laser power through a PI control loop. The evaporative cooling curve generated from the function generator (Agilent 33521A) has a sample rate of 1000 Hz, meaning 5000 laser power steps are stepped through during the 5 seconds for forced evaporative cooling. The laser power is lowered down smoothly adiabatically. We notice that, as the trap depth is reduced and the laser power is low at the end of the evaporative cooling, gravity starts to play an important role. Due to gravity, the trap can no longer hold the atoms when the laser power is very low. We found that the cut-off laser power is close to 100 mW in our experiment.

6.4 BEC Detection and Imaging Analysis

6.4.1 Imaging System for BEC

Imaging the BEC provides the density distributions of the atomic cloud from which we can obtain information such as the atom number, the density distribution, and, with the Stern-Gerlach TOF technique, the spin population. The two most popular techniques for observing BEC are in-situ and time-of-flight imaging. The in-situ imaging technique is often applied to image the atomic cloud in a trap or in the early phase of ballistic expansion. For in-situ images, dispersive imaging, such as phase-contrast imaging, is often used to image a dense cloud. The "non-destructive" feature of the dispersive imaging comes from the low heat generation since the light is off-resonant. Dispersive imaging can be used to take a real-time movie without

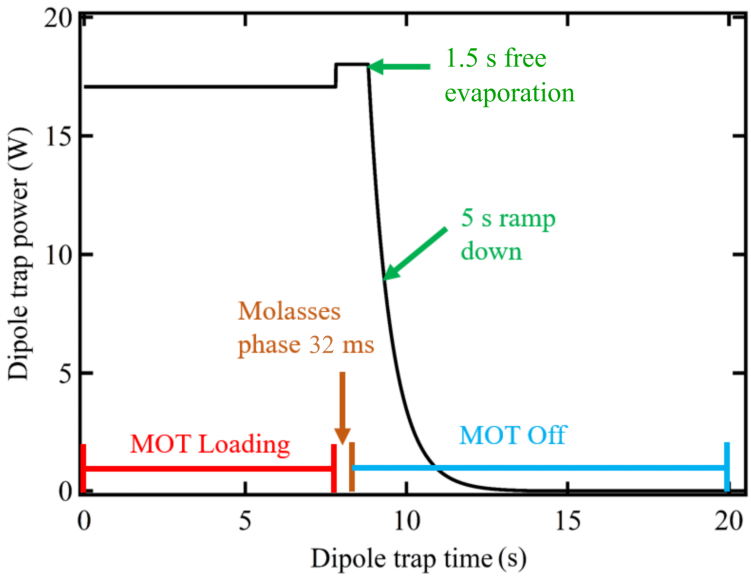

Figure 6.9: Optimized ODT ramping sequences in the experiment. The ODT is kept at a relatively small trap depth during the laser cooling process. It is then linearly ramped to U_{max} within 5 ms. After 1.5 s of free evaporation, it is exponentially ramped down during 5 s, as depicted.

destroying the BEC. Absorption imaging, as discussed in chapter four, uses near-resonant light to illuminate an atomic cloud and image the shadow cast by the atoms onto a CCD camera. Absorption imaging can be applied after time-of-flight imaging with sufficiently long expansion times so that the resonant optical density has dropped to values around unity.

Bose-Einstein condensation is experimentally observed in our lab by taking absorption images after a few milliseconds of time-of-flight after the trap is switched off. After a sudden switching off of the trap, the quantum kinetic energy and interaction energy are then rapidly converted into kinetic energy of motion. Then the atoms expand at a constant velocity when they leave the trap. We usually wait for more than 10 ms of time-of-flight before we take the absorption images so that the atomic cloud has enough time to expand so that the optical density becomes low and the cloud can be

imaged with high spatial resolution. The absorption imaging beam is $\sigma-$polarized, and is tuned to drive the optical dipole transition $|F = 2, m = -2\rangle \rightarrow |F' = 3, m = -3\rangle$ for 30 μs of exposure time. An optical pumping beam is turned on simultaneously with the imaging beam to optically pump the atoms from $|F = 1\rangle$ to $|F = 2, m = -2\rangle$ during the exposure. Atoms trapped in different sublevels of the $F = 1$ ground state are pumped into the same excited state for imaging withing a few μs, allowing easy comparison of relative atom numbers without correcting for different transition matrix elements [1].

For most of our experiments, we use the absorption images to show the spatial structure of different magnetic sublevel components separately, which requires us to spatially separate the spin components after the trap is switched off and before the absorption images are taken. Turning on a magnetic field gradient will apply a force to spin components with $m_F \neq 0$ and deflect their trajectories during the expansion. The phenomenon is known as the Stern-Gerlach effect. In our experiment, we turn on the magnetic field gradient to generate a Stern-Gerlach pulse for 9 ms after switching off the trap. The distance between each spin component after the Stern-Gerlach pulse is about 200 μm which allows us to have a clear separation between each spin component in a single image.

6.4.2 Detecting Bose-Einstein Condensation

At the end of the forced evaporative cooling, the trap depth becomes shallow, the temperature is low, and the collision rate is low. This leads to a slow-down of rethermalization, and evaporative cooling eventually stops. The Bose gas undergoes a phase transition and forms a Bose-Einstein condensate. The indicator of a trapped Bose-Einstein condensate is the appearance of a sharp peak in momentum space. After TOF expansion, this peak in momentum space is mapped to a sharp peak in position

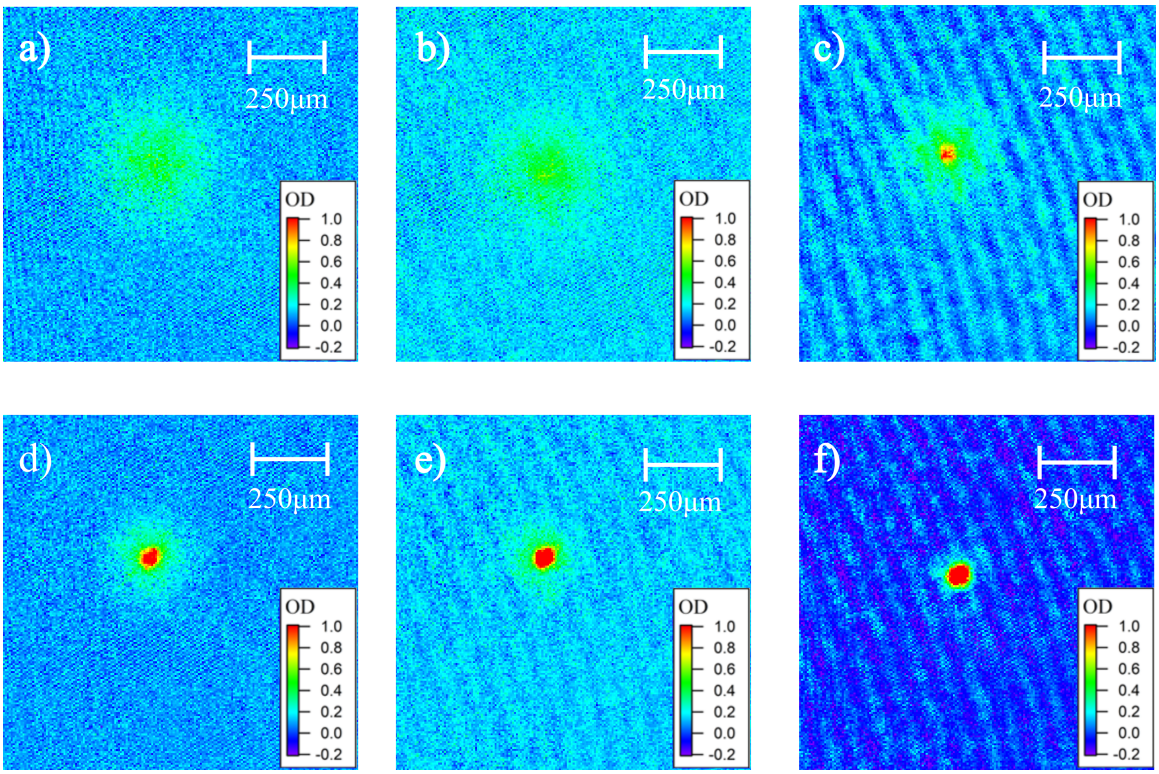

Figure 6.10: Absorption images are taken after interrupting an optimized evaporation curve at various laser powers, followed by a 10 ms time-of-flight. Figure a) to f) show the evaporation curve interrupted at the laser power of 281.2 mW, 233.7 mW, 197.6 mW, 178.6 mW, 142.5 mW, and 125.4 mW, respectively. OD stands for optical density. There is no indicate of condensates in figure a) and b). The condensate atoms appear as a sharp density peak in the images c), d), e), and f) as the condensate fraction increases. Finally, we have an almost pure BEC in image f).

space, visible in the TOF absorption images. To observe how a BEC is formed, we took several absorption pictures of the condensate fraction after interrupting the evaporation curve at various trap potentials, then atoms are released from the trap and undergo a 10 ms of time-of-flight. The thermal cloud and the condensate are shown in Fig. 6.10.

When the evaporative cooling is interrupted at a high trapping potential, which

corresponds to high laser power, as shown in Fig. 6.10a, the atomic cloud is a thermal Bose gas with no fraction of BEC. When the trap is switched off, atoms expand quickly. As the trap depth gets more shallow, the atomic cloud's temperature becomes lower and lower. The phase transition to BEC happens when the temperature of the atomic cloud reaches a critical temperature, and the thermal gas starts to condense to the lowest energy of the system and form a Bose-Einstein condensate. The phase transition is shown in Fig. 6.10c, with a sharp peak appearing at the center of the thermal gas. Continuing evaporative cooling leads to $T < T_c$, in Fig. 6.10f, almost all the thermal gas has undergone a phase transition and forms an almost pure BEC.

6.4.3 Characterizing Bose-Einstein Condensation

The false-color absorption imaging method provides a two-dimensional picture of a column optical density and contains information on the spatial distribution of the atomic cloud. When above the critical temperature, the density distribution in the thermal cloud follows the classical Gaussian distribution of a trapped thermal gas following Boltzmann statistics

$$n_{th}(x,y) = n_{th}(x_0,y_0)e^{-\frac{(x-x_0)^2}{2\sigma_x^2}-\frac{(y-y_0)^2}{2\sigma_y^2}}, \tag{6.34}$$

where σ_x and σ_y are the standard deviation of the Gaussian atomic density distribution in the x and y direction, respectively. If the temperature is close to or below the critical temperature, the density distribution becomes predominantly the Bose distribution and can be described by the Bose-enhanced Gaussian function [1]

$$\tilde{n}_{th}(x,y) = \frac{n_{th}(x_0,y_0)}{g_2(1)} g_2\left(e^{-\frac{(x-x_0)^2}{2\sigma_x^2}-\frac{(y-y_0)^2}{2\sigma_y^2}}\right), \tag{6.35}$$

where $g_2(x) = \sum_{n=1}^{\infty} x^n/n^2$. The density distribution of the thermal gas then becomes a classical Boltzmann distribution (Eq. 6.34). On the other hand, the density of the BEC fraction in the Thomas-Fermi regime takes the shape of an inverted parabolic

density distribution

$$n_{TF}(x,y) = n_{TF}(x_0,y_0) max\left\{0, \left(1 - \frac{(x-x_0)^2}{R_x^2} - \frac{(y-y_0)^2}{R_y^2}\right)^{3/2}\right\}, \tag{6.36}$$

where R_x and R_y are the Thomas-Fermi radii of the BEC in the x and y direction, respectively.

Figure 6.11 shows false-color absorption images of our atomic cloud taken after interrupting the optimized evaporation curve at several different times close to the end of forming a BEC. The images are taken by the side camera. The images show the coexistence of the condensate cloud and the thermal gas, with a bimodal feature in the density distribution, which can be described by summing up Eq. (6.35) and Eq. (6.36). The data points in Fig. 6.11 are obtained from the one-dimensional dashed line of the column optical density data. After fitting the density distribution with the bimodal function, the density of the BEC (n_{TF}) and the density of the thermal gas (n_{th}) can be obtained. Thus, the condensate fraction (CF) can be determined as $CF = n_{TF}/(n_{TF} + n_{th})$.

The temperature is determined by measuring the width of the thermal cloud at a different time during the time of flight, and the temperature can be determined by

$$T = \frac{m}{k_B}\frac{\omega_1^2 - \omega_2^2}{t_1^2 - t_2^2}, \tag{6.37}$$

where ω_1 and ω_2 are the $1/e^2$ radii of the thermal cloud at different times t_1 and t_2 during the time-of-flight.

Another important physical quantity is the trap frequency, which defines, in the absence of interactions, the potential energy of the BEC in a trap. The trap frequency depends on the trap laser power and the trap geometry. The crossed optical dipole trap used in our lab has a larger trap frequency in the axial direction but a smaller trap frequency in the radial direction, which gives an approximately axial symmetry. In our setup, we measure the trap frequency by applying a force to kick the atoms in the trap

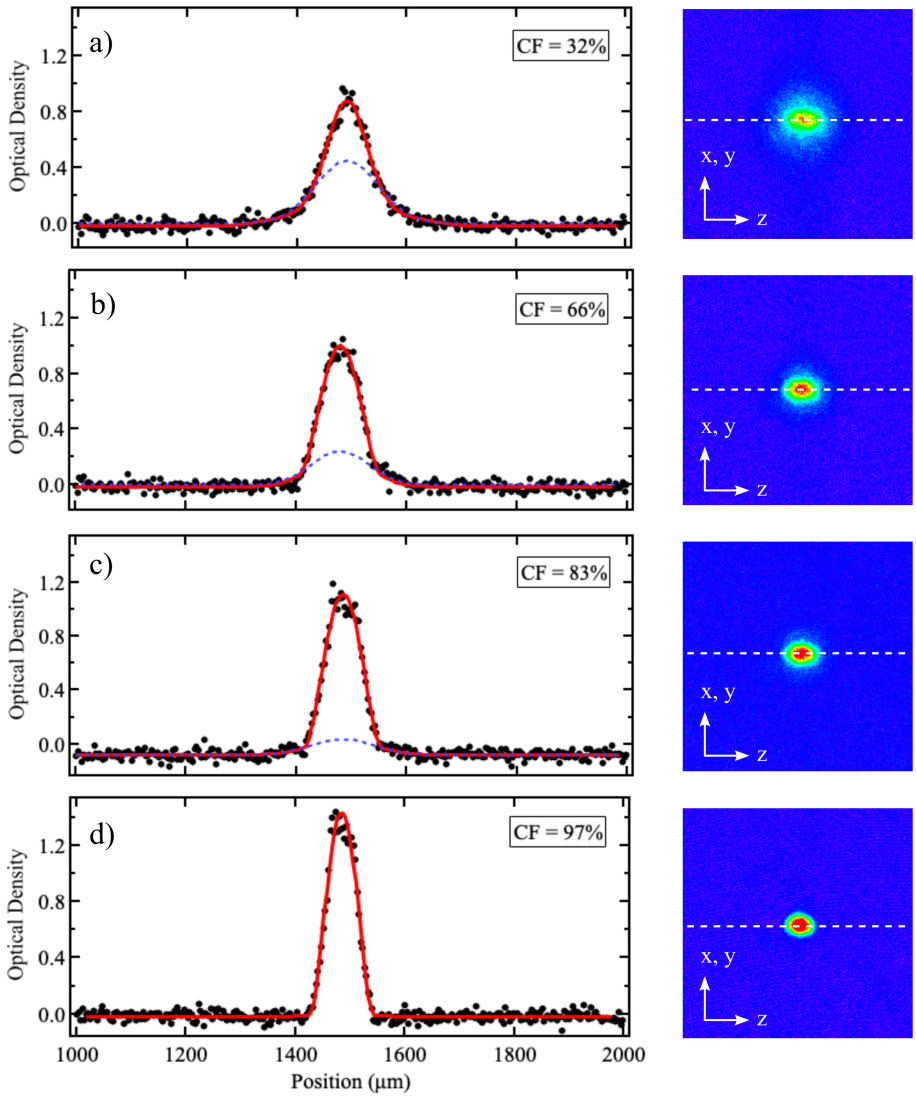

Figure 6.11: (Right) False-color absorption images of the atomic cloud are taken after interrupting an optimized evaporation curve at 4 s, 4.5 s, 4.7 s, and 5 s. The z direction is aligned with gravity. (Left) Column optical density data along the dashed lines on the right side pictures. The red solid curve is the revert of the bimodal fit, and the blue dashed curve is the classical Boltzmann distribution specifically showing only the thermal gas. The condensate fraction (CF) can be determined as $CF = n_{TF}/(n_{TF}+n_{th})$. The CF is about 32% when the evaporation time is 4 s and increases to about 97% when the evaporation time is 5 s.

so that they can slosh back and forth near the bottom of the trap. Therefore, the trap frequency can be calculated by measuring the center-of-mass position as a function of time. Since the ODT potential is only approximated well by a harmonic trap near the center, the kick should be small to minimize anharmonicities. In the axial direction, we kick the atoms using gravity by releasing them from the trap for $\sim$50 μs and recapturing them. Then, we use the side camera to record the center-of-mass position as a function of time. To measure the trap frequency in the radial direction, we first prepare atoms in the $|F = 1, m = -1\rangle$ state, and apply a weak and short magnetic field gradient pulse to kick the atoms in the trap. We then record the center-of-mass position in the x and y directions as a function of time with the top-down imaging system.

Figure 6.12 depicts the measured center-of-mass position of atoms in the trap as a function of the holding time after the displacement from the center. A sine wave is used to fit the measured data points. The trap frequency can be extracted from the sine function. We record the center-of-mass position for times up to 80 ms. For early time, the data agree well with the sine wave fit. However, large discrepancies appear between the data and the fitting curve after 60 ms, which might be due to the vibrational noise from the optical breadboard used for holding the dipole trap optics. In our new lab in Lin Hall, we will replace the old breadboard with a 60 mm thick honeycomb optical breadboard, which has a better ability to dissipate energy from induced vibrations. The trap frequency measurement results are $\omega_z = 2\pi \times 275.3$ Hz, $\omega_x = 2\pi \times 127.3$ Hz, and $\omega_y = 2\pi \times 138.5$ Hz.

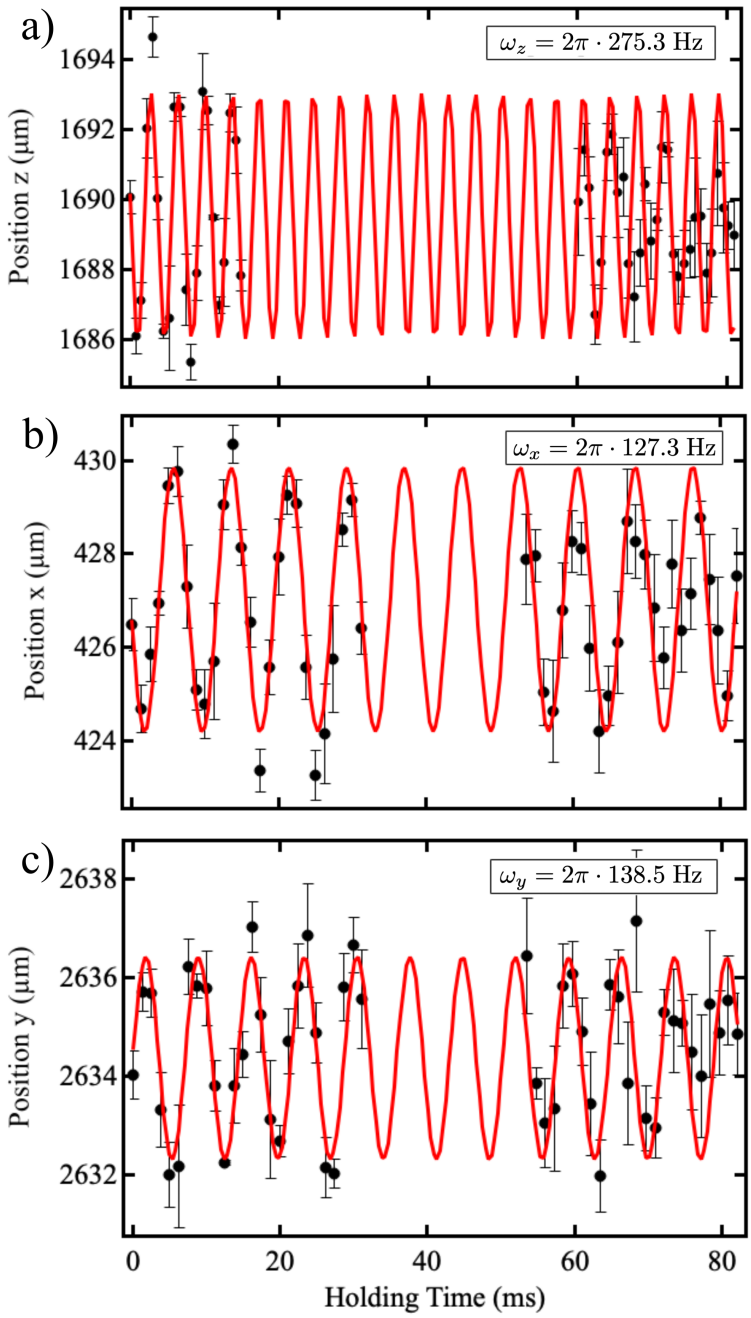

Figure 6.12: (a) to (c) are trap frequencies measured along the x, y, and z directions, respectively. Here, z is the vertical (axial ODT) direction aligned with gravity. We use a gravity kick method to excite motion of the trap frequency in the z direction and a Stern-Gerlach pulse kick method to excite the motion of the trap frequency in the x and y directions. The black dots are the measured data, and the red curve is the sine-wave fit. The fit gives trap frequencies of $\omega_z = 2\pi \times 275.3$ Hz, $\omega_x = 2\pi \times 127.3$ Hz, and $\omega_y = 2\pi \times 138.5$ Hz.

Chapter 7

Spinor Bose-Einstein Condensate

The first Bose-Einstein condensate was generated with a magnetic trap, in which only one magnetic sub-level was trapped. The atom's internal degrees of freedom were therefore frozen. This type of BEC is known as scalar BEC. On the other hand, BECs trapped in an optical trap where all magnetic sublevels are trapped simultaneously, are called spinor BEC. The spin degree of freedom is liberated.

The study of spin-exchange collisions is an active research frontier because the collisions generate correlated quantum states, including squeezed and entangled states, which have a wide range of important applications in matter-wave quantum optics because they can be controlled precisely by microwave dressing. The spin-exchange collisions amplify vacuum fluctuations in the initial states [115] and create exotic quantum many-body spin states such as spin-nematic squeezed states [116], two-mode spin squeezing [117] and non-Gaussian spin-squeezed states [118]. In addition to providing a new tool to study fundamental principles of many-body quantum mechanics [119], spinor BECs have applications in quantum metrology, quantum information processing, and many other fields. For example, high-resolution magnetometry and interferometry have been realized with sensitivities close to or below the standard quantum limit (SQL) that fundamentally limits the precision of measurements for uncorrelated atoms [120, 121]. In our experiment, we use spinor BECs with total angular momentum $F = 1$. The coherent spin dynamics are driven by spin-exchange collisions, which cause characteristic population oscillations between the $m = 0$ and $m = \pm 1$ states, and can generate entanglement between atom pairs in $m = \pm 1$ states [122].

In this chapter, we present our study of $F = 1$ sodium spinor BECs. Specifically,

we focus on the coherent spin population oscillation between magnetic sublevels in the mean-field picture. Section one presents the theory of the spin-1 system's dynamics in the mean-field ground state. Section two shows the experimental procedures to realize the $F = 1$ spin mixing dynamics. In this experiment the initial state is prepared in the $m = 1$, $m = 0$, and $m = -1$ data population fractions states with $\rho_{-1} = 0.25$, $\rho_0 = 0.5$, and $\rho_{+1} = 0.25$, respectively. Section three presents data and analysis of the spin mixing dynamics data within the single-mode approximation (SMA), and beyond the SMA.

7.1 Theoretical Model of Spin Interaction

7.1.1 Hamiltonian in the Mean-field Picture

The Hamiltonian of the general spin-F Boson gas is similar to the Hamiltonian of the spinless Boson (Eq. 6.11), which consists of two parts: a single-particle term and an interaction term. In second-quantized notation, the single-particle Hamiltonian can be described as [123]

$$\hat{H}_0 = \int d\mathbf{r} \sum_{m,m'=-F}^{F} \left\{ \hat{\Psi}_m^\dagger(\mathbf{r}) \left(-\frac{\hbar^2\nabla^2}{2M} + U_{trap}(\mathbf{r}) + \hat{V}_{ext} \right) \hat{\Psi}_{m'}(\mathbf{r}) \right\}, \tag{7.1}$$

where $U_{trap}(\mathbf{r})$ is a harmonic trap potential defined as $U_{trap}(\mathbf{r}) = \frac{1}{2}m(w_x^2x^2 + w_y^2y^2 + w_z^2z^2)$, and w_x, w_y and w_z are trap frequencies in the x, y and z directions of the trap. $\hat{\Psi}_m^\dagger(\mathbf{r})$ and $\hat{\Psi}_{m'}(\mathbf{r})$ are bosonic field operators that create and annihilate a particle at position $\mathbf{r}$. Different from the spinless case, the spinor Bose gas has internal degrees of freedom represented with indices m, m' corresponding to the magnetic sublevels of spin F. $\hat{V}_{ext}$ is the external field. In our experiment, a homogeneous magnetic field and a microwave field are the two main sources that contribute to $\hat{V}_{ext}$ in which the homogeneous magnetic field defines the quantization direction, so $\hat{V}_{ext}$ can be written

as

$$\left(\hat{V}_{ext}\right)_{mm'} = -p(\hat{F}_z)_{mm'} + q(\hat{F}_z^2)_{mm'}. \tag{7.2}$$

The first term corresponds to the linear Zeeman shift, $p = g\mu_B B_z$, where g is the Landé hyperfine g-factor and μ_B is the Bohr magneton. The second term corresponds to the effective quadratic Zeeman shift. The coefficient $q = q_B + q_{MW}$ has contributions from the external magnetic field, q_B, and the microwave field, q_{MW}. The former is calculated by using second-order perturbation theory as

$$q_B = \frac{(g\mu_B B_z)^2}{\Delta E_{hf}}, \tag{7.3}$$

where ΔE_{hf} is the hyperfine energy splitting. q_{MW} is derived in chapter five, Eq. (5.13). $\hat{F}_z$ is the spin matrix along z component, whose element is given by $(\hat{F}_z)_{mm'}$.

The interaction part of the Hamiltonian in second quantization can be written generally as

$$\hat{H}_I = \int d\mathbf{r}_1 \int d\mathbf{r}_2 \sum_{ij,kl} \hat{\Psi}_i^\dagger(\mathbf{r}_1)\hat{\Psi}_j^\dagger(\mathbf{r}_2)V(\mathbf{r}_1 - \mathbf{r}_2)\hat{\Psi}_k(\mathbf{r}_2)\hat{\Psi}_l(\mathbf{r}_1), \tag{7.4}$$

where $V(\mathbf{r}_1 - \mathbf{r}_2)$ is the potential describing the interatomic interaction. Usually, the many-body interaction problem is difficult. Here, we make several approximations to simplify the problem. First, we neglect the long-range interaction, such as dipole-dipole interaction, since it is a thousand times smaller than the short-range interaction in alkali atoms. Second, BECs are cold and dilute, so we assume that there are only binary collisions and the incident collision energy is so low that only the lowest-order incident partial waves contribute, and the other partial waves can be ignored. This means we only consider s-wave collisions. Third, we treat the two-body collision among atoms as having rotational symmetry. That is to say, the total angular momentum $f = F_1 + F_2$ is the same before and after the collision. Usually, rotational symmetry is only valid when no external field, such as a magnetic field, is applied. As the magnetic field is increased, the hyperfine spin $F_{1,2}$ are no longer good quantum numbers for describing

the atomic states. Thus collision properties are no longer governed by rotational symmetry. In practice, such influences are rarely completely absent. Nevertheless, this approximation still applies at a low magnetic field where Zeemann shifts are much smaller than the hyperfine splitting. After all those approximations, now the interatomic interaction $V(\mathbf{r}_1 - \mathbf{r}_2)$ is reduced to the form

$$V(\mathbf{r}_1 - \mathbf{r}_2) = \frac{4\pi\hbar^2}{m}\delta(\mathbf{r}_1 - \mathbf{r}_2)\sum_f a_f \hat{P}_f, \tag{7.5}$$

where the index f is the total spin $f = F_1 + F_2$. Due to the symmetry requirements of identical bosons, only the even total spin numbers remain, i.e. $f = 0, 2, ..., 2F$ ($F = F_1 = F_2$). a_f is the scattering length for collisions between atoms with total spin f. $\hat{P}_f$ is the projection operator that projects a pair of atoms into a total hyperfine spin f state. From the completeness relation for two spin-F particles, $\hat{I} = \sum_f \hat{P}_f$, and the composition law of spin operators, we have

$$\hat{F}_1 \cdot \hat{F}_2 = \frac{1}{2}\sum_{f=0}^{F}[f(f+1) - 2F(F+1)], \tag{7.6}$$

where $\hat{I}$ is the identity operator of total spin states. In a Na spinor BEC, the lowest ground state hyperfine level is $F = 1$, and thus total spin f=0 or 2. Therefore, $\hat{I} = \hat{P}_0 + \hat{P}_2$ and $\hat{F}_1 \cdot \hat{F}_2 = \hat{P}_2 - 2\hat{P}_0$ and Eq. 7.5 becomes [124]

$$V(\mathbf{r_1} - \mathbf{r_2}) = \delta(\mathbf{r_1} - \mathbf{r_2})(c_0\hat{I} + c_2\hat{F}_1 \cdot \hat{F}_2), \tag{7.7}$$

where

$$c_0 = \frac{4\pi\hbar^2}{m}\frac{a_0 + 2a_2}{3}, \qquad c_2 = \frac{4\pi\hbar^2}{m}\frac{a_2 - a_0}{3}. \tag{7.8}$$

Therefore, the interaction part of the Hamiltonian $\hat{H}_I$ is

$$\hat{H}_I = \int d\mathbf{r}\, \frac{1}{2}\sum_{ijkl}\{c_0\hat{\Psi}_i^\dagger(\mathbf{r})\hat{\Psi}_j^\dagger(\mathbf{r})\hat{\Psi}_k(\mathbf{r})\hat{\Psi}_l(\mathbf{r}) + c_2\big(\hat{\Psi}_i^\dagger(\mathbf{r})(F_v)_{il}\hat{\Psi}_l(\mathbf{r})\big)\cdot\big(\hat{\Psi}_j^\dagger(\mathbf{r})(F_v)_{jk}\hat{\Psi}_k(\mathbf{r})\big)\}, \tag{7.9}$$

where the index v runs over the three coordinates axis x, y and z. In $F = 1$ system, spin matrix F_x, F_y, and F_z can be represented by

$$F_x = \frac{1}{\sqrt{2}} \begin{pmatrix} 0 & 1 & 0 \\ 1 & 0 & 1 \\ 0 & 1 & 0 \end{pmatrix}, \qquad F_y = \frac{i}{\sqrt{2}} \begin{pmatrix} 0 & -1 & 0 \\ 1 & 0 & -1 \\ 0 & 1 & 0 \end{pmatrix}, \qquad F_z = \begin{pmatrix} 1 & 0 & 0 \\ 0 & 0 & 0 \\ 0 & 0 & -1 \end{pmatrix}. \tag{7.10}$$

After applying particle exchange symmetries and gathering similar terms, the interaction part can be written as

$$\begin{aligned} \hat{H}_I = \frac{1}{2} \int d\mathbf{r} [&(c_0 + c_2) \hat{\Psi}_1^\dagger \hat{\Psi}_1^\dagger \hat{\Psi}_1 \hat{\Psi}_1 + c_0 \hat{\Psi}_0^\dagger \hat{\Psi}_0^\dagger \hat{\Psi}_0 \hat{\Psi}_0 + (c_0 + c_2) \hat{\Psi}_{-1}^\dagger \hat{\Psi}_{-1}^\dagger \hat{\Psi}_{-1} \hat{\Psi}_{-1} \\ &+ 2(c_0 + c_2) \hat{\Psi}_{-1}^\dagger \hat{\Psi}_0^\dagger \hat{\Psi}_{-1} \hat{\Psi}_0 + 2(c_0 - c_2) \hat{\Psi}_1^\dagger \hat{\Psi}_{-1}^\dagger \hat{\Psi}_1 \hat{\Psi}_{-1} \\ &+ 2c_2 (\hat{\Psi}_0^\dagger \hat{\Psi}_0^\dagger \hat{\Psi}_1 \hat{\Psi}_{-1} + \hat{\Psi}_1^\dagger \hat{\Psi}_{-1}^\dagger \hat{\Psi}_0 \hat{\Psi}_0)]. \end{aligned} \tag{7.11}$$

The first line shows that atoms are annihilated and created in the same state, which refers to the self-scattering or density-density terms. The terms in the second line are the cross-scattering terms, and the last line describes a pair of atoms annihilated in $m = \pm 1$ states and generated in $m = 0$ state and vice versa, which represents the spin-exchange collision.

The total Hamiltonian $\hat{H} = \hat{H}_0 + \hat{H}_I$ of a spin-1 Bose gas in an external magnetic field can be described as follows

$$\begin{aligned} \hat{H} = \int d\mathbf{r} \Bigg\{ &\sum_{m=-1}^{1} \hat{\Psi}_m^\dagger(\mathbf{r}) \left(-\frac{\hbar^2 \nabla^2}{2m} + U_{trap}(\mathbf{r}) \right) \hat{\Psi}_m(\mathbf{r}) \\ &+ \sum_{mm'=-1}^{1} \hat{\Psi}_m^\dagger(\mathbf{r}) \left(-p(F_z)_{mm'} + q(F_z^2)_{mm'} \right) \hat{\Psi}_{m'}(\mathbf{r}) \Bigg\} \\ &+ \frac{1}{2} \sum_{mm'=-1}^{1} \Big\{ c_0 \hat{\Psi}_m^\dagger(\mathbf{r}) \hat{\Psi}_{m'}^\dagger(\mathbf{r}) \hat{\Psi}_{m'}(\mathbf{r}) \hat{\Psi}_m(\mathbf{r}) \\ &+ c_2 \left(\hat{\Psi}_m^\dagger(\mathbf{r}) (F_v)_{mm'} \hat{\Psi}_{m'}(\mathbf{r}) \right) \cdot \left(\hat{\Psi}_m^\dagger(\mathbf{r}) (F_v)_{mm'} \hat{\Psi}_{m'}(\mathbf{r}) \right) \Big\}. \end{aligned} \tag{7.12}$$

In our calculations for ultracold sodium prepared in the $F = 1$ manifold, we use the

most recent determined values of $a_0 = 48.91\ a_B$ and $a_2 = 54.54\ a_B$ from Ref. [125], where a_B is the Bohr radius.

7.1.2 Spin Dynamics in the $F = 1$ Ground State

The ground state of the system can be directly calculated from the Hamiltonian. However, the calculation can be heavy and even impracticable for systems with large values of N. Mean-field theory can be used to overcome the problem of solving exactly the full many-body Schrödinger equation and is usually obtained by replacing field operators with their expectation values $\Phi_m(\mathbf{r}) = \left\langle \hat{\Psi}_m(\mathbf{r}) \right\rangle$ when the total number of condensed atoms N is large, and the occupation numbers of each magnetic sub-level are also large. Using the mean-field approximation, we can evaluate the expectation value of the Hamiltonian $\hat{H}$

$$E(\Phi) = \left\langle \hat{H} \right\rangle = \int d\mathbf{r} \left\{ \sum_m \Phi_m^* \left[\frac{\hbar^2 \nabla^2}{2m} + U_{trap}(\mathbf{r}) - p\, m + q\, m^2 \right] \Phi_m + \frac{c_0}{2} n^2 + \frac{c_2}{2} \left\langle F \right\rangle^2 \right\}, \tag{7.13}$$

where $m = (-1, 0, +1)$, $n = \sum_m |\Phi_m|^2$, and $\left\langle F \right\rangle = \sum_{m,m'} \Phi_m^* (F_v)_{mm'} \Phi_{m'}$. Then the mean energy of the spin-dependent Hamiltonian is just

$$E_{spin} = \int d\mathbf{r} \ \left\{ -p\, n\, m + q\, n\, m^2 + \frac{c_2}{2} \left\langle F \right\rangle^2 \right\}. \tag{7.14}$$

In the absence of the external magnetic field, where the Zeeman terms $p = q = 0$, the $F = 1$ BECs can be divided into two categories depending on the sign of the spin-dependent interaction parameter c_2.

- For $c_2 > 0$, like sodium, the spinor gas tends to lower its energy by minimizing its average spin, $\left\langle F \right\rangle^2 = 0$. This interaction type is denoted as "antiferromagnetic", and the ground state spinor is either a polar state (0,1,0), or antiferromagnetic state $1/\sqrt{2}(1,0,1)$.

- For $c_2 < 0$, like rubidium, the condensates tend to lower their energy by maximizing their average spin. That is to say, by making $\langle F \rangle^2 = 1$ in $F = 1$ spinor gas. This interaction type is known as "ferromagnetic", and the ground state spinor can be either (1,0,0) or (0,0,1).

Similar to the spinless case discussed in chapter six, the time evolution of the spinor gas in the mean-field picture is governed by the Gross-Pitaevskii (GP) equations which can be obtained by a variational procedure [123]

$$i\hbar\frac{\partial\Phi_m}{\partial t} = \frac{\delta E}{\delta\Phi_m^*}. \tag{7.15}$$

In a spin-1 system, the GP equation contains multiple components due to the internal degrees of freedom, and becomes [123]

$$i\hbar\frac{\partial\Phi_m}{\partial t} = \left(-\frac{\hbar^2\nabla^2}{2M} + U_{trap}(\mathbf{r}) - p\,m + q\,m^2\right)\Phi_m + c_0\,n\,\Phi_m + c_2\sum_{m'=-1}^{1}\langle F\rangle\ F_{mm'}\Phi_{m'}, \tag{7.16}$$

where m takes values -1, 0, and 1. In a stationary state $\Phi_m(\mathbf{r},t) = \Phi_m(\mathbf{r})e^{-i\mu t}$ can be substituded into Eq. (7.16), where μ is the chemical potential, obtaining,

$$\left(-\frac{\hbar^2\nabla^2}{2M} + U_{trap}(\mathbf{r}) - p\,m + q\,m^2\right)\Phi_m + c_0\,n\,\Phi_m + c_2\sum_{m'=-1}^{1}\langle F\rangle\ F_{mm'}\Phi_{m'} = \mu\Phi_m. \tag{7.17}$$

Writing down the three components $m = 1,\ 0,\ -1$ explicitly, we obtain

$$\left(-\frac{\hbar^2\nabla^2}{2M} + U_{trap}(\mathbf{r}) - p + q + c_0n + c_2F_z - \mu\right)\Phi_1 + \frac{c_2}{\sqrt{2}}F_-\Phi_0 = 0, \tag{7.18a}$$

$$\left(-\frac{\hbar^2\nabla^2}{2M} + U_{trap}(\mathbf{r}) + c_0n - \mu\right)\Phi_0 + \frac{c_2}{\sqrt{2}}(F_-\Phi_{-1} + F_+\Phi_1) = 0, \tag{7.18b}$$

$$\left(-\frac{\hbar^2\nabla^2}{2M} + U_{trap}(\mathbf{r}) + p + q + c_0n - c_2F_z - \mu\right)\Phi_{-1} + \frac{c_2}{\sqrt{2}}F_+\Phi_0 = 0, \tag{7.18c}$$

where $F_\pm = F_x \pm iF_y$. The wavefunction of each spin component Φ_0, Φ_{-1}, and Φ_1 can be obtained by solving these three equations. Since the spin and spatial terms in these

wavefunctions are coupled, we refer to them as coupled Gross-Pitaevskii equations. In the next section, we will discuss the spinor wavefunction under the single-mode approximation, where the spin and spatial degrees of freedom are decoupled.

7.1.3 Single-mode Approximation

Since the Thomas-Fermi radius of our system is smaller than the spin healing length, $\xi_s = 2\pi\hbar/\sqrt{2m|c_2|n}$ [126], spin domain formation is energetically suppressed. Thus we can use the single-mode approximation (SMA) to simplify our model even further. According to the SMA, all spin components are assumed to share the same spatial dependence, and only the spin components vary in time, and thus the wave function can be written as

$$\Phi(\mathbf{r}, t) = \sqrt{N}\zeta_m(t)\Phi_{SMA}(\mathbf{r})e^{-i\mu t}, \tag{7.19}$$

where $\zeta_m(t)$ is the space-independent spinor, and μ is the chemical potential. In addition, since the sodium spinor gas has a spin-dependent interaction term $\propto |c_2|$ much weaker than the spin-independent interaction $\propto |c_0|$, we can treat the spin-dependent term as the perturbation term to the spin-independent term. Therefore the spatial wave function $\Phi_{SMA}(\mathbf{r})$ can be determined from the spin-independent term of Eq. (7.17) alone

$$\left(-\frac{\hbar^2\nabla^2}{2M} + U_{trap}(\mathbf{r}) + c_0 N|\Phi_{SMA}(\mathbf{r})|^2\right)\Phi_{SMA}(\mathbf{r}) = \mu\Phi_{SMA}(\mathbf{r}). \tag{7.20}$$

Substituting $\Phi(\mathbf{r}, t)$ into Eq. (7.16), we obtain the equation of motion of $\zeta_m(t)$

$$i\hbar\dot{\zeta_1} = (-p+q))\zeta_1 + c[(\rho_1 + \rho_0 - \rho_{-1})\zeta_1 + \zeta_0^2\zeta_{-1}^*], \tag{7.21a}$$

$$i\hbar\dot{\zeta_{-1}} = (p+q))\zeta_{-1} + c[(\rho_{-1} + \rho_0 - \rho_1)\zeta_{-1} + \zeta_0^2\zeta_1^*], \tag{7.21b}$$

$$i\hbar\dot{\zeta_0} = c[(\rho_1 + \rho_{-1})\zeta_0 + 2\zeta_1\zeta_{-1}\zeta_0^*], \tag{7.21c}$$

where $c = c_2 N \int d\mathbf{r}|\Phi(\mathbf{r})|^4 = c_2\bar{n}$ is the spin-dependent interaction energy, $\bar{n}$ is the spin density, and $\rho_i = |\zeta_i|^2$ is the fractional population of i-th spin state. The equation should also obey the normalization condition $\sum_i \rho_i = 1$, and atomic magnetization should also be conserved, $\rho_1 - \rho_{-1}$ is a constant. We further eliminate the p dependence by writing ζ_m as

$$\zeta_i = \sqrt{\rho_i} e^{i\theta_i} e^{ipmt/\hbar}. \tag{7.22}$$

We identify ρ_i as the mean fractional population and θ_i as the mean quantum mechanical phase of the i-th magnetic sublevel. Then, after some algebraic manipulation, we obtain the following equations of motion for the fractional $m = 0$ population, ρ_0, and spinor phase, $\theta \equiv \theta_1 + \theta_{-1} - 2\theta_0$,

$$\begin{aligned} \dot{\rho_0} &= \frac{2c}{\hbar}\rho_0\sqrt{(1-\rho_0)^2 - m^2}\sin\theta \\ \dot{\theta} &= -\frac{2q}{\hbar} + \frac{2c}{\hbar}(1-2\rho_0) + \frac{2c}{\hbar}\frac{(1-\rho_0)(1-2\rho_0) - m^2}{\sqrt{(1-\rho_0)^2 - m^2}}\cos\theta. \end{aligned} \tag{7.23}$$

The above two coupled equations give rise to the classical dynamics of a nonrigid momentum-shortened pendulum, with classical energy

$$E = q\,(1-\rho_0) + c\rho_0\left[(1-\rho_0) + \sqrt{(1-\rho_0))^2 - m^2}\cos(\theta)\right]. \tag{7.24}$$

It is noted that Eq. (7.24) can also be derived from $\dot{\rho_0} = -(2/\hbar)\partial E/\partial\theta$ and $\dot{\theta} = (2/\hbar)\partial E/\partial\rho_0$. This function describes the spin-dependent energy for a spin-1 spinor gas in a semi-classical approximation. The energy E is conserved and the system traces a constant-energy contour in phase space under such dynamics. Figure 7.1 shows spinor energy contours, for both a ferromagnetic condensate (Fig. 7.1a) and an anti-ferromagnetic condensate (Fig. 7.1b) in phase space (θ, ρ_0) with different effective quadratic Zeeman shifts q. When we start from the same initial state, say $(\theta = 0, \rho_0 = 0.5)$, the trajectory changes depending on the value of $q/|c|$. For example, when $q/|c| \geq 2$, the trajectory of the system is in the running-phase region where the spinor phase keeps accumulating. For $q/|c| \leq 1$, the trajectory is in the periodic-phase

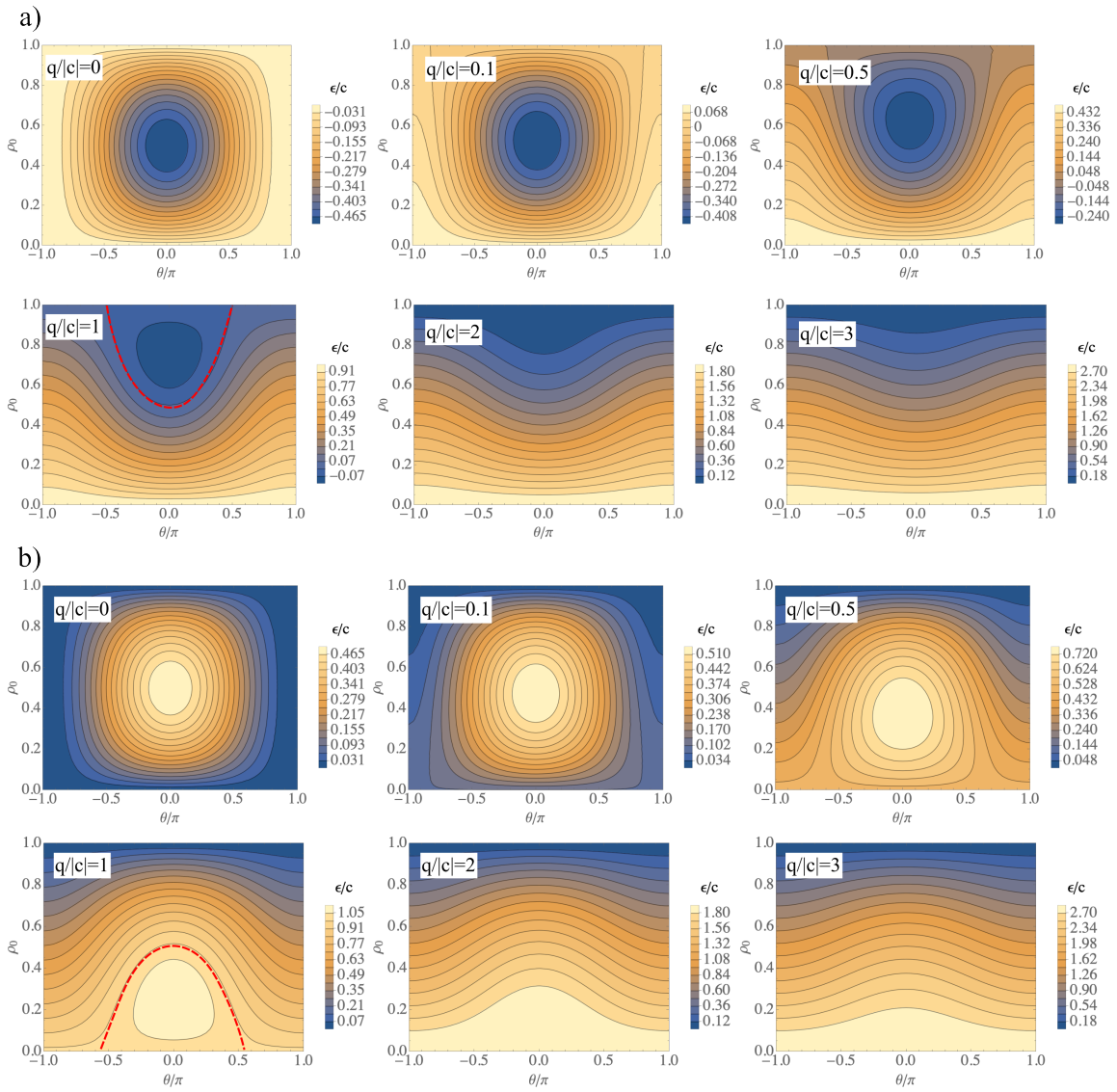

Figure 7.1: Mean-field energy contours in phase space for a ferromagnetic condensate (a) and an anti-ferromagnetic condensate (b) with magnetization $m = 0$. The color scale shows the energy, which is scaled by c. The low energy region is shaded in blue, and the high energy region is shaded in yellow. For an initial state $(\theta = 0, \rho_0 = 0.5)$, if $q/|c| \leq 1$, the spin evolution of ρ_0 are in the periodic-phase which the oscillations are bounded in the spinor phase θ. If $q/|c| \geq 2$ the spin evolution of ρ_0 is in the running-phase region where the spinor phase keeps accumulating. If $q/|c| = 1$, the spin evolution is on separatrix marked in red dashed lines with an infinite period. The sidebar on the right is the color legend for the dimensionless energy defined as ϵ/c.

region where the oscillation is bounded in spinor phase θ. The region in between the running-phase and the periodic-phase is called separatrix marked in red dashed lines in Fig. 7.1a and Fig. 7.1b [127]. When a system is evolving on the separatrix, the oscillation period becomes infinite. Note that for a ferromagnetic spinor BEC, like rubidium, the hills in phase space become valleys and vice versa because of the different sign of c. The time evolution of the anti-ferromagnetic gas is therefore different than the evolution of the ferromagnetic gas. The nature of the ground state also changes depending on the sign of c.

7.2 Spin-mixing Dynamics in an Anti-ferromagnetic Spin-1 BEC: Experiment

7.2.1 Spin-mixing in $F = 1$ Manifold

One of the salient features of spinor BECs is the spin-mixing dynamics. The population of each spin component can change via the spin exchange collision, whereas the total number of atoms is fixed, according to Eq. (7.11). For instance, in a spin-1 spinor BEC such as sodium, two atoms in the magnetic sublevel $m = 0$ can coherently and reversibly scatter into a pair of atoms in the $m = 1$ and $m = -1$ states, and vice versa creating entanglement in the process, as shown in Fig. 7.2

The cartoon in Fig. 7.3 depicts the spin exchange collision in a pair-energy diagram of a three-level spinor BEC. The linear Zeeman shift does not appear because it cancels out in the pair energy basis. On the other hand, the quadratic Zeeman shift q, which defines the energy gap between the $m = 0$ state and $m = \pm 1$ states, is important. The competition between the spin-interaction term and the quadratic Zeeman term allows for interesting spin-mixing dynamics. In an experiment, changing the spin-interaction energy $c_2\bar{n}$ is difficult, but changing the quadratic Zeeman shift is possible over a large

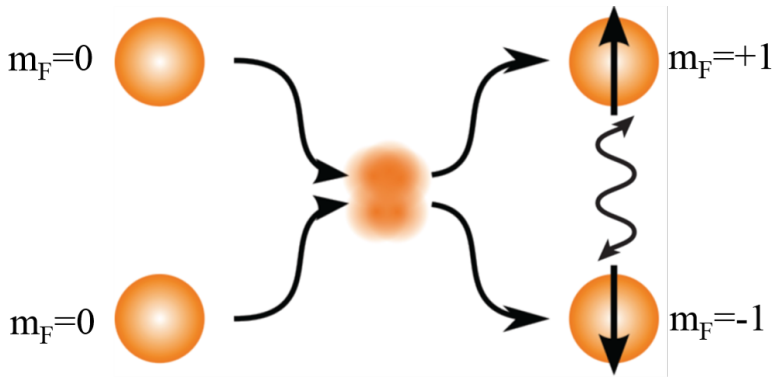

Figure 7.2: Cartoon of a spin-exchange collision in $F = 1$ system. Two atoms in the magnetic sublevel $m = 0$ can coherently and reversibly scatter into a pair of atoms in the $m = 1$ and $m = -1$ states, and vice versa, creating entanglement denoted by the wavy line.

range. As we mentioned in chapter five, the effective quadratic Zeeman shift q in our experiment is controlled in two ways: the external bias magnetic field and the microwave field. This can be described as the following equation

$$q = q_B + q_M = aB^2h + \frac{1}{2}(\Delta E_{m_F=1} + \Delta E_{m_F=-1} - 2\Delta E_{m_F=0}), \qquad (7.25)$$

where $a \approx 277$ Hz/G^2 for $F = 1$ sodium atoms, B is the bias magnetic field in units of Gauss, and ΔE_{m_F} is defined in Eq. (5.12). We can either change q by changing the magnetic field magnitude or the microwave dressing power. However, a fast-changing magnetic field is hard to realize because of the induced eddy currents. In addition, the magnetic field only allows for a positive q value. Microwave dressing is more versatile since q generated by the microwave dressing field can be either positive or negative depending on the sign of microwave detuning Δ. In addition, our microwave generator has an output power range from -30 dBm to 42 dBm, which corresponds to a large range of q. The microwave field's power and frequency can also be switched on/off or changed instantaneously within ns, which is crucial for quenching the system. The microwave envelope waveform can be generated in different forms other than a square

pulse, such as linear ramps or Blackman windows, depending on the experimental requirements.

We control the spin-mixing dynamics by quenching the $m = 0$ energy, as shown in Fig. 7.3. The detuning of the microwave dressing field is set to $\Delta = 75$ kHz blue shift from the $|F = 1, m = 0\rangle$ to $|F = 2, m = 0\rangle$ clock transition. Figure 7.3 (left) shows the energy diagram before the quench: no spin-exchange collision happens because the population transition between $m = 0$ and $m = \pm 1$ is energetically forbidden. After applying the microwave dressing field (Fig. 7.3 right), the $m = 0$ state is quenched close to $m = \pm 1$ states. The value of q depends on the power of the microwave field. Coherent spin population oscillations between $m = 0$ state and $m = \pm 1$ states can now happen after the quench. Their amplitude and period depend on the interplay between the spin-dependent interaction energy c and the effective quadratic Zeeman energy q.

7.2.2 Experimental Procedures

We start the experiment by preparing about 25,000 pure sodium BECs in a crossed-beam optical dipole trap via evaporative cooling. The trapping potential near the minimum is approximately harmonic and approximately axially symmetric. The stronger confinement direction, which is the axial direction, aligns with the direction of gravity.

We apply a bias magnetic field of B $= 429 \pm 2$ mG in the x direction of the lab coordinates (west direction), which approximately corresponds to a 300 kHz linear Zeeman shift and 51 Hz quadratic Zeeman shift of the $F = 1, m = \pm 1$ level. For the spin-mixing dynamics, the linear Zeeman shift is irrelevant since it can be removed on a rotating basis. To prepare the initial state, we start by applying the maximum available current (80 A) to the anti-Helmholtz coils during the last two seconds of

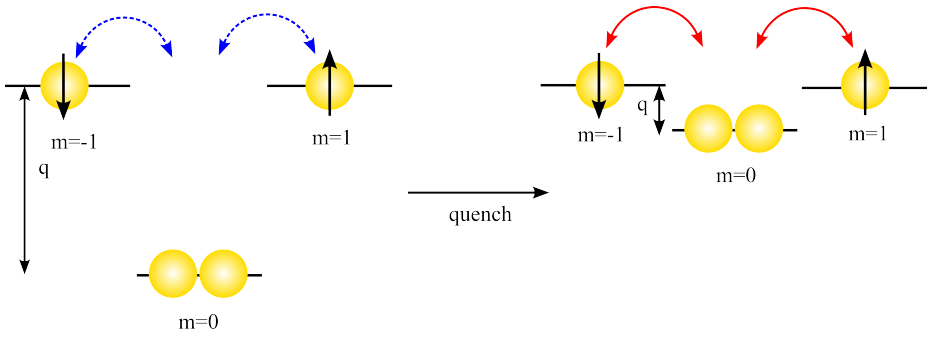

Figure 7.3: Schematic of a quenching process illustrated with pair energy levels of the $m = 0$ and $m = \pm 1$ states with single-particle detuning q. The linear Zeeman shift has been rotated out. The blue dashed arrow means no spin exchange happens, and the solid red arrow means spin exchange can happen. Left: before quenching the Hamiltonian, the effective quadratic Zeeman shift q is large, and the spin mixing dynamic is energetically forbidden. Right: after quenching, the spin mixing starts, and the competition between the spin-interaction c and q determines the exact dynamics of the spin oscillations.

the evaporative cooling to generate a magnetic field gradient. This populates most of the atoms in the $F = 1, m = -1$ state. Then we clean the unwanted atoms out of the $F = 1, m = 0$ and $F = 1, m = 1$ states using adiabatic microwave sweeps to $F = 2$ followed by resonant yellow light pulses that blow away all $F = 2$ atoms out of the trap. We wait two seconds for the magnetic field to settles down and stabilize. We apply a radio-frequency pulse, which transfers atoms from the $m = -1$ state to the $m = 0$ and $m = +1$ states (see Fig. 7.4). The pulse length is 15 μs such that the fractional populations of the $m+1$, $m = 0$, and $m = -1$ are $\rho_{-1} = 0.25$, $\rho_0 = 0.5$, and $\rho_{+1} = 0.25$, respectively. At the end of the radio-frequency pulse (t=0), we quench the system by rapidly turning on the microwave field, and the microwave dressing field is detuned from the clock transition by 75 kHz. The fast change of microwave field allows a rapid change of q, which can move the energy of a $m = 0$ pair close to

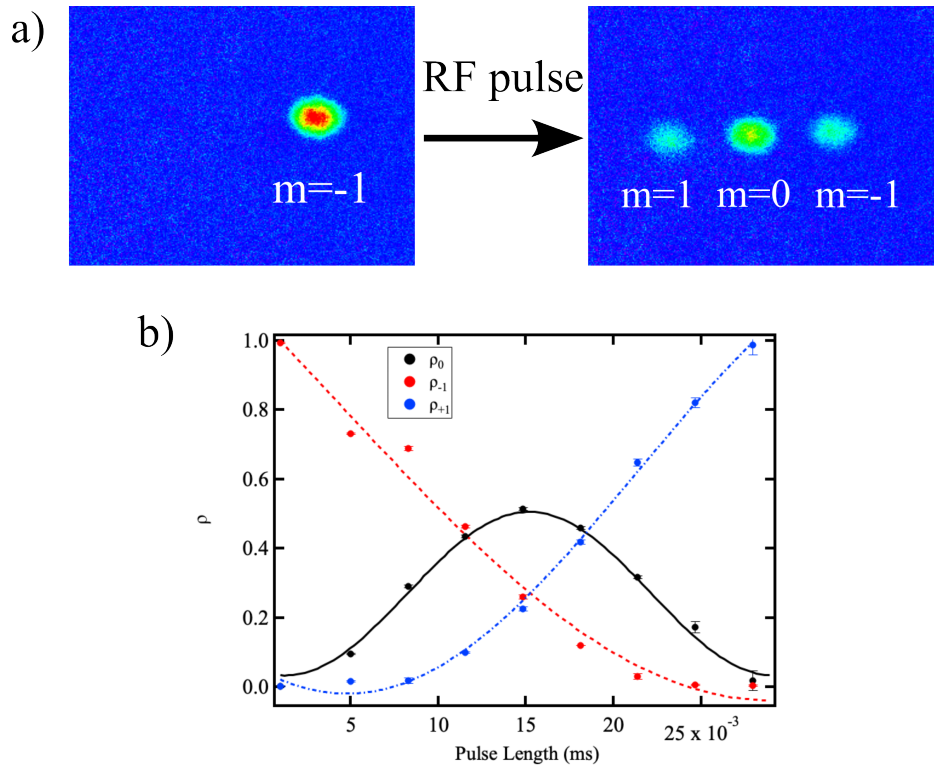

Figure 7.4: (a) A radio-frequency pulse is applied to transfer atoms from the $m = -1$ state to the $m = 0$ and $m = +1$ states. (b) The pulse length is 15 μs such that the fractional populations of the $m + 1$, $m = 0$, and $m = -1$ are $\rho_{-1} = 0.25$, $\rho_0 = 0.5$, and $\rho_{+1} = 0.25$, respectively. The circles are experimental data, the lines show the theory of the three-level system

the energy of a pair atoms with $m = 1$ and $m = -1$. The spin-mixing dynamics is initiated by this quenching of the system, and the spin population starts to oscillate between $m = 0$ state and $m = \pm 1$ states coherently. At $t = 80$ ms, the confining potential is turned off, and atoms experience a 1.5 ms free expansion before a 9 ms long Stern-Gerlach pulse is applied. Then a destructive absorption imaging of the $m = 1$, $m = 0$, and $m = -1$ spin components is taken after 10.5 ms of time-of-flight. The data is analyzed in real-time in the Igor Pro software after each experiment cycle, and we extract the number of atoms and the density profile in each of the three spin

components to analyze.

It is worth noting that the phase of the initial state is essential for the spin-mixing dynamics. The spinor phase is defined as $\theta = \theta_1 + \theta_{-1} - 2\theta_0$. For this experiment, the initial state (0.25, 0.5, 0.25) is prepared using a resonant RF pulse from (0, 0, 1), and the corresponding phase is $\theta = 0$. If the population fraction of the initial state is prepared using a RF pulse by rotating the state (0,1,0), the corresponding phase would be $\theta = \pi$. According to the mean-field energy phase diagram in Fig. 7.1, even though the system is starting with the same population distribution in these two case, the different phases will lead to different dynamics.

7.3 Data Analysis

7.3.1 Spin Oscillations within the Single-mode Approximation

We focus on our results for initial phase $\theta = 0$ and initial number fraction (0.25, 0.5, 0.25) in $m = -1$, $m = 0$, and $m = 1$, respectively. We quench the system using different microwave dressing fields such that the effective quadratic Zeeman shift q takes the value 45 Hz, 38 Hz, 35 Hz, and 30 Hz. The spin oscillations for each q value are shown in Fig. 7.5. Here we focus on the spin population oscillation in the $m = 0$ state, the population oscillation of the $m = \pm 1$ states are approximately equal due to the conservation of the magnetization. The mean value of the total atom number in this data set is about 2.5×10^4, and the trap frequencies are characterized by $\omega_z = 246.3$ Hz, $\omega_x = 135.3$ Hz, and $\omega_y = 151.2$ Hz in x, y, and z directions, respectively. The spin-dependent interaction energy is $c/h \approx 22$ Hz, and q/c are about 2.0, 1.73, 1.59 and 1.41 in Fig. 7.5(a) to Fig. 7.5(d), respectively. In the plots, black lines and dots are the experimentally measured fractional ρ_0 in $F = 1,\ m = 0$ hyperfine level as a function of quench time t for four different q values. The error bars on each data point indicate the statistical uncertainty, in the form of the standard

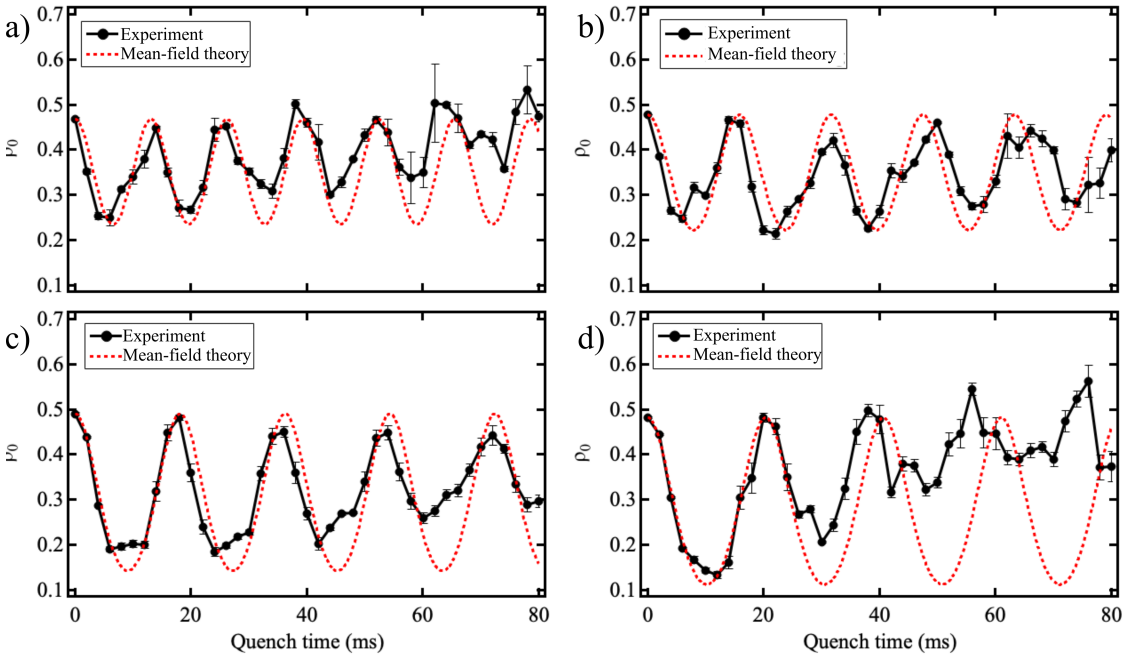

Figure 7.5: Quench-induced spin population oscillations of the $F = 1$ $m = 0$ state. The black dots are the measured experimental data. The error bars on each data point indicate the statistical uncertainty (standard error), which arises from an average of five measurements for each time t. The red dashed line is the mean-field SMA with the best fitting q. The spin oscillation data in (a), (b), and (c) correspond to experimental parameter of $q/h = 45$, $q/h = 38$, and $q/h = 35$ Hz, the best mean-field SMA fitting is at $q/h = 42$, $q/h = 35$, and $q/h = 33$ Hz, respectively. In (d), an upward drifting appears accompanied by the damping in amplitude, indicating the mean-field SMA does not fully capture the spin dynamics.

error (SE= $\sigma/\sqrt{N}$, where σ is the standard deviation) calculated from averaging five separate measurements for each time t. The main contribution to the error bars is estimated to come from the atom number variation from one experimental realization to another, which is about 20% of the total atom number in this experiment. Dashed red lines are the theoretical best fits to the mean-field single-mode approximation (SMA) models, according to Eq. (7.24).

The best mean-field SMA fit in Fig. 7.5a to Fig. 7.5b was found at $q/h = 42$, $q/h = 35$, and $q/h = 33$ Hz, which is about 2 to 3 Hz away from the q used in the experiments. In the mean-field SMA picture, the spin dynamics are governed by the competition between q and c. In Fig. 7.5a, $q/c \approx 2$ corresponds the spin mixing dynamics is in the "running phase" regime, which can be associated with the mean-field SMA phase space diagram in Fig. 7.1b. The agreement between the experimental data and theoretical prediction is good for the first two oscillations. However, discrepancies appear after a longer time of spin evolution after several oscillations. The deviations could indicate that the dynamics of a quantum system cannot be precisely captured by a classical method after a long-time of evolution. Fig. 7.5b and Fig. 7.5c show a good agreement between the mean-field SMA fittings and the experimental data. In these two figures, the ratio q/c is smaller compared to Fig. 7.5a, which leads to a larger amplitude but smaller frequency in the spin evolution. These results are also qualitatively in agreement with the mean-field SMA phase space diagram in Fig. 7.1b. However, a concern is raised by Fig. 7.5d. It shows a significant deviation between the mean-field SMA and the experimentally measured spin oscillation data. Even though the frequency is approximately the same, the amplitude of the spin oscillation changes over time. It shows damping after the first few oscillations. At the same time, an overall upward baseline drift appears and increases as time evolved. This upward drift is not captured by the mean-field SMA, which predicts fractional population oscillations with constant amplitude and period.

7.3.2 Spin Oscillations Beyond the Single-mode Approximation

To understand the discrepancies between the mean-field SMA and the experimental data shown in Fig. 7.5d, our collaborator Dr. Jianwen Jie (working as a postdoc in Dr. D. Blume's group at the time 2018-2021, University of Oklahoma), developed a new

theoretical model to explain the emergence of spin dynamics beyond the mean-field SMA [128]. As mentioned earlier when discussing Eq. (7.19), the spatial term of the wavefunction can be separated from the spin term because the spin-dependent interaction $c_2\bar{n}$ is much smaller than the spin-independent interaction $c_0\bar{n}$, which means the energy (time) scale for the spin interactions is smaller (larger) than for the density-dependent interactions. The mean-field SMA assumes that the dynamics introduced by these high-energy scales are so fast that they can be safely averaged out. As a consequence, the spatial term only represents a mean total density in the spin Hamiltonian, as shown in Eq. (7.21). However, the coupling between the spin and spatial degrees of freedom can lead to an energy transfer between the associated degrees of freedom. When some resonance conditions are fulfilled, the coupling between different degrees of freedom could dynamically change the form of the wave function and generate a large deviation from the prediction by the mean-field SMA.

A resonance effect in a spinor BEC has been discussed in Ref [129], where the resonance of the system is driven by quantum fluctuations. In our system, however, the resonance effect is triggered by the effective mean-field potential. The beyond SMA effects might be understood like this: the effective mean-field potential can generate ground and excited states for different magnetic sublevels m, which are characterized by different spatial modes, and these spatial modes are set by the density interaction $c_0\bar{n}(\mathbf{r})$. In an energy diagram with energy detuning q between the $m = 0$ and $m = \pm 1$ states, two atoms in the $m = 0$ state need an energy of $2q$ to scatter into $m = 1$ and $m = -1$ states due to energy conservation. If the effective potential induced excited state energy equals $2q$, the system is on resonance, and the following two processes may occur:

$$\begin{aligned} A &: E^{1}_{gr} + E^{-1}_{gr} = E^{0}_{gr} + E^{0}_{exc} \\ B &: E^{0}_{exc} + E^{0}_{exc} = E^{\pm 1}_{gr} + E^{\mp 1}_{exc}. \end{aligned} \tag{7.26}$$

These equations show two possible coupling channels: A. two atoms in $m = \pm 1$

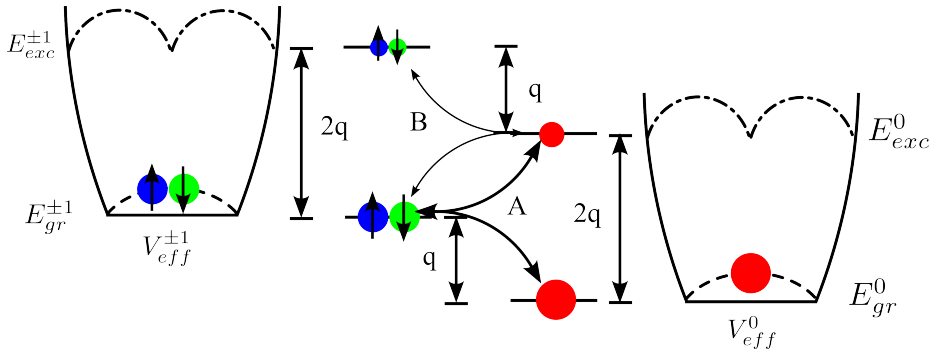

Figure 7.6: Mean-field driven beyond the SMA process. The effective mean-field potential generates ground (dashed lines) and excited states (dash-dotted lines) for both $m = \pm 1$ (left) and $m = 0$ (right), which are characterized by different spatial modes. If the excitation energy is equal to $2q$, two possible coupling channels occur (A) two atoms in $m = \pm 1$ ground states collide; one goes to $m = 0$ ground state, and the other goes to m=0 excited state or vice versa. (B) one atom in $m = \pm 1$ excited state and one atom in $m = \pm 1$ ground state collide, becoming two atoms in $m = 0$ excited states or vice versa. We thank Dr. D. Blume's group for this figure.

ground states collide; one goes to the $m = 0$ ground state, and the other goes to the $m = 0$ excited state or vice versa. B. one atom in $m = \pm 1$ excited state and one atom in $m = \pm 1$ ground state collide and become two atoms in $m = 0$ excited states or vice versa, as shown in Fig. 7.6. When the system is on resonance, the quench-induced spin oscillation dynamics cannot be fully captured by the SMA which always provides the population oscillations with constant amplitude and period. Instead, a "drifting" phenomenon occurs with changing amplitude and period in oscillation, indicating the beyond SMA dynamics. Since the drifting of the population oscillations can be derived from the coupled Gross-Pitaevskii equations, shown in Eq. (7.18), the dynamically induced beyond-SMA physics discussed here is mean-field in nature. Quantum fluctuations are not at play. Moreover, since the resonance condition depends on the single-particle detuning between the $m = 0$ and the $m = \pm 1$ atom, which is

characterized by the effective quadratic Zeeman shift q, the resonance can be avoided by changing q to some other regimes. This flexibility of changing q is realized in our experiment by tuning the microwave dressing field.

To further understand the beyond-SMA dynamics, we quantitatively study the dynamics close to resonance where the baseline drifting occurs and away from the resonance. In this data set, the mean atom number is $\sim 2.36\times10^4$, the geometry of the trap is approximately cylindrical symmetric with trap frequencies of $\omega_z = 255$ Hz, $\omega_x = 107$ Hz, and $\omega_y = 113$ Hz in the z, x, and y directions, respectively. Furthermore, the spin healing length, defined as $\xi = \hbar/\sqrt{2Mc_2\bar{n}}$, is comparable to the Thomas-Fermi radius in the z-direction, which indicates our initial state is well described by the SMA.

Figure 7.7a and 7.7b show the quench-induced spin oscillation for a q tuned away from the resonance and q tuned close to resonance, respectively. The black dots are the measured experimental data showing the number fraction of atoms in $F = 1,\ m = 0$ hyperfine level. The red error band on top of the experimental data indicates the statistical uncertainty that arises from averaging 9 or 10 data sets for each time t. The blue squares and the green diamonds show the fractional population ρ_0 obtained by solving the mean-field SMA equations and coupled Gross-Pitaevskii equations. The error bars reflect the average of 9-10 separate simulations. Figure 7.7a shows the spin population oscillation within the SMA, where q is tuned average from the resonance. The population fraction ρ_0 has a fixed spin oscillation amplitude and period. The experimental data, the data simulated using the mean-field SMA, and simulation using coupled GP equations agree with each other quite well. The experimental data (black dots) in Fig. 7.7b shows the upward drifting of the spin oscillation when q is tuned towards the resonance. This behaviour deviates from the mean-field SMA simulation (blue squares). On the other hand, the coupled mean-field GP equations (green

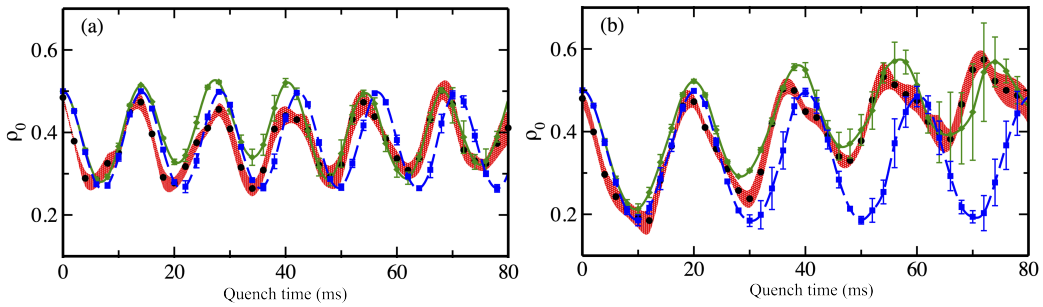

Figure 7.7: Quench-induced spin oscillation for q away from the resonance (a) and q close to resonance (b). The black dots are the measured experimental data showing the number fraction of atoms in $F = 1,\ m = 0$ hyperfine level. The red error bands are standard erros for the average of 9 or 10 data sets for each time t. The blue squares and the green diamonds are simulations using the mean-field SMA equations and coupled GP equations. The simulation data are the theoretical best fit with $q/h = 37.6$ Hz for (a) and $q/h = 28.2$ Hz for (b). A good agreement between the experimental data and the mean-field SMA simulation is shown in (a), where the system is away from resonance. In contrast, in (b), when the system is close to resonance the experimental data agree well only with the coupled GP equations, but not with the SMA equation. This indicates physics beyond the SMA. Figures are complied by Dr. Jianwen Jie from our experimental data and his theoretical simulations.

diamonds) reproduce the experimental data quite well. Therefore we deduce that the drifting is due to the coupling between the spin and spatial degrees of freedom when the system is at or close to a resonance which is driven by the mean-field potential; the quantum effects seem to play a minor or no role.

It is worth noting that the simulation curves in Fig. 7.7 are the theoretical best fit, which is $q/h = 37.6$ Hz for (a) and $q/h = 28.2$ Hz for (b). The experimental data were taken at $q/h = 42$ Hz for (a) and $q/h = 32$ Hz for (b) which is about 4 Hz difference from the theoretical predictions. The error bars of the theoretical simulations correspond to the statistical uncertainty that arises from averaging the

results for 9-10 different N values for each time t, where N is the number of atoms founded from the experimental data, and we assume the system is closed, so the total number of atoms are conserved. In the resonant case, the error bars on both experimental data and the coupled GP equation simulation grow large when drifting happens. In contrast, the increase of the error bar in the SMA simulation is not obvious. This might be explained by the energetic degeneracy described in Eq. (7.26), which causes the number preserving population oscillation period to depend sensitively on the particle number.

Due to the energetic degeneracy, the spin components could be excited from the ground state to a spatial excited state and obtain the spatial structure. In order to give further insight into this point of view, the GP simulation of each spin component's density is plotted in Fig. 7.8 along with the corresponding absorption images of the experimental data. The simulation data uses atom number $N = 2.4 \times 10^4$ and the spin oscillation time is $t = 66$ ms. Figure 7.8a, 7.8b and 7.8c, 7.8d show the GP simulated atom density in the $m = 0$ state and the $m = \pm 1$ states, respectively. Two different representations are chosen. Figures in the first column show the atom density in three dimensions plotted as functions of the axial axis z and the radial axis ρ. If the system is described by the SMA, the peak density should be located at $z = 0$ and $\rho = 0$ in both figures. Apparently, some spatial structures appear in the $m = \pm 1$ density such that the highest peak is at $z = 0$ and $\rho \neq 0$. Such behavior cannot be captured within the SMA. Figures in the second column show the integrated two-dimensional component densities as functions of z and $e_{xy} = (x + y)/\sqrt{2}$. This representation is consistent with the experimental pictures which were taken by the side camera. Figure 7.8e is an experimental image that shows the individual density profile of three spin components, which correspond to $N \approx 2.43 \times 10^4$ and spin oscillation time $t = 68$ ms. This figure agrees qualitatively with the integrated two-dimensional

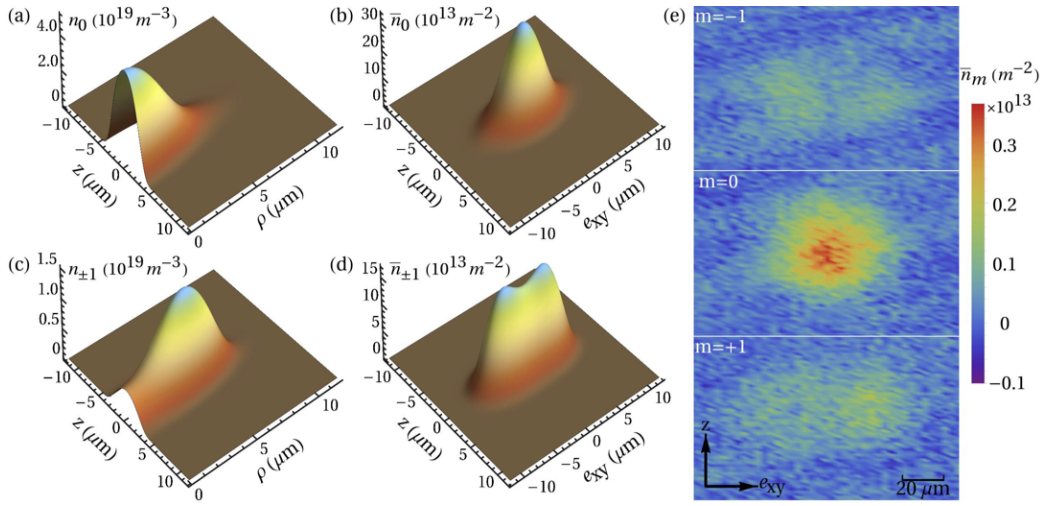

Figure 7.8: Density plot from GP simulation and experimental data. (a) and (b) show the density profile of n_0. (c) and (d) show the density profile of $n_{\pm1}$. In (a) and (c), the three-dimensional densities are shown as functions of vertical (axial ODT) axis z and the horizontal (radial ODT) axis ρ; the normalization is $\int n_m(\vec{r},t)d\vec{r}$. (b) and (d) are the integrated two-dimensional densities as functions of z and $e_{xy} = (x+y)/\sqrt{2}$, which has the same representation as the experimental pictures. (e) Experimental images of the density profiles in $m = -1$, $m = 0$, and $m = +1$ from top to bottom; the sidebar on the right defines the color code for the experimental images. Figures are complied by Dr. Jianwen Jie from our experimental data and his theoretical simulations.

densities obtained by solving the coupled GP equations despite the slightly different spin oscillation times.

To gain more insight into the resonance phenomenon, we scanned the effective quadratic Zeeman coefficient q around the resonance and mapped out the resonance. Figure 7.9 shows the resonance mapping as a function of quench time. The initial state was prepared in ($\rho_{-1} = 0.25$, $\rho_0 = 0.5$, $\rho_1 = 0.25$) as in the previous cases. The Hamiltonian was quenched using ten different q values from $q/h = 35$ Hz to $q/h = 27$ Hz. The black dots are the measured experimental data showing the number fraction of atoms in $F = 1$, $m = 0$ hyperfine level, and black lines serve as a guide

that connects the data points. The error bars are the standard error that arises from averaging ten data sets for each time t. In these data sets, the trap frequencies in the x, y, and z directions are $\omega_x = 147.24$ Hz, $\omega_y = 132.05$ Hz, and $\omega_z = 245.96$ Hz, respectively. The mean value of the total atom number is $\sim$ 26,000. In Fig. 7.9a, $q/h = 35$ Hz, the spin population oscillation in $m = 0$ state has a fixed spin oscillation amplitude and period for the first three oscillations. Damping occurs at the fourth oscillation, which is at a long spin evolution time, but no obvious drifting is observed. Therefore the system is considered away from the resonance, which can be captured by the mean-field SMA. As the value of q decreases, the damping becomes more obvious at long spin evolution time, and the drifting also appears in the oscillation. Figure 7.9d to 7.9g show the spin oscillation with $q/h = 32$ Hz to $q/h = 29$ Hz. Upward drifting starts at the second oscillation, accompanied by amplitude damping, indicating the system is close to the resonance where the coupling between the spin and spatial degrees of freedom happens. In Fig. 7.9h and Fig. 7.9i, the upward drifting is gone. However, the amplitude of the oscillations shows strong decay after the second oscillation with large error bars in a long spin evolution time.

Our resonance mapping depends sensitively on the exact values of trap frequencies in the x and y directions, which differ by a few tens of Hz in the experiment. The theoretical simulation is a symmetrical model which assumes that the trap frequencies in the x and y directions are exactly equal. Therefore, the theory only qualitatively agrees with the experimental mapping data.

To inspect the statistical uncertainty in the long time regime of spin evolution, we measure the number fraction in $m = 0$ for 90 times individually at a spin evolution time of 60 ms. Then we plot the number of occurrences (Frequency) as a function of population fraction (ρ_0) in histograms, as shown in Fig. 7.10. At $q/h = 35$ Hz, shown in Fig. 7.10a, where the system is off-resonance, the density distribution obeys

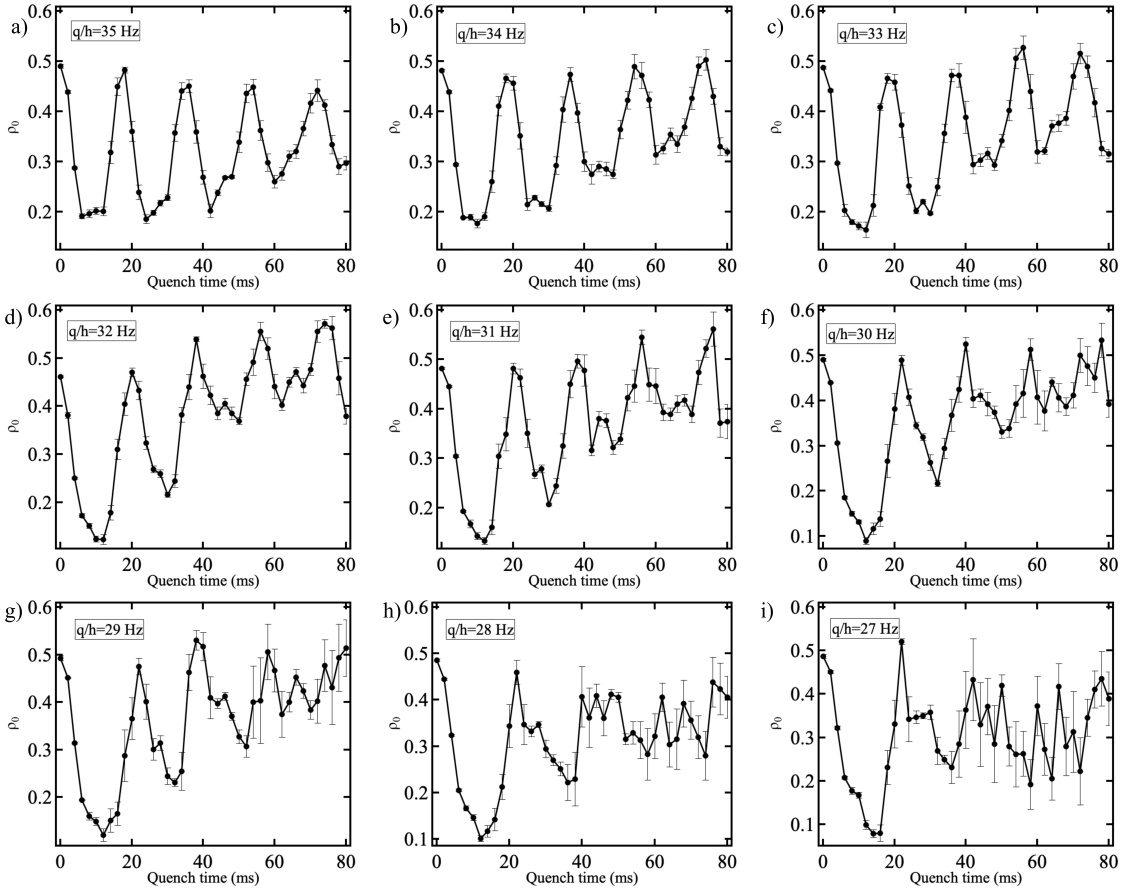

Figure 7.9: Resonance mapping of the quench-induced spin oscillations by scanning $q/h = 35$ Hz to $q/h = 27$ Hz. The black dots are the measured experimental data showing the number fraction of atoms in the $F = 1,\ m = 0$ hyperfine level. The error bars on top of the experimental data as the standard errors that arise from averaging ten data sets for each time t. The trap frequencies in the x, y, and z directions are $\omega_x = 147.24$ Hz, $\omega_y = 132.05$ Hz, and $\omega_z = 245.96$ Hz, respectively. The mean value of the total atom number is $\sim$ 26K. In (a), the spin oscillation has no drift at $q/h = 35$ Hz, which indicates the system is away from the resonance. The spin oscillation in (b) to (g) shows upward drifting, indicating the system is close to resonance. In (h) and (i), the upward drifting is gone, but the oscillations amplitude decay and data uncertainty increase as the increase of evolution time.

a Gaussian distribution where ρ_0 ranges from 0.18 to 0.4 with a maximum at about $\rho_0 \approx 0.25$. In Fig. 7.10b when $q/h = 34$ Hz, the distribution is still Gaussian, but with a broader width. As the value of q/h becomes small, the system approaches the resonance, and the Gaussian distribution starts to deform. In Fig. 7.10e where $q/h = 31$ Hz, the density in ρ_0 is almost non-Gaussian and evenly distributed from 0.3 to 0.65. The mean value of the distribution increases from somewhere close to 0.25 to about 0.45, which agrees with the upward-drifting spin oscillation result shown in Fig. 7.9e. At $q/h = 27$ Hz, the distribution changes back to a Gaussian-like distribution, and the mean value is back to $\sim$0.3, indicating the spin oscillation no longer has an upward drift.

7.4 Summary

Starting from an initial state of our $F = 1$ sodium spinor BEC with 50% of atom in $m_F = 0$ and 25% of atom each in $m_F = \pm 1$, we investigated the coherent spin-population oscillation between $m_F = 0$ and $m_F = \pm 1$ states after a quench of effective quadratic Zeeman shift q.

Scanning q, we identified a new resonance phenomenon, driven by mean-field coupling between spin and spatial degrees of freedom and not by quantum fluctuations. In plots of $m_F = 0$ population faction versus time, the resonance causes an upward drift of the baseline and a corresponding damping of the spin-population oscillations. We mapped the resonance as a function of q using the baseline as an indicator, as well as the non-Gaussian broadening of the distribution of $m_F = 0$ fractions near the resonant. A mean-field theory that goes beyond the SMA done by Dr. Qingze Guan and Dr. Jianwen Jie in the theory group of Dr. D. Blume fits the experimental results well.

Understanding such resonance can be important for future quantum technologies

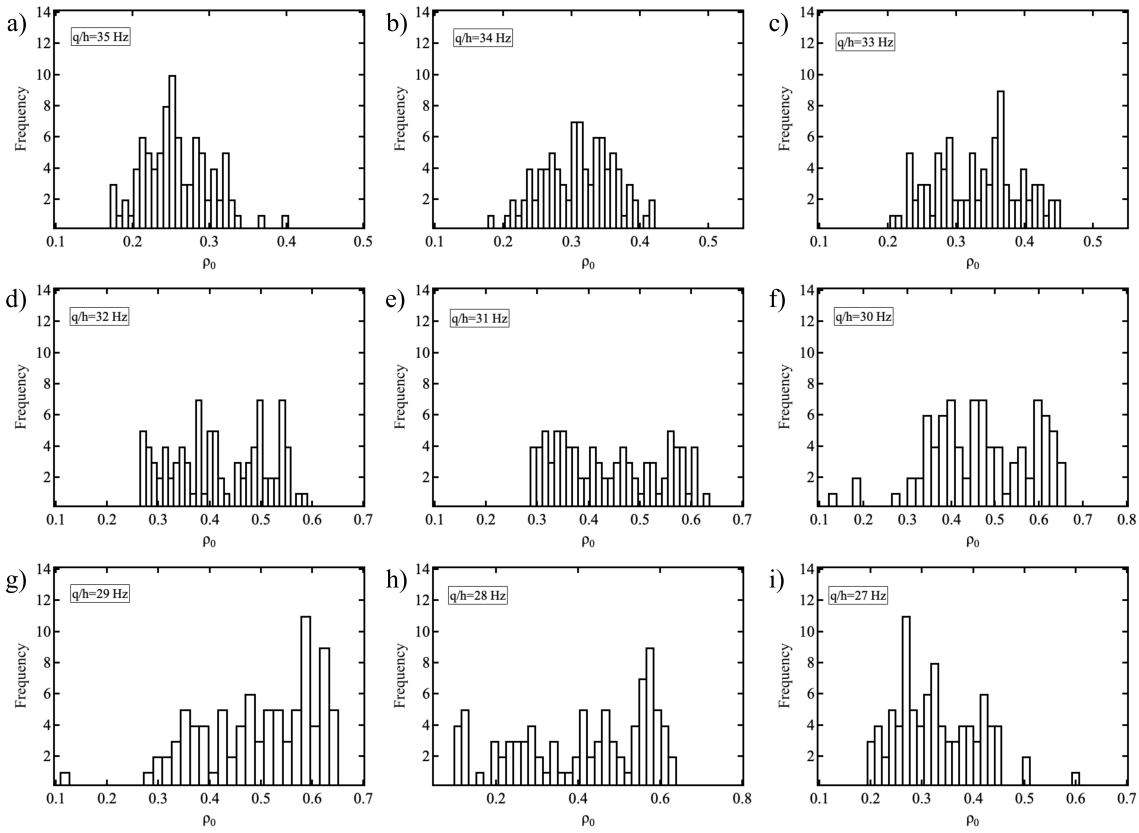

Figure 7.10: Mapping the spin-spatial resonance via histogram bars of the density distribution of ρ_0 at the spin oscillation time $t = 60$ ms. The trap frequency and the total atom number are the same as for Fig. 7.9, and a total of 90 data points were taken for each q value. When $q/h = 35$ Hz, away from the resonance, the density distribution of ρ_0 is Gaussian-like, and the mean value is about 0.25. As q/h decreases, the density distribution deviates from a Gaussian. At $q/h = 31$ Hz, the distribution is non-Gaussian, and the mean value is about 0.45 with large uncertainty. At $q/h = 27$ Hz, the distribution changes back to Gaussian-like distribution, and the mean value is back to $\sim$0.3.

based on spin-squeezing and spin-exchange in neutral gas, such as quantum enhanced magnetometry because they affect the time evolution that generated squeezing and entanglement in non-trivial ways.

Chapter 8

Spin-mixing Atom Interferometry

Interferometry is a measurement method based on one of the fundamental principles of waves: interference. Interferometric signals can be obtained by coherently splitting and recombining a monochromatic light wave and counting changes from bright to dark fringes in the interference pattern. A change of the pattern can contain information about the object or phenomenon being studied, such as a changing index of refraction along one path that causes a relative phase shift between the interfering beams. Interferometry has been demonstrated to make precise measurements of small quantities that are not achievable in any other way. One of the quintessential uses of precision interferometry was in 1887 when Michelson and Morley set up an optical Michelson interferometer to measure the speed of the light, which helped disprove the existence of ether. Recently LIGO's Michelson interferometers successfully detected the direct signal of gravitational waves. Besides using light waves for interferometry, ultracold atoms can also be used. Atoms can be considered as matter waves when the temperature is cold enough, due to the increase of de Broglie wavelength of atoms with respect to the change of temperature. Generating interference patterns from atoms is possible in this kind of matter-wave interferometry. Compared to light, the cold atom's slow motion allows for a longer time to accumulate phase before interfering, allowing for longer interrogation times. Therefore, atoms can achieve higher sensitivity than light in some potential sensing applications.

Atom interferometry has been proved to be one of the most precise measurements in physics. Several experiments achieved in laboratories have demonstrated that atom interferometers can be excellent in sensing applications [28, 29], cartography mapping [130], and tests of fundamental physics [131, 132, 133]. The performance of an

atom interferometer is usually characterized by its sensitivity. For the interferometer prepared in separable states, the attainable sensitivity is fundamentally bounded by the standard quantum limit (SQL) $\Delta\theta \sim 1/\sqrt{\bar{n}}$ [134], also known as the shot noise limit. However, when interferometers are performed with quantum states where particles are entangled, sensitivities beyond the SQL can be achieved [135]. An example is the SU(1,1) interferometer which is constructed by replacing the passive beam splitters in a Mach-Zehnder interferometer with active nonlinear parametric amplifiers [136]. It has been tested to overcome the SQL and gain sensitivity enhancement compared to its classical counterpart [137, 138, 139, 140].

One fundamental question is understanding which quantum states offer an advantage for quantum metrology. For example, spin-squeezed states [141] and some other many-body entangled states such as Greenberger-Horne-Zeilinger (GHZ) are useful for quantum-enhanced metrology [142, 143]. In spinor Bose-Einstein condensates (BECs), the entanglement between particles can be generated through spin-exchange collisions. In the three-level $F = 1$ system, the spin-exchange collision is shown in Fig. 7.2: the spin-mixing dynamics happen as a pair of $m = 0$ atoms couple to $m = 1$ and $m = -1$ states after colliding with each other and generate entanglement. The mechanism has been realized as a proof-of-principle SU(1,1) interferometer [144] in spinor BEC, which is an atomic analog of parametric amplification in optical four-wave mixing [145]. The $m = 0$, $m = -1$, and $m = 1$ states are analogous to the pump, probe, and conjugate light beams in optical four-wave mixing, respectively.

This chapter focus on the experiments with seeded nonlinear interferometers enabled by spin-mixing dynamics (SMD). We experimentally prepare different initial states through either a double-sided seeding or single-sided seeding method. We use microwave-dressing to control the spin-mixing dynamics of the system. At long spin evolution time, the interferometer enters into the so-called depleted pump regime,

where the interference fringes of the interferometer become highly non-sinusoidal. In section one, we work out a theoretical model of spin-mixing interferometry after briefly introducing the SU(2) and SU(1,1) interferometers. Section two describes the initial state preparation method of single- and double-sided seeded interferometers and the experimental procedures to realize a spin-mixing interferometer. In the last section, we show our data on spin-mixing dynamics and interference fringes of the atom interferometers and then compare them with the theoretical simulation using the truncated Wigner approximation. We also calculate our interferometer's sensitivity using the error propagation method. Our data suggest that the sensitivities of our seeded interferometers can reach below the SQL, indicating a metrological enhancement of phase sensitivity due to quantum effects and non-linearity in our system, useful for magnetometry. Our current research about seeded spin-mixing interferometry in the regime of long evolution time paves the way for the light-pulse atom interferometry experiment, which involves the coupling spin and momentum degrees of freedom, for inertial sensing and gravimetry, which will be performed in the future.

In this chapter, the standard quantum limit is obtained by assuming our interferometers are linear. Under this assumption, the state (probe state) used to probe the imprinted phase and the subsequent time evolution during the "recombining" step always yield sinusoidal interference fringes. In our experiment, we observe non-sinusoidal fringes, and compare sensitivities to the limits for the linear (sinusoidal) case.

8.1 Theory of Interferometry

8.1.1 SU(2) and SU(1,1) Interferometry

One of the classical interferometer configurations is the Mach-Zehnder interferometer depicted in Fig. 8.1a. A light beam is coupled into one port of a passive linear beam splitter and split into two beams that propagate along different paths. The

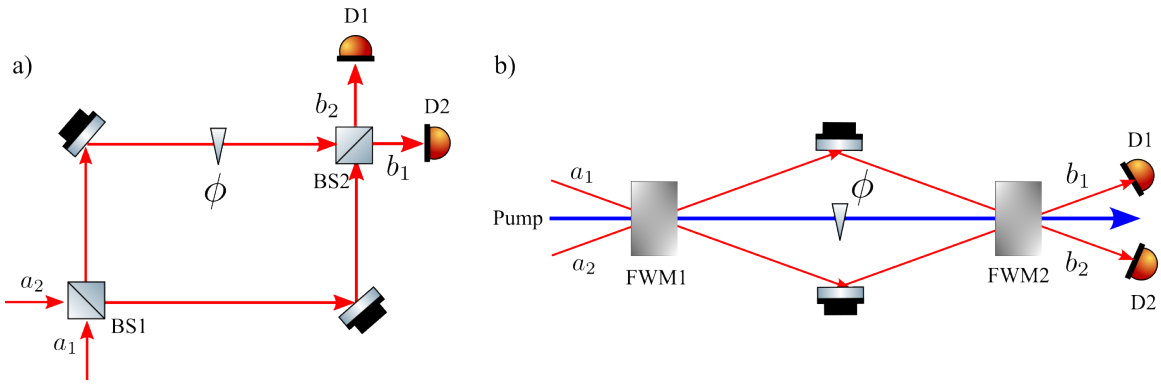

Figure 8.1: (a) A SU(2) Mach-Zehnder interferometer. Light enters one of the two input ports a_1 or a_2 and is split by a 50/50 linear beam splitter BS1. The two light beams accumulate a relative phase shift ϕ before entering another 50/50 linear beam splitter. The two light beams b_1 and b_2 leaving the interferometer are detected by photodetectors D1 and D2. (b) A SU(1,1) interferometer. The passive linear beam splitters in the SU(2) Mach-Zehnder interferometer are replaced with active nonlinear parametric amplifiers, such as four-wave mixers (FWM1 and FWM2). The pumping light is phase shifted by ϕ. The outgoing light beams b_1 and b_2 are quantum correlated.

relative phase shift, φ, along the different paths can be determined by measuring the position of interference fringes in the output beams. The phase sensitivities of classical interferometers are limited by the standard quantum limit. This type of interferometer can be characterized by the group SU(2) [136]. SU(2) group is equivalent to the rotation group in three dimensions which contain the three Hermitian generators

$$\begin{aligned} J_x &= \frac{1}{2}(a_1^\dagger a_2 + a_2^\dagger a_1), \\ J_y &= -\frac{i}{2}(a_1^\dagger a_2 - a_2^\dagger a_1), \\ J_z &= \frac{1}{2}(a_1^\dagger a_1 - a_2^\dagger a_2), \end{aligned} \tag{8.1}$$

where the the annihilation operators a_i and creation operators $a_j^\dagger$ obeys bosonic commutation relations $[a_i,\ a_j] = [a_i^\dagger,\ a_j^\dagger] = 0$ and $[a_i,\ a_j^\dagger] = \delta_{ij}$. The geometric picture of the SU(2) interferometry process can be represented on a Bloch sphere, as

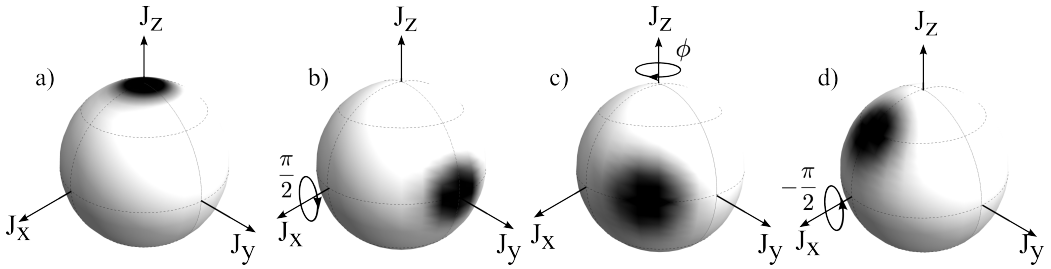

Figure 8.2: The performance of a Mach-Zehnder SU(2) interferometer can be represented using a Bloch sphere. The input state is prepared at the north pole of the sphere (a). The first beam splitter performs a $\frac{\pi}{2}$ rotation about the J_x (b). The phase shifts accumulated along the beam path correspond to a rotation ϕ about the J_z (c). The second beam splitter performs a $-\frac{\pi}{2}$ rotation about the J_x axis (d).

illustrated in Fig. 8.2. Let the initial state be $|\psi\rangle$, which is the state prepared at the north pole on the Bloch sphere, as illustrated in Fig. 8.2a. The first beam splitter in Fig. 8.1a is the equivalent to applying a $\pi/2$ pulse along the J_x direction of the Bloch sphere, as shown in Fig. 8.2b. The overall phase shifts $\Delta\phi$ are equivalent to a rotation about J_z direction by a phase of ϕ on the Bloch sphere, which is depicted in Fig. 8.2c. The last beam splitter applies a -$\pi/2$ pulse to rotate the state about the J_x axis again, as shown in Fig. 8.2d. So ϕ can now be measured by measuring the spin population along the J_z axis. The state vector $|\psi'\rangle$ leaving the interferometer is $|\psi'\rangle = e^{i\frac{\pi}{2}J_x}e^{-i\phi J_z}e^{-i\frac{\pi}{2}J_x}|\psi\rangle$.

SU(1,1) interferometry can be realized by replacing the passive linear beam splitters in the SU(2) Mach-Zehnder interferometer with active nonlinear parametric amplifiers such as four-wave mixers, as shown in Fig. 8.1. The group SU(1,1) also has three Hermitian generators K_x, K_y, and K_z, which are defined as [136]

$$\begin{aligned} K_x &= \frac{1}{2}(a_1^\dagger a_2^\dagger + a_1 a_2) \\ K_y &= -\frac{i}{2}(a_1^\dagger a_2^\dagger - a_1 a_2) \\ K_z &= \frac{1}{2}(a_1^\dagger a_1 + a_2^\dagger a_2 + 1). \end{aligned} \tag{8.2}$$

In these equations, K_x and K_y contain terms $a_i^\dagger a_j^\dagger$ and $a_i a_j$ that create or annihilate two particles at the same time. This nonlinear process generates entanglement between the particles and generates spin-squeezing, which can lead to quantum enhancement in the phase sensitivity of the interferometers. In our sodium spinor Bose-Einstein condensate, the active nonlinear parametric amplifiers are realized by the spin-mixing dynamics, which are responsible for generating quantum correlations and entanglement.

8.1.2 Theoretical Background of Spin-1 Interferometry

We start with $F = 1$ spinor BECs consisting of N sodium atoms confined in a tight 3D trap. We assume the Thomas-Fermi radius of the spinor BEC is smaller than the spin healing length, and the spin-dependent interaction is much weaker than the density-dependent interaction. Hence, we can apply the single-mode approximation (SMA) [146], which assumes all spin components share the same spatial density. As a result, the dynamics are governed by the spin Hamiltonian in the SMA is [147]:

$$\begin{aligned} \hat{H}_{\mathrm{SMD}} &= \frac{c}{N}(\hat{a}_0^\dagger \hat{a}_0^\dagger \hat{a}_{+1}\hat{a}_{-1} + \hat{a}_0 \hat{a}_0 \hat{a}_{+1}^\dagger \hat{a}_{-1}^\dagger) \\ &+ \frac{c}{N}(\hat{N}_0 - \frac{1}{2})(\hat{N}_+ + \hat{N}_-) + q(\hat{N}_+ + \hat{N}_-). \end{aligned} \tag{8.3}$$

The first term on the right-hand side of Eq. (8.3) is identical to the four-wave mixing term in nonlinear quantum optics [136], which here describes spin-exchange collisions between atoms. The second term in Eq. (8.3) refers to an energy shift due to elastic collisions, and the last term describes the effective quadratic Zeeman shift which contributes to the linear phase shift during interferometers. The operators $\hat{a}_m^\dagger$ and $\hat{a}_m$ satisfy the bosonic commutation relation $[\hat{a}_m^\dagger, \hat{a}_m]$=1 where $\hat{a}_m^\dagger$ create and $\hat{a}_m$ destroy an atom in hyperfine state $|F = 1, m = m\rangle$. The number operator for each mode is $\hat{N}_m$ which is defined as $\hat{N}_m = \hat{a}_m^\dagger \hat{a}_m$. The coefficient q is the effective quadratic energy shift and has the same definition as Eq. (7.25). The spin-dependent interaction parameter c, $c = c_2\bar{n}$ has the same definition as what we defined in chapter seven.

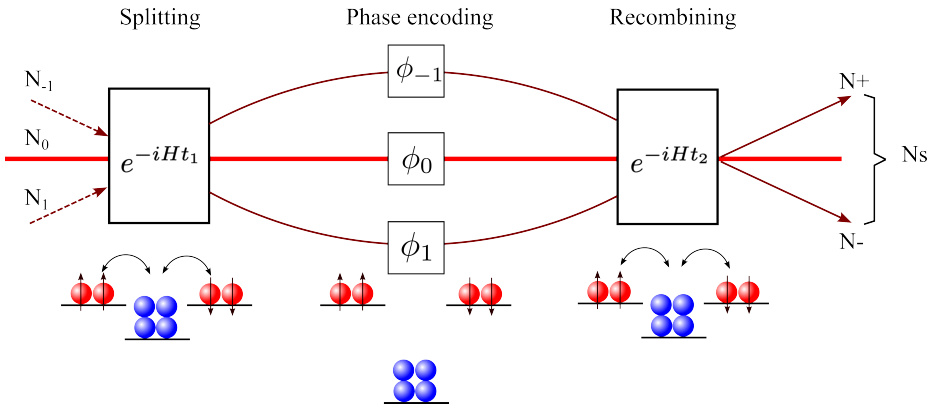

Figure 8.3: Schematic of our three-mode nonlinear interferometer based on spin-mixing dynamics. Initial state $(N_{-}1,\ N_0,\ N_1)$ is made of pure BECs in the $m = 0$ state with some initial seeds in the $m = \pm 1$ states. The spin-mixing dynamics Hamiltonian H triggers the nonlinear "path" splitting or recombining by creating (annihilating) paired atoms in $|F = 1,\ m = \pm 1\rangle$ components from (into) $|F = 1,\ m = 0\rangle$. The phase encoding shifts the spin component $|1,\ 0\rangle$ and adds a relative phase $\phi = 2\pi \times 2q\tau$ to the overall spinor phase $\phi = \phi_1 + \phi_{-1} - 2\phi_0$. In the end, the total number of atoms, $N_s = N_+ + N_-$, in $|F = 1,\ m = \pm 1\rangle$ is measured.

Sometimes, the undepleted pump approximation (UPA) is applied to simplify $\hat{H}_{\rm SMD}$ by replacing $a^\dagger$ and a with a complex number $\sqrt{N_0}e^{-i\phi_0}$, which reduces Eq. (8.3) to a form in terms of the SU(1,1) operators [148]

$$H_{\rm UPA} = \frac{c}{N}(2N_0K_x) + (2K_z - 1)\left[\frac{c}{N}(N_0 - \frac{1}{2}) + q\right]. \tag{8.4}$$

Physically, the undepleted pump approximation is valid when the majority of the atoms are in the $m = 0$ pump mode. This places restrictions on the initial state and on the evolving time of the interferometers.

Our three-mode nonlinear interferometers based on spin-mixing dynamics are realized in three major blocks, as shown in Fig. 8.3. First, we prepared initial state $|\Psi(t = 0)\rangle$ with some classical seeds in the side modes (the $|1, \pm 1\rangle$ components) at spin evolution time $t = 0$. After quenching the system by tuning the ratio $|q|/c$, the

system starts to evolve under the spin-mixing Hamiltonian H_{SMD} for variable time t_1,

$$|\Psi(t_1)\rangle = e^{-iH_{\mathrm{SMD}}t_1/\hbar}\,|\Psi(t=0)\rangle\,. \tag{8.5}$$

The spin-exchange collisions cause the atoms to change from $|1,\ 0\rangle$ state to the $|1,\ \pm1\rangle$ and generates entanglement between them. This step is referred to as "splitting".

Second, a phase imprinting operation is performed on $|\Psi(t_1)\rangle$ for time τ,

$$|\Psi(t_1+\tau)\rangle = e^{-iH_{ps}(q)\tau/\hbar}\,|\Psi(t_1)\rangle \tag{8.6}$$

the phase imprinting operator corresponds to the last term in Eq. (8.3). When $|q| \gg c$, the last term of the spin-mixing dynamics Hamiltonian dominates, and the spin-exchange collisions are energetically forbidden. Hence, the phase shift Hamiltonian H_{ps} is simply

$$\hat{H}_{ps} = q(\hat{N}_+ + \hat{N}_-). \tag{8.7}$$

With this steps, the phase encoding shifts the spin component $|1,\ 0\rangle$ and adds a relative phase $\phi = 2\pi \times 2q\tau$ to the overall spinor phase $\phi = \phi_1 + \phi_{-1} - 2\phi_0$.

The last step is refered to as "recombining". It is realized by applying an approximate time-reversal dynamics of the splitting process. The entangled probe states become disentangled and traced back to the input state if no additional phase is added. The commonly adopted approach for realizing time-reversed dynamics comes from time-forward evolution with a sign-flipped Hamiltonian [149]. In the spinor BEC system, an exact time reversal is only possible in the limit of infinitely small evolution times. An approximate time-reversal can be achieved by applying phase shift Hamiltonian H_{ps} with a certain q value. Then, we apply H_{SMD} again,

$$|\Psi(t_1+\tau+t_2)\rangle = e^{-iH_{\mathrm{SMD}}t_2/\hbar}\,|\Psi(t_1+\tau)\rangle\,, \tag{8.8}$$

where t_2 is the time for "recombining," which is set equal to t_1 to accomplish time-reversal spin evolution as described in Ref [140]. With the presence of a finite encoding

phase, the "recombining" mechanism does not couple the entangled probe state back to the same state as the input state. Instead, it gives rise to a phase-dependent output state. This approximate time-reversal dynamic is constrained to short-term spin evolution [150], where the time-reversal dynamic is applied before the probe states become too deeply entangled to be disentangled. For long-term spin evolution, the cyclic dynamics method has been employed to realize the nonlinear atom interferometer in Ref [149]. After this procedure, the number of atoms in each spin component is measured.

8.1.3 Phase Estimation: Fisher Information and Cramér-Rao Bound

The phase shift θ during the interferometer cannot be directly measured. Instead, the phase estimation relies on the measurement outcomes μ, and the probability of the outcome, $P(\mu|\theta)$, which is conditioned on the parameter θ. We assume the unbiased phase estimator operator $\Theta(\mu)$ to estimate the phase θ associating each set of measurement outcomes μ, such that $\bar{\Theta} = \sum_\mu \Theta(\mu)P(\mu|\theta) = \theta$. We start from two equalities

$$\begin{aligned} \frac{\partial\bar{\Theta}}{\theta} = \frac{\partial}{\partial\theta}\sum_\mu \Theta(\mu)P(\mu|\theta) = 1 \\ \frac{\partial}{\partial\theta}\sum_\mu P(\mu|\theta) = 0. \end{aligned} \tag{8.9}$$

These two equations lead to

$$\sum_\mu (\Theta(\mu) - \theta)\frac{\partial}{\partial\theta}P(\mu|\theta) = 1. \tag{8.10}$$

We square both sides of the equation and apply the Cauchy-Schwartz inequality to obtain

$$(\Delta\theta)^2 \sum_\mu P(\mu|\theta)\left[\frac{\partial}{\partial\theta}\log P(\mu|\theta)\right]^2 \geq 1. \tag{8.11}$$

From this equation, the sensitivity $\Delta\theta$ has a lower bound which can be written as

$$\Delta\theta \geq \Delta\theta_{CR} = \frac{1}{\sqrt{F(\theta)}}, \tag{8.12}$$

where

$$F(\theta) = \sum_{\mu} \frac{1}{P(\mu|\theta)} \left(\frac{\partial P(\mu|\theta)}{\partial \theta} \right)^2 . \tag{8.13}$$

$\Delta\theta_{CR}$ is called the Cramér-Rao bound, which is one of the most famous results in parameter-estimation theory and expresses the lowest possible uncertainty among all unbiased estimators that can be achieved. $F(\theta)$ is called Fisher information. An upper bound to the Fisher information is obtained by maximizing Eq. (8.13) over all possible generalized measurements in quantum mechanics [151], called quantum Fisher information. We have $F_Q[\hat{\rho}_\theta] \geq F(\theta)$, where $\hat{\rho}_\theta = e^{-i\hat{J}\theta}\hat{\rho}e^{i\hat{J}\theta}$. Therefore, the corresponding bound on the phase sensitivity is called quantum Cramér-Rao [151, 152] bound, which is defined as

$$\Delta\theta_{CR} \geq \Delta\theta_{QCR} = \frac{1}{\sqrt{F[\hat{\rho}, \hat{J}]}}. \tag{8.14}$$

Generally, for a pure state $\hat{\rho}$ and any unitary transformations generated by some Hermitian $\hat{J}$, the quantum Fisher information is $F_Q[\hat{\rho}, \hat{J}] = 4(\Delta\hat{J})^2$. If a state $\hat{\rho}$ is separable, that is $\hat{\rho}_{sep} = \hat{\rho}_1 \otimes \hat{\rho}_2 \otimes ... \otimes \hat{\rho}_N$, then the quantum Fisher information of any separable state of N qubits is [152]

$$F[\hat{\rho}_{sep}, \hat{J}] \leq N \tag{8.15}$$

Therefore the lowest sensitivity one can possibly achieve for any separable states according to Eq. (8.14) is $1/\sqrt{N}$, which is known as the standard quantum limit. On the other hand, if states are entangled in a way that is useful for quantum metrology, the quantum Fisher information can violate the upper bound in Eq. (8.15)

$$F[\hat{\rho}, \hat{J}] > N, \tag{8.16}$$

and the quantum state is helpful in estimating a phase shift θ, with a sensitivity overcoming the standard quantum limit. The maximum value of the quantum Fisher

information obtained for genuine N-particle entangled states is given by

$$F[\hat{\rho}, \hat{J}] \leq N^2, \tag{8.17}$$

which defines the ultimate Heisenberg limit of sensitivity $\Delta\theta_{HL} = 1/N$ [153].

In our experiment, the mean value $\langle \hat{N}_s \rangle$ and the standard deviation ΔN_s after the spin-mixing dynamics of the "splitting" and "recombining" steps are the two important physical quantities to characterize the interferometer performance. Here $\langle \hat{N}_s \rangle$ is the total number of atoms in $|F = 1,\ m = \pm 1\rangle$ states. We define,

$$\langle \hat{N}_s \rangle = \langle \hat{N}_{+1} \rangle + \langle \hat{N}_{-1} \rangle, \tag{8.18}$$

where $\langle \hat{N}_s \rangle = \langle \hat{N}_s(t) \rangle = \langle \Psi(t) | \hat{N}_s(t) | \Psi(t) \rangle$, and

$$\Delta N_s = \sqrt{\langle \hat{N}_s^2 \rangle - \langle \hat{N}_s \rangle^2}. \tag{8.19}$$

We analyze $\langle \hat{N}_s \rangle$ and ΔN_s as a function of relative phase θ to find regions with the best sensitivity. The phase sensitivity $\Delta\theta$ is defined through error propagation [137], and it is evaluated at time $t = t_1 + \tau + t_2$,

$$\Delta\theta = \frac{\Delta N_s(t)}{|\partial N_s(t)/\partial\theta|}. \tag{8.20}$$

The phase sensitivity $\Delta\theta$ is then compared to the lowest possible sensitivity of separable states, which is the standard quantum limit (SQL) $1/\sqrt{N_s(t_1)}$, to show if there is an enhanced gain for the nonlinear interferometer.

In addition, the lower bound for the error propagation-based sensitivity is set by the quantum Cramér-Rao bound

$$\Delta\theta_{QCR} = \frac{1}{\sqrt{F_Q[|\Psi(t_1)\rangle, \hat{N}_s/2]}}, \tag{8.21}$$

where the quantum Fisher information F_Q depends on $|\Psi(t_1)\rangle$ and the linear phase generator $\hat{N}_s/2$. We further assume our state is a pure state after the spin-mixing

dynamics of the "splitting", then the quantum Cramér-Rao bound is obtained from $\Delta\theta_{QCR} = 1/\Delta H_s(t_1)$. Ideally, one should use a state which gives maximum F_Q to optimize the interferometric gain and operate in the regime where the error propagation-based sensitivity $\Delta\theta$ is as close as possible to the best achievable phase sensitivity. For comparison, we also plot the Heisenberg limit $\Delta\theta_{HL}$ which is defined in terms of the number $N_s(t_1)$ of atoms at side modes at time t_1,

$$\Delta\theta_{HL} = \frac{1}{N_s(t_1)}. \tag{8.22}$$

The Heisenberg limit is the ultimate limit for the phase sensitivity that can be reached in an ideal system with the absence of noise.

8.2 Single- and Double-Sided Seeding Atom Interferometers

We use ^{23}Na spinor Bose-Einstein condensates to experimentally realize the seeded spin-mixing interferometer. The preparation detail of the spinor Bose-Einstein condensates has been discussed in chapter six. The scheme of the interferometry experiment can be divided into five blocks: initial state preparation, entangled probe state generation via spin-mixing dynamics, phase encoding, approximate time-reversal dynamics to disentangle the states, and measurement by taking images of the three spinor components.

8.2.1 Initial State Preparation

We start the experiment by preparing ∼25000 atoms in a pure sodium BEC in a crossed-beam optical dipole trap via evaporative cooling. The trapping potential near the minimum is approximately harmonic and approximately axially symmetric. The trapping laser beam is far red-detuned, having wavelength $\lambda = 1064$ nm and a beam waist ($1/e^2$ radius) of ~ 26 μm. The measured trap frequencies are $\omega_{\{z,x,y\}} \approx$

$2\pi \times \{248, 123, 125\}$ Hz, and the strongest confinement direction z is aligned with the direction of gravity. The trap frequency fluctuation in the x and y directions is larger than the fluctuation in the z direction. The day-to-day measurements show about ± 15 Hz fluctuations in the x and y directions. A bias magnetic field is fixed at $B = 0.428$ G and applied along the z direction to split the $F = 1$ hyperfine manifolds. The bias magnetic field corresponds to a linear Zeeman shift of 300 kHz$\cdot h$ and a quadratic Zemman shift between $m = 0$ and $m = \pm 1$ magnetic sublevels of 141 Hz$\cdot h$.

The atomic population fraction in each sublevel can be controlled by applying an empirically determined bias magnetic field at the end of forced evaporation. With this method, we populate most of the atoms into the $|F = 1, m = 0\rangle$ state before initializing the spin-mixing interferometry experiment. In order to have a pure state of $|F = 1, m = 0\rangle$ before seeding, atoms in the unwanted states $|F = 1, m_F = \pm 1\rangle$ have to be cleaned. This step is realized by applying two consecutive one-millisecond microwave sweep signals through the $\Delta m = 0$ resonances, such that the atoms in $|F = 1, m_F = \pm 1\rangle$ states are adiabatically transferred to $|F = 2, m_F = \pm 1\rangle$ states, respectively. Immediately after all unwanted atoms are in the $F = 2$ manifold, we apply a short, 200 μs, pulse of on-resonant light which couples the $F = 2$ and $F' = 3$ state to give a momentum kick to the $F = 2$ atoms, causes the unwanted atoms to leave the optical dipole trap. In the end, we prepare $\sim$21,000 atoms in the desired state $|F = 1, m_F = 0\rangle$, and all other hyperfine states are empty. The various pulses are illustrated in Fig. 8.4.

The initial seeded states are prepared independently at the beginning of each interferometry experiment with either single- or double-sided seeding, as illustrated in Fig. 8.4. For single-sided seeding, a small number fraction of atoms are coherently prepared only in $|F = 1,\ m = -1\rangle$ state through two consecutive microwave π pulses. Atoms are transferred from $|F = 1,\ m = 0\rangle$ state to $|F = 1,\ m = -1\rangle$ state through

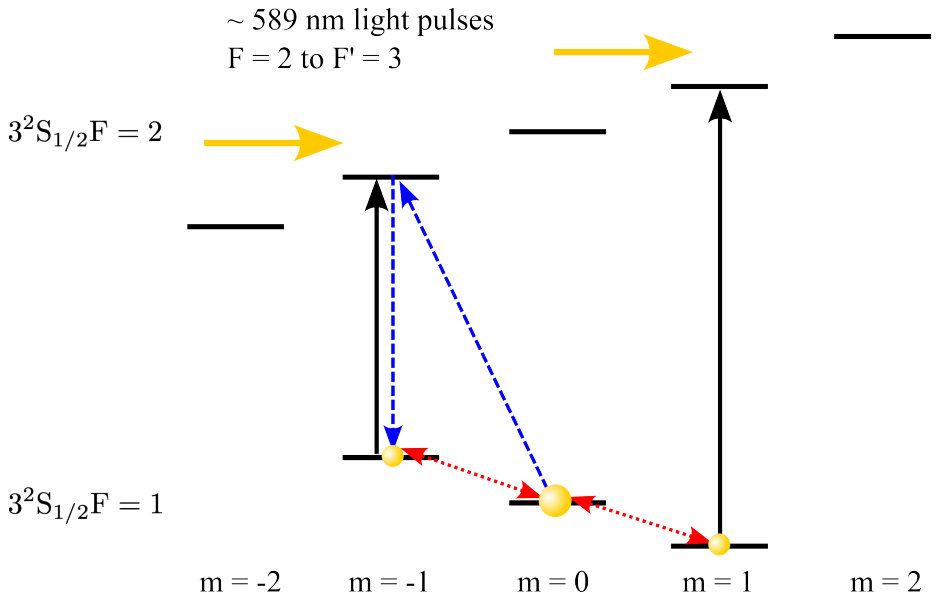

Figure 8.4: State preparation. We adiabatically sweep the microwave field (black arrows) to transfer atoms from unwanted $F = 1$ states to the $F = 2$ manifold, followed by resonant light pulses (yellow arrows) to clean those atoms out of the trap. The single-sided seeding is realized using two consecutive microwave π pulses (blue dash arrows). The double-sided seeding is realized by applying a radio-frequency pulse (red dot arrows) to seed $|F = 1,\ m = \pm 1\rangle$, simultaneously.

an intermediate state $|F = 2,\ m = -1\rangle$. The fraction of the seed is controlled by the power of the microwave field, and we seed 10% of total atoms in $|F = 1,\ m = -1\rangle$ state. The microwave pulse is generated via a versatile microwave source controlled by a field programmable gate array (FPGA) which has the capability to modulate the power and frequency on fast time scales [65]. The microwave signal is emitted from the same homemade microwave antenna which was discussed in chapter five. For double-sided seeding, instead of using the microwave pulses to prepare the seeding, we apply a short on-resonant rf pulse (300 kHz) which is on resonance with the linear Zeeman shift between the sublevels in the $F = 1$ manifold. After receiving the rf pules, atoms are transferred from $|F = 1,\ m = 0\rangle$ state to $|F = 1,\ m = -1\rangle$ and

$|F = 1,\ m = 1\rangle$ states simultaneously with the same amount of atoms, the quadratic Zeeman shift is ignored because the effects are negligible at 300 kHz. The number of atoms in seeds can be controlled either by changing the duration or the power of the radio frequency pulse. In the end, both seeding methods give 10% of seeds for the spin-mixing interferometry.

8.2.2 Experimental Interferometry Sequence

After preparing the initial seeded states, the spin-mixing interferometry can be experimentally realized in the following three steps: state splitting, phase imprinting, and state recombining.

After preparing the initial seeded states, the states-splitting step is realized by applying the spin-mixing Hamltonian H_{SMD}: An off-resonant microwave-dressing field ($\Delta = 75$ kHz blue-detuned from the $|1, 0\rangle$ to $|2, 0\rangle$ clock transition) is switched on within 5 μs. This quenches the condensates. The effective quadratic Zeeman is shifted to the target value q and remains there for a variable spin-mixing time t_1. The system evolves and the atomic population is transferred from $m = 0$ states to $m = \pm 1$ states due to the spin-exchanging collision.

The phase imprinting step happens at the end of the first spin-mixing dynamics, after evolution time t_1. We apply a relative phase shift to the system by changing the quadratic Zeeman shift q, such that $|q| \gg c$. This is experimentally realized by decreasing the detuning of the microwave field from $\Delta = 75$ kHz to $\Delta = 30$ kHz as well as increasing the microwave power. Since our Rabi frequency for coupling $|F = 1,\ m = 0\rangle$ to $|F = 2,\ m = 0\rangle$ is less than 10 kHz, our detuning is still sufficiently large compared to the Rabi frequency, as verified by the fact that we didn't observe a large number of atom loss during the experiment. Due to the large ratio of $|q|/c$ during the phase imprinting, the spin-exchange collisions are energetically suppressed.

Therefore, the phase imprinting does not lead to noticeable population changes and only causes an extra q-dependent spinor phase shift. The relative spin phase shift induced by the microwave kick is defined by equation $\phi \approx -2\pi \times 2q\tau$, which depends on the effective quadratic Zeeman shift q and the pulse length τ. Here we keep τ constant for 1 ms and scan the relative phase ϕ by scanning q. The range of q values is from $q/h = -100$ Hz to $q/h = -1040$ Hz.

After phase imprinting, the entangled states "recombine" under another H_{SMD} for time t_2 (t_2=t_1). During this process, the entangled $m = \pm 1$ pair partially disentangle and transfer back to the $m = 0$ state. With different imprinted phases, we can either control the evolution of N_s to continue evolving or recover back the approximate initial state. After a total time $t = t_1 + \tau + t_2$, the optical dipole trap is switched off, a 9 ms long Stern-Gerlach pulse is applied, and the false color absorption images are taken to measure the atom number for the three spin components.

By measuring the final $m = 0$ spin population as a function of applied phase shift, we can map interference fringes for this type of spin-mixing interferometer. We can also change the spin-mixing duration $t_{1,2}$ to change the number of atoms in the side modes of the interferometer and investigate the spin population in either the short-time or the long-time evolution regime.

8.3 Experimental Results

8.3.1 Spin-mixing Dynamics of Different Initial States

The spin-mixing dynamics for initial states that are prepared using either single-sided seeding or double-sided seeding methods with a total of 10% of atoms in the side modes ($|F = 1,\ m = \pm 1\rangle$), and the effective quadratic Zeeman shift of $q/h = -5$ Hz are shown in Fig. 8.5.

Figure 8.5a and 8.5b show the spin oscillations with initial states prepared us-

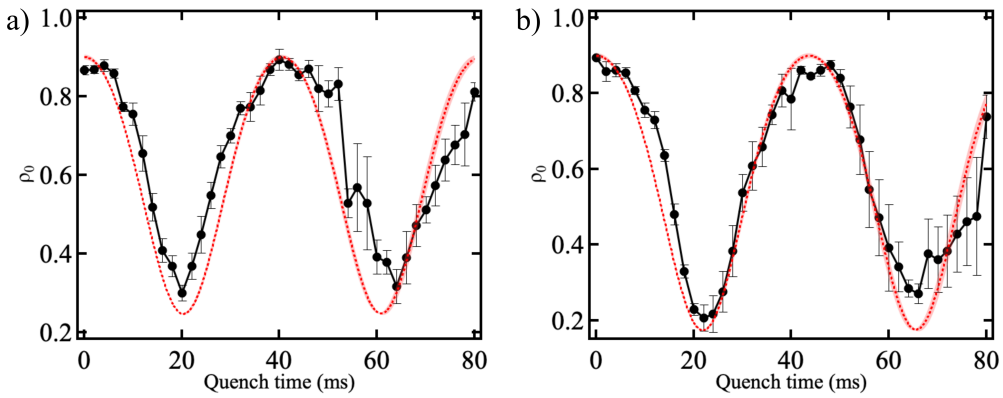

Figure 8.5: Spin-exchanging collisions with initial states are prepared by (a) double-sided seeding and (b) single-sided seeding. The black dots and lines are experimental data of fractional population in the $|1,\ 0\rangle$ component, ρ_0, as a function of spin evolution time. The error bars are the standard error of over five experimental runs. Red dashed lines are the TWA simulation fitted with $q/h = -5$ Hz, $c/h = 18.5$ Hz, and $N = 21000$. The red error bands indicate the statistical uncertainty that arises from averaging 1000 data sets at each time step.

ing double-sided seeding and single-sided seeding method, respectively. The black dots are the measured experimental data showing the number fraction of atoms in $|F = 1\ m = 0\rangle$ state as a function of time after quench. The error bars are the standard error (SE= $\sigma/\sqrt{N}$, where σ is the standard deviation) that arise from averaging five data sets for each time t. More data will need to be taken to get a good estimate of the uncertainty. The error bars are smaller at early time and increase as the evolution time increase. The main contribution to the error bars might come from the atom number variation from one experimental realization to another, and the fluctuation is about 20% of the total atom number. The red dashed lines are theoretical predictions of the spin-mixing dynamics using the truncated Wigner approximation. The simulation was done using parameters $q/h = -5$ Hz and a number of atoms $N = 21000$. Due to some fluctuation of the trap frequency in the radial direction, we fit the data with

spin-dependent interaction strength $c/h = 18.5$ Hz. The time steps are set to 0.1 ms, and the number of simulation data points is 800 during 80 ms of spin evolution time. The red error bands on the top of the theoretical prediction indicate the statistical uncertainty that arises from averaging over an ensemble of 1000 data sets at each time step. Since the initial state prepared with double-sided seeding is sensitive to the initial phase, during the simulation, we set the initial phase $\phi = 0$. Figures show a good agreement of oscillation period and amplitude between the experimental and theoretical data using the truncated Wigner approximation. The spin oscillations are sinusoidal. The population fraction in the $m = 0$ state starts with $\sim$90% of the total atom number N. During spin-exchange collisions, atoms transfer from the $|F = 1,\ m = 0\rangle$ state to $|F = 1,\ m = \pm 1\rangle$ which leads to population decrease in the $|F = 1,\ m = 0\rangle$ state until an evolution time of $t \approx 20$ ms. Then the process is reversed, and the population in $|F = 1,\ m = 0\rangle$ returns to $\sim$ 0.9N at $\sim$ 40 ms, consistent with the simulation result. After 60 ms of spin evolution, the deviation between the experimental data and the theoretical simulation becomes larger and larger, and the error bars of the experimental data grow larger than the simulation, which could be due to technical noise such as magnetic field noise, number fluctuation, or microwave amplitude noise.

8.3.2 Interference Fringes

Just like with optical interferometers, interference patterns can be observed at the output of atom interferometers. Figure 8.6 shows the interference fringes of our double-sided seeding spin-mixing interferometry. In Fig. 8.6a to Fig. 8.6d, the final number fraction in the $m = 0$ state, ρ_0, is plotted as a function of the imprinted phase Φ with different spin-mixing times. Figure 8.6a to 8.6d show fringes for spin-mixing time of 8 ms, 10 ms, 13 ms, and 18 ms, respectively, in the states splitting and

recombining steps. The pulse length of the phase imprinting step is 1 ms, so the total interferometry times in each sub-figure of Fig. 8.6, where the data is plotted, are 17 ms, 21 ms, 27 ms, and 37 ms, respectively.

For comparison, the interference fringes for single-sided seeding spin-mixing interferometry are plotted in Fig. 8.7. The same interferometry parameters are used as the double-sided seeding interferometer except for the initial state. Figure 8.7a to 8.7d reflect the spin-mixing times of $t_1 = t_2 = 8$ ms, 10 ms, 13 ms, and 18 ms, respectively. The total interferometry times are 17 ms, 21 ms, 27 ms, and 37 ms in each sub-figure.

In the plots, black circles are the mean value of experimentally measured fractional, ρ_0, in $|F = 1\, m = 0\rangle$ state as a function of the imprinted phase. The error bars indicate standard errors calculated from averaging five separate measurements for each phase value Φ. The red dashed lines are the theoretical simulation from the truncated Wigner approximation. The red error bands around the red dashed lines are theoretical fitting indicate the statistical uncertainty that arise from averaging an ensemble of 100 trajectories at each phase value. Here, the simulation uses parameters $q/h = -5$ Hz for the spin-mixing dynamics and $N = 21000$ as the atom number. The spin-dependent interaction strength $c/h = 19$ Hz was used to fit the data in Fig. 8.6 and $c/h = 22$ Hz was used to fit the data in Fig. 8.7. Phase Φ is scanned from $2\pi\times0.2$ to $2\pi\times2.08$ with step of $2\pi\times0.04$. Experimental results agree reasonably well with the theoretical model for these parameters.

Generally, both the experimental results and the theoretical simulations in single- or double-sided seeding interferometry have an apparent fringe contrast. Moreover, the oscillations of each fringe pattern have a period of 2π, which is expected. Specifically, in Fig. 8.6a and Fig. 8.7a, where the spin evolution time is relatively short (8 ms), both the experimental data and the TWA simulations show close-to-sinusoidal fringe patterns. For a relatively short spin evolution time, a small number of atoms are

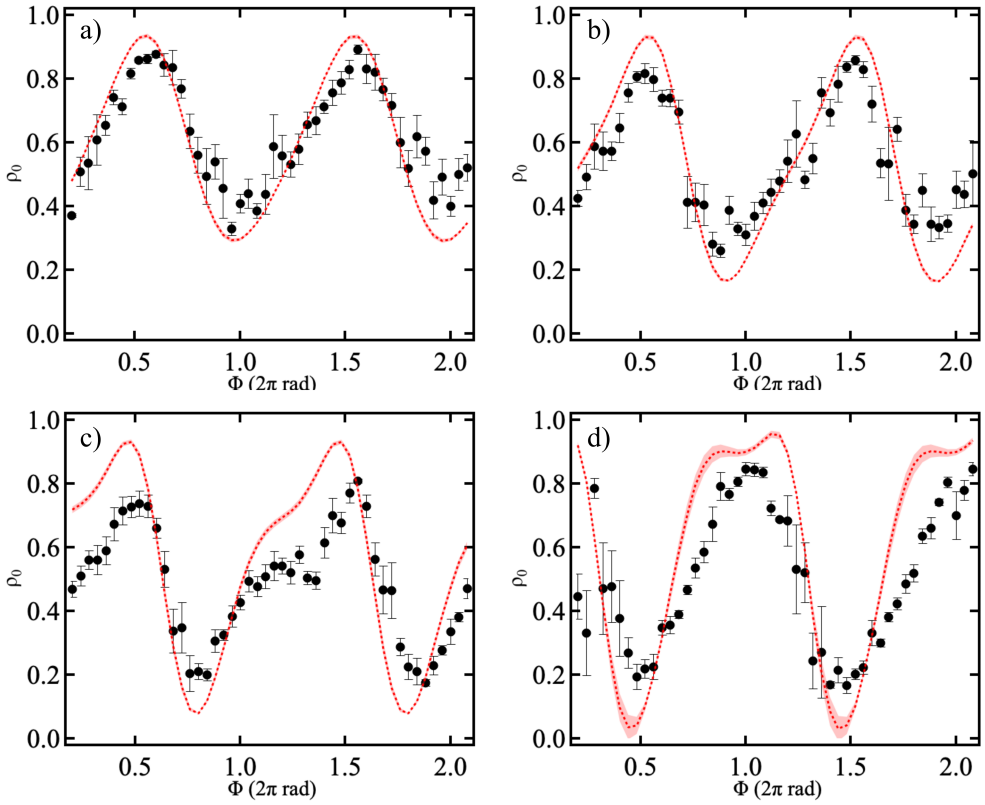

Figure 8.6: Interference fringes for the double-sided seeding interferometer presented in terms of fractional population in the $|1,\ 0\rangle$ component, ρ_0, as a function of imprinted phase Φ. The spin-mixing time $t_1 = t_2$ of "splitting" and "recombining" steps from (a) to (d) are 8 ms, 10 ms, 13 ms, and 18 ms, respectively. Black circles are the mean values of experimental data. Error bars are standard errors calculated from averaging five separate measurements. Red dashed lines are TWA simulation results with parameters $q/h = -5$ Hz, $c/h = 19$ Hz, and $N = 21000$. The red error bands arise from averaging over an ensemble of 100 trajectories for each phase value. The experimental data and the TWA simulation show close-to-sinusoidal fringe patterns in (a) at the short spin-mixing time of 8 ms. Interference fringes become non-sinusoidal in (b), (c), and (d) when the spin-mixing time increases, which indicates the nonlinear nature of the interferometer.

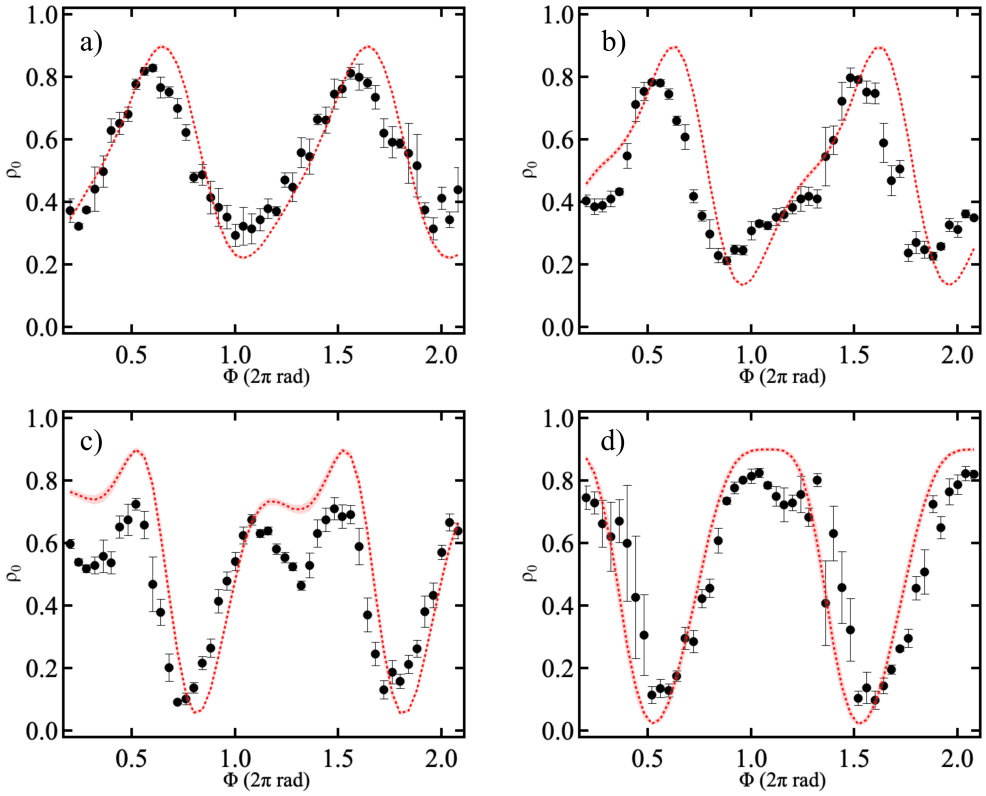

Figure 8.7: Interference fringes for the single-sided seeding interferometer presented in terms of fractional population in the $|1,\ 0\rangle$ component, ρ_0, as a function of imprinted phase Φ. The spin-mixing time $t_1 = t_2$ of "splitting" and "recombining" steps from (a) to (d) are 8 ms, 10 ms, 13 ms, and 18 ms, respectively. Black circles are the mean values of experimental data. Error bars on each data point are standard errors calculated from averaging five separate measurements. Red dashed lines are TWA simulation results with parameters $q/h = -5$ Hz, $c/h = 22$ Hz, and $N = 21000$. The red error bands arise from averaging over an ensemble of 100 trajectories each phase value. The single-sided seeding interferometer performs similarly to the one with double-sided seeding in terms of interference patterns.

transferred to the side modes due to spin-exchange collisions, and the probe states become lightly entangled. As the spin evolution time increases, the non-sinusoidal fringe patterns are more and more evident in the sub-figure (b), (c), and (d) of Fig. 8.6 and Fig. 8.7, respectively. This is because the system is no longer in the undepleted pump regime and the non-sinusoidal feature is caused by pump depletion. For long evolution time, the number of entangled pairs of atoms in $m = \pm 1$ states is increased, and spin squeezed and non-Gaussian squeezed states can be generated [149]. It is also worth noting that ρ_0 in the TWA simulation (red line) reaches $\sim$0.9 at phase $\Phi = 2\pi \times 0.5$ and $\Phi = 2\pi \times 1.5$ in (a), (b) and (c), and at $\Phi = 2\pi$ and $\Phi = 4\pi$ in (d), in both Fig. 8.6 and Fig. 8.7. An approximate close-to-perfect time-reversal dynamic happens close to these phase shifts which is important for the spin-mixing interferometry. Usually, interference fringes close to these phases have steep slopes, indicating some non-linear effects that could possibly lead to metrological gain in the phase estimation. Experimental data agree with the model qualitatively but do not have the same results as the theoretical prediction. This could be due to the technical noise such as atom loss, field or microwave noise, and number fluctuations. We also notice that the phase of the highest peak in figure (d) is shifted by $\sim \pi$ compared to the other sub-figures in both Fig. 8.6 and Fig. 8.7. This phase difference is induced by the spin-mixing dynamics. Our TWA simulations also show the fringes at 18 ms of spin evolution time have $\sim 0.4\pi$ phase shifts compared to the others at spin evolution time of 8 ms, 10 ms, and 13 ms, respectively.

8.3.3 Phase Sensitivity Measurement

In our experiment, the phase sensitivity of the spin-mixing interferometry is obtained using the error propagation method, which is defined in Eq. (8.20). $\langle N_s(t) \rangle$ is the average total atom number in $|F = 1,\ m = \pm 1\rangle$ states which can be obtained

by applying Gaussian fit to Stern-Gerlach absorption images. $\Delta N_s(t)$ is the statistical uncertainty which is defined as the standard deviation of $N_s(t)$. To calculate the phase sensitivity, we narrow the measurements to a small phase range where the metrological gain is more likely to happen than in other areas, due to the theoretical predictions. Then we measure the phase with relatively high resolution, and each phase value is measured ten times to calculate averages and standard deviations.

Figure 8.8 shows the phase sensitivity estimations when the spin-mixing time t_1 is 10 ms, and the initial state is prepared with the single-sided seeding method. In Fig. 8.8a and Fig. 8.8c, the black circles are the experimental data which show the mean value of the total number in the $|F = 1,\ m = \pm 1\rangle$ states $\langle N_s(t)\rangle$ as a function of imprinted phase Φ. Each data point is averaged from ten data sets for each phase Φ. The black circles in Fig. 8.8b and Fig. 8.8d are the standard deviation of the experimental data $N_s(t)$. In order to use the error propagation equation, we introduce two different fitting methods to fit our experimental data. The data in Fig. 8.8a and Fig. 8.8b are fitted with a polynomial regression model up to the eighth order, which is shown as the red line. In Fig. 8.8c and Fig. 8.8d, we use Hermite interpolation up to the third order between each data point. The red lines are the interpolation result. The phase sensitivity estimation results (black lines) resulting from the two different fitting methods are shown in Fig. 8.8e and Fig. 8.8f, respectively. The red lines in Fig. 8.8e and Fig. 8.8f are the standard quantum limit normalized to unity, for comparison. The black lines are the calculated phase sensitivity using the error propagation method normalized to the standard quantum limit. The SQL here is defined as $\Delta\Phi_{\mathrm{SQL}} = 1/\sqrt{\langle N_s(t_1)\rangle}$, where $\langle N_s(t_1)\rangle$ is the mean value of the total atom number in $|F = 1,\ m = \pm 1\rangle$ states right after the "splitting" step, and $t_1 = 10$ ms. Here, we measured $N_s(t_1)$ 30 times, and the red error band on top of the SQL indicates the statistical uncertainty that arises from averaging 30 data points measured at t_1.

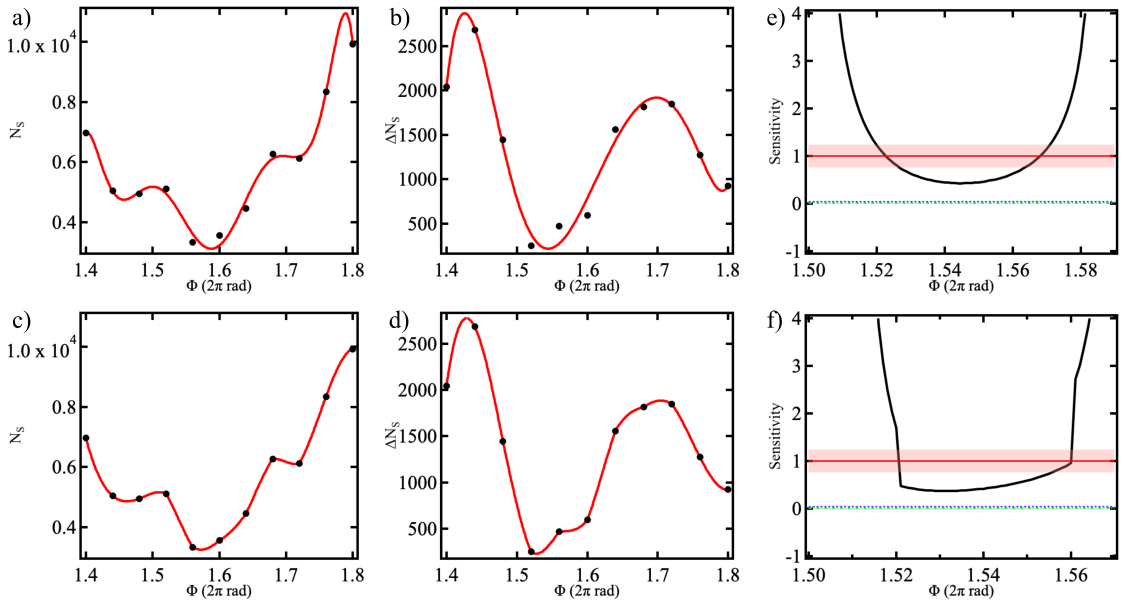

Figure 8.8: Phase sensitivity measurement using error propagation method. Black circles in (a) and (c) are the experimental data showing the mean value of the total number in the $|F = 1,\ m = \pm 1\rangle$ states as a function of phase. Each point is an average of ten data. Black circles in (b) and (d) are the standard deviation of the experimental data. The experimental data are fitted with a polynomial regression model up to the eighth order in (a) and (b), and are interpolated using the Hermite function up to the third order in (c) and (d), as shown in the red lines. Black lines in (e) are the phase sensitivity estimation using the fitting from (a) and (b). Black lines in (f) are the phase sensitivity using the fitting from (c) and (d), respectively. Results are normalized to the SQL. The red lines in (e) and (f) are the normalized SQL defined as $1/\sqrt{\langle N_s(t_1)\rangle}$ where $t_1 = 10$ ms. Red bands are the standard deviation that arises from averaging 30 data points measured at t_1. Blue dash lines are the quantum Cramér-Rao bound of the probe states, and green dash and dot lines are the Heisenberg sensitivity limit.

Compared with the SQL (red line), the black lines below the SQL from $\Phi = 2\pi \times 1.52$ to $\Phi = 2\pi \times 1.56$ indicates the metrological gain in phase sensitivity. For comparison, we also drew the quantum Cramér-Rao bound of the probe states in blue dash lines and the Heisenberg sensitivity limit in the green dash and dot lines, all normalized to the SQL.

The meaning of the standard quantum limit is by assuming the atoms $N_s(t_1)$ in the probe states are separable. Therefore the lowest achievable sensitivity for atoms in separable states is bounded by the quantum Cramér-Rao bound, which is equivalent to the SQL. However, in our experiment, the atoms $N_s(t_1)$ are forming spin-mixing induced probe states with entanglement generated between each pair of atoms in the $|F = 1,\ m = \pm 1\rangle$ states. The quantum Cramér-Rao bound of the entangled states is then supposed to give a better sensitivity than the SQL. The results in Fig. 8.8e and Fig. 8.8f show that with the same atom number, $N_s(t_1)$, prepared in the separable probe states and the entangled probe states, the phase sensitivity of the entangled states (black line) induced by the spin-mixing dynamics can overcome the SQL (red line) and achieve metrological gain compared to its classical reference.

We further explore the phase sensitivity with different initial states: the initial states prepared with the single-sided seeding, the initial states prepared with the double-sided seeding, for different spin-mixing time. Figure 8.9 shows the phase sensitivity of single-sided seeding atom interferometers. The black lines are the calculated phase sensitivity using the error propagation method normalized to the standard quantum limit. The red lines are standard quantum limits normalized to unity, and the red error band on top of the SQL indicates the statistical uncertainty that arises from averaging 30 data points measured at the end of the first spin-mixing time t_1. For comparison, we draw the quantum Cramér-Rao bound of the probe states in blue dash lines and the Heisenberg sensitivity limit in the green dash and

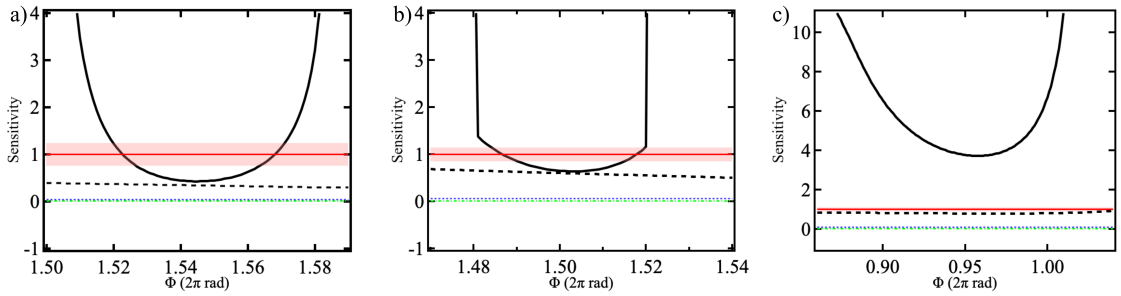

Figure 8.9: Phase sensitivities of single-side seeded spin-mixing interferometers with the spin-mixing time, t_1, of (a) 10 ms, (b) 13 ms, and (c) 18 ms. When $t_1 = 10$ ms, the maximum metrological gain is obtained at $\Phi = 2\pi \times 1.54$ with $G = 3.69$ dB indicating a metrological gain. Dashed black lines are the phase sensitivities calculated from the TWA simulated data, with a gain of 5.25 dB at $\Phi = 2\pi \times 1.58$. The gain becomes smaller at $t_1 = 13$ ms, and there is no gain at $t_1 = 18$ ms.

dot lines, all normalized to the SQL. Figure 8.9a to 8.9c show the phase sensitivities obtained with t_1 equal to 10 ms, 13 ms, and 18 ms, respectively. At $t_1 = 10$ ms, the experimental error propagation data (black line) goes below the SQL (red line) from $\Phi \approx 2\pi \times 1.52$ to $\Phi \approx 2\pi \times 1.57$. The maximum gain is found at $\Phi = 2\pi \times 1.54$ with $G = 3.69$ dB where the metrological gain is defined as $G = 10\log_{10}(\Delta\Phi_{\mathrm{SQL}}/\Delta\Phi)$. For comparison, the black dashed line is the TWA simulated error propagation data, and the maximum gain is obtained at $\Phi = 2\pi \times 1.58$ with $G = 5.25$ dB, which is $\sim$1.6 dB greater than the experimental result. At $t_1 = 13$ ms, the experimental gain is $G = 1.96$ dB at $\Phi = 2\pi \times 1.5$, and the TWA simulated gain is $G = 3.44$ dB at $\Phi = 2\pi \times 1.56$. Both theoretical and experimental data show that the metrological advantage of the interferometry is weaker at $t_1 = 13$ ms than $t_1 = 10$ ms. In Fig. 8.9c, the minimum experimental data is about four times above the SQL, and the theoretical simulation is very close to the SQL, indicating no metrological gain is obtained when $t_1 = 18$ ms.

Figure 8.10 shows the phase sensitivity of double-sided seeding interferometers.

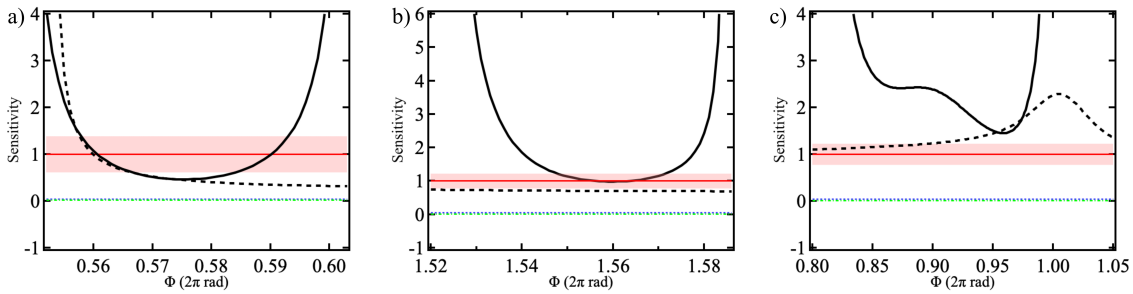

Figure 8.10: Phase sensitivities of double-sided seeding atom interferometers with the spin-mixing time, t_1, of (a) 8 ms, (b) 13 ms, and (c) 18 ms. When $t_1 = 8$ ms, the maximum metrological gain is obtained at $\Phi = 2\pi \times 0.56$ with $G = 4.77$ dB indicates a metrological gain. Dashed black lines are the phase sensitivities calculated from the TWA simulated data, with a gain of 5.53 dB at $\Phi = 2\pi \times 0.66$. The gain becomes barely visible at $t_1 = 13$ ms, and no gain at $t_1 = 18$ ms.

We use the same way to obtain the error propagation data, TWA simulation data, Cramér-Rao bound, and the Heisenberg sensitivity limit as in Fig. 8.9 with the same legends. Figure 8.10a to 8.10c show the phase sensitivities obtained with t_1 equals to 8 ms, 13 ms, and 18 ms, respectively. At $t_1 = 8$ ms, the experimental error propagation data (black line) goes below the SQL (red line) from $\Phi \approx 2\pi \times 0.56$ to $\Phi \approx 2\pi \times 0.59$. The maximum gain is found at $\Phi = 2\pi \times 0.575$ with $G = 4.77$ dB. For comparison, the TWA simulated error propagation shown in the black dashed line has the maximum gain at $\Phi = 2\pi \times 0.66$ with $G = 5.53$ dB. In Fig. 8.10b, where $t_1 = 13$ ms, the experimental error propagation data is within the error band of the SQL, indicating little metrological enhancement in this interferometry. The TWA simulated error propagation data is closer to the SQL than that in Fig. 8.10a shows the metrological advantage of the interferometry is theoretically weaker at $t_1 = 13$ ms than $t_1 = 8$ ms. In Fig. 8.10c, experimental data is above the SQL indicates no metrological gain is obtained when $t_1 = 18$ ms.

It must be pointed out that the discrepancies between the experimental data and

the TWA simulations are still somewhat large in both Fig. 8.9 and Fig. 8.10. It might be explained from two different perspectives: (1) From the theoretical point of view, with 10% of initial seeding, after several milliseconds of spin-mixing dynamics, lots of atoms are coupled from $|F = 1, m = 0\rangle$ state to $|F = 1, m = \pm 1\rangle$ states. The system is in a deeply entangled regime where the undepleted pump approximation [148] cannot capture the dynamics of the system very well. Therefore, a full quantum calculation might be better to describe the system [150]. (2) From the experimental point of view, atom number fluctuations from one experiment realization to another and atom loss during one experimental cycle, will cause the realistic spin-mixing interferometer to exhibit a significant deviation between the experimental data and the theoretical simulation.

Generally speaking, our experimental phase sensitivity data suggests that our spin-mixing interferometry with seeded states and intermediate time evolution beats the standard quantum limit. However, when increasing the spin evolution time, the results are perturbed by fluctuations. There are several things we can do to improve the interferometry performance at a longer spin evolution time. On the one hand, since the error propagation method relies on calculating the derivative of the actual atom number in $|F = 1,\ m = \pm 1\rangle$ states with respect to the phase change, we can increase the data resolution by narrowing the step size, increasing the accuracy of data interpolation, and improving the error propagation method. On the other hand, taking much more data for each point and doing appropriate post-selection on atom numbers can help to narrow the uncertainty in the future.

8.4 Summary

We demonstrated experimental spin-mixing interferometry with microwave-dressed $F = 1$ anti-ferromagnetic sodium spinor BECs. Contrary to previous work, our

interferometer operates with seeded initial states and in the regime of intermediate to long evolution time. We analyzed the metrological enhancement which suggests gain of up to 4.77 dB beyond the standard quantum limit for certain operating parameters and evolution times which starting with 10% seeded initial states. Our experiment is currently limited by technical noise such as shot-to-shot number fluctuations and atom loss from the trap.

Chapter 9

Conclusions

9.1 Final Remarks

This final chapter summarises the thesis and also concludes my seven-plus years as a Ph.D. student. I joined the group in January 2016. I still remember the first time I walked into the lab, and there were just a few optics on the optical tables. We built up the experimental system from the ground up. In May 2016, we created our first sodium MOT, which was a very tiny yellow dot. After another two years of hard work, we finally achieved our sodium spinor BECs in January 2018. Our experimental system was then optimized to provide a BEC of $\sim 10^4$ sodium atoms in our daily experiments. From 2019 to 2022, we performed interesting experiments using our BEC to study spin dynamics and atom interferometry. We also had challenges: 2020 was a hard year like no other. We had to shut down the lab for more than a half year due to the Covid-19 pandemic and slowly recovered to normal life after the university reopened. On July 16th, 2022, I finished taking the last data in the old lab in Nielsen Hall 360, and a day later, we started to move to our new lab in Lin Hall, where we will have a brand new laboratory to begin a new journey. It has been an unforgettable experience to witness a lab built from nothing.

In this thesis, we showed our experimental demonstration of the first all-optical Bose-Einstein Condensation with sodium atoms at the University of Oklahoma. The sodium atoms were loaded from the MOT in an optical dipole trap created by two focused laser beams intersecting at the center of the ultra-high vacuum chamber under a 90° angle. The atoms were subsequently evaporatively cooled down to quantum degeneracy by ramping down the laser power with two exponential ramps. BECs with an internal spin degree of freedom, also called spinor BECs, offer rich opportunities

to explore quantum dynamics since the spins can interact with each other to create entanglement, spin squeezing, and exotic many body states. The dynamics are controllable via external magnetic and microwave fields.

Using the spinor BEC as a platform, we observed coherent spin population oscillations after quenching the system using a microwave-dressed field. This type of spin oscillation dynamics was thought to be well described using the mean-field theory and the single-mode approximation, which assumes that the different hyperfine states share the same time-independent spatial mode. This implies that the resulting spin Hamiltonian only depends on the spin interaction strength and not on the density interaction strength. However, we experimentally observed, in certain parameter regimes, an upward drifting on a coherent spin oscillation at long spin evolution time, which is beyond the single-mode approximation physics. The theory group of Dr. Blume helped us to verify the drifting dynamic, which is a dynamically-induced mean-field driven resonance mechanism resulting from the coupling between the spin and spatial degrees of freedom of the spinor wave function, can be predicted by solving a set of coupled mean-field Gross-Pitaevskii equations. The resonance we observed and mapped is a new type of spin-spatial coupling resonance driven by the mean-field not by the quantum fluctuating.

In our spin-mixing atom interferometer experiments, we experimentally demonstrated two types of interferometry based on the different initial states: single-sided seeding interferometers and double-sided seeding interferometers. Our spin-mixing atom interferometers rely on the entangled states generated via spin-exchange collisions. We use the entangled states as the probe states and perform an interferometer mechanism that contains three major steps: "splitting", phase imprinting, and "recombining". We experimentally show the interference pattern in terms of the fractional in $|F = 1,\ m = 0\rangle$ as a function of the imprinted phase at a different spin-mixing time.

We also calculated the phase sensitivity of the interferometers at different times and compared it with the standard quantum limits, quantum Cramér-Rao Bound and the Heisenberg sensitivity limit. Our results show the metrological gain of sensitivities using our nonlinear interferometry schemes in the intermediate time of spin evolution. Specifically, we obtained a metrological gain of 3.96 dB in the single-sided atom interferometer with spin-mixing time $t_1 = 10$ ms and 4.77 dB in the double-sided atom interferometer with spin-mixing time $t_1 = 8$ ms. Our current research on spin-mixing interferometry paves the way for light-pulse atom interferometry, which involves the coupling between the spin and momentum degrees of freedom, which is planned for the future.

9.2 Future Plans

In early August 2022, we moved our lab from the third floor of Nielsen Hall to the basement of the new Lin Hall, where the new laboratories meet the NIST-A requirements on vibrations, temperature, and humidity, as well as electromagnetic interference. With this world-class research facility, our future experiments will be performed in low-noise and high-stability environments, which is especially important for precision measurement experiments, such as atom interferometry. After setting up the new laboratory, we plan to extend the spin-mixing interferometry to the light-pulse interferometry, transferring entanglement from the spin degree of freedom to well-separated momentum modes.

Our Mach-Zehnder light-pulse atom interferometry relies on coherently splitting and recombining the matter waves after generating entangled pairs of atoms in $|F = 1,\ m = \pm 1\rangle$ states via spin-exchange collisions. The spatially-dependent splitting and recombining of the matter-wave are realized by transferring the momentum from light pulses to atoms via either Raman diffraction or Bragg diffraction mechanism,

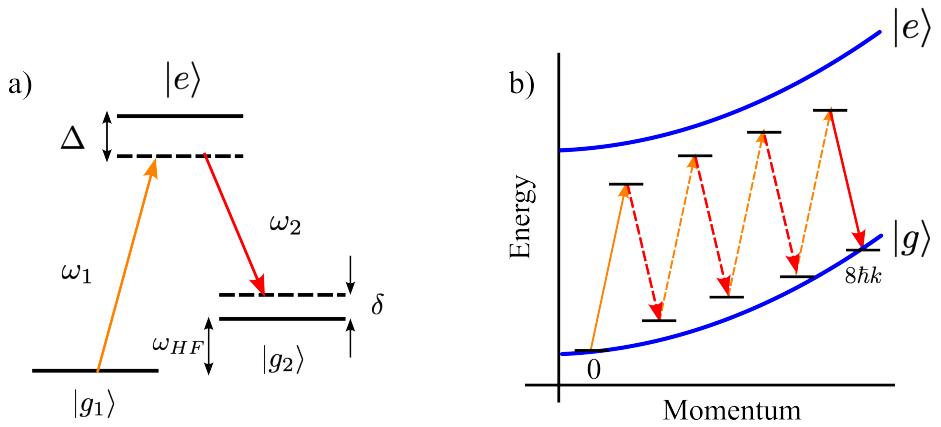

Figure 9.1: Energy diagrams of different light pulse schemes for interferometry. Energies are not drawn to scale. (a) Raman diffraction is realized with a two-photon transition in a three-level system. Atoms are transferred from the ground states $|g_1\rangle$ to $|g_2\rangle$ via an exited state $|e\rangle$ with two-photon detuning δ and one-photon detuning Δ. (b) Bragg diffraction with n=4 Bragg order and $8\hbar k$ momentum has been transferred. Solid lines are the resonance transition between the initial and final momentum states. Dashed lines are virtual transitions.

depicted in Fig. 9.1. In Raman diffraction, as shown in Fig. 9.1a, the internal state changes during the two-photon process from the ground states $|g_1\rangle$ to $|g_2\rangle$ via an exited state $|e\rangle$. The momentum gain is equal to $2\hbar k$. In contrast to Raman diffraction, Bragg diffraction does not involve any change in the internal states. In fact, it is possible to choose a high diffraction order, as shown in Fig. 9.1b, to achieve high momentum-splitting. By choosing a nth Bragg order, atoms coherently scatter $2n$ photons and gain a momentum of $2n\hbar k$. One of the drawbacks of using the Bragg diffraction scheme is that high-powered laser beams are mandatory to achieve high-order multiphoton Bragg diffraction [154]. Therefore, we plan to use Raman diffraction first to transfer $2\hbar k$ momentum to atoms.

The schematic of our Mach-Zehnder light-pulse atom interferometer is shown in Fig. 9.2a. It consists of three stimulated Raman pulses separated with free propagation

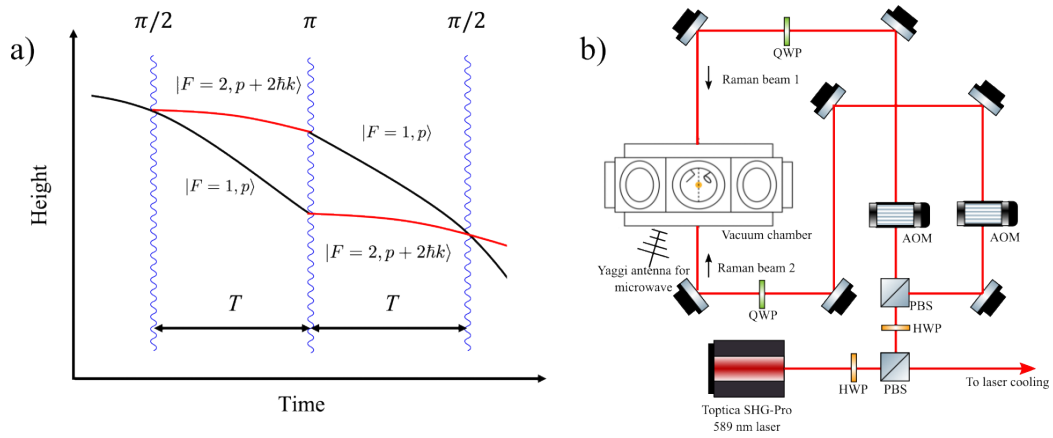

Figure 9.2: (a) Mach-Zehnder light-pulse atom interferometry. A sequence of three Raman pulses ($\pi/2$-π-$\pi/2$ configuration) is applied to a free-falling BEC separated with free propagation time of T. Atoms exchange between two ground states F=1 and F=2 as well as their momentum due to the sequence of three Raman pulses. (b) A simplified optical layout for generating stimulated Raman pulses.

time of T, and each of them couples the two hyperfine ground states of ^{23}Na ($F = 1$ and $F = 2$ states). The first pulse spatially separates the atomic cloud and prepares a superposition of the states with the same weight for both $|F = 1,\ p\rangle$ and $|F = 2,\ p + 2\hbar k\rangle$ states to implement a matter-wave beam splitter ("$\pi/2$" pulse). The second light pulse ("π" pulse) redirects and exchanges the internal states and momentum modes of the two clouds and implements a matter-wave mirror. The final light pulse (another "$\pi/2$" pulse), recombines the two wave packets and causes them to interfere at the output. A simplified optical layout for generating stimulated Raman pulses is illustrated in Fig. 9.2b. During the evaporation cooling stage, the MOT cooling and repumping beam will be redirected to generate the stimulated Raman pulses, which are detuned by 800 MHz with two AOMs. After the entangled BECs are released from the optical trap, a sequence of three counter-propagating circularly-polarized Raman pulses is applied to realize the interferometry. With this setup, we will study several questions such as (1) what is the role of spin-exchange collisions

in light-pulse atom interferometry; (2) Can we achieve quantum-enhanced sensitivity in the light-pulse atom interferometer; (3) What are the effects of decoherence and losses on the light-pulse atom interferometer?

The spinor BEC system is a fascinating prototyping system to learn in detail about future quantum technologies such as quantum enhanced sensors and quantum parametric amplifiers. It allows us to gain insight into exotic squeezed and many-body quantum states. Although our current system is more of a prototyping system that allow us to learn about the fundamentals of atom interferometry in spin space, one can imagine that, in the future, such systems could be miniaturized and become practical for real world field applications. For example, a BEC setup has recently been ruggedized in a box of a few feet side length and installed on the international space station as a turn-key system. In the future, one could imagine future miniaturization using small size vacuum chamber, atom chips, pyramid MOT beams and integrated opto-electronic diode laser system.

References

[1] W. Ketterle, D. S. Durfee, and D. M. Stamper-Kurn, "Making, probing and understanding Bose-Einstein condensates," arXiv:cond-mat/9904034 (1999).

[2] D. D. Osheroff, R. C. Richardson, and D. M. Lee, "Evidence for a New Phase of Solid He^3," Phys. Rev. Lett. **28**, 885 (1972).

[3] D. D. Osheroff, W. J. Gully, R. C. Richardson, and D. M. Lee, "New Magnetic Phenomena in Liquid He^3 below 3 mK," Phys. Rev. Lett. **29**, 920 (1972).

[4] D. J. Wineland and H. Dehmel, "Proposed 1014 $\Delta\upsilon < \upsilon$ laser fluorescence spectroscopy on t1+ mono-ion oscillator iii," Bull. Am. Phys. Soc. **20**, 637 (1975).

[5] T. Hänsch and A. Schawlow, "Cooling of gases by laser radiation," Optics Communications **13**, 68 (1975).

[6] A. Ashkin, "Acceleration and Trapping of Particles by Radiation Pressure," Phys. Rev. Lett. **24**, 156 (1970).

[7] D. J. Wineland, R. E. Drullinger, and F. L. Walls, "Radiation-Pressure Cooling of Bound Resonant Absorbers," Phys. Rev. Lett. **40**, 1639 (1978).

[8] W. D. Phillips and H. Metcalf, "Laser Deceleration of an Atomic Beam," Phys. Rev. Lett. **48**, 596 (1982).

[9] S. Chu, L. Hollberg, J. E. Bjorkholm, A. Cable, and A. Ashkin, "Three-dimensional viscous confinement and cooling of atoms by resonance radiation pressure," Phys. Rev. Lett. **55**, 48 (1985).

[10] E. L. Raab, M. Prentiss, A. Cable, S. Chu, and D. E. Pritchard, "Trapping of Neutral Sodium Atoms with Radiation Pressure," Phys. Rev. Lett. **59**, 2631 (1987).

[11] A. Aspect, E. Arimondo, R. Kaiser, N. Vansteenkiste, and C. Cohen-Tannoudji, "Laser Cooling below the One-Photon Recoil Energy by Velocity-Selective Coherent Population Trapping," Phys. Rev. Lett. **61**, 826 (1988).

[12] X. Luo, Y. Zou, L. Wu, Q. Liu, M. Han, M. Tey, and L. You, "Deterministic entanglement generation from driving through quantum phase transitions," Science **355**, 620 (2017).

[13] A. Vinit and C. Raman, "Precise measurements on a quantum phase transition in antiferromagnetic spinor Bose-Einstein condensates," Phys. Rev. A **95**, 011603 (2017).

[14] K. Jiménez-García, A. Invernizzi, B. Evrard, C. Frapolli, J. Dalibard, and F. Gerbier, "Spontaneous formation and relaxation of spin domains in antiferromagnetic spin-1 condensates," Nature Communications **10**, 1422 (2019).

[15] M. R. Matthews, B. P. Anderson, P. C. Haljan, D. S. Hall, C. E. Wieman, and E. A. Cornell, "Vortices in a Bose-Einstein Condensate," Phys. Rev. Lett. **83**, 2498 (1999).

[16] C. Cheng, G. Rudolf, J. Paul, and T. Eite, "Feshbach resonances in ultracold gases," Rev. Mod. Phys. **82**, 1225 (2010).

[17] R. Mohit and T. Edward, "Crossover from Bardeen-Cooper-Schrieffer to Bose-Einstein Condensation and the Unitary Fermi Gas," Annual Review of Condensed Matter Physics **5**, 209 (2014).

[18] G. Markus, M. Olaf, E. Tilman, H. T. W., and B. Immanuel, "Quantum phase transition from a superfluid to a Mott insulator in a gas of ultracold atoms," Nature **415**, 39 (2002).

[19] J. Léonard, A. Morales, P. Zupancic, T. Esslinger, and T. Donner, "Supersolid formation in a quantum gas breaking a continuous translational symmetry," Nature **543**, 87 (2017).

[20] J. Li, J. Lee, W. Huang, S. Burchesky, B. Shteynas, F. Top, A. O. Jamison, and W. Ketterle, "A stripe phase with supersolid properties in spin–orbit-coupled Bose–Einstein condensates," Nature **543**, 91 (2017).

[21] F. Anders, A. Idel, P. Feldmann, D. Bondarenko, S. Loriani, K. Lange, J. Peise, M. Gersemann, B. Meyer-Hoppe, S. Abend, N. Gaaloul, C. Schubert, D. Schlippert, L. Santos, E. Rasel, and C. Klempt, "Momentum Entanglement for Atom Interferometry," Phys. Rev. Lett. **127**, 140402 (2021).

[22] J. F. Barry, D. J. McCarron, E. B. Norrgard, M. H. Steinecker, and D. DeMille, "Magneto-optical trapping of a diatomic molecule," Nature **512**, 286 (2014).

[23] L. Anderegg, B. L. Augenbraun, E. Chae, B. Hemmerling, N. R. Hutzler, A. Ravi, A. Collopy, J. Ye, W. Ketterle, and J. M. Doyle, "Radio Frequency Magneto-Optical Trapping of CaF with High Density," Phys. Rev. Lett. **119**, 103201 (2017).

[24] S. Truppe, H. J. Williams, M. Hambach, L. Caldwell, N. J. Fitch, E. A. Hinds, B. E. Sauer, and M. R. Tarbutt, "Molecules cooled below the Doppler limit," Nature Physics **13**, 1173 (2017).

[25] A. L. Collopy, S. Ding, Y. Wu, I. A. Finneran, L. Anderegg, B. L. Augenbraun, J. M. Doyle, and J. Ye, "3D Magneto-Optical Trap of Yttrium Monoxide," Phys. Rev. Lett. **121**, 213201 (2018).

[26] S.Falke, N. Lemke, C. Grebing, B. Lipphardt, S. Weyers, V. Gerginov, N. Huntemann, C. Hagemann, A. Al-Masoudi, S. Häfner, S. Vogt, U. Sterr, and C. Lisdat, "A strontium lattice clock with 3×10^{-17} inaccuracy and its frequency," New Journal of Physics **16**, 073023 (2014).

[27] T. Kobayashi, D. Akamatsu, K. Hosaka, Y. Hisai, M. Wada, H. Inaba, T. Suzuyama, F. Hong, and M. Yasuda, "Demonstration of the nearly continuous operation of an ^{171}Yb lattice clock for half a year," Metrologia **57**, 065021 (2020).

[28] P. Cheiney, L. Fouché, S. Templier, F. Napolitano, B. Battelier, P. Bouyer, and B. Barrett, "Navigation-Compatible Hybrid Quantum Accelerometer Using a Kalman Filter," Phys. Rev. Applied **10**, 034030 (2018).

[29] R. Geiger, V. Ménoret, G. Stern, N. Zahzam, P. Cheinet, B. Battelier, A. Villing, F. Moron, M. Lours, Y. Bidel, A. Bresson, A. Landragin, and P. Bouyer, "Detecting inertial effects with airborne matter-wave interferometry," Nature Communications **2**, 474 (2011).

[30] A. Browaeys and T. Lahaye, "Many-body physics with individually controlled Rydberg atoms," Nature Physics **16**, 132 (2020).

[31] S. Ebadi, A. Keesling, M. Cain, T. T. Wang, H. Levine, D. Bluvstein, G. Semeghini, A. Omran, J.-G. Liu, R. Samajdar, X.-Z. Luo, B. Nash, X. Gao, B. Barak, E. Farhi, S. Sachdev, N. Gemelke, L. Zhou, S. Choi, H. Pichler, S.-T. Wang, M. Greiner, V. Vuletić, and M. D. Lukin, "Quantum optimization of maximum independent set using Rydberg atom arrays," Science **376**, 1209 (2022).

[32] J. Wurtz, P. L. S. Lopes, N. Gemelke, A. Keesling, and S. Wang, "Industry applications of neutral-atom quantum computing solving independent set problems," 2022.

[33] H. J. Metcalf and P. van der Straten, "Laser cooling and trapping of atoms," J. Opt. Soc. Am. B **20**, 887 (2003).

[34] S. Chu, J. E. Bjorkholm, A. Ashkin, and A. Cable, "Experimental Observation of Optically Trapped Atoms," Phys. Rev. Lett. **57**, 314 (1986).

[35] C. J. Foot, *Atomic physics* (Oxford, Oxford; New York, 2005).

[36] J. Dalibard and C. Cohen-Tannoudji, "Laser cooling below the Doppler limit by polarization gradients: simple theoretical models," J. Opt. Soc. Am. B **6**, 2023 (1989).

[37] D. S. Weiss, E. Riis, Y. Shevy, P. J. Ungar, and S. Chu, "Optical molasses and multilevel atoms: experiment," J. Opt. Soc. Am. B **6**, 2072 (1989).

[38] M. Vangeleyn, P. F. Griffin, E. Riis, and A. S. Arnold, "Single-laser, one beam, tetrahedral magneto-optical trap," Opt. Express **17**, 13601 (2009).

[39] K. Dieckmann, R. J. C. Spreeuw, M. Weidemüller, and J. T. M. Walraven, "Two-dimensional magneto-optical trap as a source of slow atoms," Phys. Rev. A **58**, 3891 (1998).

[40] C. C. Nshii, M. Vangeleyn, J. P. Cotter, P. F. Griffin, E. A. Hinds, C. N. Ironside, P. See, A. G. Sinclair, E. Riis, and A. S. Arnold, "A surface-patterned chip as a strong source of ultracold atoms for quantum technologies," Nature Nanotechnology **8**, 321 (2013).

[41] D. A. Steck, "Sodium D line data," Report, Los Alamos National Laboratory, Los Alamos **124**, 74 (2000).

[42] F. Papoff, F. Mauri, and E. Arimondo, "Transient velocity-selective coherent population trapping in one dimension," J. Opt. Soc. Am. B **9**, 321 (1992).

[43] A. J. Kerman, V. Vuletić, C. Chin, and S. Chu, "Beyond Optical Molasses: 3D Raman Sideband Cooling of Atomic Cesium to High Phase-Space Density," Phys. Rev. Lett. **84**, 439 (2000).

[44] H. F. Hess, "Evaporative cooling of magnetically trapped and compressed spin-polarized hydrogen," Phys. Rev. B **34**, 3476 (1986).

[45] C. S. Adams, H. Lee, N. Davidson, M. Kasevich, and S. Chu, "Evaporative Cooling in a Crossed Dipole Trap," Phys. Rev. Lett. **74**, 3577 (1995).

[46] K. B. Davis, M. Mewes, M. A. Joffe, M. R. Andrews, and W. Ketterle, "Evaporative Cooling of Sodium Atoms," Phys. Rev. Lett. **74**, 5202 (1995).

[47] S. V. Kagwade, C. R. Clayton, D. Chidambaram, and G. P. Halada, "Photochemical breakdown of acetone on copper," Electrochimica Acta **46**, 2337 (2001).

[48] C. Klempt, T. van Zoest, T. Henninger, O. Topic, E. Rasel, W. Ertmer, and J. Arlt, "Ultraviolet light-induced atom desorption for large rubidium and potassium magneto-optical traps," Phys. Rev. A **73**, 013410 (2006).

[49] A. L. Schawlow, "Spectroscopy in a new light," Rev. Mod. Phys. **54**, 697 (1982).

[50] D. W. Preston, "Doppler-free saturated absorption: Laser spectroscopy," American Journal of Physics **64**, 1432 (1996).

[51] K. B. MacAdam, A. Steinbach, and C. Wieman, "A narrow-band tunable diode laser system with grating feedback, and a saturated absorption spectrometer for Cs and Rb," American Journal of Physics **60**, 1098 (1992).

[52] G. B. Armen, "Phase sensitive detection: the lock-in amplifier," Department of Physics and Astronomy, The University of Tennessee (2008).

[53] C. C. Bradley, J. G. Story, J. J. Tollett, J. Chen, N. W. M. Ritchie, and R. G. Hulet, "Laser cooling of lithium using relay chirp cooling," Opt. Lett. **17**, 349 (1992).

[54] A. S. Parkins and P. Zoller, "Laser cooling of atoms with broadband real Gaussian laser fields," Phys. Rev. A **45**, 6522 (1992).

[55] H. Cheng, W. Zhang, H. Ma, L. Liu, and Y. Wang, "Laser cooling of rubidium atoms from background vapor in diffuse light," Phys. Rev. A **79**, 023407 (2009).

[56] S. C. Bell, M. Junker, M. Jasperse, L. D. Turner, Y.-J. Lin, I. B. Spielman, and R. E. Scholten, "A slow atom source using a collimated effusive oven and a single-layer variable pitch coil Zeeman slower," Review of Scientific Instruments **81**, 013105 (2010).

[57] K. Hue, N. Luick, L. Sobirey, J. Siegl, T. Lompe, H. Moritz, L. W. Clark, and C. Chin, "Calibrating high intensity absorption imaging of ultracold atoms," Opt. Express **25**, 8670 (2017).

[58] D. A. Smith, S. Aigner, S. Hofferberth, M. Gring, M. Andersson, S. Wildermuth, P. Krüger, S. Schneider, T. Schumm, and J. Schmiedmayer, "Absorption imaging of ultracold atoms on atom chips," Opt. Express **19**, 8471 (2011).

[59] I. Serre, L. Pruvost, and H. Duong, "Fluorescence imaging efficiency of cold atoms in free fall," Appl. Opt. **37**, 1016 (1998).

[60] J. F. Sherson, C. Weitenberg, M. Endres, M. Cheneau, I. Bloch, and S. Kuhr, "Single-atom-resolved fluorescence imaging of an atomic Mott insulator," Nature **467**, 68 (2010).

[61] W. Muessel, H. Strobel, M. Joos, E. Nicklas, I. Stroescu, J. Tomkovič, D. B. Hume, and M. K. Oberthaler, "Optimized absorption imaging of mesoscopic atomic clouds," Applied Physics B **113**, 69 (2013).

[62] M.-S. Chang, "Coherent spin dynamics of a spin-1 Bose-Einstein condensate," Ph.D. thesis, Georgia Institute of Technology, 2006.

[63] X. Li, F. Zhou, M. Ke, P. Xu, X.-D. He, J. Wang, and M.-S. Zhan, "High-resolution ex vacuo objective for cold atom experiments," Appl. Opt. **57**, 7584 (2018).

[64] T. Li, J. Huang, Q. Qu, B. Wang, L. Li, W. Ren, W. Shi, J. Zhao, X. Zhao, J. Ji, M. Ye, Y. Yao, D. Lü, Y. Wang, W. Chen, and L. Liu, "Space qualified microwave source for cold atom clock operating in orbit," Review of Scientific Instruments **89**, 113115 (2018).

[65] I. Morgenstern, S. Zhong, Q. Zhang, L. Baker, J. Norris, B. Tran, and A. Schwettmann, "A versatile microwave source for cold atom experiments controlled by a field programmable gate array," Review of Scientific Instruments **91**, 023202 (2020).

[66] P. Treutlein, T. W. Hänsch, J. Reichel, A. Negretti, M. A. Cirone, and T. Calarco, "Microwave potentials and optimal control for robust quantum gates on an atom chip," Phys. Rev. A **74**, 022312 (2006).

[67] N. J. Engelsen, R. Krishnakumar, O. Hosten, and M. A. Kasevich, "Bell Correlations in Spin-Squeezed States of 500 000 Atoms," Phys. Rev. Lett. **118**, 140401 (2017).

[68] P. Böhi, M. F. Riedel, J. Hoffrogge, J. Reichel, T. W. Hänsch, and P. Treutlein, "Coherent manipulation of Bose–Einstein condensates with state-dependent microwave potentials on an atom chip," Nature Physics **5**, 592 (2009).

[69] M. Tanasittikosol, J. D. Pritchard, D. Maxwell, A. Gauguet, K. J. Weatherill, R. M. Potvliege, and C. S. Adams, "Microwave dressing of Rydberg dark states," Journal of Physics B: Atomic, Molecular and Optical Physics **44**, 184020 (2011).

[70] G. Breit and I. I. Rabi, "Measurement of Nuclear Spin," Phys. Rev. **38**, 2082 (1931).

[71] C. D. Hamley, "Spin-nematic squeezing in a spin-1 Bose-Einstein condensate," Ph.D. thesis, Georgia Institute of Technology, 2012.

[72] F. Gerbier, A. Widera, S. Fölling, O. Mandel, and I. Bloch, "Resonant control of spin dynamics in ultracold quantum gases by microwave dressing," Phys. Rev. A **73**, 041602 (2006).

[73] L. Zhao, J. Jiang, T. Tang, M. Webb, and Y. Liu, "Dynamics in spinor condensates tuned by a microwave dressing field," Phys. Rev. A **89**, 023608 (2014).

[74] S. R. A. Leslie, "On spinor condensates as amplifiers, sensors and tunable quantum playgrounds for studies of spin," Ph.D. thesis, University of California, Berkeley, 2008.

[75] T. Oberschulte, T. Wendrich, and H. Blume, "FPGA-based low-cost synchronized fiber network for experimental setups in space," Journal of Instrumentation **16**, P11016 (2021).

[76] A. Schwettmann, J. Sedlacek, and J. P. Shaffer, "Field-programmable gate array based locking circuit for external cavity diode laser frequency stabilization," Review of Scientific Instruments **82**, 103103 (2011).

[77] I. D. Conway Lamb, J. I. Colless, J. M. Hornibrook, S. J. Pauka, S. J. Waddy, M. K. Frechtling, and D. J. Reilly, "An FPGA-based instrumentation platform for use at deep cryogenic temperatures," Review of Scientific Instruments **87**, 014701 (2016).

[78] A. D. Inc., *A technical tutorial on digital signal synthesis*, 1999.

[79] S. N. Bose, "Planck's Gesetz und Lichtquantenhypothese," Zeitschrift für Physik **26**, 178 (1924).

[80] A. Einstein, "Quantum Theory of a Monoatomic Ideal Gas A Translation of Quantentheorie Des Einatomigen Idealen Gases (Einstein, 1924)," 1925.

[81] F. London, "The λ-Phenomenon of Liquid Helium and the Bose-Einstein Degeneracy," Nature **141**, 643 (1938).

[82] L. Tisza, "Transport Phenomena in Helium II," Nature **141**, 913 (1938).

[83] D. A. Bell, H. F. Hess, G. P. Kochanski, S. Buchman, L. Pollack, Y. M. Xiao, D. Kleppner, and T. J. Greytak, "Relaxation and recombination in spin-polarized atomic hydrogen," Phys. Rev. B **34**, 7670 (1986).

[84] H. F. Hess, "Evaporative cooling of magnetically trapped and compressed spin-polarized hydrogen," Phys. Rev. B **34**, 3476 (1986).

[85] D. G. Fried, T. C. Killian, L. Willmann, D. Landhuis, S. C. Moss, D. Kleppner, and T. J. Greytak, "Bose-Einstein Condensation of Atomic Hydrogen," Phys. Rev. Lett. **81**, 3811 (1998).

[86] E. A. Cornell and C. E. Wieman, "Nobel Lecture: Bose-Einstein condensation in a dilute gas, the first 70 years and some recent experiments," Rev. Mod. Phys. **74**, 875 (2002).

[87] W. Ketterle, "Nobel lecture: When atoms behave as waves: Bose-Einstein condensation and the atom laser," Rev. Mod. Phys. **74**, 1131 (2002).

[88] C. C. Bradley, C. A. Sackett, J. J. Tollett, and R. G. Hulet, "Evidence of Bose-Einstein Condensation in an Atomic Gas with Attractive Interactions," Phys. Rev. Lett. **75**, 1687 (1995).

[89] D. M. Stamper-Kurn, M. R. Andrews, A. P. Chikkatur, S. Inouye, H.-J. Miesner, J. Stenger, and W. Ketterle, "Optical Confinement of a Bose-Einstein Condensate," Phys. Rev. Lett. **80**, 2027 (1998).

[90] T. Weber, J. Herbig, M. Mark, H. Nägerl, and R. Grimm, "Bose-Einstein Condensation of Cesium," Science **299**, 232 (2003).

[91] Y. Takasu, K. Maki, K. Komori, T. Takano, K. Honda, M. Kumakura, T. Yabuzaki, and Y. Takahashi, "Spin-Singlet Bose-Einstein Condensation of Two-Electron Atoms," Phys. Rev. Lett. **91**, 040404 (2003).

[92] S. Kraft, F. Vogt, O. Appel, F. Riehle, and U. Sterr, "Bose-Einstein Condensation of Alkaline Earth Atoms: ^{40}Ca," Phys. Rev. Lett. **103**, 130401 (2009).

[93] S. Stellmer, M. Tey, B. Huang, R. Grimm, and F. Schreck, "Bose-Einstein Condensation of Strontium," Phys. Rev. Lett. **103**, 200401 (2009).

[94] Y. N. Martinez de Escobar, P. G. Mickelson, M. Yan, B. J. DeSalvo, S. B. Nagel, and T. C. Killian, "Bose-Einstein Condensation of ^{84}Sr," Phys. Rev. Lett. **103**, 200402 (2009).

[95] K. Aikawa, A. Frisch, M. Mark, S. Baier, A. Rietzler, R. Grimm, and F. Ferlaino, "Bose-Einstein Condensation of Erbium," Phys. Rev. Lett. **108**, 210401 (2012).

[96] A. Griesmaier, J. Werner, S. Hensler, J. Stuhler, and T. Pfau, "Bose-Einstein Condensation of Chromium," Phys. Rev. Lett. **94**, 160401 (2005).

[97] M. Lu, N. Q. Burdick, S. Youn, and B. L. Lev, "Strongly Dipolar Bose-Einstein Condensate of Dysprosium," Phys. Rev. Lett. **107**, 190401 (2011).

[98] Y. Miyazawa, R. Inoue, H. Matsui, G. Nomura, and M. Kozuma, "Bose-Einstein Condensation of Europium," arXiv preprint arXiv:2207.11692 (2022).

[99] J. Klaers, J. Schmitt, F. Vewinger, and M. Weitz, "Bose–Einstein condensation of photons in an optical microcavity," Nature **468**, 545 (2010).

[100] W. Greiner, L. Neise, and H. Stöcker, *Thermodynamics and Statistical Mechanics* (Springer, New York, 1995).

[101] K. Huang, *Statistical Mechanics* (Wiley, New York, 1987).

[102] F. Dalfovo, S. Giorgini, L. P. Pitaevskii, and S. Stringari, "Theory of Bose-Einstein condensation in trapped gases," Rev. Mod. Phys. **71**, 463 (1999).

[103] W. Krauth, in *Advances in Computer Simulation*, edited by J. Kertész and I. Kondor (Springer Berlin Heidelberg, Berlin, Heidelberg, 1998), pp. 1–35.

[104] N. Bogoliubov, "On the theory of superfluidity," J. Phys **11**, 23 (1947).

[105] L. P. Pitaevskii, S. Stringari, and S. Stringari, *Bose-einstein condensation* (Oxford University Press, Oxford, 2003), No. 116.

[106] E. P. Gross, "Structure of a quantized vortex in boson systems," Il Nuovo Cimento (1955-1965) **20**, 454 (1961).

[107] L. P. Pitaevskii, "Vortex lines in an imperfect Bose gas," Sov. Phys. JETP **13**, 451 (1961).

[108] C. J. Pethick and H. Smith, *Bose–Einstein Condensation in Dilute Gases*, 2 ed. (Cambridge University Press, Cambridge, 2008).

[109] N. Radwell, G. Walker, and S. Franke-Arnold, "Cold-atom densities of more than 10^{12} cm^{-3} in a holographically shaped dark spontaneous-force optical trap," Phys. Rev. A **88**, 043409 (2013).

[110] J. Kim and D. Cho, in *Proceedings of the eighth symposium on laser spectroscopy* (KAERI, Korea, Republic of, 2000), p. 353.

[111] W. Petrich, M. H. Anderson, J. R. Ensher, and E. A. Cornell, "Behavior of atoms in a compressed magneto-optical trap," J. Opt. Soc. Am. B **11**, 1332 (1994).

[112] M. Okano, H. Hara, M. Muramatsu, K. Doi, S. Uetake, Y. Takasu, and Y. Takahashi, "Simultaneous magneto-optical trapping of lithium and ytterbium atoms towards production of ultracold polar molecules," Applied Physics B **98**, 691 (2010).

[113] K. M. O'Hara, M. E. Gehm, S. R. Granade, and J. E. Thomas, "Scaling laws for evaporative cooling in time-dependent optical traps," Phys. Rev. A **64**, 051403 (2001).

[114] O. J. Luiten, M. W. Reynolds, and J. T. M. Walraven, "Kinetic theory of the evaporative cooling of a trapped gas," Phys. Rev. A **53**, 381 (1996).

[115] C. Klempt, O. Topic, G. Gebreyesus, M. Scherer, T. Henninger, P. Hyllus, W. Ertmer, L. Santos, and J. J. Arlt, "Parametric Amplification of Vacuum Fluctuations in a Spinor Condensate," Phys. Rev. Lett. **104**, 195303 (2010).

[116] C. D. Hamley, C. S. Gerving, T. M. Hoang, E. M. Bookjans, and M. S. Chapman, "Spin-nematic squeezed vacuum in a quantum gas," Nature Physics **8**, 305 (2012).

[117] B. Lücke, M. Scherer, J. Kruse, L. Pezzé, F. Deuretzbacher, P. Hyllus, O. Topic, J. Peise, W. Ertmer, J. Arlt, L. Santos, A. Smerzi, and C. Klempt, "Twin Matter Waves for Interferometry Beyond the Classical Limit," Science **334**, 773 (2011).

[118] H. Strobel, W. Muessel, D. Linnemann, T. Zibold, D. B. Hume, L. Pezzè, A. Smerzi, and M. K. Oberthaler, "Fisher information and entanglement of non-Gaussian spin states," Science **345**, 424 (2014).

[119] I. Bloch, J. Dalibard, and W. Zwerger, "Many-body physics with ultracold gases," Rev. Mod. Phys. **80**, 885 (2008).

[120] M. Vengalattore, J. M. Higbie, S. R. Leslie, J. Guzman, L. E. Sadler, and D. M. Stamper-Kurn, "High-Resolution Magnetometry with a Spinor Bose-Einstein Condensate," Phys. Rev. Lett. **98**, 200801 (2007).

[121] D. Linnemann, H. Strobel, W. Muessel, J. Schulz, R. J. Lewis-Swan, K. V. Kheruntsyan, and M. K. Oberthaler, "Quantum-Enhanced Sensing Based on Time Reversal of Nonlinear Dynamics," Phys. Rev. Lett. **117**, 013001 (2016).

[122] K. Helmerson and L. You, "Creating Massive Entanglement of Bose-Einstein Condensed Atoms," Phys. Rev. Lett. **87**, 170402 (2001).

[123] Y. Kawaguchi and M. Ueda, "Spinor Bose–Einstein condensates," Physics Reports **520**, 253 (2012).

[124] D. M. Stamper-Kurn and M. Ueda, "Spinor Bose gases: Symmetries, magnetism, and quantum dynamics," Rev. Mod. Phys. **85**, 1191 (2013).

[125] S. Knoop, T. Schuster, R. Scelle, A. Trautmann, J. Appmeier, M. K. Oberthaler, E. Tiesinga, and E. Tiemann, "Feshbach spectroscopy and analysis of the interaction potentials of ultracold sodium," Phys. Rev. A **83**, 042704 (2011).

[126] D. M. Stamper-Kurn and M. Ueda, "Spinor Bose gases: Symmetries, magnetism, and quantum dynamics," Rev. Mod. Phys. **85**, 1191 (2013).

[127] W. Zhang, D. L. Zhou, M.-S. Chang, M. S. Chapman, and L. You, "Coherent spin mixing dynamics in a spin-1 atomic condensate," Phys. Rev. A **72**, 013602 (2005).

[128] J. Jie, Q. Guan, S. Zhong, A. Schwettmann, and D. Blume, "Mean-field spin-oscillation dynamics beyond the single-mode approximation for a harmonically trapped spin-1 Bose-Einstein condensate," Phys. Rev. A **102**, 023324 (2020).

[129] M. Scherer, B. Lücke, G. Gebreyesus, O. Topic, F. Deuretzbacher, W. Ertmer, L. Santos, J. J. Arlt, and C. Klempt, "Spontaneous Breaking of Spatial and Spin Symmetry in Spinor Condensates," Phys. Rev. Lett. **105**, 135302 (2010).

[130] B. Stray, A. Lamb, A. Kaushik, J. Vovrosh, A. Rodgers, J. Winch, F. Hayati, D. Boddice, A. Stabrawa, A. Niggebaum, M. Langlois, Y. Lien, S. Lellouch, S. Roshanmanesh, K. Ridley, G. de Villiers, G. Brown, T. Cross, G. Tuckwell, A. Faramarzi, N. Metje, K. Bongs, and M. Holynski, "Quantum sensing for gravity cartography," Nature **602**, 590 (2022).

[131] M. Pitkin, S. Reid, S. Rowan, and J. Hough, "Gravitational Wave Detection by Interferometry (Ground and Space)," Living Reviews in Relativity **14**, 5 (2011).

[132] B. Barrett, G. Condon, L. Chichet, L. Antoni-Micollier, R. Arguel, M. Rabault, C. Pelluet, V. Jarlaud, A. Landragin, P. Bouyer, and B. Battelier, "Testing the universality of free fall using correlated 39K–87Rb atom interferometers," AVS Quantum Science **4**, 014401 (2022).

[133] M. Jaffe, P. Haslinger, V. Xu, P. Hamilton, A. Upadhye, B. Elder, J. Khoury, and H. Müller, "Testing sub-gravitational forces on atoms from a miniature in-vacuum source mass," Nature Physics **13**, 938 (2017).

[134] V. Giovannetti, S. Lloyd, and L. Maccone, "Quantum Metrology," Phys. Rev. Lett. **96**, 010401 (2006).

[135] C. M. Caves, "Quantum-mechanical noise in an interferometer," Phys. Rev. D **23**, 1693 (1981).

[136] B. Yurke, S. L. McCall, and J. R. Klauder, "SU(2) and SU(1,1) interferometers," Phys. Rev. A **33**, 4033 (1986).

[137] L. Pezzè, A. Smerzi, M. K. Oberthaler, R. Schmied, and P. Treutlein, "Quantum metrology with nonclassical states of atomic ensembles," Rev. Mod. Phys. **90**, 035005 (2018).

[138] Z. Zhang and L. Duan, "Generation of Massive Entanglement through an Adiabatic Quantum Phase Transition in a Spinor Condensate," Phys. Rev. Lett. **111**, 180401 (2013).

[139] J. P. Wrubel, A. Schwettmann, D. P. Fahey, Z. Glassman, H. K. Pechkis, P. F. Griffin, R. Barnett, E. Tiesinga, and P. D. Lett, "Spinor Bose-Einstein-condensate phase-sensitive amplifier for SU(1,1) interferometry," Phys. Rev. A **98**, 023620 (2018).

[140] D. Linnemann, H. Strobel, W. Muessel, J. Schulz, R. J. Lewis-Swan, K. V. Kheruntsyan, and M. K. Oberthaler, "Quantum-Enhanced Sensing Based on Time Reversal of Nonlinear Dynamics," Phys. Rev. Lett. **117**, 013001 (2016).

[141] M. Kitagawa and M. Ueda, "Squeezed spin states," Phys. Rev. A **47**, 5138 (1993).

[142] J. J. Bollinger, W. M. Itano, D. J. Wineland, and D. J. Heinzen, "Optimal frequency measurements with maximally correlated states," Phys. Rev. A **54**, R4649 (1996).

[143] H. Lee, P. Kok, and J. P. Dowling, "A quantum Rosetta stone for interferometry," Journal of Modern Optics **49**, 2325 (2002).

[144] C. Gross, T. Zibold, E. Nicklas, J. Estève, and M. K. Oberthaler, "Nonlinear atom interferometer surpasses classical precision limit," Nature **464**, 1165 (2010).

[145] R. E. Slusher, L. W. Hollberg, B. Yurke, J. C. Mertz, and J. F. Valley, "Observation of Squeezed States Generated by Four-Wave Mixing in an Optical Cavity," Phys. Rev. Lett. **55**, 2409 (1985).

[146] S. Yi, O. E. Müstecaplıoğlu, C. P. Sun, and L. You, "Single-mode approximation in a spinor-1 atomic condensate," Phys. Rev. A **66**, 011601 (2002).

[147] C. K. Law, H. Pu, and N. P. Bigelow, "Quantum Spins Mixing in Spinor Bose-Einstein Condensates," Phys. Rev. Lett. **81**, 5257 (1998).

[148] M. Gabbrielli, L. Pezzè, and A. Smerzi, "Spin-Mixing Interferometry with Bose-Einstein Condensates," Phys. Rev. Lett. **115**, 163002 (2015).

[149] Q. Liu, L. Wu, J. Cao, T. Mao, X. Li, S. Guo, M. Tey, and L. You, "Nonlinear interferometry beyond classical limit enabled by cyclic dynamics," Nature Physics **18**, 167 (2022).

[150] Q. Zhang and A. Schwettmann, "Quantum interferometry with microwave-dressed $F = 1$ spinor Bose-Einstein condensates: Role of initial states and long-time evolution," Phys. Rev. A **100**, 063637 (2019).

[151] S. L. Braunstein and C. M. Caves, "Statistical distance and the geometry of quantum states," Phys. Rev. Lett. **72**, 3439 (1994).

[152] L. Pezzé and A. Smerzi, "Entanglement, Nonlinear Dynamics, and the Heisenberg Limit," Phys. Rev. Lett. **102**, 100401 (2009).

[153] M. J. Holland and K. Burnett, "Interferometric detection of optical phase shifts at the Heisenberg limit," Phys. Rev. Lett. **71**, 1355 (1993).

[154] H. Müller, S. Chiow, Q. Long, S. Herrmann, and S. Chu, "Atom Interferometry with up to 24-Photon-Momentum-Transfer Beam Splitters," Phys. Rev. Lett. **100**, 180405 (2008).

Appendix A

Angular Momentum Coupling

Here, we assume that the orbital angular momentum $L = 0$. Since for sodium atoms the nuclear spin I is $\frac{3}{2}$ and electron spin s is $\frac{1}{2}$, the total angular momentum is $F = I + S$. Therefore, we can expand the coupled states via the compeletness relations in the uncoupled basis, $|F, M_F\rangle = \sum |I, I_z, S, S_z\rangle \langle I, I_z, S, S_z|F, M_F\rangle$:

$$\begin{aligned}
|2,2\rangle &= |\frac{3}{2},\frac{3}{2};\frac{1}{2},\frac{1}{2}\rangle \\
|2,1\rangle &= \frac{\sqrt{3}}{2}|\frac{3}{2},\frac{1}{2};\frac{1}{2},\frac{1}{2}\rangle + \frac{1}{2}|\frac{3}{2},\frac{1}{2};\frac{1}{2},-\frac{1}{2}\rangle \\
|2,0\rangle &= \frac{1}{\sqrt{2}}|\frac{3}{2},-\frac{1}{2};\frac{1}{2},\frac{1}{2}\rangle + \frac{1}{\sqrt{2}}|\frac{3}{2},\frac{1}{2};\frac{1}{2},-\frac{1}{2}\rangle \\
|2,-1\rangle &= \frac{1}{2}|\frac{3}{2},-\frac{3}{2};\frac{1}{2},\frac{1}{2}\rangle + \frac{\sqrt{3}}{2}|\frac{3}{2},-\frac{1}{2};\frac{1}{2},-\frac{1}{2}\rangle \\
|2,-2\rangle &= |\frac{3}{2},-\frac{3}{2};\frac{1}{2},-\frac{1}{2}\rangle \\
|1,1\rangle &= \frac{1}{2}|\frac{3}{2},\frac{1}{2};\frac{1}{2},\frac{1}{2}\rangle - \frac{\sqrt{3}}{2}|\frac{3}{2},\frac{3}{2};\frac{1}{2},-\frac{1}{2}\rangle \\
|1,0\rangle &= \frac{1}{\sqrt{2}}|\frac{3}{2},-\frac{1}{2};\frac{1}{2},\frac{1}{2}\rangle - \frac{1}{\sqrt{2}}|\frac{3}{2},\frac{1}{2};\frac{1}{2},-\frac{1}{2}\rangle \\
|1,-1\rangle &= \frac{\sqrt{3}}{2}|\frac{3}{2},-\frac{3}{2};\frac{1}{2},\frac{1}{2}\rangle - \frac{1}{2}|\frac{3}{2},-\frac{1}{2};\frac{1}{2},-\frac{1}{2}\rangle
\end{aligned} \tag{A.1}$$

In sodium ground hyperfine manifolds $F = 1$ and $F = 2$. The spin flip transition induced by the magnetic oscillatory field between eight $|F, M_F\rangle$ is

$$\begin{aligned}
\langle F, M_F|\sigma_i|F, M_F\rangle = &\left(\sum \langle F, M_F|I, I_z, S, S_z\rangle \langle I, I_z, S, S_z|\right) \\
&\times \sigma_i \left(\sum |I, I_z, S, S_z\rangle \langle I, I_z, S, S_z|F, M_F\rangle\right),
\end{aligned} \tag{A.2}$$

where σ_i is the Pauli spin matrix, which is defined as:

$$\sigma_x = \begin{pmatrix} 0 & 1 \\ 1 & 0 \end{pmatrix} \qquad \sigma_y = \begin{pmatrix} 0 & i \\ -i & 0 \end{pmatrix} \qquad \sigma_z = \begin{pmatrix} 1 & 0 \\ 0 & -1 \end{pmatrix}. \tag{A.3}$$

Appendix B

Bias Coils Current Control Circuits

The current control circuits of the bias coils are made of three parts: the external set point circuit, the temperature controller circuit, and the sensing circuit. Fig. B.1 shows the temperature controller circuits. The commercial temperature controllers (PTC5K-CH wavelength) can output ± 5 A control current with faster ramp time and lower noise. It receives the external set point signal at point 5. To sense the current, the current in the Helmholtz Coils is pick up at points 1 and 2, the it is fed to the sensor of the temperature controller at points 3 and 4.

The external set point circuit diagram is illustrated in Fig. B.2. The external set point value is ranged from -5 V to 5 V which is programmed from the LabVIEW. The circuit can convert a range of the LabVIEW signal to 0.5 V to 5.5 V which is a range the temperature controller can interpret.

The sensing circuit diagram is shown in Fig. B.3. The sensing circuit is designed

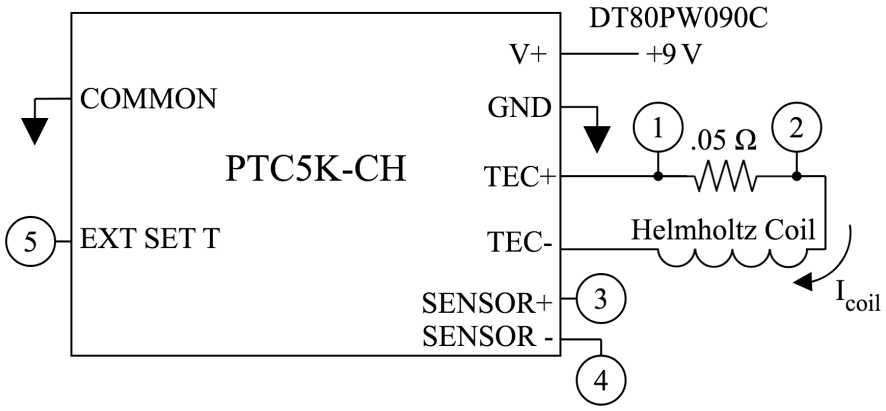

Figure B.1: Circuit diagram of the temperature controller. Point 5 receives the external set point signals. Points 1 and 2 pick up the current signal from the Helmholtz coil and send it to the sensor of the temperature controller at points 3 and 4

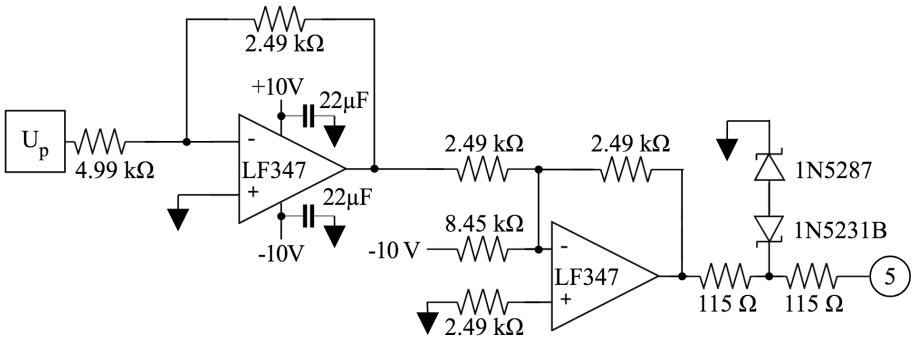

Figure B.2: Circuit diagram to generate the external set point. U_p is the signal generated from the LabVIEW.

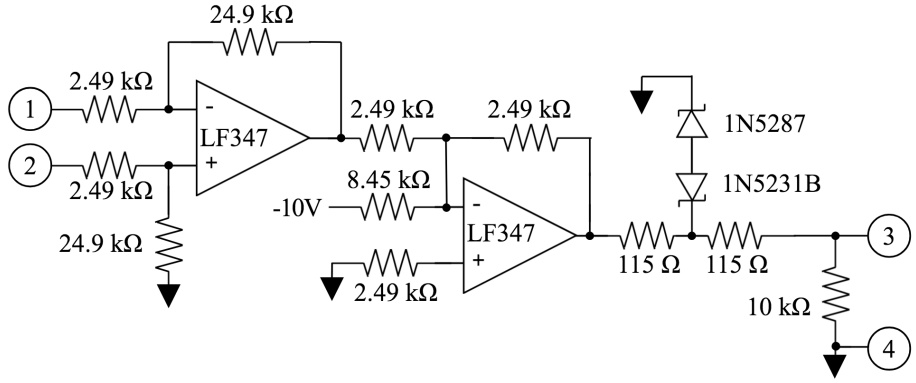

Figure B.3: Circuit diagram of the sensing circuit. The current in Helmholtz Coils is picked up in points 1 and 2, and converted to a value which can be interpreted by the temperature controller at points 3 and 4.

to sense current and present fake temperature to the temperature controller. Points 1 and 2 pick up the current in Helmholtz Coils. A 10 kΩ resistor is connected across the points 3 and 4, and work as a 10 kΩ thermistor.